DEVELOPING LASER POWDER BED FUSION TI6AL4V-REINFORCED NANOPARTICULATE COMPOSITES FOR AEROSPACE APPLICATIONS

by

MPHO MASHABELA

Dissertation submitted in fulfilment of the requirements for the degree

MASTER OF ENGINEERING

in

MECHANICAL ENGINEERING

in the

Department of Mechanical and Mechatronics Engineering

Faculty of Engineering, Built Environment, and Information Technology

at

Central University of Technology, Free State

BLOEMFONTEIN

2024

Supervisor: Prof. Maina Maringa

Co-supervisor: Dr. Thywill C. Dzogbewu

© Central University of Technology, Free State

DECLARATION OF INDEPENDENT WORK

DECLARATION WITH REGARD TO INDEPENDENT WORK

I, MPHO MASHABELA, identity number_____ and student number _____, do hereby declare that this research project submitted to Central University of Technology, Free State, for the degree, MASTER OF ENGINEERING IN MECHANICAL ENGINEERING, is my own independent work; and complies with the Code of Academic Integrity, as well as other relevant policies, procedures, rules and regulations of Central University of Technology, Free State; and has not been submitted before to any institution by myself of any other person in fulfilment (or partial fulfilment) of the requirements for the attainment of any qualification.

11/11/2024

SIGNATURE OF STUDENT **DATE**

© Central University of Technology, Free State

ABSTRACT

The aim of this research study was to investigate the reinforcement of titanium alloy Ti6Al4V(ELI) using nanoparticulate materials. Initially, titanium diboride (TiB_2) and carbon nanotubes (CNTs) were selected as suitable materials for reinforcement. However, due to the unavailability of titanium diboride in the local market, the focus was turned to CNTs due to their availability locally and their excellent properties of strength, hardness, and Young's modulus. The original intention was to have individual CNTs attached to Ti6Al4V(ELI) particles. However, agglomeration of the CNTs prevented them from successfully attaching onto Ti6Al4V(ELI) particles. Therefore, reinforcement was carried out using CNT agglomerates dispersed in Ti6Al4V(ELI). Mixing of the two powders was carried out in three separate stages using different mixing techniques for six different volume fractions of CNTs, including 3 %, 8 %, 15 %, 20 %, 25 %, and 30 %. Analysis of the mixed powder was then carried out using scanning electron microscopy (SEM) and optical microscopy used for the built tracks.

The first stage of preliminary mixing of the Ti6Al4V powder with the CNTs was carried out at two separate levels. In the first level, the two powders were mixed mechanically. In the second level, acetone and ethanol were used as dispersion agents. Dispersion of CNTs in Ti6Al4V(ELI) at both levels proved to be insufficient. However, the use of the two dispersion agents provided better dispersion compared to the dry mixing of powders. Furthermore, a comparison of the effectiveness of the two dispersion agents showed that ethanol provided better dispersion compared to acetone. Determining the effectiveness of dispersion based on the size (area and perimeter) and number of the agglomerates in each sample, it was concluded that while using acetone as a dispersant lowered the average area of agglomerates, the use of ethanol led to a wider dispersion of CNTs with a marginal increase in the average areas of CNT agglomerates at increased % volume CNTs and was thus preferable. Thus, the effectiveness of dispersion was achieved where ethanol was used compared to acetone and manual mixing. These results were quantified using a continuous statistical approach in which the agglomerates in each sample were measured. Using this approach, the agglomerates in the ethanol samples generally had smaller sizes with respect to area and perimeter as opposed to the agglomerates found in the acetone and mechanically mixed samples.

© Central University of Technology, Free State

The second stage of mixing was more rigorous and included manual mixing, turbula mixing, and mechanical-turbula-further manual mixing (hereafter referred to as combined mixing), which was done separately in this order. Combined mixing produced better dispersion and separation of CNTs. However, it also brought about defects in Ti6l4V(ELI) particles occurring from the increased manual mixing process applied in an effort to separate the CNT agglomerates. Turbula mixing was the least effective and had the greatest separation of the two powders due to the rotary mixing process inherent in it and the difference in densities between the two materials. Manual mixing was much improved from the one used in the preliminary stage due to the use of a different tool. This tool had a larger surface area than the initial tool used, providing better contact between powder particles and thus improved dispersion. The results showed that the effectiveness of mixing was better achieved at the low vol.% of CNTs in Ti6Al4V(ELI) of 3 % and 8 %. Increasing the vol.% of CNTs in Ti6Al4V(ELI) above these values led to increased agglomeration of CNTs in the mixture. The presence of single CNT fibres was observed to be more prevalent at low volume fractions of 3 % and 8 %. Although single CNTs were observed at a lower volume of CNTs, this was not at a large scale. This showed that a much-needed technique for the separation of CNTs is required.

Sodium dodecyl sulphate (SDS) was used as a surfactant in the final mixing stage. The same techniques used in the second stage of mixing were employed in this stage. In manual mixing, SDS achieved good dispersion of CNTs in Ti6l4V(ELI). However, significant agglomeration of CNTs occurred at 8 % and 30 % vol. of CNTs. The case of agglomeration at 8 % vol. of CNTs in Ti6Al4V(ELI) is an anomaly as it is expected only at higher content of CNTs. This mixing technique produced defects in the particles of Ti6Al4V(ELI) at 8 % and 25 % vol. of CNTs in Ti6Al4V(ELI). The defects occurred on the surfaces of Ti6Al4V(ELI) particles at 8 % and 25 % vol. of CNTs in Ti6Al4V(ELI). When turbula mixing was used, agglomeration of CNTs increased from 15 % to 30 % vol. of CNTs in Ti6Al4V(ELI). The number of clusters of CNTs and Ti6Al4V(ELI) particles increased at 25 % and 30 % vol. of CNTs in Ti6Al4V(ELI), likely due to the combination of SDS and increased rotational speeds of the mixer which provided more particle-particle and CNT interaction. Combined mixing produced clusters of tightly packed Ti6Al4V(ELI) particles and CNTs, which were most prominent at 8 % and 15 % vol. of CNTs in Ti6Al4V(ELI). At 20 %, 25 %, and 30 % vol. of CNTs in Ti6Al4V(ELI), increased agglomeration of CNTs was observed. The combined mixing technique produced the

© Central University of Technology, Free State

most particle defects of the three techniques used at this stage, which were observed in different forms at 3 %, 8 %, 20 %, 25 %, and 30 % vol. of CNTs in Ti6Al4V(ELI). The use of SDS produced samples with enhanced CNT attachments to Ti6Al4V(ELI) particles.

The known optimum laser scanning speed and scanning power of 0.6 ms^{-1} and 100 W, respectively, of Ti6Al4V(ELI) printed on an M2 LaserCusing® machine from Concept Laser GmbH, were used as a starting point to develop a matrix of laser scanning speeds and scanning powers for the nanocomposite. This was done based on the thermophysical properties of the two constituents and the Reuss rule for composites. Printed single tracks based on this matrix were analysed to determine the best process parameters of laser power and scanning speed from the best ones amongst them. Stable tracks were obtained at a laser power of 60 W and 80 W. However, the geometrical features produced track builds with aspect ratios above 0.5. The formation of keyholes became dominant in tracks built at laser powers of 100 W to 180 W, and the formation of pores increased for values of laser power of 160 W to 180 W. Linear energy density showed an inverse linear relationship with the scanning speed, the aspect ratio showed an initial decrease followed by an increase for the highest scanning speed. This is a behaviour similar in trend to those observed at a laser power of 60 W somewhat, and 100 W, 140 W and 160 W. The curves obtained at laser powers of 80 W and 120 W were inverted. This difference in behaviour warrants further investigation. Nonlinearity of laser energy density (LED) was observed between laser powers of 60–140 W; however, linearity occurred at laser powers of 160–180 W, which warrants further research. For all the other values of laser power used in this work, apart from 60 W, the concave upwards curves of aspect ratio and the fact of the minimum values of aspect ratio being higher than the threshold value of 0.5 imply that optimum process parameter sets of laser power and scanning speed do not exist. Further research is thus required to establish the best processing parameter sets for processing.

© Central University of Technology, Free State

ACKNOWLEDGEMENTS

Firstly, I would like to acknowledge the Creator and almighty God for the strength and perseverance He gave me to complete this degree. I then pass my acknowledgements to my supervisor and co-supervisor without who this work would not have started and come to completion.

I further acknowledge my family and friends for their encouragement, help, and prayers that have carried me through to this finale.

I acknowledge the financial support received from the South African Research Chairs Initiative of the Department of Science and Innovation and National Research Foundation of South Africa (Grant № 97994) and the Collaborative Program in Additive Manufacturing (Contract № CSIR-NLC-CPAM-21-MOA-CUT-03).

I extend my appreciation to the technical personnel from the Department of Industrial Engineering (Stellenbosch University) for their continued support and resources.

© Central University of Technology, Free State

DEDICATION

I dedicate this dissertation to my unborn children Malachi, Seetsa, Thatego, Elli, Warena, and Zachariah.

© Central University of Technology, Free State

Central University of Technology, Free State

TABLE OF CONTENTS

© Central University of Technology, Free State

© Central University of Technology, Free State

© Central University of Technology, Free State

© Central University of Technology, Free State

© Central University of Technology, Free State

© Central University of Technology, Free State

LIST OF FIGURES

© Central University of Technology, Free State

© Central University of Technology, Free State

Central University of Technology, Free State

© Central University of Technology, Free State

© Central University of Technology, Free State

© Central University of Technology, Free State

© Central University of Technology, Free State

© Central University of Technology, Free State

© Central University of Technology, Free State

© Central University of Technology, Free State

© Central University of Technology, Free State

LIST OF TABLES

© Central University of Technology, Free State

© Central University of Technology, Free State

LIST OF ABBREVIATIONS

Ai_2O_3	Aluminium oxide
AiB_2	Aluminium diboride
AiN	Aluminium nitride
$Al\ (OH)_3$	Aluminium hydroxide
AM	Additive manufacturing
B_4C	Boron carbide
$BaSO_4$	Barium sulphate
$BaTiO_3$	Barium titanate
$CaCO_3$	Calcium carbonate
CC	Carbon composites
CCNCs	Ceramic-ceramic nanocomposites
CMC	Ceramic matrix composites
CNCs	Ceramic nanocomposites
CNSs	Carbon nanostructures
CNTs	Carbon nanotubes
C_p	Specific heat capacity
CTE	Coefficient of thermal expansion
ρ	Density
DMLS	Direct metal laser sintering
FDM	Fused deposition modelling
Fe	Iron
Fe_2O_3/Fe_2O_4	Ferric oxide
GCMC	Glass matric ceramic composites
GMCs	Glass matrix composites
HAZ	Heat-affected zone
k	Thermal conductivity
LBPF	Laser powder bed fusion
LED	Linear energy density
LOM	Laminated object manufacturing
m	Metre
m/s	Metre per second

© Central University of Technology, Free State

$Mg(OH)_2$	Magnesium hydroxide
MMNCs	Metal matrix nanocomposites
mms^{-1}	Millimetre per second
MNCs	Metal nanocomposites
µm	Micrometre
μm^2	Micrometre squared
MWCNTs	Multi-walled carbon nanotubes
Nb	Niobium
Nm	Nanometre
$S.m^{-1}$	Siemens
SDS	Sodium dodecyl sulphate
SiC	Silicon carbide
SiN	Silicon nitride
SLM	Selective laser melting
SLS	Selective laser sintering
SWCNTs	Single walled carbon nanotubes
Ta	Tantalum
TaC	Tantalum carbide
3DP	Three-dimensional printing
TiB_2	Titanium diboride
TiC	Titanium carbide
TiN	Titanium nitride
TiO_2	Titanium dioxide
W	Tungsten
WC	Tungsten carbide
W	Watts
ZnO	Zinc oxide
ZrB_2	Zirconium diboride
ZrO_2	Zirconium oxide

© Central University of Technology, Free State

CHAPTER 1 - INTRODUCTION

1.1 Background

The rapid growth in the aerospace industry has led to a demand for lighter, stronger, cost-effective, and reliable materials that can also function at elevated operating temperatures. This rapid growth is largely due to a demand for new commercial aircraft, increased global military expenditure, high market activity in the space sector, and substantial as well as developing ongoing research since the COVID-19 pandemic (Blakey-Milner et al., 2021).

Aerospace materials can be classified as metal materials, inorganic non-metallic materials, polymer materials and composite materials. Each material has unique properties that make it suitable for different applications (Xia, 2023). Primary materials for structural parts of aircraft include aluminium and aluminium alloys, and steel and steel alloys. Aluminium alloys have primarily been used for both commercial and military aircraft for more than 80 years and are lightweight, easy to manufacture and have low maintenance costs (Dursun & Soutis, 2014). The first application of steel in aerospace applications was in 1915 with the Junkers J.I armoured plane, where one wing was composed of steel, which had good properties of strength and hardness. (Ouissi, et al., 2019). The demand for aluminium alloys reached their peak in World War II in 1943. Aluminium alloy Al7075 was first used in the Boeing B-29 bomber (Li et al., 2023).

The use of Ti6Al4V(ELI) in the aerospace industry has increased over the years at the expense of traditional materials such as steel and aluminium. The increased use of Ti6Al4V(ELI) is due to its low density, high corrosion resistance, high specific strength, low coefficient of thermal expansion, and lack of galvanic corrosion at joints with carbon fibre/epoxy resin composites (Henriques, 2009; Eliaz, 2019). The low coefficient of thermal expansion (CTE) of Ti6Al4V of 8.6 W/m.K makes it more compatible with carbon fibre-reinforced polymers (CFRPs) with CTEs of 1.6 W/m.K than steel and aluminium (Budhe et al., 2018).

Cost reductions in aircraft operation and purchase have become a driving force for many airline companies (Martin & Roman, 2010). Cost reduction can be achieved by reducing fuel consumption through weight reduction of the aircraft. Weight reduction

© Central University of Technology, Free State

not only reduces fuel consumption but also increases payload and range. The need for improved and optimised materials with reference to their mechanical properties can lead to a longer period between maintenance and repairs on aircraft, thus reducing the cost of maintenance (De Almeida & Oliveira, 2023).

Nanomaterials provide both new opportunities and challenges in the aerospace sector. Their small-scale size and large specific areas, which provide a stronger bonding mechanism between fibre and matrix, lead to effective stress transfer, give them an advantage when dispersed and enhance the performance of composites. The stiffness of metallic nanoparticles ranges between 100–180 GPa, with strength values ranging between 216–1460 MPa (Guo & Luo, 2013) compared to those aluminium alloys of strengths ranging between 182–529 MPa (Li et al., 2023) and steel (304L and 316L) between 200–300 MPa, martensite steel between 400–600 MPa (Sunil et al., 2021). By introducing a nanomaterial into a matrix (the parent material), the strength and stiffness of the parent material can be improved significantly. This can also lead to an improvement in the specific properties of the parent material by reducing the weight and thus improving the performance of the material. This is due to the low density of nanomaterials compared to traditional materials. They offer excellent thermal conductivity (silicon carbide, copper, nanodiamond, and silver nanoparticles with thermal conductivity of 490 W/m.k, 383 W/m.k, 1000 W/m.k, and 429 W/m.k, respectively versus those of 304L and 316 L steel (12.94–28.72 W/m.k, (13.93–29.25 W/m.k), respectively) and aluminium alloys (92–152 W/m.k)) (Simpson et al., 2018; Zhang & Li, 2023; Chacko & Rabiei., 2024), which can effectively help dissipate heat and maintain stability of avionics equipment (Arepalli & Moloney, 2015; Xia, 2023). Among nanomaterials, carbon nanotubes (CNTs) have attracted attention from researchers as reinforcement materials due to their unique properties (Garg et al., 2021).

CNTs have excellent chemical, mechanical, and physical properties of high tensile strength, ultra-lightweight, special electronic structures, and high chemical and thermal stability (Anzar, et al., 2020). CNTs can maintain stable properties in environments of extremely high temperatures and are widely studied for the manufacture of engine parts and insulation materials (Xia, 2023; Arepalli & Moloney, 2015). Developments in the synthesis, processing and characterisation of thin CNT sheets and carbon nanostructures (CNSs) grown from carbon fibres present an

© Central University of Technology, Free State

opportunity to exploit their multifunctional properties for spacecraft components (Arepalli & Moloney, 2015).

The metal forming process is a primary mechanical forming process used to shape metals and alloys in which the material is subject to mechanical forces. In these processes, the bulk material, which is in the form of ingots, blooms, and billets, is reduced to the required shapes and sizes. Metal forming processes are classified according to the type of stress applied to the material, that is, compression-type (forging, rolling, and extrusion), tension-type (drawing), and combined compression and tension (deep drawing, embossing). Mechanical forming processes improve the mechanical properties of a material, including ultimate tensile strength, hardness, and reduced ductility. It also produces grain flows in the direction in which the material has been processed. The grain flow improves strength against fracture during use (Gupta et al., 2009). The shortfall of this process is the higher power consumption, prolonged cycle times, limited in producing complex shapes, higher initial costs, wastage of material, and thickness variations that can impact accuracy (Mengdi et al., 2019).

Additive manufacturing (AM) is a technology that is used to produce 3D structures layer by layer in accordance with a defined geometry. The technology offers the opportunity to produce objects with complex shapes, dimensional accuracy, cost reductions in product development, reduced labour costs, quick production of exact customised replacements on site, helps eliminate excess parts, and offers room to modify components to the latest designs (Attaran, 2017). In the process of producing nanocomposites using AM, defects will likely occur due to the complex thermodynamic behaviour of the constituents under the laser beam, the influence of manufacturing parameters, and the different physical properties of the constituent powders. The van der Waals forces that exist between nanoparticles are greater than their respective weights and result in agglomeration and poor mobility. This not only adds to defects when nanomaterials are added but also enhances existing defects. These defects can lead to degradation and poor performance of the final parts produced (She et al., 2023). Agglomeration also leads to a reduction of the reinforcing effect of CNTs and takes away from the advantage of their nanoscale. Moreover, the formation of agglomerates can cause increased localised porosity. Warping, a deformation and distortion that occurs in final parts caused by uneven cooling or uneven residual

© Central University of Technology, Free State

stresses in final parts, is likely to occur in the nanocomposite due to the different thermophysical properties of the constituents (She et al., 2023).

1.2 Problem Statement

Ti6Al4V(ELI) is an alloy that finds vast applications in various sectors including the automotive and aerospace industries, armour, medical, consumer goods, industrial and marine. (Muhammad, et al., 2020). In the aerospace sector, applications include the manufacture of compressor casings, jet engine rings and discs, and wing flap tracks (Williams & Boyer, 2020). In the automotive sector, applications include the production of connecting rods, valves, valve springs, and valve retainers (Froes, et al., 2004). In the armour industry, the alloy has been used on the M2 Bradley Fighting Vehicle tank hatch, M1 Abrams battle tank turret blow-off panels, and Vickers Shipbuilding and Engineering Limited (VSEL) towed Howitzer (Burton et al., 1996). In the medical field, it is used for prosthetics, dental implants, hearing aids and surgical instruments (Smallman, 2016). In the consumer goods sector, it is used in the production of bicycle frames, eyeglass frames, cooking pans and golf club heads. In the marine sector, it is used for naval hulls and propellers (Smallman, 2016; Ranjith et al., 2019). Despite these vast areas of application, the metal alloy has limitations where high-temperature applications are concerned. Normal working temperature applications range between 200–400°C. At temperatures above 400 °C its microstructure and mechanical properties can be compromised. Mechanical properties, including strength, hardness, and stiffness, decrease at high temperatures (Moloi et al., 2024).

Metal matrix nanocomposites (MMNCs) are nanocomposites that are composed of metal matrices and nano reinforcing phases. The reinforcing phase can be in the form of a fibre or a particulate in which the particulate or fibre is in the nanoscale range. Properties, including strength, modulus of elasticity, thermal stability, hardness, and high-temperature application, are significantly improved in the nanocomposite. This increases the areas of application, including automotive, aerospace, structural material manufacture, and electronic packaging, (Al-Mutairi et al., 2022; Abdollah et al., 2018). However, due to their tendency to agglomerate due to the strong van der Waals forces that exist between the fibres, there is a concern about their dispersion and, therefore, formation of homogenous mixtures (Rubel et al., 2019; Suzuki, 2013).

© Central University of Technology, Free State

The two fundamental techniques for deagglomeration (Figure 1.1) using steric- and electrostatic stabilisation are employed to deagglomerate nanofibres (Khairunnisa et al., 2021). Steric stabilisation incorporates a surfactant or polymer into the nanoparticles. Large molecules of surfactants are absorbed on the surfaces of nanoparticles to prevent their agglomeration. Increased concentration of absorbed molecules of surfactant increases osmotic repulsive forces, which, in turn, keep the nanoparticles apart. Electrostatic stabilisation uses ultrasonication, a process in which sonic waves are applied to the reinforcement to break down the bundles (Behari, et al., 2022). In both processes of deagglomeration, dispersion agents (chemicals) such as solvents and emulsifiers are incorporated (Petridis, et al., 2019). Several dispersion agents are available, including methanol, ethanol, glycol, butanol, ethylene glycol, ethanolamine, propanol, and ethylenediamine (Liu et al., 2017). Emulsifying agents include polymers, including sodium lauryl sulphate, sodium dioctyl sulfosuccinate, and tragacanthins. Emulsifiers are substances that form a thin film around the dispersed material. They form a barrier around a dispersed droplet by adsorbing onto the oil-water interface and decreasing the interfacial tension of the system. Some emulsifiers transmit a charge on the surface of the drop, thus reducing the physical contact between droplets (Tekade, 2018). Emulsifiers are surface active agents and are used for aqueous and oily phases (Galadari, 2014). Dispersion agents are used to improve dispersion stability. According to the Derjaguin, Landau, Vervey, and Overbeek (DLVO) theory, particles in aqueous media can be agglomerated when van der Waals forces' attraction is greater than electrostatic repulsion. By adding suitable dispersion agents, steric hindrance and electrostatic stabilisation can be obtained, which prevents materials from agglomerating (Seo &Paik, 2016). Both electrostatic and steric stabilisation offer advantages depending on the type of mixing process used. Where sonication/ultrasonication is applied, electrostatic stabilisation will have to be carried out. In the case of the application of a surfactant, steric stabilisation will be applied. The choice of dispersion agents over emulsifiers is based on the application of powder materials in the present studies. A surfactant is applied to aid the shortfalls of solvents and to increase deagglomeration further.

© Central University of Technology, Free State

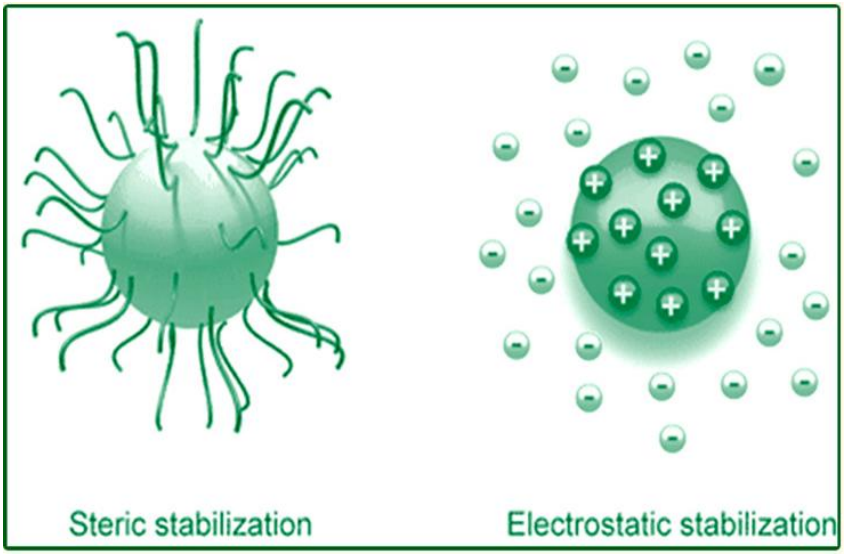

Figure 1.1 Two fundamental stabilisation techniques (Behari, et al., 2022)

(Khairunnisa et al., 2021). Therefore, it is important to identify suitable mixing techniques and a suitable dispersant agent to minimise agglomeration. The possibility of combining mixing techniques is attractive. However, the possibility of physical damage to particles demands care in the use of combined methods of mixing, as damaged particles lead to poor spreading of powder in laser powder bed fusion (LBPF) and, therefore, poor mechanical properties (Du Plessis, 2019). The difference between the thermophysical properties of CNTs and Ti6Al4V(ELI) poses a new challenge to develop process parameters that will produce continuous and stable track builds.

The process parameters in selective laser melting (SLM) are influenced by several factors, including the different thermophysical properties between the constituents of the nanocomposite materials, the reinforcing volume fraction of CNTs, and the mixing technique and dispersion agents used. The starting point, in this case, is the known optimum processing parameters of Ti6Al4V(ELI). The Reuss model can then be used to predict the influence of the reinforcing vol.% of CNTs on the thermophysical and physical properties of the CNTs/Ti6Al4V(ELI) nanocomposite mixtures.

1.3 Limitations to the study

The following were identified as limitations to the study:

- Access to facilities and advanced equipment.
- Limited access to dispersion agents due to budget constraints and availability locally.

© Central University of Technology, Free State

- Restrictions to carry out different experiments as guided by literature due to health and safety concerns posed by CNTs.
- The risk assessment carried out on CNTs (Appendix D)

1.4 Research Questions

The present research addressed the following questions:

- Which nanoparticle material is the best candidate for reinforcement of Ti6Al4V(ELI)?
- What mixing process gives rise to the mixture with the best dispersion of CNTs and the best homogeneity of the nanoparticles/Ti6Al4V(ELI) mixture?
- In which way can the agglomeration of CNTs be minimised?
- How does the volume fraction of reinforcing CNTs affect their mixing with particles of Ti6Al4V(ELI)?
- Which process parameter set of laser power and scanning speed gives rise to the best AM parts for different volume fractions of CNT?
- How do the differences in thermophysical properties between the reinforcement and Ti64 matrix affect the process parameters?

1.5 Aim of the Study

The aim of this study was to identify the best dispersant and method of mixing CNTs and Ti6Al4V(ELI) particles and the best process parameters to build CNT/Ti6Al4V(ELI) parts based on a study of their single tracks built using an M2 LaserCusing® from Concept Laser GmbH.

1.5.1 Objectives of the Study

- To determine a suitable dispersant for deagglomeration of CNTs.
- To determine a suitable technique for mixing of CNT/Ti6Al4V(ELI) powders.
- To determine the best process parameters of laser power and scanning speed for selected volume fractions of reinforcement based on studies of the microstructure and physical integrity of built single tracks.

1.6 Research Methodology

This research started with a review of the literature, followed by an investigation of the mechanical and physical properties of different nanoparticles to determine the most suitable one for use as reinforcement for Ti6Al4V(ELI) matrices. Various methods of

© Central University of Technology, Free State

mixing were evaluated by studying the resulting mixtures' scanning electron microscope (SEM) images to determine the homogeneity of the mixture and dispersion of the reinforcing nanoparticles. Based on results from preliminary mixing on the extent to which uniform dispersion of the nanoparticles and homogeneity of the mixture of powder were achieved, further mixing was carried out using other techniques and dispersion agents to improve dispersion and homogeneity. Further mixing was carried out using a different dispersion agent and the same mixing methods as the previous stage of mixing. Powder mixtures of different volume fractions of the reinforcing nanoparticles were used to print single tracks. Preliminary predictions of the best process parameters were made based on the thermal physical properties of the constituents of the mixture. An inspection of built tracks followed this and thereafter resorted to a driven process of determining the best process parameters based on experience. Figure 1.1 shows a compressed outline of the methodology as explained.

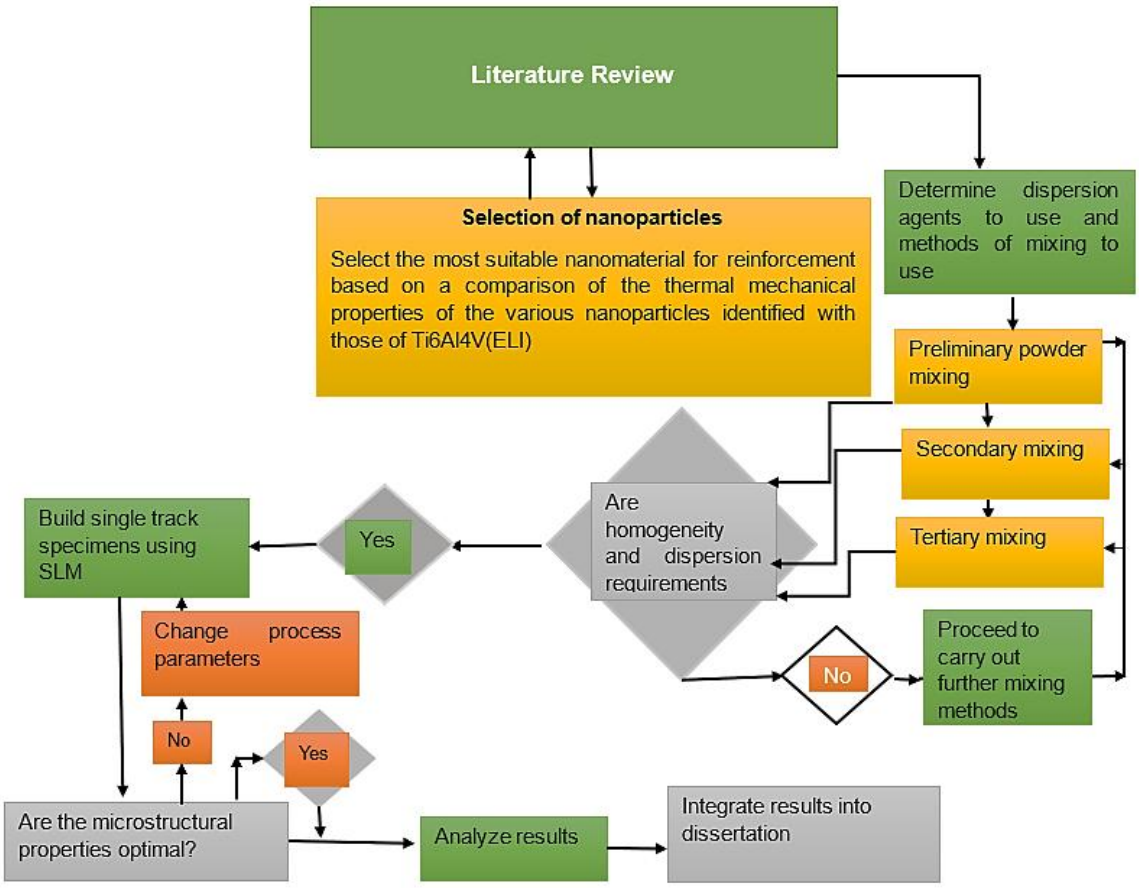

Figure 1.2 Research flow diagram

© Central University of Technology, Free State

1.7 Dissertation Outline

The dissertation includes eight chapters whose contents are now summarised:

Chapter 1: In this chapter, a background and introduction to the research study are given, and the problem statement, aim of the study, objectives, and an overview of the methodology are presented.

Chapter 2: In this chapter, the literature related to the research topic is reviewed and used to identify what has already been achieved and gaps that need to be addressed.

Chapter 3: This chapter contains the research methodology for these studies.

Chapter 4: This chapter contains preliminary information on mixing of powders using two dispersion agents (acetone and ethanol) and manual mixing of dry powders. The information in this chapter advises the need for the use of other methods of mixing to improve the dispersion of the nanoparticles and homogeneity of the mixed powders.

Chapter 5: Secondary mixing, given the results obtained from preliminary mixing is evaluated in this chapter, and one dispersion agent is used given its observed effectiveness in preliminary mixing. Three mixing methods are considered, including mechanical and combined mixing. To further determine the effectiveness of each method of mixing, quantitative image analysis using a manual approach and a threshold method were carried out to quantify the dispersion of CNTs in the mixture.

Chapter 6: This chapter is based on tertiary mixing using a surfactant as a dispersant, given that the results in Chapter 5 show a need to explore other avenues for reducing the agglomeration of CNTs. In this case, a surfactant instead of a process agent is used to detach CNTs from one another, reduce the surface tension on Ti6Al4V(ELI) particles to enable ease of attachment of CNTs, and thus increase the efficiency of reinforcement of Ti6Al4V(ELI) by CNTs.

Chapter 7: In this chapter, an analysis of the top surfaces of single-track builds from the CNT/Ti6Al4V(ELI) powder mixtures obtained from preliminary mixing, details of which are presented in Chapter 4, is discussed. The model developed in this work from known process parameters of Ti6Al4V(ELI) and the thermophysical properties of the CNTs and Ti6Al4V(ELI) is presented at the onset of this chapter. This model was used to develop a test matrix to determine the optimal set of process parameters. An

© Central University of Technology, Free State

analysis of the results arising from the application of the process parameters in this test matrix is presented, and the alternative approach adopted is discussed.

Chapter 8: This chapter contains the conclusions of the dissertation and recommendations for further work.

1.6 Conclusion

This chapter provides a background into material limitations in the aerospace sector. It also highlights the need for composite materials, more importantly nanocomposites. The added advantage of using CNTs as reinforcement material and the challenges that arose are discussed. The use of dispersion agents and surfactants to help minimise agglomeration of CNTs is presented. Finally, the process of attempting to establish process parameters is discussed.

References

1. Abdollah, S., Dadkhah, M., Fino, P. and Pavese, M., 2018. An overview of metal matrix nanocomposites reinforced with graphene nanoplatelets; mechanical, electrical and thermophysical properties. *Metals, 8*(6), pp. 423.
2. Al-Mutairi, N. H., Mehdi, A. H. and Kadhim, B. J., 2022. Nanocomposite materials definitions, types and some of their applications: A review. *European Journal of Research Development and Sustainability (EJRDS), 3*(2), pp. 102–108.
3. Anzar, N., Hasan, R., Tyagi, M., Yadav, N. and Narang, J., 2020. Carbon nanotube-A review on Synthesis, Properties and plethora of applications in the field of biomedical science. Sensors International, 1, pp.100003.
4. Arepalli, S. and Moloney, P., 2015. Engineered Nanomaterials in Aerospace. *MRS Bulletin, 40*, pp. 804–811.
5. Attaran, M., 2017. The rise of 3D printing: The advantages of additive manufacturing over traditional manufacturing. *Business Horizons, 60*(5), pp. 677–688.
6. Behari, M., Das, D. and Mohanty, A. M., 2022. Influence of surfactant for stabilization and pipeline transportation of iron ore water slurry: A review. *ACS Omega, 7*(33), pp. 28708–28722.
7. Blakey-Milner, B. et al., 2021. Metal additive manufacturing in aerospace: A review. *Materials & Design, 209*, pp. 110008.

© Central University of Technology, Free State

8. Burton, L. R., Hoppel, C. P., Kaste, R. P. and Army Research Lab Aberdeen Proving Ground MD, 1996. *Feasibility of a 7,000-lb 155-mm Towed Howitzer,* Port Royal Road, Springfield, VA: Army Research Laboratory.

9. Chacko, Z. and Rabiei, A., 2024. Thermal conductivity of steel-steel composite metal foam through computational modeling. *Materials Research Proceedings*, *39*, pp. 17-24.

10. De Almeida, E. E. and Oliveira, A. V., 2023. *An economic analysis for the determinants of flight speed in the air transport of passengers,* Sao Jose dos Campos, Brazil: Nature Portfolio.

11. Du Plessis, A., 2019. Effects of process parameters on porosity in laser powder bed fusion revealed by X-ray tomography. *Additive Manufacturing*, *30*, pp.100871.

12. Dursun, T. and Soutis, C., 2014. Recent developments in advanced aircraft aluminium alloys. *Materials & Design*, *56*, pp. 862–871.

13. Froes, F. H., Friedrich, J. K. and Bergoint, D., 2004. Titanium in the family automobile: the cost challenge. *JOM, 56*, pp. 40–44.

14. Galadari, H. I., 2024. Hot topics in cosmetic dermatology. *Dermatologic Clinics*, *42*(1), p.i.

15. Garg, A., Chalak, H. D., Belarbi, M. O., Zenkour, A. M. and Sahoo, R., 2021. Estimation of carbon nanotubes and their applications as reinforcing composite materials–an engineering review. Composite Structures, 272, pp.114234.

16. Guo, D., Xie, G. and Luo, J., 2013. Mechanical properties of nanoparticles: basics and applications. Journal of Physics D: Applied Physics, 47(1), pp.013001.

17. Gupta, H. N., Gupta, R. C. and Mittal, A., 2009. *Manufacturing Processes. Second edition ed*. New Delhli: New Age International (P) Limited, Publishers.

18. Henriques, V., 2009. Titanium production for aerospace applications. Journal o*f Aerospace Technology and Management, 1*(1), pp. 7–17.

19. Khairunnisa, S., Wonoputri, V. and Samadhi, T. W., 2021. Effective deagglomeration in biosynthesized nanoparticles: A mini review. *In IOP Conference Series: Materials Science and Engineering*, 1 April, pp. 1–10.

20. Li, S.S., Yue, X., Li, Q.Y., Peng, H.L., Dong, B.X., Liu, T.S., Yang, H.Y., Fan, J., Shu, S.L., Qiu, F. and Jiang, Q.C., 2023. Development and applications of aluminum alloys for aerospace industry. Journal of Materials Research and Technology, 27, pp. 944-983.

© Central University of Technology, Free State

21. Mengdi, G., He, K. and Li, L., 2019. A review on energy consumption, energy efficiency and energy saving of metal forming processes from different hierarchies. *Processes, 7*(6), pp. 3–25.

22. Muhammad, U. F. et al., 2020. On the investigation of surface integrity of Ti6Al4V ELI using Si-mixed electric discharge machining. *Materials, 13*(7), pp. 1549.

23. Moloi, T., Dzogbewu, T. C., Maringa, M. and Muiruri, A., 2024. Quasi-static tensile properties of DMLS TI6AL4V (ELI) specimens exposed to two different heat treatment processes and tested at different elevated temperatures. *Results in Engineering*, *22*, pp.102290.

24. Ouissi, T. et al., 2019. Comparison of aluminum alloys from aircraft of four nations involved in the WWII conflict using multiscale analyses and archival study. *Heritage, 2*(4), pp. 2784–2801.

25. Petridis, L. V., Kokkinos, N. C., Mitropoulos, A. C. and Kyzas, G. Z., 2019. Graphene aerogels for oil absorption. *Interface Science and Technology, Elsevier,*30, pp. 173–197.

26. Plesa, I. et al., 2016. Properties of polymer composites used in high-voltage applications. *Polymers, 8*, pp. 1–63.

27. Ranjith Kumar, G., Rajyalakshmi, G. and Swaroop, S., 2019. A critical appraisal of laser peening and its impact on hydrogen embrittlement of titanium alloys. Proceedings of the Institution of Mechanical Engineers, Part B: Journal of Engineering Manufacture, 233(13), pp. 2371–2398.

28. Rubel, R. I., Ali, M. H., Jafor, M. A. and Alam, M. M., 2019. Carbon nanotubes agglomeration in reinforced composites: A review. *AIMS Materials Science, 6*(5), pp. 756–780.

29. Seo, J. and Paik, U., 2016. Preparation and characterization of slurry for chemical mechanical planarization (CMP). In Advances in Chemical Mechanical Planarization (CMP), pp. 273–298. Woodhead Publishing.

30. Simpson, S., Schelfhout, A., Golden, C. and Vafaei, S., 2018. Nanofluid thermal conductivity and effective parameters. Applied Sciences, 9(1), pp. 87.

31. Singh, R. P., Singh, P. and Singh, K. R., 2021. Introduction to composite materials: Nanocomposites and their potential applications. In: Composite Materials. s.l.: CRC Press, pp. 1–28.

32. Smallman, R. E., 2016. Modern Physical Metallurgy. 4th Edition ed. Essex: Elsevier.

33. Sunil, S., Kapoor, R., Sarkar, S. K., Biswas, A., Donthula, H. and Sen, D. J. A. M., 2021. Ultra-high strength steel made from AISI 304L using a

© Central University of Technology, Free State

novel thermo-mechanical processing technique. Acta Materialia, *221*, pp. 117379.

34. Suzuki, S., 2013. Physical and chemical properties of carbon nanotubes. *BoD–Books on Demand.*

35. Tekade, R. K., 2018. Basic fundamentals of drug delivery. Academic Press.

36. Williams, J. C. and Boyer, R. R., 2020. Opportunities and issues in the application of titanium alloys for aerospace components. *Metals, 10*(6), pp. 705.

37. Xia, Q., 2023. Overview of aerospace materials and their applications. Theoretical and Natural Science*, 13*, pp. 115–120.

38. Zhang, A. and Li, Y., 2023. Thermal conductivity of aluminum alloys—A review. *Materials*, *16*(8), pp. 2972.

© Central University of Technology, Free State

CHAPTER 2 - LITERATURE REVIEW

Some of the material contained in this chapter has been published in peer-reviewed media as follows:

1. **Mpho Mashabela, Maina Maringa and Thywill Dzogbewu**, "Nanoparticulate reinforced composites and their application to additively manufactured TI6AL4V for use in the aerospace sector", Manufacturing Rev. Vol, No (2022) © M. Mashabela et al., Published by EDP Sciences 2022, https://doi.org/10.1051/mfreview/2022027

2.0 SUMMARY

In this chapter, an introduction to nanocomposites, Ti6Al4V(ELI), composite materials in general and the theory of elastic deformation of composite materials, CNTs, (SLM) and single tracks is presented. The topic of nanocomposites is further divided into the classification of nanocomposites, methods of fabrication, types of bonds, and theories used to determine the elastic properties of nanocomposites. The discussion on Ti6Al4V(ELI) is further divided into the mechanical properties of the alloy based on different methods of fabrication, applications in aerospace and other industries, and limitations of the alloy. An introduction to CNTs, their classification, and their applications is then presented, followed by a brief discussion on the advantages of their properties in their use as reinforcement. AM, specifically SLM, is then discussed in some detail with specific reference to the build process, process parameters, and defects in built parts. Finally, the theory of single tracks and the effect of process parameters on their formation is discussed. An overview of this chapter is provided in Figure 2.1

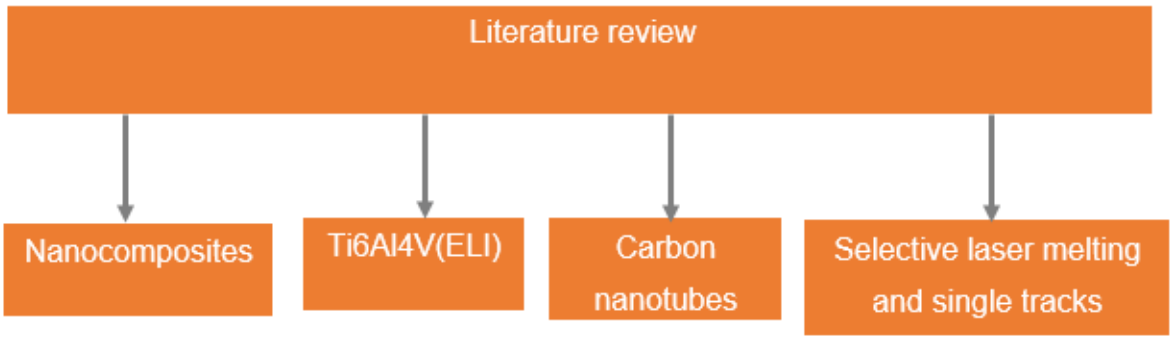

Figure 2.1 Overview of Chapter 2

© Central University of Technology, Free State

2.1 Introduction to Nanocomposites

Nanocomposites are materials that have a matrix or parent material that is reinforced by one or more materials, and the reinforcement material has dimensions between 1–100 nm. Their unique properties of low density, high Young's modulus, wear resistance, flame resistance, low porosity, thermal stability, high chemical resistance and good electric conductivity make them better materials than normal composite materials (Singh et al., 2021; Sen, 2020). The properties of nanocomposites are largely influenced by the properties of the individual material, their morphology, and the interfacial characteristics (Idumah & Obele, 2021). The study of nanocomposites goes back nearly 50 years. The first reference to nanocomposites dates to 1976, when polyamide nanocomposites were first presented. A detailed examination of polymer/layered silicate clay mineral composites was carried out by Toyota researchers in the early 1980s, which gave way to a wide study of nanocomposites by academia and industrial laboratories (Okpala, 2013).

Nanocomposites have become a driving innovation across various sectors, such as electronics, energy storage, industrial applications, energy applications, and medicine (Gomes et al., 2023; Anwer et al., 2023). The idea behind the addition of reinforcement materials at the nanoscale is to create a relationship between the matrix and reinforcement materials to produce novel properties that meet or exceed design expectations. The properties of a nanocomposite are characterised by several factors, including the type of matrix material, as well as volume of reinforcement, size, orientation, and shape of the reinforcement phase (Chaturvedi & Deshmukh, 2022). The advantages of nanocomposites over conventional composites are detailed in Figure 2.2.

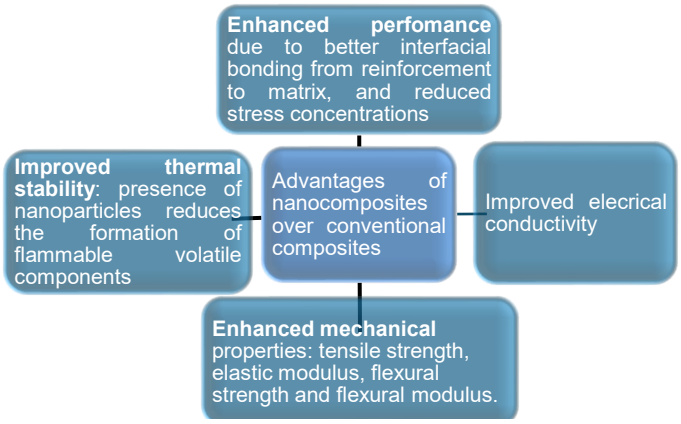

Figure 2.2 Advantages of nanocomposites over conventional composites (Rashid, et al., 2024)

© Central University of Technology, Free State

2.1.1 Classification of Nanocomposites

The main constituents of a nanocomposite are a matrix and a reinforcement phase. The matrix phase maintains the reinforcement phase in place by positioning itself around it. The main role matrices play is to protect the reinforcing phase from damage and to transfer stress to it (Wu & Chen, 2023). The reinforcement phase enhances the matrix phase by improving its properties, including mechanical, physical, and electrical (James, et al., 2021). The nanocomposite can be classified based on the type of matrix present, whether a polymer, metal or ceramic. Thus, a nanocomposite in which the matrix is a polymer, metal or ceramic is known as a polymer nanocomposite (PNC), metal nanocomposite (MNC) or ceramic (CNC) nanocomposite. Nanocomposites can be further classified into ceramic-ceramic nanocomposites (CCNCs), where both the matrix and reinforcing phase are ceramics (Sen, 2020). In Figure 2.3, the various categories of nanocomposites, depending on whether they are polymer-based or not, are presented. Since the focus of the present studies is on metal nanocomposites, a more comprehensive discussion of them is presented here, while the discussion of other types of composites is limited.

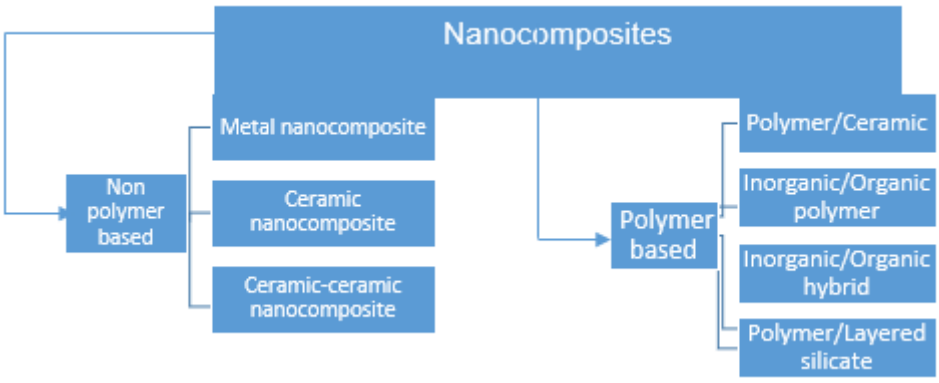

Figure 2.3 Classification of nanocomposites (Sen, 2020)

2.1.1.1 Types of Matrices

Matrices hold the reinforcing materials in place, transfer stress to them and protect them from damage and are the primary base for composites. There are four main types of matrices, which include polymers, ceramics, metals and carbon-carbon matrices (Sharma et al., 2020; Fatchurrohman & Sulaiman, 2021). Polymers are materials consisting of a large number of atoms held together by covalent bonds and exist in long chains (Syed, 2009). They are used mainly for their lightweight nature

© Central University of Technology, Free State

and ease of fabrication. Polymer matrices consist of thermosets (epoxies, polyesters, vinyl esters, phenolics, and polyamides) and thermoplastics (polyethylene, polypropylene, polyamide-imide, polyetherimide, polyether ether ketone (PEEK), polyphenylene sulfide, liquid crystal polymers and nylon) (Ramakrishnan et al., 2022; Saba et al., 2017). Some typical working temperatures for thermosets include phenolics (0–110 °C), epoxy (0–150 °C), and polyamide (0–220 °C). For thermoplastics, working temperatures of some materials include nylon (0–90 °C), polyethylene (0–95 °C), polyamide-imide (0–230 °C), PEEK (0–250 °C), and polyetherimide (0–180 °C) (Liu, et al., 2024; Diaham, 2020). High-performance polymers, including Upilex-S®, Kapton, and Ultem, have working temperatures of 355 °C, (300–350 °C) for Kapton and Upilex, respectively (Ho & Schroeder, 2020). The values of yield strength and elastic modulus, respectively, for some polymers include polyethylene (18–29 MPa) (0.62–0.86GPa) (Ashby, 2012), Ultem (40–76.1 MPa) (2.05–2.2GPa), (Kaplun, 2020) and epoxy (5–19MPa) (0.5–1.8GPa) (Baptista et al., 2016). Metal matrices normally employ lightweight alloys such as magnesium, aluminium, and titanium as matrices. Some typical working temperatures of these MMCs include magnesium alloys with working temperatures up to 125 °C (Turowska & Adamiec, 2015). Titanium alloy Ti6Al4V(ELI) has working temperatures between 250–400 °C (Moloi et al., 2024). There are other high-temperature titanium alloys whose temperatures range between 400–600 °C, which include IMI 834, IMI 829, Ti-6246, and Ti-6242 (Gogia, 2005). Metal matrices have good values of ductility (10–25%), strength (240 MPa–460 MPa) and moderate stiffness (45 GPa–128 GPa) and are mainly used in car engines and turbines. Ceramics are mainly used in high-temperature applications. Ceramics are a combination of metals or intermediate metals such as silicon, boron and arsenic, with non-metal such as oxygen, nitrogen, or carbon. Ceramic matrices include mainly alumina (Al_2O_3) and silica (SiO_2) and consist of inorganic non-metallic substances. Ceramics are resistant to oxidation and corrosion, and are hard, strong, and able to resist high temperatures (Balasubramanian, 2012).

2.2 Metal Matrix Composites

Metal matrix composites (MMCs) consist of continuous matrices of metallic alloys with a reinforcement phase of ceramic phase or metallic phase. Matrix materials include

© Central University of Technology, Free State

copper, aluminium, nickel, titanium, steel, and magnesium, with commonly used reinforcements listed in Table 2.1 and Figure 2.4.

Table 2.1 Some MMCs and typically used reinforcements

	Types of reinforcements			
Matrix	**Continuous fibres**	**Discontinuous fibres**	**Whiskers**	**Particulates**
Aluminium	Boron, Silicon carbide, Alumina, Graphite	Alumina, Alumina-silica	Silicon carbide	Silicon carbide, Boron carbide
Magnesium	Graphite, Alumina		Silicon carbide	Silicon carbide, Boron carbide
Titanium	Silicon carbide, Coated boron			Titanium carbide
Copper	Graphite, Silicon carbide, Niobium-titanium (wires), Niobium-tin (wires)			Silicon carbide, Boron carbide, Titanium carbide

Figure 2.4 shows reinforcement materials for MMCs and their different categories

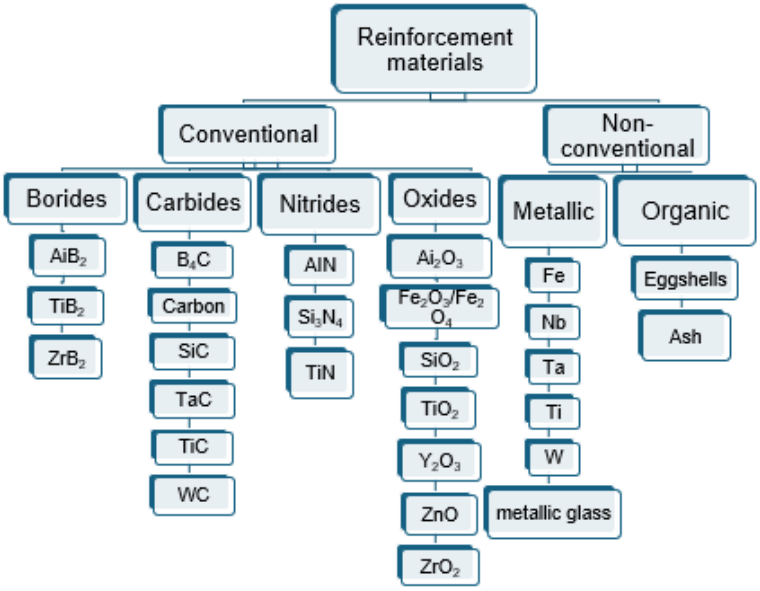

Figure 2.4 Reinforcement material for MMCs (Rashid, et al., 2024)

Key to Figure 2.14

AiB_2 –aluminium diboride. **TiB_2**–titanium diboride, **AiB_2** –aluminium diboride, **TiB_2**–titanium diboride, **ZrB_2**–zirconium diboride, **B_4C**–boron carbide, **SiC**–silicon carbide, **TaC**–tantalum carbide, **TiC**–titanium carbide, **WC**–tungsten carbide, **AiN**–aluminium nitride, **Si_3N_4** –silicon nitride, **TiN**–titanium nitride, **Ai_2O_3**–aluminium oxide, **Fe_2O_3/Fe_2O_4**–ferric oxide, **SiO_2**–silicon dioxide (silica), **TiO_2** –titanium dioxide, **Y_2O_3**–Yttrium oxide, **ZnO**–zinc oxide, ZrO_2–zirconium oxide, **Fe**–iron, **Nb**–niobium, **Ta**–tantalum, **Ti**–titanium, **W**–tungsten

© Central University of Technology, Free State

Typically, aluminium-based, titanium-based and magnesium-based MMCs are used for lightweight structures in the aerospace, automotive, and defence applications. Steel is used for tooling applications, nickel is recommended for heavy industries, and copper alloys for electronic packaging (Seetharaman & Gupta, 2021). The properties of specific strength and specific modulus of MMCs, together with those for other materials such as carbon fibre-reinforced polymers (CFRPs), glass matrix composites (GMCs), glass-ceramic matrix composites (GCMC), carbon-carbon (CC) composites, as well as nickel, aluminium and titanium matrices are presented in Figure 2.5 and Figure 2.6.

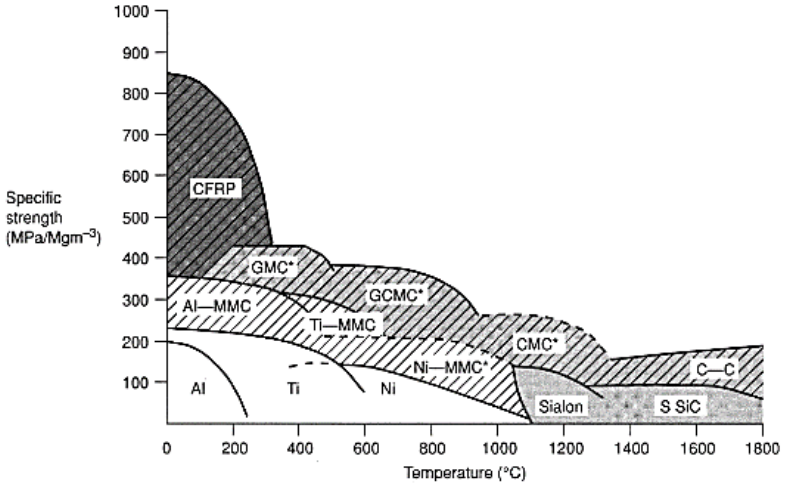

Figure 2.5 Specific strength versus temperature for metal-MMCs, ceramic-MMCs, CFRPs, glass matrix composites, glass ceramic matrix composites, carbon-carbon composites, titanium, aluminium and nickel matrices (Koczak, et al., 1993)

From Figure 2.5, the following can be deduced: firstly, the working temperatures of Al-MMCs are lower than Ti-MMCs and Ni-MMCs with high specific strengths. Secondly, where Ti-MMCs and Ni-MMCs have reduced specific strengths, their temperature applications become higher than those of Al-MMCs. The alloys on their own have much lower specific strengths and temperature applications compared to when a composite is formed. Ceramic composites and glass ceramic composites have much higher temperature applications compared to Al-MMCs, Ti-MMCs, and Ni-MMCs; however, they have the disadvantage of a reduction in specific strengths. It is also evident from Figure 2.5 that carbon-carbon composites have excellent temperature applications, while CFRPs have the highest specific strengths, even higher than MMCs, ceramics and carbon composites.

© Central University of Technology, Free State

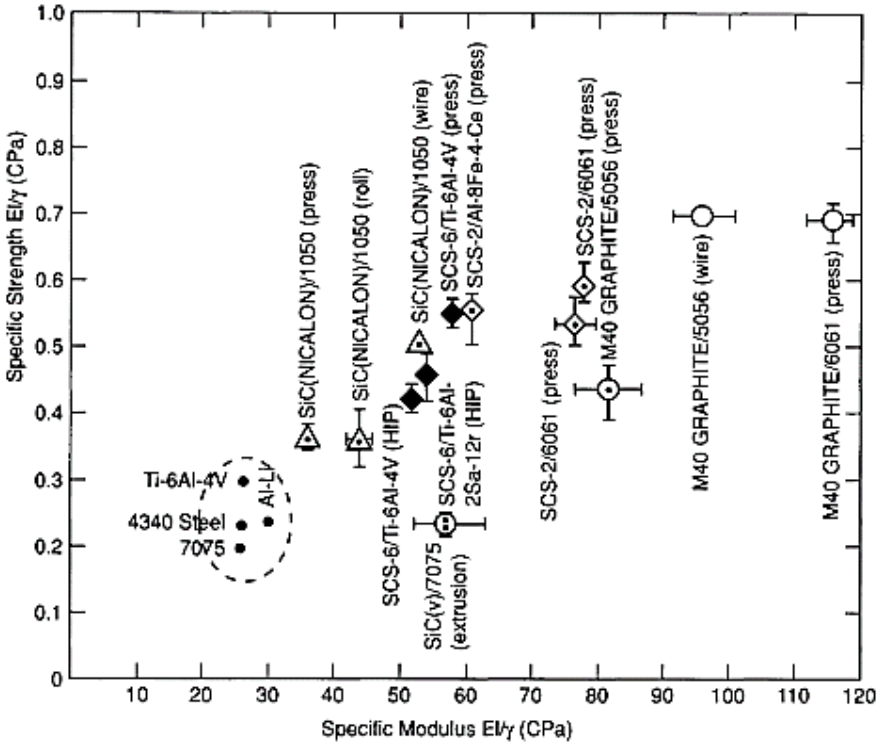

Figure 2.6 Specific modulus versus specific strength for MMCs and metallic matrices (Koczak et al., 1993)

In Figure 2.6, the specific modulus of metal alloys is much lower in comparison to MMCs with different reinforcements. It is also evident that where an allotrope of carbon, graphite, is used as a reinforcement, the MMCs have much higher specific modulus and specific strengths. From this figure, it is evident that metallic alloys on their own have limited mechanical properties of specific strength and specific modulus and that the formation of composites will improve their properties.

2.2.1 Background on Ti6Al4V(ELI)

Titanium-aluminium-vanadium alloy (Ti6Al4V) is primarily used for aerospace applications, with other applications in the biomedical field, armour and automotive industries. The alloy is used in aerospace applications mostly for low-pressure compressors (compressor discs), inlet chamber turbine blades, rotor head, and airframe structures (fuselage, tail and wing surfaces, and support structure for the floor) (Ke et al., 2022). This titanium alloy is a two-phase (α + β) alloy, having both alpha (α) and beta (β) phase grains in its microstructures. The alloy is made up of 6 wt.% aluminium, which stabilises the α phase and increases the beta transus temperature (Tβ), and 4 wt.% vanadium, which stabilises the β phase and decreases

© Central University of Technology, Free State

the beta transus temperature (Tβ) (Oosthuizen, 2010; Sieniawski et al., 2013). It is also made up of other alloying elements, including iron (Fe), carbon (C), nitrogen (N), hydrogen (H), and oxygen (O), in various percentages, as shown in Table 2.2.

Table 2.2 Chemical Composition of Ti6Al4V (wt.%) (ATI, 2012)

Al	**V**	**O**	**Fe**	**Mo**	**C**	**Si**	**Mn**
6.31	4.06	0.18	1.16	0.02	0.016	0.01	0.01
Cu	B	Zr	Y	N	Sn	Cr	Ti
0.02	0.001	0.02	0.001	0.008	0.02	0.01	88.174

Aluminium stabilises the α phase, while vanadium stabilises the β phase. The β phase is a more ductile allotrope due to the higher number of slip planes in its body-centred cubic (bcc) crystal structure, and the α phase is less ductile but much stronger than the β allotrope. The presence of aluminium as a stabiliser at high concentrations gives rise to good strength characteristics and corrosion resistance at elevated temperatures. While vanadium is a biologically toxic element, Ti6Al4V is biologically inert (Hashmi, 2014). The volume fractions of the α and β phases can be adjusted to alter the ductility and hardness of the material. The higher the β content in the alloy, the denser the alloy becomes; this is especially important when it comes to bone replacement because the alloy must be compatible with the surrounding biological tissue to prevent stress shielding (El-Bagoury et al., 2019). The mechanical behaviour of Ti6Al4V is changed significantly when wt.% of the β phase is more than 50% at 970 °C. At low volume fractions, β has little significance on the deformation of the lamellar colonies. Therefore, the deformation of lamellar colonies is greatly influenced by the secondary alpha phase which has deformation characteristics similar to those of the primary alpha phase (Chong et al., 2021).

Experiments carried out by Reda et al., (2015) showed that the α→β transformation of Ti6Al4V takes place at 987 °C, whilst Zhang & McDowell (2008) stated that at temperatures higher than 980 °C, the β phase is composed of equiaxed β grains (Figure 2.7(b)). Slow cooling of the material from the β phase field into the two-phase field (α + β) results in a coarse lamellar microstructure (Figure 2.6(a)) in the two-phase region and deposition of the α phase on further cooling below the dual phase/alpha phase, phase transformation line. Heat treatment processes can produce fully lamellar

© Central University of Technology, Free State

or bimodal (also known as duplex) microstructures (Figure 2.7(c)). The bimodal microstructures may consist of globular, and Widmanstatten features separately or together. Lamellar microstructures form due to slow cooling where phase transformation takes place from the β phase at the beta transus temperature (T_β), to form colonies of hexagonal close-packed (hcp) α-phase/β-phase lamellae within large bcc β grains. The equiaxed microstructure is formed after phase transformation into the α + β two-phase below the beta transus temperature and consists of a globular α phase distributed in a primary β matrix. The mechanical properties of lamellae microstructure are characterised by low ductility and fatigue initiation resistance, with good creep and crack growth resistance. Equiaxed microstructures are characterised by medium strength and ductility at room temperature, high fatigue crack initiation resistance and low fatigue crack propagation properties (Fan et al., 2016).

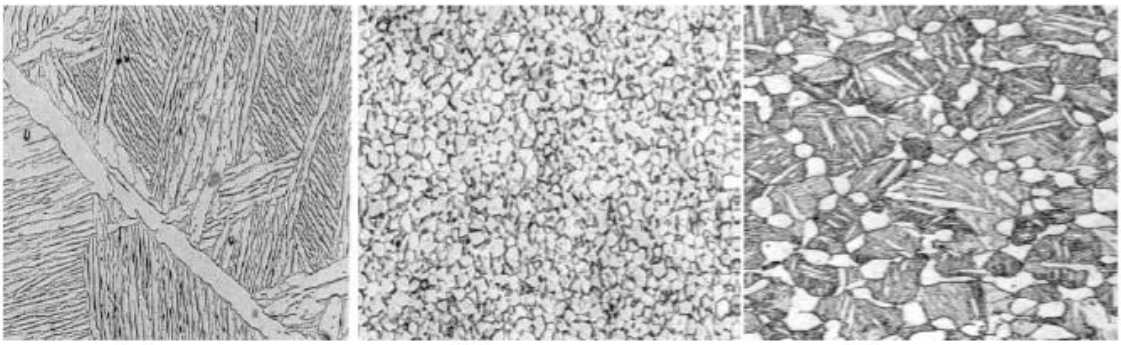

Figure 2.7 Microstructures for Ti6Al4V showing (a) lamellar (b) equiaxed and (c) bimodal microstructure (Fan et al., 2016)

2.2.1.1 Mechanical Properties of Ti6Al4V Fabricated by Different Processes

The mechanical properties of Ti6Al4V fabricated by different processes are tabulated in Table 2.3. The mechanical properties of Ti6Al4V are affected by its microstructure, which changes with the fabrication process to which it is exposed. The microstructure resulting from the use of the SLM process produces Ti6Al4V with higher values of strength and lower values of ductility (except from manufacture through direct energy deposition (DED)) compared to microstructures produced through other AM (electron beam melting (EBM)) and conventional methods of manufacture shown in Table 2.3 (Liu & Shin, 2019). The data in this table represents the best results for each AM method of fabrication based on build direction and post-processing. This is important to note as the build direction and post-processing procedures carried out after the

© Central University of Technology, Free State

LBPF processes do affect the mechanical properties of produced parts (Narasimharaju, et al., 2022) due to the effect of the two factors on their microstructures.

Table 2.3 Mechanical properties of Ti6Al4V fabricated through different processes (Liu & Shin, 2019)

Fabrication process	Condition of specimens	Orientation of specimens	Ultimate tensile (MPa)	Yield strength (MPa)	Percentage elongation
SLM	As built, machined	Horizontal	1269 ± 9	1195 ± 19	5 ± 0.5
DED	As built, machined	Horizontal	1163 ± 22	1105 ± 19	4 ± 1
EBM	As built, machined	Longitudinal	1073–1116	1001–1051	11–15
Wrought	-	Longitudinal	942 ± 8	836 ± 9	12.5 ± 1.2
Forged	Mill annealed	-	1030	970	16
Cast	-	-	980	865	13.5
ASTM			860	795	10

2.2.1.2 Importance of Ti6Al4V in Aerospace Applications

The use of Ti6Al4V in the aerospace industry has increased over the years at the expense of traditional materials, such as steel and aluminium. It is also used in the manufacturing of consumer goods (bicycle frames, eyeglass frames, cooking pans, and golf club heads), sporting equipment, pacemakers, heart valves, contact lenses and orthopaedic devices in the biomedical field, as well as exhaust valves, connecting rods, and suspension springs in the automotive industry (Jewell & Kimball, 2017; Mohan Agarwal et al., 2021). The alloy has a high corrosion resistance and high specific strength and stiffness (Eliaz, 2019). One of the advantages of using Ti6Al4V in the aerospace sector is the lack of galvanic corrosion at joints with CFRPs (Adamos & Lotus, 2021). It exhibits high values of specific strength (232–265 MPa m^3/kg), good values of yield strength (795 MPa), hardness (341 HV), and Young's modulus (113.8 GPa) (Davis, 2001; Shunmugavel et al., 2015). The use of Ti6Al4V in various

© Central University of Technology, Free State

sectors of the aerospace industry and for different components of aerospace equipment by percentage is presented in Figure 2.8.

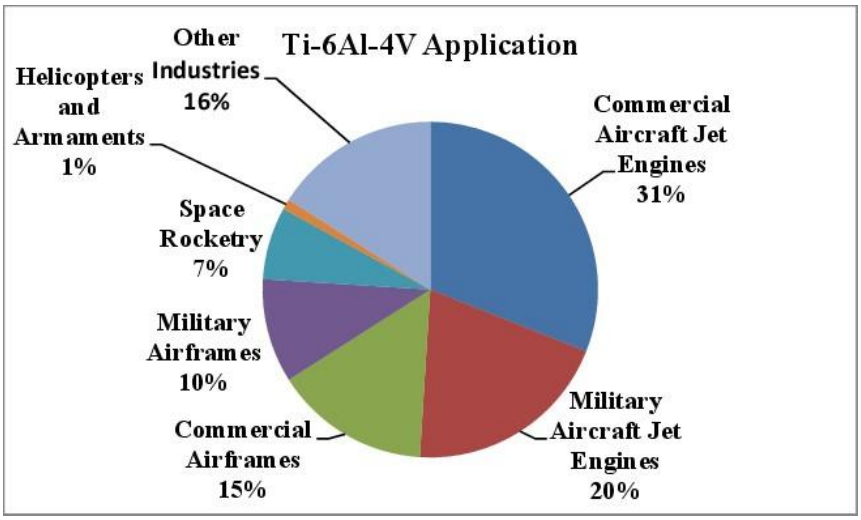

Figure 2.8 Application of Ti6Al4V in the aerospace industry by percentage (Thesiya et., 2015)

The Ti6Al4V alloy has high values of specific strength at a maximum temperature of 460 °C compared to other metallic materials such as steel and aluminium (Figure 2.9). Based on Figure 2.9, composites have higher values of specific strength compared to Ti6Al4V. However, their working temperature range is limited to above zero to 250 °C compared to the higher upper range for Ti6Al4V and, therefore, makes Ti6Al4V preferentially suitable for higher temperature applications at which composites cannot be used (Khan et al., 2019).

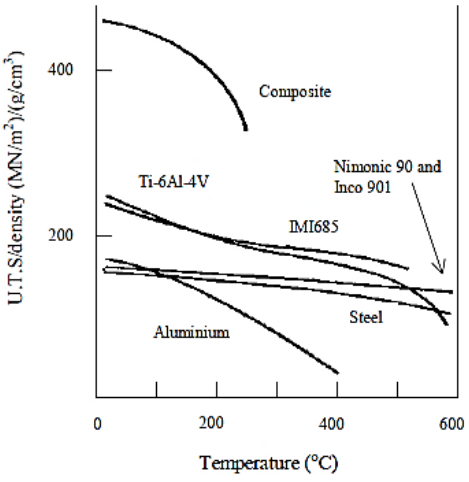

Figure 2.9 Comparison of specific strengths of various materials versus temperature (Khan et al., 2019)

© Central University of Technology, Free State

Materials used for airframes date back to 1903 when an airframe was made from a wooden structure. After 1927, aluminium alloys became dominant in aerospace applications. Titanium and titanium alloys became production materials in the 1950s with Ti6Al4V being one of the first titanium alloys to be developed. The alloy remains the predominantly used material for aerospace applications. In recent years, aluminium-based alloys and steel materials have been replaced by Ti6Al4V due to its lightweight properties (Zhang et al., 2018; Boyer et al., 2015). The design of joints for airframe materials, especially where heterogeneous materials are used, requires consideration in the prevention of galvanic corrosion and the elimination of stress caused by a difference in the coefficient of thermal expansion (CTE) of the materials (Inagaki, 2014).

The Lockheed Martin F-22 Raptor, which went into service in the United States of America at the end of 2005, has a structural weight that consists of 42% titanium alloys (Cotton, 2002). Figure 2.10 shows the bulkhead frames (made in pieces that are welded together) of the F22 Raptor fuselage. Titanium alloys make up approximately 93% of the materials in the Lockheed SR-71 Blackbird's (manufactured with titanium in the 1990s) structural weight, with Ti6Al4V dominating amongst these alloys (Boyer et al., 2015).

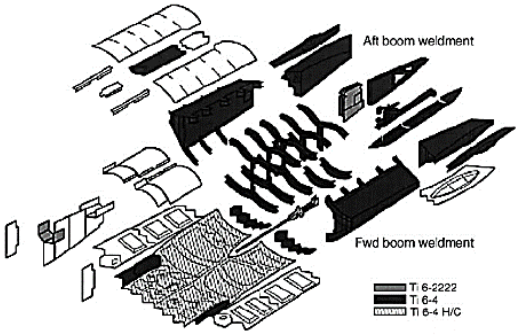

Figure 2.10 Schematic of F22 fuselage assembly showing application of titanium and titanium alloys (Boyer et al., 2015)

The continued demand to raise the operating temperatures of gas turbine engines has led to a demand for improved materials (Lagow, 2016). Aluminium-based alloys have excellent strength-to-weight ratios, but their upper temperature of application of 130 °C limits their application in gas turbines. Three hundred (300) series stainless steel offers similar strength to most titanium alloys; however, it has the disadvantage of

© Central University of Technology, Free State

having 50% more density than titanium alloys. Titanium alloys have high strength-to-weight ratios and are thus able to provide similar strength to that of stainless steel at a 50% reduced weight. In comparison to titanium alloys, 300 series stainless steel offers cost reductions; however, it is limited in high-temperature applications (Whittaker, 2016). Titanium alloy Ti6Al4V is used for the manufacture of airfoils, disks, and casings of low-pressure compressors located towards the front end of gas turbines, where temperatures only rise to 230 °C (Figure 2.11) (Williams & Boyer, 2020). Titanium alloys Ti-6Al-2Sn-4Zr-6Mo (Ti-2646) and Ti-5.8Al-4Sn-3.5Sr-0.7Nb-0.5Mo (Ti-834) have been applied near the front end of low- and high-pressure compressors and other high-pressure sections of compressors for gas turbines where temperatures are high. Figure 2.12 shows that Ti-2646 is applied in gas turbine compressor sections where temperatures rise to 430 °C and Ti-834 towards the rear end of the compressors, where temperatures rise to 730 °C (Palmer et al., 2020).

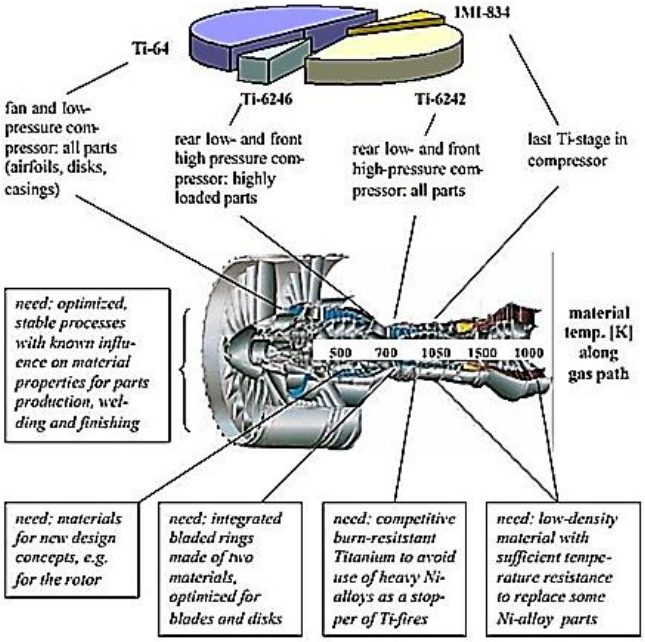

Figure 2.11 Example of application titanium alloys used in a gas turbine (Esslinger,1960)

© Central University of Technology, Free State

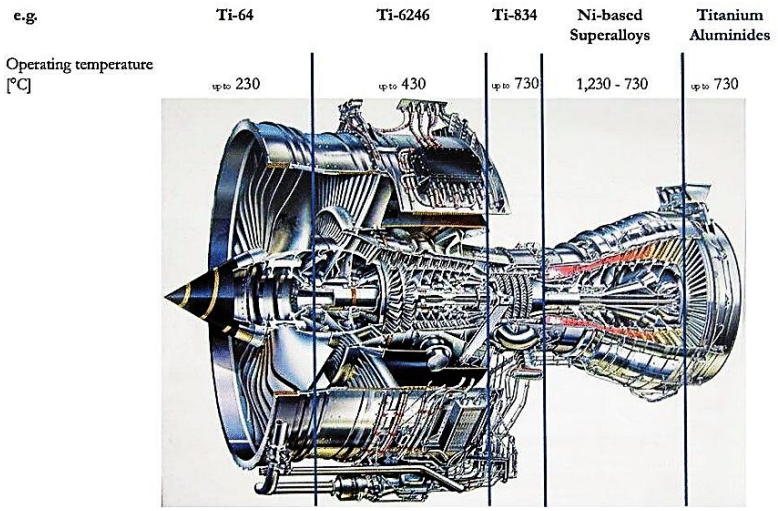

Figure 2.12 Example of temperature application of titanium alloys used in a gas turbine (AL-Nafeay et al., 2021)

Titanium alloy Ti-834 is prone to environmental degradation in the form of the brittle and hard alpha case formation that is known to form in the presence of oxygen and at high temperatures, which then limits its applications (Whittaker, 2016). Titanium alloy Ti6Al4V has traditionally not been used for temperature applications above 350 °C (Palmer et al., 2020) and has, therefore, been restricted from use in the combustion chamber where temperatures range between 400–700 °C and gas turbines where temperatures can rise to 1000 °C (Vasile et al., 2020). The considerable strength associated with Ti-2646 makes it difficult to machine as it tends to crush the cutting edge of tools (Gomez-Gallegos et al., 2018), which is a disincentive for its use. The possible use of nanocomposite materials, which offer high values of stiffness and strength, high-temperature applications, and low CTE, offers alternatives to address the shortfalls mentioned in the preceding work (Rashid et al., 2024).

The mismatch of the CTEs is relevant in hybrid frames and the repair of composite structures and components (James & Wanhill, 2018). The low CTE of Ti6Al4V of 8.6 W/mK gives better compatibility with CFRPs than steel and aluminium with their CTEs of 16.3 W/mK and 23 W/mK, respectively (Budhe et al., 2018). Therefore, the increased use of CFRPs in the aerospace industry to improve fuel consumption has led to an attendant increase in the use of Ti6Al4V in the industry (Poutord, et al., 2013). The alloy thus finds applications in the manufacturing of fighter aircraft such as the UCAV Harrier GR7, Gripen JAS39, Mirage 2000, Eurofighter, EADS Mako MiG29, and commercial aircraft including Airbus A380, Boeing 787, FALCON 900, and the Airbus

© Central University of Technology, Free State

A300–600 series. It is also used for general aviation craft such as the V22 tilt rotor aircraft helicopter (Lorell, 1995). An example of composite applications in the fighter aircraft F18E is shown in Figure 2.13 (Quilter, 2004), and a cross-section of a helicopter blade is shown in Figure 2.14.

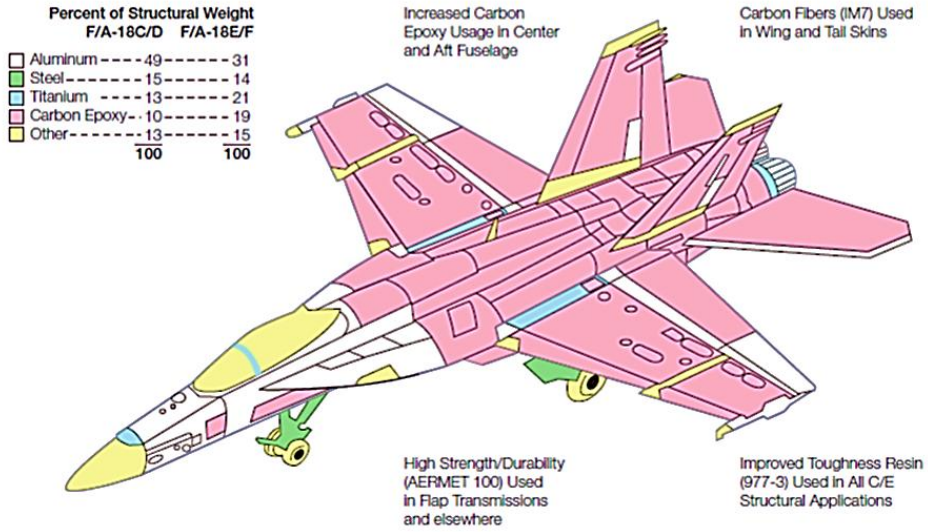

Figure 2.13 Application of CFRPs in the Fighter Aircraft F18E (Quilter, 2004)

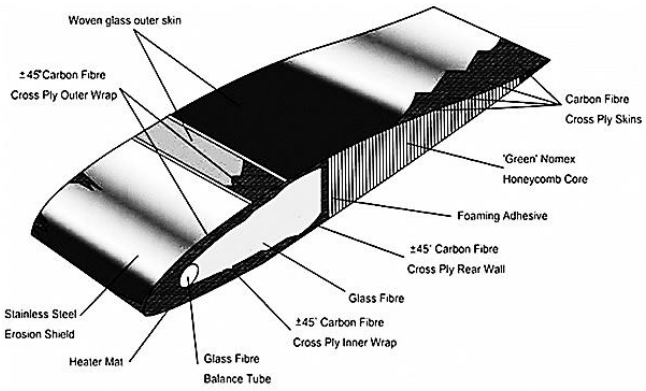

Figure 2.14 Cross-section through a helicopter blade showing applications of CFRPs (Camargo et al., 2024)

2.2.1.3 Applications of Ti6Al4V in Other Industries

The application of Ti6Al4V is not only limited to the aerospace industry but has wide usage in other industries, including automotive, medical, armour, consumer goods, and industrial and marine industries. A summary of these applications is given in Table 2.4.

© Central University of Technology, Free State

Table 2.4 Other applications of Ti6Al4V(ELI) (Smallman, 2016)

Sector	Common components	Predominant alloys
Aerospace	Compressor casings, jet engine rings, discs, wing flap tracks	Ti6Al4V
Automotive	Connecting rods, valves, valve springs and retainers	Ti6Al4V
Armour	M2 Bradley fighting vehicle tank hatch, M1 Abrams battle tank turret blow-off panels, VSEL towed Howitzer	Ti6Al4V
Medical	Prosthetics (knee, hip, and shoulder parts), dental implants, heart valves, hearing aids, connecting devices (bone screws, plates, rods, hooks and nails, staples and cables), and surgical instruments (blades and dental drills)	Commercially pure (CP) Grades 5, 23 Ti6Al4V
Consumer goods	Bicycle frames, eyeglass frames, cooking pans, and golf club heads	Ti–3Al–2.5V
Industrial and Marine - Power generation	Cryogenic applications, heat exchangers, tubing condensers, and pickling baskets.	Ti6Al4V
- Nuclear power stations	Oil and gas risers used for production.	
- Nuclear waste	Piping and cables used in the deep sea	

The vast application of Ti6Al4V in the various industries seen in the preceding material underscores its great importance. Given the limitation presented in the aerospace industry in the gas turbine, where its applications are limited to the low-pressure compressor due to temperature restrictions. The alloy can be further enhanced by nanoparticle reinforcement to improve its mechanical and thermophysical properties to extend its application in other areas within the aerospace sector.

In MMCs, the objective of introducing reinforcements is normally the enhancement of stiffness, creep resistance, strength, hardness, wear resistance, and high-temperature utility. However, it is necessary to ensure that these properties are achieved without compromising the toughness of the resulting materials. The relationship between strength and toughness in MMCs is affected by local stress concentration, deformation, and the presence of dense, large-angle grain boundaries that advance the formation of micropores. The design configuration of a composite offers the possibility to improve strength and toughness in MMCs simultaneously, provided that precision of the structural elements is carried out (Sadeghi & Cavaliere, 2023).

© Central University of Technology, Free State

Before delving further into NMCs, it is necessary first to understand the nature and types of composites currently available, topics that will be covered in the ensuing material.

2.3 Types of Reinforcements

Three main types of reinforcements are classified according to their aspect ratio, and these include particulates, short fibres or whiskers, and continuous fibres (HG & Xavior, 2018). Figure 2.15 illustrates these types of reinforcements.

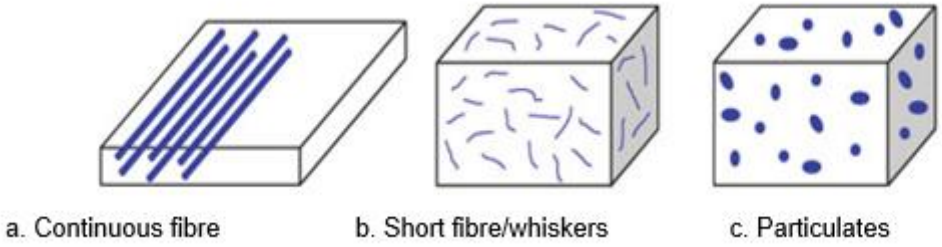

Figure 2.15 Classification of reinforcements (a) continuous fibres (b) short fibres/whiskers (c) particulates (HG & Xavior, 2018)

2.3.1 Natural and Synthetic Reinforcement

Fibre reinforcement is further classified into natural and synthetic. Natural fibres are found in the form of plant, animal, and mineral fibres (Amin et al., 2022; Bhattacharyya et al., 2015). Natural fibres have low tensile strength and low density, a tendency to absorb moisture, leading to the development of odour and discolouration due to rotting and begin to deteriorate at temperatures above 200 °C, which leads to a breakdown of their mechanical properties (Balla et al., 2019; Ku et al., 2011). Plant fibres can be classified into primary and secondary, in which primary fibres are grown for their fibre content whilst secondary fibres are a by-product of some preliminary use. Primary fibres include jute, kenaf, sisal, hemp, and cotton, whilst secondary fibres include pineapple, cereal, stalks, oil, palm, coir and agave. Animal fibres mainly comprise of proteins and can be classified into α-keratin fibres (wool, hair, and feathers) and fibroin fibres (silk and spider web). Mineral fibres are predominantly made from asbestos and have a fully crystalline structure (Bhattacharyya et al., 2015). Natural fibres are used to reinforce both thermoplastic and thermoset matrices. Natural fibres such as jute, sisal, silk, and coir are economical, abundant, and lightweight due to their low densities and high toughness and are biodegradable. Jute can be used for applications where

© Central University of Technology, Free State

a high strength-to-weight ratio and weight reduction are a requirement (Verma & Seanal, 2019). Synthetic fibres consist of glass, carbon and polymers, such as aramid and Kevlar, and are man-made fibres. Glass fibres dominate amongst the class of synthetic fibres, and their applications include large, low-cost structures such as wind turbine blades, ships, and civil engineering structures. Other applications include the manufacturing of circuit boards, windows, light bulbs, tableware, and the reinforcement of concrete and cement (Bilisik, 2018). Aramid fibres are used in applications where good energy-absorbing properties are required (Ogin et al., 2016). Table 2.5, Figure 2.16, and Table 2.6 show some natural and synthetic reinforcement fibres, respectively and their properties.

Table 2.5 Types of natural reinforcement fibres and their properties (Verma & Senal, 2019)

Type of fibre	**Density** **(kg/m^3)**	**Water absorption** **(%)**	**Young's modulus** **(GPa)**	**Tensile strength** **(MPa)**
Sisal	800–700	56	15	268 - low (Jones et al., 2001)
Roselle	800–750	40–50	17	170–350 - low (Jones et al., 2001
Banana	950–750	60	23	180–430 - medium (Jones et al., 2001)
Date palm	463	60–65	70	125–200 - low (Jones et al., 2001)
Coconut	143–380	130–180	19–26	120–200 - low (Jones et al., 2001)
Reed	490	100	37	70–140 - low (Jones et al., 2001)
Jute	1.46	12	55	400–800 - high (Halip, 2019; Taylor, 2000)
Flax	1.4	7	27	800–1500 - high (Halip, 2019; Taylor, 2000)
Sunhemp	1.48	8	70	550–900 - high (Halip, 2019; Taylor, 2000)
Pineapple	1.56	-	62	170 - low (Taylor, 2000)

© Central University of Technology, Free State

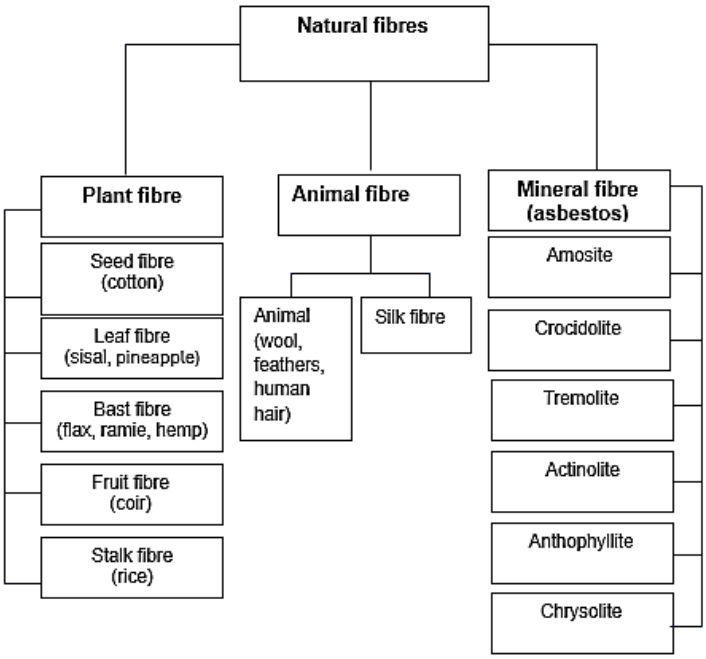

Figure 2.16 Classification of natural fibres

Table 2.6 Types of synthetic fibres and their properties (Ogin et al., 2016)

Material	**Density** **(kg/m^3)**	**Young's modulus** **(GPa)**	**Tensile strength** **(MPa)**	**Tensile strain to failure ε_f** **(%)**	**Coefficient of thermal expansion in the axial direction of the fibre** **(10^{-6}/K)**
E-glass	2600	76	2000	2.6	4.9
Kevlar™	1450	130/10 (axial/radial)	3000	2.3	-6
HM carbon	1950	380/12 (axial/ radial)	2400	0.6	-0.7
HS carbon	1750	230/20 (axial/radial)	3400	1.4	-0.4

Carbon fibres are the most expensive among synthetic fibres and are used for high-performance structures such as aerospace components, racing cars and general automotive applications (Ahmad, 2020).

2.3.1.1 Carbon Nanotube Reinforcements

CNTs (tubular in shape) are made from thin sheets of graphite, an allotrope of carbon, with diameters in the nanoscale. A single layer of graphene, has dimensions between 0.4 nm and 2 nm, depending on the synthesising temperature. In graphene, each carbon atom is connected evenly to three atoms of carbon (Eatemadi et al., 2014).

© Central University of Technology, Free State

Single-walled carbon nanotubes (SWCNTs) are made from a single layer of graphene (Figure 2.17a). Multi-walled carbon nanotubes (MWCNTs) are distinguished from SWCNTs by their multi-walled Russian doll structure in which one layer is inserted inside the previous layer (Figure 2.17(b). Multi-walled CNTs have a more rigid structure than SWCNTs. A comparison of the two types of CNTs is presented in Table 2.7 (Saifuddin et al., 2013).

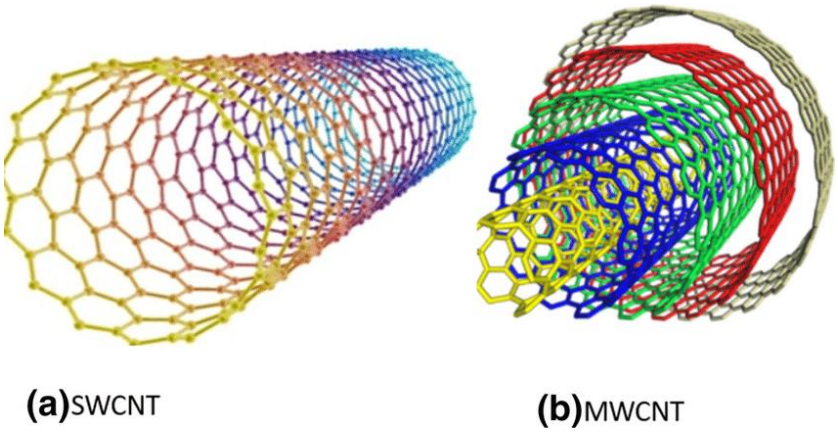

Figure 2.17 Illustration of CNTs (a) single-walled CNTs (b) multi-walled CNTs (Saifuddin et al., 2013)

Table 2.7 A comparison of SWCNTs and MWCNTs (Saifuddin et al., 2013)

Comparison of SWCNTs and MWCNTs	
SWCNTs	**MWCNTs**
Consists of a single layer of graphene	Consists of multiple layers of graphene
Catalyst required for synthesis	No catalyst is required for synthesis
Synthesis of bulk material is difficult and requires proper control over the growth and atmospheric conditions	Synthesis of bulk material is simple
Not fully dispersed and, therefore, form agglomerates	Homogenous dispersion is possible with no apparent agglomerates
Easily characterised and evaluated	Complex structure, making it difficult to evaluate
Easily twisted and pliable	Not easily twisted
Chances of defect during functionalisation are possible	Fewer defects, especially if the arc discharge method is used in their formation

The covalent bond that exists between carbon atoms in CNTs is chemically stable. The thermal conductivity of CNTs (MWCNTs) is similar to that of diamond of

© Central University of Technology, Free State

3000 W $m^{-1}K^{-1}$. CNTs possess superior electrical and thermophysical properties to Ti6Al4V. Their values of specific heat (c_p), density (ρ), thermal conductivity (k) and electrical conductivity (σ) are given in Table 2.8. It is evident from Table 2.8 that the thermophysical properties of SWCNTs' density and thermal conductivity are much better than those of MWCNTs, while MWCNTs have a better electrical conductivity than SWCNTs (Alkasasbeh et al., 2020). CNTs exhibit excellent mechanical properties, with an elastic modulus similar to that of diamond of ~1TPa. They are 100 times stronger than steel and have a density of one-sixth that of steel. They have excellent bendability and plasticity due to their hollow and closed structure. Their excellent properties make them suitable for the reinforcement of MMCs. Given the strength (240 MPa–460 MPa) and moderate stiffness (45 GPa–128 GPa) of MMCs, their addition into these matrices is expected to enhance these properties, thus extending their applications in the aerospace industry (Saberi et al., 2024; Ali et al., 2023).

Table 2.8 Thermophysical properties of SWCNTs and MWCNTs (Alkasasbeh et al., 2020)

Thermophysical properties	**SWCNTs**	**MWCNTs**
k (W. $m^{-1}K^{-1}$)	6000	3000
ρ (Kg. m^{-3})	2600	1600
c_p (J. $kg^{-1}K^{-1}$)	425	796
δ s ($S.m^{-1}$)	10^6-10^7	1.9^{-4}

CNTs are used to reinforce metals, polymers, and ceramic matrices to enhance their strength, elastic modulus, and toughness. SWCNTs have tensile strengths that range between 13–52 GPa and elastic modulus that range between 320–1470 GPa. However, they are prone to fabrication defects that can lower their strength (Byrne et al., 2009; Yu et al., 2000). MWCNTs support interwall coupling between graphene walls, which improves their interwall shear strength and load transfer. They have strengths in the range of 11–63 GPa with elastic modulus between 270–950 GPa (Byrne et al., 2009; Yu et al., 2000).

CNTs are used in various industries, including electronics, plastics, composites, and energy storage. Their applications are dominated by polymers and composites, as shown by Figure 2.18, which depicts the revenue and market share of CNTs based on

© Central University of Technology, Free State

their applications. Their unique properties make them suitable reinforcements together with fibre-reinforced polymer composites (FRP) to form CNT/FRP (Ali et al., 2023).

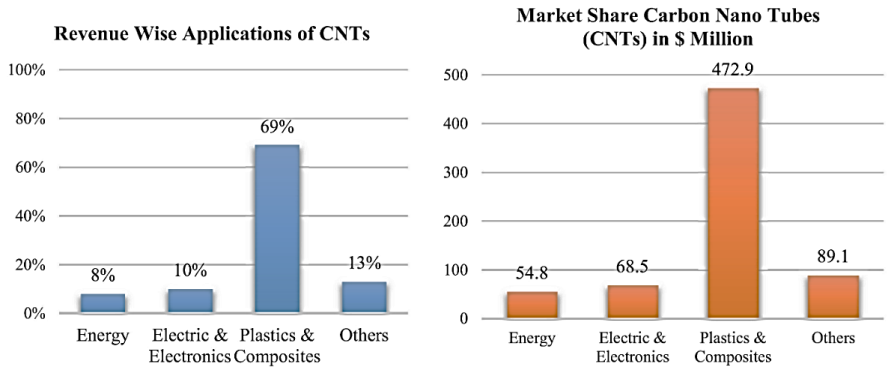

Figure 2.18 Market share and revenue based on CNT applications (Ali, et al., 2023)

2.3.1.2 Particulate Natural and Synthetic Reinforcements

Particle reinforcement fillers are made up of natural and synthetic fillers. Natural fillers occur in nature and are obtained through processes such as washing, milling, sieving, and drying. Some of these fillers include bentonite, montmorillonite, silica, wollastonite, talc, mica, glass beads, kaolin clay, rock dust, slag dust, hydrated lime, fly ash, hydraulic cement, loess (fragments of pre-existing minerals and rock formed by the accumulation of dust). Plant fillers include kenaf and ramie, whilst animal-derived fillers include cotton and silk. Synthetic fillers are derived from material processing or heavy chemical processing and are classified into subgroups which include oxides (TiO_2, FeO_3O_4), hydroxides ($Al(OH)_3$, $Mg(OH)_2$), salts (($CaCO_3$), ($BaSO_4$), $BaTiO_3$)), metals (boron, steel), and silicates (talc, mica) (Sztorch et al., 2022; Chen et al., 2022). The use of particulate reinforcements in composites achieves less strengthening effects compared to fibre reinforcements in their longitudinal directions. Reinforcement is a function of the interfacial bond strength, and its effectiveness is, therefore, a function of the length available for stress transfer (Ghaffar, 2017). The very short lengths in any direction that are available on the surfaces of small particles imply that full stress transfer is not possible and, thus, the much lower strengthening effects of particulates (Debnath et al., 2004). A particulate gives rise to increased stiffness, hardness, strength, and toughness. The advantages of using particulate reinforcement include low cost, ease of production, forming, handling, and compounding compared to fibre

© Central University of Technology, Free State

reinforcements (Gergely & Degicsher, 2000). The nature of the filler has a significant influence on the compounding method. Fillers that are heat and shear-sensitive require a different compounding method than those that tend to agglomerate. Melt compounding is a method in which the shear stress (hydrodynamic force) induced in a polymer melt is used to break down aggregated fillers to the nanoscale. This method is a much simpler method that can be used without incorporating surface modifications to filler materials. Other methods, including the intercalation and in-situ-polymerisation methods, require the fillers to be modified using organic surfactants (Tanashi, 2010). For fillers that are heat and shear-sensitive, pressure-assisted sintering is a process in which an external pressure is applied during the sintering process to achieve high densification (Mumtaz et al., 2024). It is generally believed that this process achieves densification by increasing the sintering driving force, assists in particle arrangement and prevents grain growth by decreasing diffusivity and, thus, the grain boundary mobility (Fang & Wang, 2010). In this process, the temperature can be decreased to almost half of the melting point of ceramics. Pressure sintering of glass and copper powder mixtures at various temperatures produce fully densified composites (Gopal & Manivasagam, 2019). Particulate fillers are predominantly used for polymers, more specifically thermoplastics, to facilitate compounding and increase stiffness and are mostly ceramic fillers (DeArmitt & Hancock, 2003). The properties of particulate (filler) reinforcements are influenced by their size, shape, and surface chemistry. (Park & Seo, 2011). Some common mineral fillers and their applications are shown in Table 2.9.

Table 2.9 Some common mineral fillers and their applications (Park & Seo, 2011)

Type of filler	**Application**
Kaolin clay	Reinforced nylon, wire, and cable
Talc	Stiffness, abrasion – polypropylene
Mica	Stiffness, polypropylene
Silica	Reinforced rubber, epoxy
Wollastonite	Reinforced plastics, coatings
Glass fibre-beads	Reinforced plastics
Aluminium trihydrate	Flame retardance
Magnesium hydroxide	Flame retardance
Crystobalite	Abrasion resistance/plastics
Titanium dioxide	Plastics, colourant, filler

© Central University of Technology, Free State

2.3.1.3 Particulate Reinforced Composite

A particulate composite is characterised by particles dispersed within a matrix. The particles can vary in size, shape, and orientation. Particulates can be categorised into three subclasses: general, flakes and filled/skeletal particles (Figure 2.19). A flake composite is made of flakes with a larger contact area to enhance the thermal conductivity of the composite (Upadhyay et al., 2020), in the case of heat transfer or to enhance the transfer of stress. A filled/skeletal composite is made of continuous skeletal filled by a second material, such as occurs in the case of a honeycomb core filled with insulating material. A general particulate is made of spherical or ellipsoidal particles dispersed in a matrix (Staab, 2015). Particulate reinforced composites are made of natural or synthetic particles. Natural particles include minerals such as calcium carbonate, kaoline, aluminium trihydrate, clay, feldspar, nepheline syenite, natural silica and mica, talc and agricultural waste. Synthetic fillers are made of processed mineral products, which include carbon black, fumed silica, and aluminium hydroxide. Particle sizes range between 0.1 μm to 2 mm (Upadhyay et al., 2020).

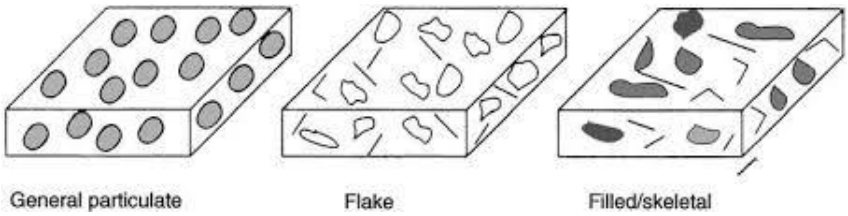

Figure 2.19 Classification of particulate composites (Staab, 2015)

The main properties of fillers that significantly influence the mechanical properties of composites include particle size distribution, particle shape, and surface area. The shape of fillers influences the flow of the matrix and relief of stress upon the application of load onto a composite. Spherical fillers will allow easier flow of the matrix and stress relief compared to irregular-shaped fillers. The particle size distribution (PSD) determines the extent to which particles fill voids between particles and improves the packing density of the material (Nagrale et al., 2023). Lind et al. (2010) studied the particle size distribution of 35% alumina with a particle size of 120 nm, 20% alumina with an addition of 0.5% $Al(NO_3)_3$ (120 nm) and 10% alumina with an addition of 5% Zn (120 nm) all spray-dried with a 1.0 mm nozzle measured at 0.15 bar and 3.0 bar, respectively. The authors found that despite the addition of reinforcement of alumina nitrate, zinc nitrate, or silica particles, the mean particle size of the agglomerates

© Central University of Technology, Free State

ranged between 5–10 µm with a small number of large particles >100µm. On the other hand, Afolabi et al. (2022) studied the effects of syntactic foam made from hollow glass microspheres (HGM) in an epoxy matrix. The parameters included particle size variations between (20–24 µm), (25–44µm), and (50–60 µm) and reinforcement of 5, 10, 15, 20 and 25 vol%. Their work showed that the highest flexural strength was achieved at 5% vol% fraction in the range of 50–60 µm particle size variation, while the flexural modulus increased with particle size variation. The highest particle size distribution was found to be 31.02 in the 25–44 µm range. The results showed an increase in properties as the particle size distribution increased with a limiting reinforcement of 5%. The results presented by Lind et al. show no effect of volume reinforcement.

The shape and size of the filler affect the surface roughness. Irregularly shaped fillers have led to higher surface roughness of composite parts, and so do larger fillers. Marghalani (2010) studied the effect of filler geometry and particle size on the surface roughness of resin composites. Particle sizes were in the range of 100–1500 nm, and fillers were spherically and irregularly shaped. Among the experimental data investigated, the lowest surface roughness was found in the spherically shaped reinforcement samples, whilst rough surfaces were obtained in irregularly shaped fillers. The author also established that for both geometries, surface roughness increased with an increase in particle sizes. In this case, the particle sizes played a role in the surface finish, irrespective of the geometry. Therefore, the selection of particle sizes and shape geometry should be taken into consideration when designing a composite. The influence of the filler on the matrix also depends on the type and composition of the filler and its mechanical properties. The selection of the filler material should be based on its ability to meet the desired properties of a design, as no single filler can fulfil all the properties (Liu et al., 2021).

Magnesium has a high corrosion rate and, as such, is reinforced with nano particulates to enhance the necessary mechanical properties (including Young's modulus and yield strength) and to reduce its susceptibility to corrosion for engineering and biomedical applications. Niobium (Nb) and tantalum (Ta) particles are used to reinforce magnesium through a process of powder metallurgy (Vahid et al., 2017). When a copper matrix is reinforced with tungsten carbide (WC), hardness values of

© Central University of Technology, Free State

360–370 HV are obtained, which are higher than the normal values for copper of 100 HV (Deshpande et al., 2006). When natural rubber and styrene-butadiene are blended and reinforced with soy protein particles, they show improved mechanical properties and faster rates of curing (Jong, 2019). Cermet is an example of a ceramic-metal composite. A common type of cermet is cemented carbide, which is made of hard particles of refractory carbide ceramic, such as tungsten carbide (WC) or titanium carbide (TiC), rooted in a matrix of a metal such as cobalt (Co) or nickel (Ni) (Heydari et al., 2021).

2.3.1.4 The Effect of Nanoparticles on the Properties of Nanoparticle-Reinforced Composites

The reduction in the size of reinforcing particles to the nanoscale level has a significant effect on the interaction between particles and dislocations in the matrix (Casati & Vedani, 2014). The mechanical properties of particulate composite materials, including tensile strength, hardness, and Young's modulus, improve with a decrease in the size of particles, whilst wear resistance increases with an increase in the size of particles at the micro- and macro-scale, but not generally so at the nanoscale (Ashraf et al., 2018). The rate of wear increases as particle size increases because larger particles with a higher wear resistance cover greater surfaces and are, therefore, better able to control the rate of wear. Smaller particles are only able to cover small surface areas and wear along with the matrix. (Fu et al., 2008; Sachit et al., 2018). Reinforcements, having smaller particle sizes, improve the flexural strength because of increased particle surface area, which causes high surface energy at the interface between matrix and filler material (Kundie et al., 2018). Sachit et al. (2018) reported significant improvement in mechanical properties of tensile strength, hardness, and other properties, such as wear resistance, at particle sizes below 20 nm, with three times more improvement observed at 11 nm in their experiments (Sachit et al., 2018).

Guo et al. (2017) reported improved strength and increased interface shear stress at the nanoscale size. The studies carried out by Guo also highlighted the existence of clean interfaces between the matrix and the reinforcement fillers, with no compounds forming at the interfaces (Guo et al., 2018). It has been shown that the large aspect ratios of layered silicates are responsible for improved mechanical properties in particulate-polymer composites. It has also been reported that smaller calcium

© Central University of Technology, Free State

carbonate particles lead to higher strength of filled polypropylene composites. Moreover, nanoscale silica has been found to provide higher strength in polypropylene composites (Kontou et al., 2023). Alumina trihydrate-filled epoxy containing small reinforcing particles showed improved toughness. The mechanical properties of nanocomposites are affected by particle size and the reinforcement loading or volume/mass fraction in the matrix (Fu et al., 2008).

Unuoha et al. (2017) conducted experiments on the effect of filler loading and particle size on the mechanical properties of the periwinkle shell-filled recycled polypropylene composite. The tensile strength of this composite increased with increasing volume fraction of filler up to 15 % and decreased at filler volume fractions of 20 % and above. The decrease in strength at the higher volume fraction of the reinforcing filler was due to agglomeration of the filler material that prevented proper dispersion of particles within the matrix. The presence of aggregates will provide crack initiation sites or act to enhance crack propagation, which will lead to premature failure in the composite when stress is applied (Abd-Elaziem, 2023). The strength of the composite also increased with a decrease in particle size because smaller particles provide larger surface areas, which enhances the interfacial bonding between matrix and filler materials. Unuoha et al. (2017) further observed improved yield strength and Young's modulus of the composite up to a volume fraction of the reinforcing filler of 15 %, a decrease of the two properties above this value and an increase with decreasing particle size. The flexural strength and hardness of the composite increased up to volume fractions of the reinforcing filler of 20 % and 25 % (Onuoha et al., 2017).

The wear resistance of a material decreases when volume fractions of nanoparticles are increased in composite materials (Njoku et al., 2011; Onuoha et al., 2017). Güler et al. (2017) investigated the effect of nanoparticle content on zinc aluminium alloy (ZA27) reinforced with aluminium oxide (4%) and nano graphite particulates (1,2,3, and 4 % vol.). They found that the wear loss of the composite increased with increasing nanoparticle loading of 4% alumina oxide and 4 % nanographite particulates. They also found that the hardness increased for 1, 2, 3% vol% of nanographite particulates and 4 % aluminium oxide due to the high content of 4 % of alumina oxide owing to its hardness; however, the hardness decreased at 4% nanographite particulates due to the softness and laminated structure of nanographite (Güler et al., 2017).

© Central University of Technology, Free State

Nanoparticles offer higher rigidity and higher yield strength to matrices. They also yield higher fracture toughness in the resulting composites (Sulima et al., 2008). The improvement of the properties of a nanocomposite, like those of other composites, largely depends on the transfer of load from matrix to filler. The interactions of these constituent phases define the interfacial bond through which the transfer of stress from filler to matrix and vice versa occurs (Sadeghpour et al., 2020).

2.3.1.5 The Interfacial Bond

The interfacial bond between the reinforcing phase (fibre and particles) and matrix plays an important role when it comes to determining the mechanical properties of a composite. Good bonding between the fibre and matrix produces high strength and stiffness in the resulting composite. (Hench & Jones, 2005).

The interface is the surface formed between the reinforcing phase and matrix and maintains the bond between them (Papanicolaou et al., 2021). The interfacial bond is a weak link for most composite materials, and controlling its strength is a complex problem. (Hench & Jones, 2005). Improved interfacial bonding can be obtained by using satisfactory agents for organic and inorganic composites (Kumudinie, 2001).

Bonding mechanisms can be associated with processes including absorption and wetting, electrostatic attraction, reaction bonding and exchange reaction bonding, as shown in Figure 2.20. In this figure, interfacial bonds are shown to be formed by (a) molecular entanglement, (b) electrostatic entanglement, (c) interdiffusion of elements, (d) chemical reaction between group A and group B atoms of the other surface, (e) chemical reaction forming a new compound, and (f) mechanical interlocking.

© Central University of Technology, Free State

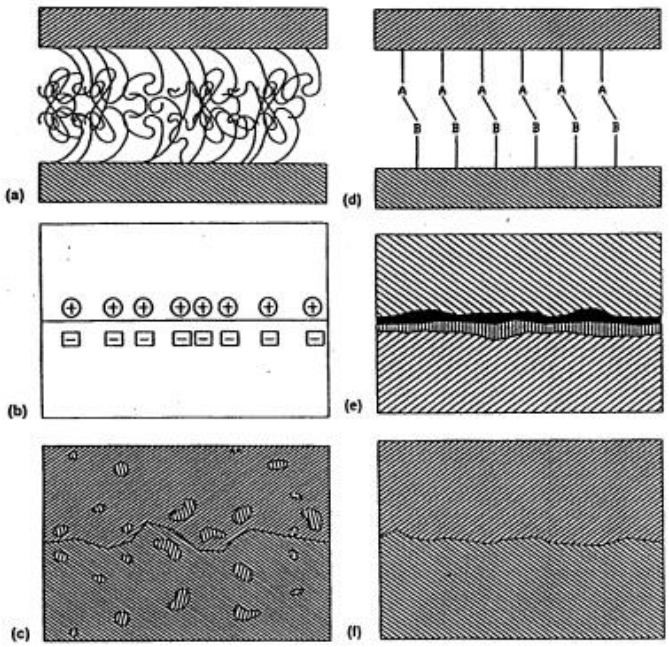

Figure 2.20 Interface bonds (Hench & Jones, 2005)

Other low-energy bonding mechanisms include van der Waals forces, hydrogen bonding, hydrophobic bonding, and π bonds (Zhao et al., 2022; Dhotel et al., 2013). The strength of the interface determines the ability of a composite to transfer stresses from the matrix to the fibre. In the case of bonding based on wetting, the strength of the interface is maximum when the surface tension of the reinforcing material, which is a solid, and the surface tension of the matrix, being a liquid, are nearly the same. In the case of interdiffusion, the interfacial bond is strengthened by an increase in the number of molecules and the strength of the bond between molecules. Mechanical bonding promoted by surface oxidation treatments is an important type of bonding in polymer matrices and carbon fibre. However, the strength of the interfacial bond in this case is not strong in transverse tension unless many re-entrant angles on the fibre surface are present, but the longitudinal shear strength may be important depending on the degree of roughness (Teklal et al., 2018).

Premature failure in MMCs, such as interfacial cracking or cavitation, is caused by poor interfacial bonding. In addition, interfacial chemical reaction is an important factor for many MMCs (Thakur et al., 2023). The process that leads to the production of MMCs tends to involve high temperatures, during which the highly reactive nature of the metal matrices produces thick interfacial layers (intermetallic compounds) such as

© Central University of Technology, Free State

aluminium carbide (Al_4C_3) and particle fragmentation, which are prone to brittleness (Kareem et al., 2024). Such interfacial layers lead to embrittlement and weakening of the composite. The mechanical properties of composites and nanocomposites arising from the strength of the interface can be determined by several theoretical models that are discussed in the ensuing sections.

2.4 Theoretical Models for Predicting the Elastic Properties of Composites and Their Use in Designing Nanoparticulate Composites

The elastic properties of composites are based on fundamental principles of mechanics that dictate the models used to describe them. The process of predicting elastic properties of composites from properties of the fibre and matrix is a well-developed field; however, integrating manufacturing defects (arising from the use of harmful chemicals during manufacture and the use of wrong materials when constructing a product, including screws, bolts, and fasteners) to properly estimate these properties is not a fully developed field. (Ogunleye & Rusnakova, 2022).

2.4.1 The Voigt Rule (Rule of Mixtures - RoM) for Strength and Stiffness

The Voigt rule or Iso-Strain rule is based on the axial stiffness and strength of continuous fibre reinforcement is also referred to as the Iso-strain model and defines the upper bound of the effective stiffness (Kundalwal, 2017; Wiśniewska et al., 2019).

In this rule, the axial stress in a continuous longitudinally aligned fibre-reinforced composite stress is given by the equation:

$$\boldsymbol{\sigma_c = v_f \sigma_f + \left(1 - v_f\right)\sigma_m} \qquad \textbf{(2.1)}$$

But from the Iso-Strain rule, the axial strain in the reinforcement ϵ_f, in the matrix ϵ_m and in the composite ϵ_c are all equal. Thus, Equation 2.1 can be rewritten in terms of the stiffness of the constituents as follows.

$$\boldsymbol{E_c = v_f E_f + \left(1 - v_f\right)E_m} \qquad \textbf{(2.2)}$$

where E_c = modulus of the composite; E_f = modulus of the fibre (that is assumed to be isotropic); E_m = modulus of the matrix, which is also assumed to be isotropic. The foregoing equations are used to predict the strength and stiffness of composites in the axial direction of the continuous, longitudinally aligned reinforcing fibres in the order they have been presented here, respectively.

© Central University of Technology, Free State

2.4.2 The Reuss Rule (Inverse Rule of Mixtures - IRoM) for Strength and Stiffness

The Iso-Stress or Reuss model defines the lower bound for the stiffness of composites and provides a better estimate of the stiffness of particulate composites. The total transverse strain (ϵ_c) is equal to the volume-weighted sum of the strains of the fibre and matrix, thus (Kundalwal, 2017):

$$\boldsymbol{\epsilon_c = V_f \epsilon_f + \left(1 - V_f\right)\epsilon_m} \tag{2.3}$$

But from the Iso-Stress rule: $\sigma_c = \sigma_f = \sigma_m$. Therefore,

$$\boldsymbol{E_c = \left(\frac{E_f E_m}{E_f V_m + E_m V_f}\right)^{-1}} \tag{2.4}$$

The Reuss model is used to predict the stiffness of composites in directions orthogonal or perpendicular to the longitudinal directions of the continuous, longitudinally aligned reinforcing fibres and assumes iso-stress in these directions. It is a simplified model, just as is the Voigt rule (Kundalwal, 2017).

Figure 2.21 shows an example of the Voigt and Reuss models. In Figure 2.21, composites of tungsten-reinforced copper matrix at different percentages of tungsten are seen to have different values of the modulus of elasticity. The experimentally obtained values of stiffness for the composites seen in the form of scatter points in this graph fall within the Voight model (upper bound) and IROM (lower bound).

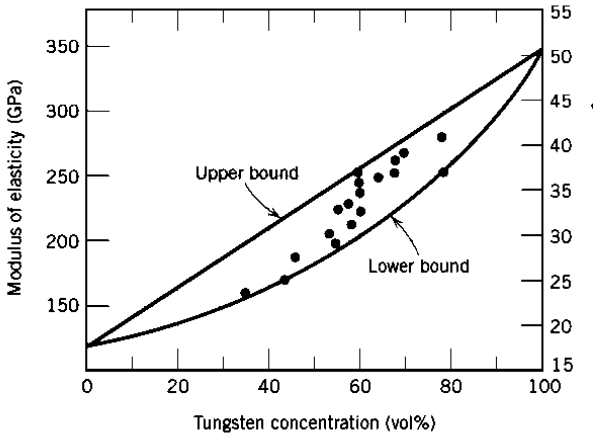

Figure 2.21 Modulus of elasticity versus volume fraction of tungsten for tungsten particles dispersed within a copper matrix (Callister & Rethwischet, 1940)

© Central University of Technology, Free State

2.4.3 Van der Poel's Theory

Van der Poel's theory provides an accurate method for determining the shear modulus of a particulate composite. Originally, this method was complicated and had errors. It also came with a table of values of shear modulus for which the Poisson's ratio of the matrix was set to 0.5. It has since been re-examined, the errors in it corrected and modified to allow its use for materials with any values of Poisson's ratio (Smith, 1975).

For isotropic materials, the elastic constants for elastic modulus (E), shear modulus (G), bulk modulus (K), and Poisson's ratio (ν) are known to be related by the following expression in which only two constants are required to characterise the initial elastic behaviour for an isotropic material (De Vaucorbeil et al., 2020).

$$\boldsymbol{E = \frac{9KG}{3K+G}} \tag{2.5}$$

$$\boldsymbol{\upsilon = \frac{3K-2G}{6K+2G}} \tag{2.6}$$

The relationship between the elastic constants is shown in Table 2.10.

Table 2.10 Relationship between elastic constants (Maringa, 2022)

	E	**G**	**K**
E	E	$2G(1+v)$	$3K(1-2v)$
G	$\left[E/2(1+v)\right]$	G	$\left[3K(1-2v)/2(1+v)\right]$
K	$\left[E/3(1-2v)\right]$	$\left[2G(1+v)/3(1-2v)\right]$	K

Van der Poel's theory provides the following two relationships for composites (Smith, 1975):

$$\boldsymbol{K = K(G_m, K_f, K_m, \upsilon)} \tag{2.7}$$

$$\boldsymbol{G = G(G_f, G_m, \nu_f, \nu_m, \upsilon)} \tag{2.8}$$

In these two equations, the symbol υ, stands for the volume fraction of the reinforcing phase. The equation in 2.5 also arises from Kerner's theory. When the elastic constants E_m, ν_m, E_f, ν_f of the matrix and filler material are known, the corresponding values of the elastic constants K_m, G_m, K_f, G_f can be determined using Equations 2.5 and 2.6. The elastic constants K_c and G_c of the composite can be calculated as a function of the volume fraction (υ) of the reinforcing phase from Equations 2.7 and 2.8.

© Central University of Technology, Free State

The corresponding values E_c and ν_c can then be calculated from Equations 2.5 and 2.6. The calculated E_c and ν_c values are then compared to experimental data values to confirm the accuracy of Van der Poel's theory in predicting the two elastic constants for a specific composite.

Figure 2.22 represents the ratio of elastic modulus E_c/E_m plotted as a function of filler volume fraction of glass spheres-reinforced epoxy resin matrix. The matrix, in this case, was made from diglycidyl ether of bisphenol-A (DGBEA). The H1 and H2 curves represent the lower and higher bounds, respectively, predicted by the Hashin-Shtrikman's theory.

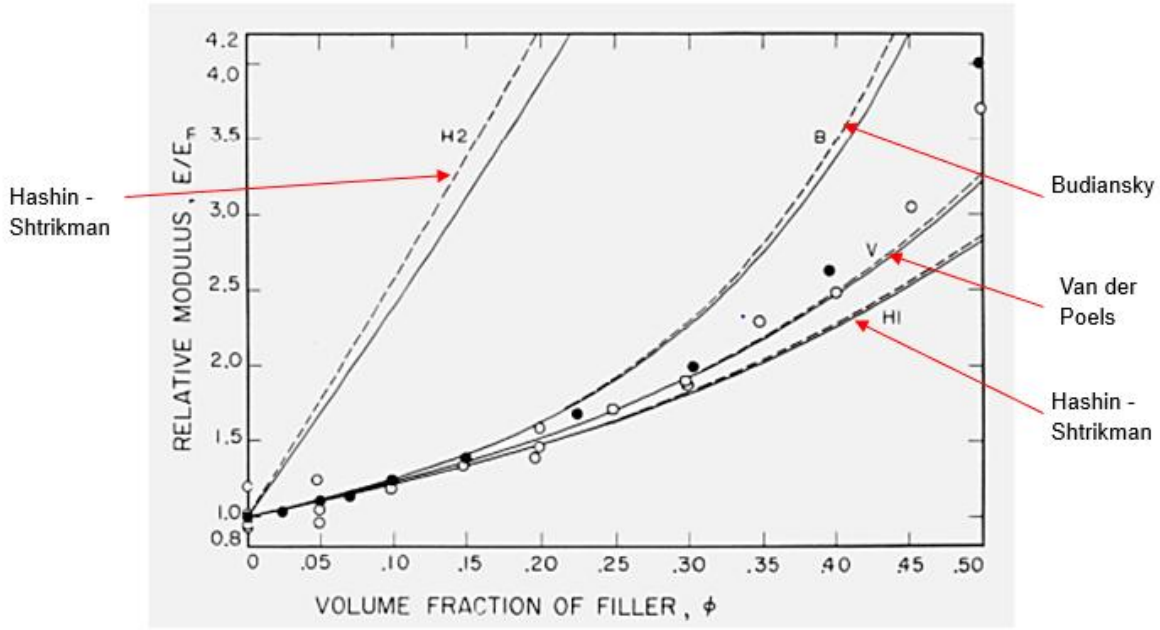

Figure 2.22 A plot of relative Young's modulus E/E_m versus the filler volume fraction (Smith, 1976)

The predicted values from Budiansky's (not discussed in the literature) and Van der Poel's theories (*B* and *V*) curves and least upper curves (H2) and highest lower bounds of (H1) of the Hashin-Shtrikman theory are shown as pairs of solid and dashed lines (Figure 2.22). The solid and dashed lines in this figure represent predicted values using these three theories based on experimental values of stiffness and Poisson's ratio for the fresh (1–2 weeks) and age-hardened (200 days) samples, respectively. The H1 curve is calculated using Hashin-Shtrikman's highest lower bounds for shear and bulk modulus. The H2 curve is calculated using the Hashin-Shtrikman least upper

© Central University of Technology, Free State

bounds for shear and bulk modulus. In Figure 2.22, the open circles represent data obtained by calculating a theoretical value of the elastic modulus of the matrix E_m from data from samples tested 1–2 weeks after preparation. The data from experiments carried out on samples tested 200 days after preparation is represented as solid circles based on calculated theoretical values of E_m. The values obtained using Van der Poel's theory are in good agreement with the experimentally obtained values for a filler content of up to 35 % and offer a better fit compared to the Hashin-Shtrikman curve. However, at filler volume fractions of 50 %, the measured values exceed the predictions based on Van der Poel's theory (Smith, 1976).

2.4.4 Halpin-Tsai Semi-Empirical Equations

The Halpin-Tsai semi-empirical equations can be used to predict the elastic modulus of composite materials based on geometry, orientation of reinforcement, and the elastic properties of the matrix and reinforcement materials (Shokrieh et al., 2015). The transverse stiffness E_2 of a laminar with continuous fibres is the most important elastic property and is important in correctly predicting the mechanical behaviour of a composite material (Mounier, 2012), where delamination of the laminates is the predominant failure mode. An approach based on the strength of the material underestimates the true value of E_2, which leads to the lower bound or the Reuss model. The Halpin-Tsai model offers flexibility and adaptability, is the preferred choice over other models, and allows sensible interpolations between the lower and upper bounds of composite materials (Giner et al., 2018). The Halpin-Tsai model for longitudinally aligned reinforcing fibres is represented by Equation 2.9:

$$\frac{E_2}{E_m} = \frac{1+\xi\eta V_f}{1-\eta V_f} \qquad (2.9)$$

where:

$$\eta = \frac{E_f/E_m - 1}{E_f/E_m + \xi} \qquad (2.10)$$

In these two equations, the symbols E_f and E_m stand for the stiffness of the fibre and matrix, respectively, η is a stress partitioning factor, ξ is a shape parameter that is dependent on the geometry, distribution or packing arrangement, and loading direction of all the reinforcing fibres. For the conditions where $\xi \to 0$, Equation 2.9 reduces to the lower bound value (E_2) predicted by the Reuss rule, and where $\xi \to \infty$,

© Central University of Technology, Free State

Equation 2.9 reduces to the upper bound values (E_1) predicted by the Voigt rule. For composites reinforced with randomly oriented fibres, the following modified Halpin-Tsai equations are used:

$$\boldsymbol{E_c = E_m\left[\frac{3}{8}\left(\frac{1+\xi\eta_L V_f}{1+\eta_L V_f}\right)+\frac{5}{8}\left(\frac{1+2\eta_T V_f}{1-\eta_T V_f}\right)\right]} \qquad (2.11)$$

where:

$$\eta_L = \frac{E_f/E_m - 1}{E_f/E_m + \frac{2l}{d}} \qquad (2.12)$$

and

$$\eta_T = \frac{E_f/E_m - 1}{E_f/E_m + 2} \qquad (2.13)$$

The Halpin-Tsai semi-empirical equations for predicting the elastic properties of composites are widely used to calculate different configurations of composite materials (Giner et al., 2015). Though they are good for predictions at lower volume fractions of reinforcement, they lead to underestimates at larger volume fractions. As noted earlier, they offer the advantage of flexibility; however, they have the drawback of dependency of their predictions on parameters that need to be determined experimentally (Giner et al., 2018).

In summary, it is noted that the Voigt and Reuss models are used to predict the upper bounds of strength for composites for the first model and the upper and lower bounds of the elastic moduli for composites, respectively, for different contents of filler. The Hashin-Shtrikman theory provides a narrower range of the upper and lower bounds than the previous two models and is particularly used to predict values of the coefficient of thermal expansion for composites. Van der Poel's theory provides an accurate method for determining the shear modulus of particulate composites. The Halpin-Tsai semi-empirical model is the most widely used of all existing models and predicts both the longitudinal and transverse elastic moduli of composites.

The foregoing discussion aside, it is important to note that the methods of fabrication of composites affect the integrity and evenness of the reinforcing fibres, as well as porosity. The mechanical properties of composites are also affected. Henceforth the

© Central University of Technology, Free State

following discussions is on the different methods of fabrication using traditional methods.

2.5 Methods of Producing Metal Matrix Nanocomposites (MMNCs)

The fabrication processes of normal composites are the same for nanocomposites. Figure 2.23 presents a schematic of the various processes used to fabricate MMCs, ceramic, and polymer composites. This is followed by brief discussions of the various processes used to fabricate MMCs and, finally, descriptions of casting and powder metallurgy processes applied to nanocomposites and their disadvantages.

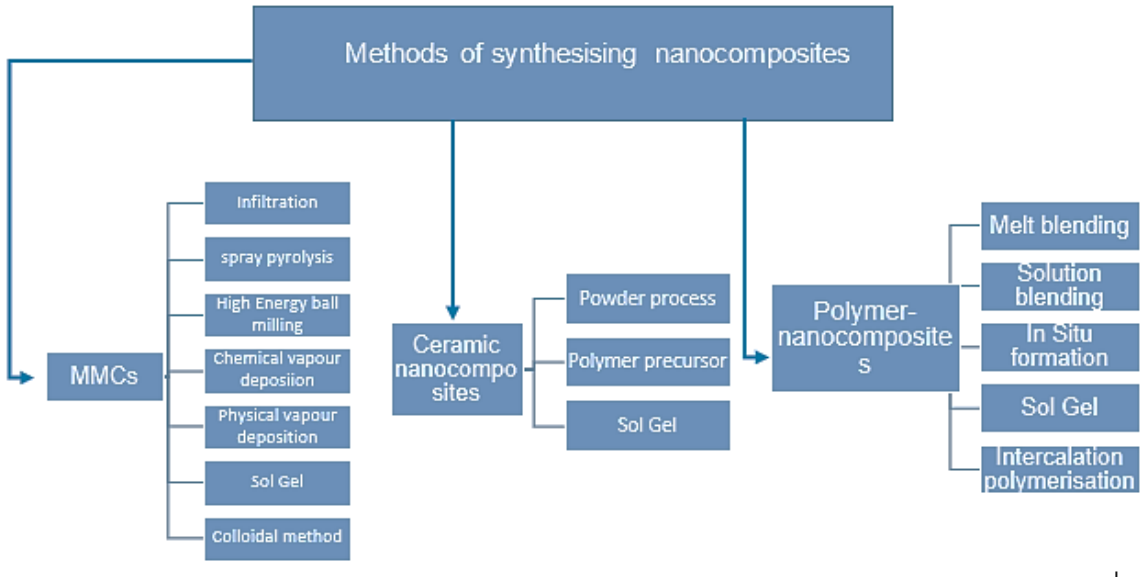

Figure 2.23 Classification of synthesis methods for fabrication of MMCs, CNCs, and PNCs (Seetharaman et al., 2021)

The properties of MMNCs are not only affected by the reinforcing phase but also by the type of manufacturing technique used to produce them. The process of manufacture plays a vital role in predicting the mechanical and physical properties of nanocomposite material (Kalra et al., 2018). There are two ways in which MMNCs can be produced, including primary (combining and consolidation) and secondary (shaping or joining) processes. The primary and secondary processes are determined by the matrix and reinforcement material and their respective mechanical and thermophysical properties. The primary process is also determined by the ability of the process to minimise damage to the dispersed phase, preservation of its strength and promotion of wetting and bonding between the matrix and reinforcement phase, and the state of the constituents, either liquid or solid state (Mussatto et al., 2017). Secondary

© Central University of Technology, Free State

processes include reactive squeeze casting and rapid solidification, exothermic dispersion, reactive hot pressing and self-propagating high-temperature synthesis (SHS) (Cabeza et al., 2017).

2.5.1 Pressure Infiltration Process (PIP)

In the pressure infiltration method, a preformed dispersed reinforcement (particulate, fibre, woven ceramic, non-woven ceramic material) is soaked in a molten matrix (commonly used matrix is aluminium) that fills the spaces between the dispersed reinforcement phases. The process is carried out either by the capillary force of the dispersed phase (spontaneous infiltration) or external pressure (vacuum, gaseous, mechanical, electromagnetic, centrifugal, or ultrasonic) that is applied to the liquid matrix phase (forced or pressure filtration) (Etemadi et al., 2018). Figure 2.24 shows a schematic representation of this process

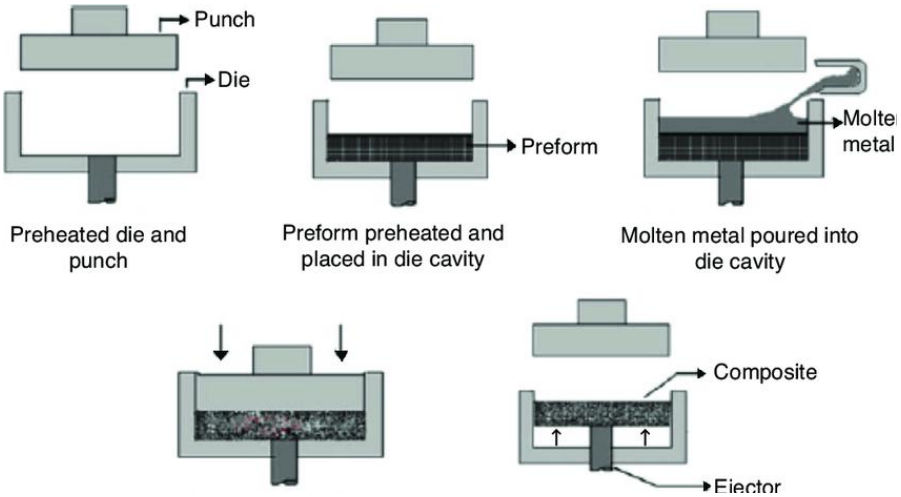

Figure 2.24 A schematic representation of the pressure infiltration process (Kannan & Ramanujan, 2018)

2.5.2 Spray Pyrolysis

Spray pyrolysis is a process in which a thin film layer is created over the surface of a substrate. A solution or coating material is directly applied over the substrate, as shown in Figure 2.25, where the coating material increases the strength and improves the appearance of the substrate. Coating materials can be in the form of nickel oxide, zinc oxide, manganese acetate, copper chloride, copper indium chloride, zinc chloride, tin chloride, valence spinel hausmannite, zinc oxide doped with aluminium (Shunmugasundaram et al., 2021).

© Central University of Technology, Free State

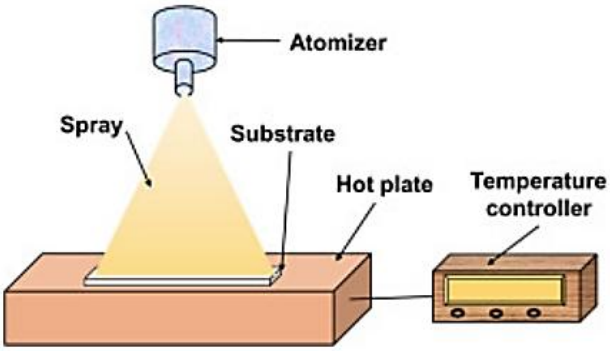

Figure 2.25 Schematic representation of the spray pyrolysis process (Salehabadi et al., 2023)

2.5.3 High-Energy Ball Milling

High-energy ball milling is an effective method to synthesise MMCs and employs mechanical alloying of powders using a high-energy ball mill. Mechanical alloying is a powder metallurgy process that uses repeated cold welding, fracturing and rewelding of powder particles in a high-energy ball mill (Stalin et al., 2018). The initial particles are plastically deformed, then welded together and fractured repeatedly. Thereafter, singularly or in conjunction with each other, processes such as cold pressing, sintering, hot pressing, and extrusion are used to form fully dense nanocomposites (Cabeza et al., 2017). Figure 2.26 is a schematic representation of high-energy ball milling in which (A) represents the high-energy ball chamber, (B) the breaking phase, and (C) the welding phase.

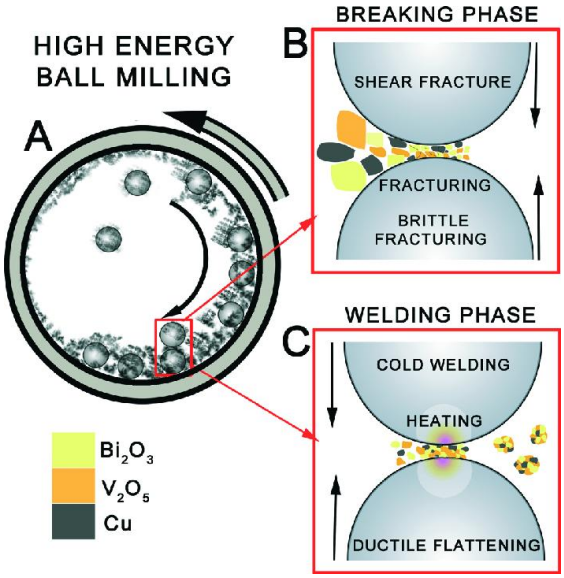

Figure 2.26 Schematic representation of energy ball milling (Merupo et al., 2015)

© Central University of Technology, Free State

Chamber A in Figure 2.26 contains hard balls and a mixture of the initial reactants at defined ratios; Chamber B is where repeated fracturing of bulk reactants causes the formation of composite particles with desired compositions. Chamber C is where small agglomerations form to yield the final morphology of the mixed powder. Though this method would have been advantageous to the present study, however, it would have led to defects of Ti6Al4V particles.

2.5.4 Vapour Deposition Methods

Vapour deposition methods include physical vapour deposition (PVD) and chemical vapour deposition (CVD). Both processes involve the transferal of the coating material to the surface of a workpiece, molecule by molecule or atom by atom. A precursor or a combination of gases in the CVD method flows over a heated workpiece in a chamber. As a result of a chemical reaction on the surface of the workpiece and the duration of exposure, a thin phase forms on its surface. The reinforcement is distributed at the surface and is used for applications where hardness and wear resistance are required. Therefore, these are considered surface composites. (Sunil, 2015). In the PVD process, the deposited material is transformed into atomic particles by a thermal physical process of collision. The atoms are then directed to the substrate in a vacuum environment or gaseous plasma under low-pressure conditions, in which they condense to form a physical coating (Baptista et al., 2018).

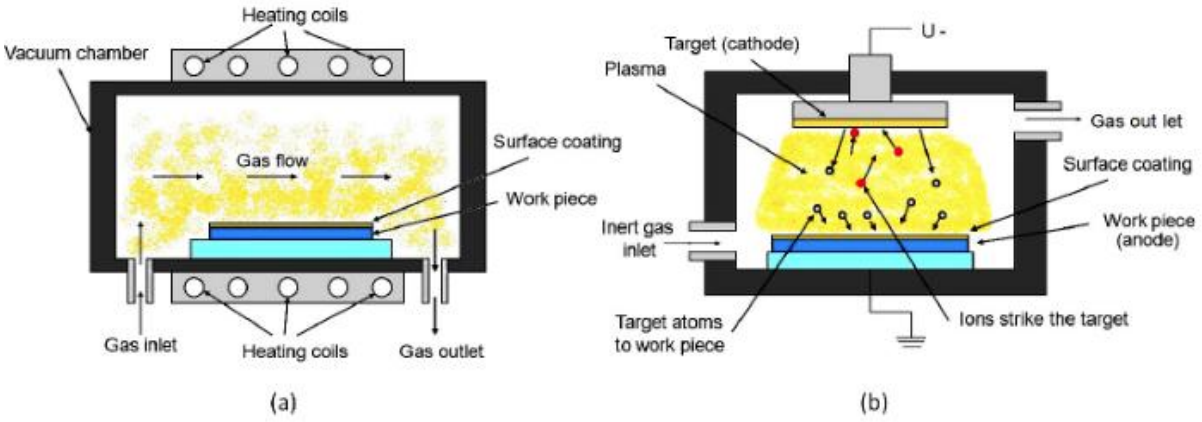

Figure 2.27 Schematic representation of (a) chemical vapour deposition and (b) physical vapour deposition (Sunil, 2015)

© Central University of Technology, Free State

2.5.6 Sol-Gel Process

The sol-gel process (Figure 2.28) is carried out at low temperatures (normally less than 100 °C) in the liquid state. The final product is a solid formed through polymerisation that involves the establishment of M-OH-M or M-O-M, where the letters M and O represent the metal atoms and oxygen atoms in the raw material and hydroxide, respectively (Bokov et al., 2021). Materials that can be produced through this process include metal oxides, nitrides, and carbides. The key process includes the hydrolysis and condensation of an inorganic or metal-organic precursor that produces a sol (solution) such that ensuing chemical reactions and/or mild thermal treatments transform it into a gel that is transformed further through a calcination process into the end product (Mahato et al., 2023).

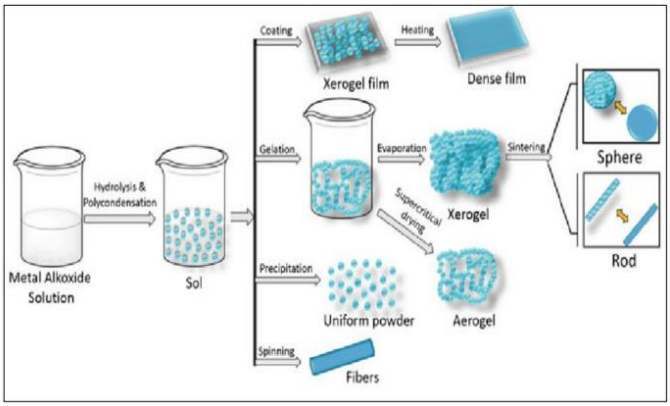

Figure 2.28 Schematic representation of the sol-gel process (Badanayak & Vastrad, 2021)

2.5.7 Colloidal Method

The colloidal method is a traditional method for synthesising nanomaterials with strictly controlled size, morphology, and composition. It combines several approaches; however, only the solvent approach is discussed. With the solvent approach, in addition to its primary role, it also serves as a stabilising agent for colloidal nanocrystals (Gulevich et al., 2024). There are two principal ways to prepare colloids, including dispersion of large particles or droplets of colloidal dimensions (1–1000 nm in diameter) by milling, spraying or application of shear (shaking, mixing, high-shear mixing) and condensation of small, dissolved molecules into larger colloidal particles through precipitation, condensation, or redox reactions (Everett, 2007). A colloid consists of a dispersed phase (or discontinuous phase) distributed uniformly in a finely

© Central University of Technology, Free State

divided state in a dispersion medium (continuous phase) (Jaiswal et al., 2015). The mixture is termed a colloid when they do not settle down (remain suspended) under the influence of gravity (Spruijt & Biesheuvel, 2014).

2.5.8 Casting and Powder Metallurgy Processes, Their Use for Producing Nanocomposites and Their Shortcomings

The concern in producing MMNCs through casting and powder metallurgy processes is poor ductility, toughness, and formability, which arise from a lack of sufficient wetting of the reinforcement by the matrix. Low ductility and formability are caused by the segregation or agglomeration of the reinforcement material, reinforcement-induced voids and fractures, particle de-bonding and cracking via casting and powder metallurgy processes (Kareem, et al., 2024; Casati & Vedani, 2014). Controlling the distribution of reinforcement to obtain a uniform microstructure is difficult using casting routes due to the difference in densities between the reinforcement and matrix (Rozhbiany & Jalal, 2019). Selective lase melting, an LBPF manufacturing process in AM, also has shortcomings experienced in normal casting routes, which include short periods of processing (0.02 m/s) from melting to complete solidification (Manakari et al., 2016). It is, therefore, also prone to the same problem of poor wetting. The effect of the different densities of the reinforcement and matrix applies to this method as well (Larimian et al., 2020). Segregation and agglomeration are also prevalent, particularly in the present case of using CNTs (Gu et al., 2020).

2.6 Additive Manufacturing Technologies

AM technologies make use of 3D computer-aided design (CAD) to manufacture 3D models (Perry et al., 2020). Parts are produced by adding material in the form of solid or liquid layer by layer to give a complete part. The technology uses a precise manufacturing process that requires minimum post-processing (Davoudinejad et al., 2018). The technology is currently used in the manufacturing sector by scientists, medical doctors, market researchers, and artists. Scientists/researchers typically use it to rapidly produce models that they can further study or for theoretical comprehension (Wong & Hernandez, 2012). The aerospace industry uses AM technology, such as LPBF printing systems and fused deposition modelling (FDM). Other applications of AM technologies include those in the automotive, healthcare, and construction industries. Though various AM technologies exist, the processes in each technology are similar (Negi et al., 2013).

© Central University of Technology, Free State

AM technologies can be classified according to the physical state of the raw material, which are powder, liquid, or solid, and according to the mechanisms used for fusing material, be it through ultraviolet (UV) light, thermally, using a laser or electron beam (Joshi & Sheikh, 2015). Figure 2.29 gives a classification of AM technologies.

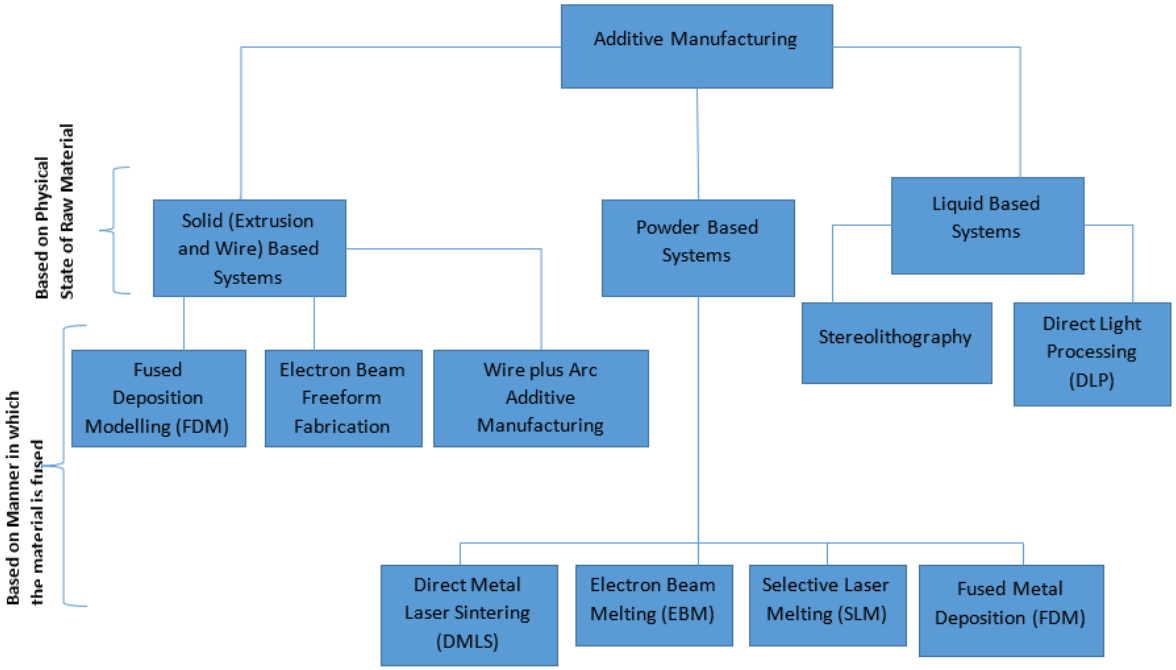

Figure 2.29 Classification of AM technologies (Joshi & Sheikh, 2015)

SLS uses powder as a feed material that is fused or sintered using a carbon dioxide laser beam. This process uses polymer-based materials as the feed materials and differs from SLM, which uses metallic powders as feed materials and a high-power density fibre laser. It can also be used to manufacture composites of reinforced polymers, such as polyamide reinforced with fibreglass (Yehia et al., 2024; Wegner, 2016; Valino et al., 2019). The electron beam melting process (EBM) uses an electron beam to melt the feed material, which is in powder form. The electron beam is powered by a high voltage between 30–60 KV. This process is limited to metals, and because of oxidation, which occurs easily amongst metals, it is carried out in a high-vacuum chamber. It also allows the processing of a large variety of pre-alloyed metals such as steel, copper, and titanium alloys (Sidambe, 2015). Binder jetting (BJT) is an AM technology in which a liquid binder is used to bond powder material (Abdulhameed et al., 2019). This process can handle a wide variety of polymers, including polylactide, poly (lactide-co-glycolide), polycaprolactone, and polylactic acid (Wong & Hernandez,

© Central University of Technology, Free State

2012; Ligon et al., 2017). Lamination object manufacturing (LOM) is an AM process that makes use of paper, metal, or polymers in sheet form as a feed material. It welds together precisely cut sheet material to form a 3D part (Abdulhameed et al., 2019). The sheets are laminated into solid blocks by adhesion-joining, clamping and ultrasonic or laser welding (Pilipovic et al., 2011). Vat polymerisation (VPP) is the process of solidifying liquid materials by exposing them to UV light. It makes use of a digital light processing (DLP)-based video projector that contains a micro-opto-electro-mechanical mirror array and a digital micro-mirror device (DMD) to modulate a collimated UV light source, which is subsequently focused onto an imaging plane placed either at the bottom or top surface of the transparent vat (Davoudinejad et al., 2018). FDM is used for modelling and prototyping. This process manufactures parts or models layer by layer. It uses thermoplastic filaments, which are heated to a semi-liquid state and then extruded onto a build platform according to a sliced CAD model computer-controlled path. The thermoplastics used in this process are production-grade materials (Peko et al., 2017; Dandgaval & Bichkar, 2016). Direct metal laser sintering (DMLS) is an AM technology that uses a high-energy laser beam from CAD designs to fuse powder particles on a powder bed (Singh et al., 2016). The DMLS technology allows the manufacturing of parts using different metallic materials such as cobalt-chrome, nickel-alloy, stainless steel, and titanium (Bineli et al., 2011). SLM uses a high-energy laser beam to fuse and melt metallic powdered materials (aluminium, stainless steel, titanium alloys) to form a 3D part (Valino et al., 2019; Lashgari et al., 2022).

2.6.1 Selective Laser Melting

SLM is a powder bed fusion AM technology that uses a laser energy source (laser beam) to fuse powder particles on a powder bed selectively. This AM technology is governed by various process parameters (Figure 2.30) that determine the outcome of the parts produced. The SLM process can be divided into three distinct stages, as shown in this figure, which include the scanning of the laser to build single tracks, overlapping of single tracks to form a layer, and subsequent overlapping of individual layers to form the bulk material. (Aboulkhair et al., 2019).

© Central University of Technology, Free State

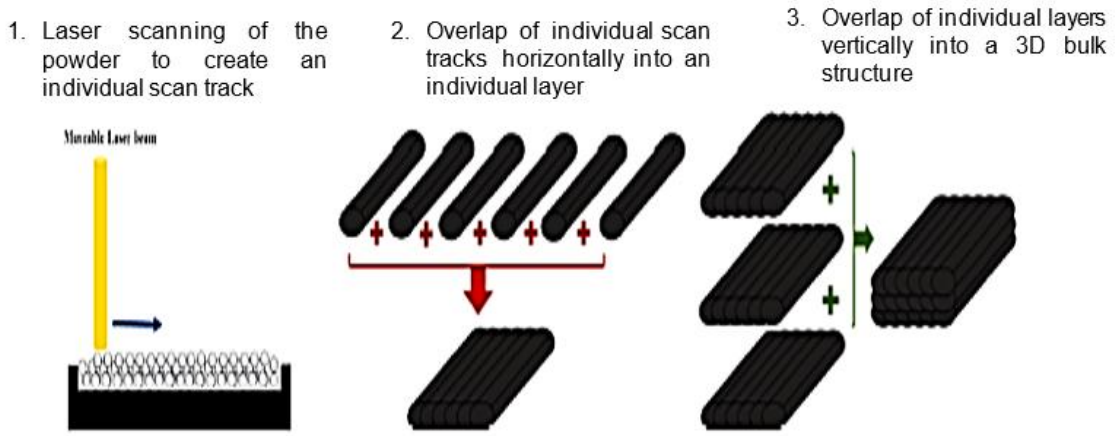

Figure 2.30 Schematic representation of the SLM process (Aboulkhair et al., 2019)

During the SLM process, the irradiated powder melts to generate a dynamic melt pool. The stability of the melt pool is governed by the set of process parameters used during processing. The laser power and scanning speed determine the width and depth of the melt pool, while the track length is determined by the setting for the start and end of the movement of the laser beam in one direction. When laser irradiation takes place, various phenomena occur, including absorption and scattering of the laser beam, heat transfer, phase transformation, chemical reactions, fluid dynamics, evaporation, and reflection. Upon the laser beam impinging on powder, the material's reflectivity and conductivity determine the amount of energy to be reflected and transmitted for melting of the powder particles. Subsequent solidification of the melt is based on its ability to conduct the latent heat away from the solid/liquid interface. The SLM process differs from traditional methods of manufacturing due to its rapid cooling/solidification process that occurs at a rate of 10^4–10^7 K/s (Yadroitsev et al., 2013; Ruban et al., 2014; Gokuldoss, Kolla & Eckert, 2017).

The process parameters in SLM include laser power, hatch distance, scan pattern, laser beam diameter, scan angle, beam spatial distribution, wavelength, particle size distribution, layer thickness, shape of powder particles, flowability of powder, the thickness of the deposited layer, and the type of protective gas atmosphere used. Aboulkhair et al. (2019) grouped 15 important process parameters in SLM into scan-related, powder-related and temperature-related categories, as shown in Figure 2.31. Gajera et al. (2019) identified laser power, scanning speed, layer thickness and hatch spacing as the most important process parameters in the DMLS manufacturing

© Central University of Technology, Free State

process in terms of their effect on the mechanical and physical properties of built parts. Spears and Gold (2016) identified 50 key process parameters in SLM, clustered in the four categories of laser scanning parameters, material properties of the powder, powder bed and re-coater parameters and built environment parameters, details of which are contained in Table 2.11

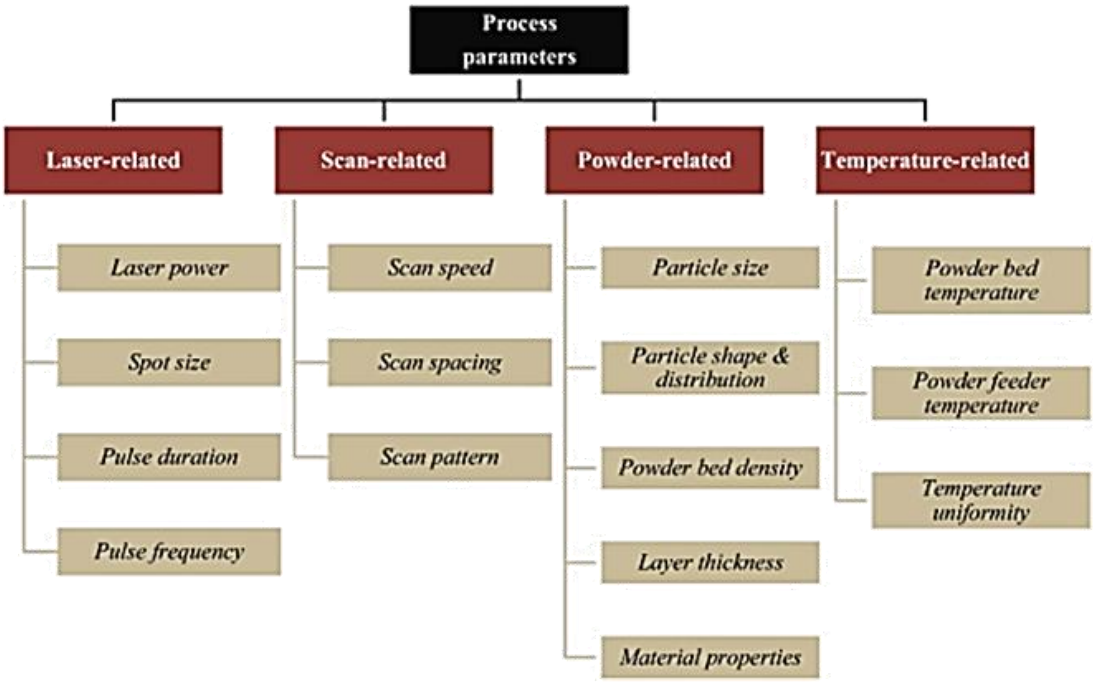

Figure 2.31 Process parameters in selective laser melting (Aboulkhair et al., 2019)

Table 2.11 Key Process Parameters in SLM (Spears & Gold, 2016)

	Parameter	Description	Controlled or predefined
No.	**Laser Scanning Process Parameters**		
1	Average power (P_L)	Measure of total energy output of a laser	Controlled
2	Mode	Pulsed or continuous wave	Predefined
3	Peak power (P_{peak})	Maximum power inside a pulse	Predefined
4	Pulse width (PW)	Laser pulse length operating in pulse mode	Predefined
5	Frequency (f)	Pulses/unit time	Predefined
6	Wavelength (λ)	Distance between crests	Predefined
7	Polarisation	Orientation of waves	Predefined
8	Beam quality (M^2)	Linked to the intensity profile, used to determine the focus of the beam. Used to predict theoretical spot size	Predefined
9	Intensity profile I (x,y,t)	Determines energy added at a particular spot	Predefined
10	Spot size (d_x and d_y)	Width and length of elliptical spot	Controlled
11	Scan velocity (v)	Speed at which the laser beam moves over the powder bed	Controlled
12	Scan spacing (S_s)	Distance between parallel passes of the laser beam	Controlled
13	Scan strategy	Pattern used by the laser beam when scanning over the surface of the powder	Controlled

© Central University of Technology, Free State

	Material Properties of the Powder		
14	Bulk density (ρ_b)	Powder density	Predefined
15	Thermal conductivity (k_b)	The ability of a material to conduct heat	Predefined
16	Heat capacity (cp,b)	Measures energy needed to raise the temperature of a material	Predefined
17	Latent heat of fusion (Lf)	The energy required to move from solid to liquid and liquid to solid	Predefined
18	Melting temperature (T_m)	The temperature at which a solid melts	Predefined
19	Boiling temperature (T_b)	The temperature at which material vaporises	Predefined
20	Melt pool viscosity (μ)	The measure of resistance of the melt to flow	Predefined
21	Coefficient of thermal expansion (α)	A measure of volume change of a material upon heating or cooling	Predefined
22	Surface free energy (γ_{sl})	Required free energy to form a new unit area of solid-liquid interface area	Predefined
23	Vapour pressure (p_v)	Measures the likelihood of a material to vaporise	Predefined
24	Heat (enthalpy) of reaction (H_r)	The energy linked to the chemical reaction of material (for example, the formation of an oxide)	Predefined
25	Material absorptivity ($A_{b,m}$)	Measures the unit laser energy absorbed by a material	Predefined
26	Diffusivity (D)	Only important for solid-state sintering but not for melting	Predefined
27	Solubility (S)	Solubility of a material in a liquid	Predefined
28	Particle morphology (A_R, f_{circ}, f_{elong},)	Measures of shape of individual particles and distribution (aspect ratio, circularity, and elongation)	Predefined
29	Surface roughness (R_A)	Mean arithmetic of the surface profile	Predefined
30	Particle size distribution	Distribution of particle sizes (typically diameter) in a sample of powder	Predefined
31	Pollution	An ill-defined factor which describes the change in the properties of the powder. This can be due to dust found on the powder	Predefined
	Properties of the Powder Bed and Recoat Parameters		
32	Density (ρ_p)	A measure of the packing density of particles of powder	Predefined
33	Thermal conductivity (k_p)	A measure of the ability of the powder bed to conduct heat	Predefined
34	Heat capacity ($c_{p,p}$)	A measure of the energy needed to raise the powder bed temperature	Predefined
35	Absorptivity (A_p)	A measure of the laser energy absorbed and is dependent on the area of the powder bed and the type of powder	Predefined
36	Emissivity (ϵ)	The ratio of radiated energy to that of a black body	Predefined
37	Deposition system parameters	Velocity of recoater, type of recoater, pressure, dosing	Controlled
38	Layer thickness (L)	The height of a single layer of powder	Controlled
39	Powder bed temperature (T_p)	The bulk temperature of a powder bed	Controlled
	Build Environment Process Parameters		
40	Shield Gas	Typically, argon gas is used. Other gasses that are used include helium and nitrogen	Predefined
41	Oxygen level (%O_2)	The presence of oxygen can lead to the formation of oxides of the metal with the consequence of oxide formation in metal, change in wettability, or energy required for melting	Controlled

© Central University of Technology, Free State

42	Shield gas molecular weight (MW_g)	Influences the heat balance and diffusivity into and out of the part	Predefined
43	Shield gas viscosity (μ_g)	Could possibly influence the free activity of the melt pool	Predefined
44	Thermal conductivity ($k_{c,g}$)	The measure of the powder bed's ability to conduct heat	Predefined
45	Heat capacity of gas ($C_{p,g}$)	Measure of energy required to raise the temperature of the powder bed	Predefined
46	Pressure (p) (gas chamber)	Affects the vaporisation of metal and oxygen content	Controlled
47	Gas flow velocity (v_g)	Affects convective cooling and removal of condensate	Controlled
48	Convective heat transfer coefficient (h_c)	This determines convective cooling of the melted part by gas flowing over its surface	Predefined
49	Ambient temperature ($T\infty$)	It is able to impact powder preheat and residual stresses and appears in the equation for heat balance	Controlled
50	Surface free energy ($\gamma_{g/}$)	Present between liquid and surrounding gas. Is able to influence the shape of the melt pool	Predefined

The SLM process parameters of laser power, scanning speed, spot size, and hatch spacing are critical in obtaining better surface finish, hardness, and dimensional accuracy (Ruban et al., 2014). Laser power and scanning speed have the most significant influence on the physical and mechanical properties of printed parts (Hanzi et al., 2015).

The laser energy beam supplies power to the powder, and its density is defined by the laser power, layer thickness, hatch spacing, and scanning speed. The correct laser density is important in ensuring sufficient melting of the particles of powder. (Ganeriwala, 2015). The scanning speed describes how fast or how slow the laser beam moves over the powder bed and can be adjusted to yield the desired melting. SLM machines typically use a Gaussian laser where the power decreases exponentially away from the centre of the laser. The laser spot size (Figure 2.32b) of the beam is defined as the radial distance (radius) from the centre point of the maximum irradiance to the $1/e^2$. The hatch spacing or distance (Figure 2.32a) is defined as the distance between the centre lines of two adjacent laser passes or tracks that are parallel to each other. The process parameters, which include hatch distance/spacing, laser spot size, layer thickness, hatch overlap and scan strategy are shown in Figure 2.32a.

© Central University of Technology, Free State

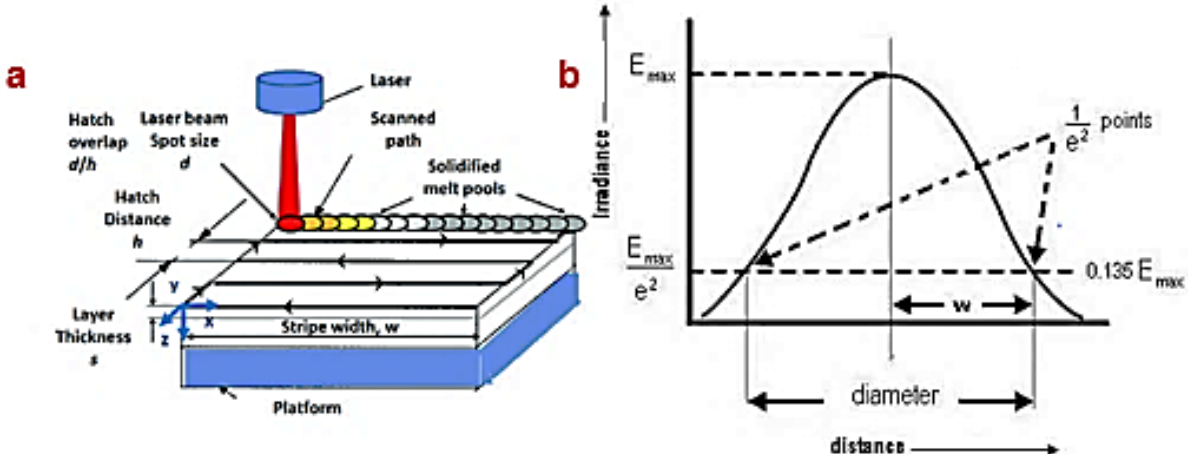

Figure 2.32 Depiction of (a) hatch distance and (b) laser spot (Criales et al., 2017)

2.6.1 Single Tracks

Process parameters influence the continuity or discontinuity of single tracks. Yadroitsev et al. (2015) reported that the formation of stable continuous single tracks is determined by process parameters, which, in order of importance, include laser power density, powder layer thickness, scanning speed, and powder particle size. Considering that SLM is a track-by-track and layer-by-layer process, the quality of a part produced using this method is influenced by the quality of every single laser-melted track and every single layer. The experiments carried out by Guo et al. (2018) showed that stable continuous tracks were possible at higher laser power and low scanning speeds, as shown in Figure 2.32, for the powder composition, as different compositions require their own set of process parameters. In SLM, stable continuous tracks are desired as they generate good stable bonds between adjacent tracks and, subsequently, a fully dense 3D part (Balbaa et al., 2020). However, the ripple effect that arises from the creation of shear stress gradients in a melt (Balhara et al., 2021) is unavoidable during SLM. Ripples have a great influence on the structure of the surface and reflectivity of products. Ripple marks between layers could evolve into cracks that can lead to failure of structures during fatigue loading (Wang et al., 2018). Thus, post-surface treatment is needed to remove or minimise them. A schematic of the rippling effect is shown in Figure 2.33.

© Central University of Technology, Free State

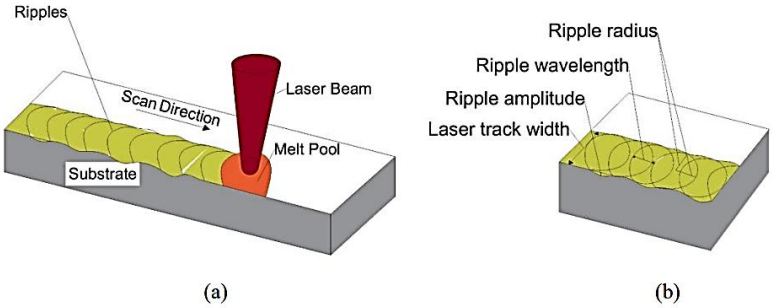

Figure 2.33 (a) Schematic of ripple formation (b) terms applied to ripple formation (Balhara et al., 2021)

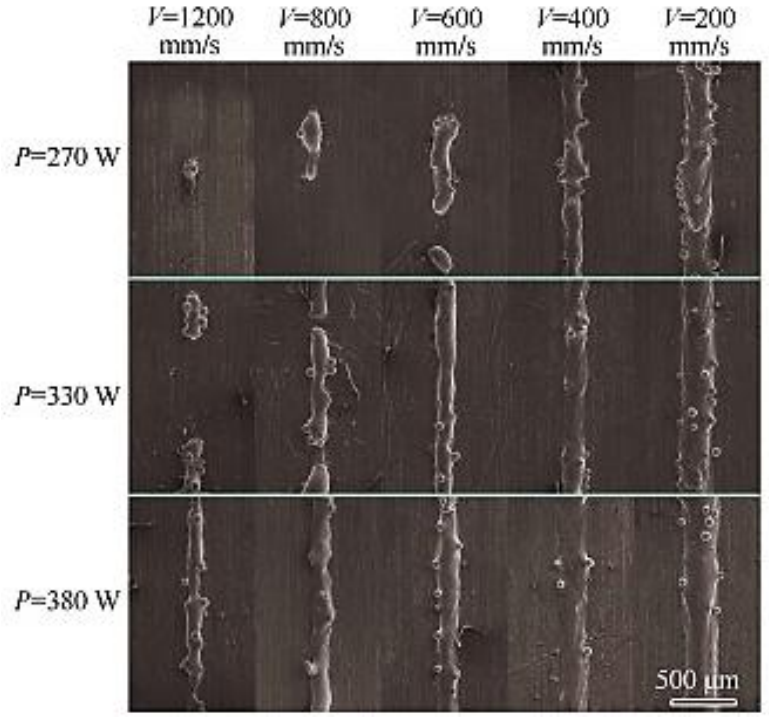

Figure 2.34 SEM micrograph showing single tracks for niobium pre-alloyed powder at different laser power and scanning speeds (Guo et al., 2018)

Further observation of Figure 2.34 shows satellites at the edge and on the surface of the single tracks, a magnified view of which is shown in Figure 2.35. These satellites are formed due to the incomplete melting of the powder particles in the circumferential zone of the laser spot. Satellites can also form from small droplets of material that are expelled from the melt pool (oxidising in-flight), which then land on the powder bed. These small droplets can land on the part being fabricated, which can get trapped if not completely melted during remelting of subsequent layers (Zenani et al., 2020). Satellites can lead to surface irregularities in the final built part. Another surface

© Central University of Technology, Free State

irregularity is known as “balling”, which can be classified into two types, namely ellipsoidal and spherical balls. Ellipsoidal balls, which result from insufficient laser energy input, have a size of $\sim 500 \mu m$ and are known to cause significant damage to SLM parts. Spherical balls result from splashing of the molten pool due to high scanning speeds and have a size of $\sim 10 \mu m$, causing less damage to SLM parts (Oyar, 2020). Balling leads to high surface roughness (Figure 2.35) and can hinder the success of the build. Unrestricted balling can prevent the uniform deposition of layers, resulting in the likelihood of failure in the produced part (Aboulkhair et al., 2019).

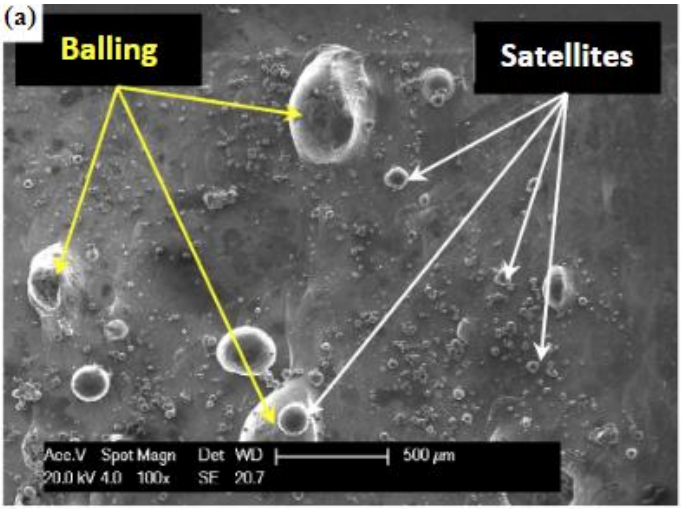

Figure 2.35 Balling and satellites on the surface of an SLM aluminium alloy (Aboulkhair et al., 2019)

Balling is a periodic undulation of single tracks and has previously been reported in LBPF processes. The Raleigh-Plateau instability of a liquid jet is used to explain this periodic undulation (Zhang et al., 2022). The Raleigh-Plateau instability describes an infinite falling stream of fluid breaking into smaller droplets with the same volume but less surface area. This is a surface-driven instability and occurs when the length of a cylindrical jet is greater than the circumference, causing it to be unstable (Ding et al., 2015). A Raleigh-Plateau instability takes place during the solidification process of a track, which can cause the balling phenomenon and high surface roughness in the final part (Viale et al., 2022). The Raleigh-Plateau instability is further explained by Figure 2.36, showing the influence of the Plateau-Rayleigh instability on a single track: (a) in the xy plane; (b) instability of a single-track melt; (c) depth of the melt pool

© Central University of Technology, Free State

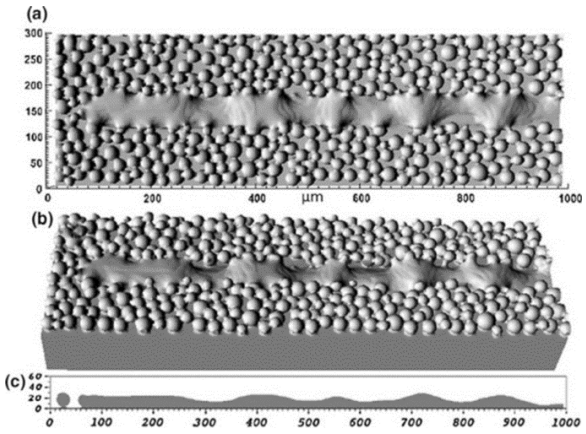

Figure 2.36 The influence of the Plateau-Rayleigh instability on a single track (Viale et al., 2022).

Controlling the intensity of a laser beam is critical to avoiding the "keyhole" effect shown in Figure 2.37. The keyhole effect is caused by intense heat from a laser beam, which causes deep penetration through the layers of powder. As a result, the powder melt evaporates, and the vapour (gas bubble) is entrapped in the wake of the laser beam because there is not sufficient time for the gas bubbles to escape due to the rapid solidification process inherent in the process (Yadroitsava et al., 2015). In Figure 2.37 that the keyhole effect is most prominent at the higher laser power of 380 W and a scan speed of 200 mm.s^{-1}, as opposed to the laser power of 330 W and a scan speed of 200 mm.s^{-1}, as the intensity of the laser beam in the former case is able to penetrate deeper into the layer.

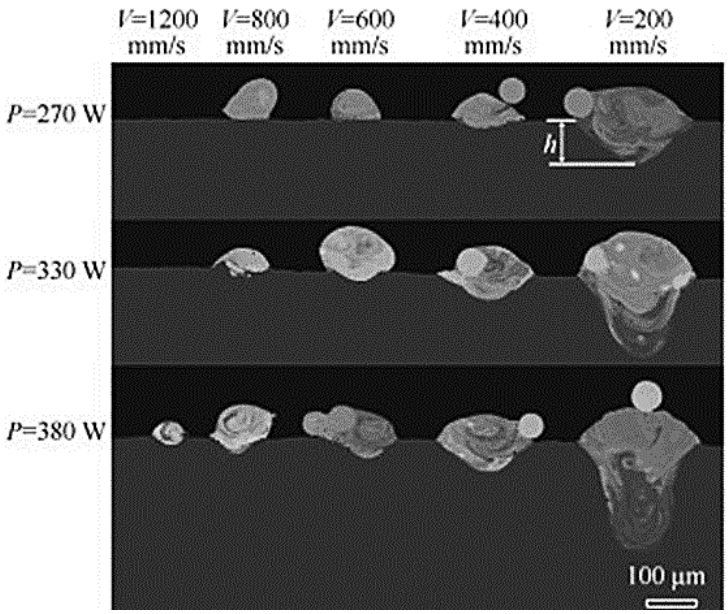

Figure 2.37 The keyhole effect (Yadroitsava et al., 2015)

© Central University of Technology, Free State

Single tracks are characterised by the geometrical features shown in Figure 2.38. The image shows a cross-section through a single track to highlight these features, which include track height (*H*), track width (*W*), depth of penetration (*Hf*), track area (*S*), and area of penetration (*Sf*). The formation of a single track is not only due to the powder placed directly underneath the laser spot but adjacent powders are also involved in the process due to scattering of radiation, conduction through the substrate and capillary phenomenon. The heat-affected zone (HAZ) in Figure 2.39 can have a width twice as large as the single track after scanning, which is caused by the increase in temperature from the laser energy, causing a high-temperature gradient of the surface of the substrate (Yadroitsev et al., 2015; Alkahari et al., 2014).

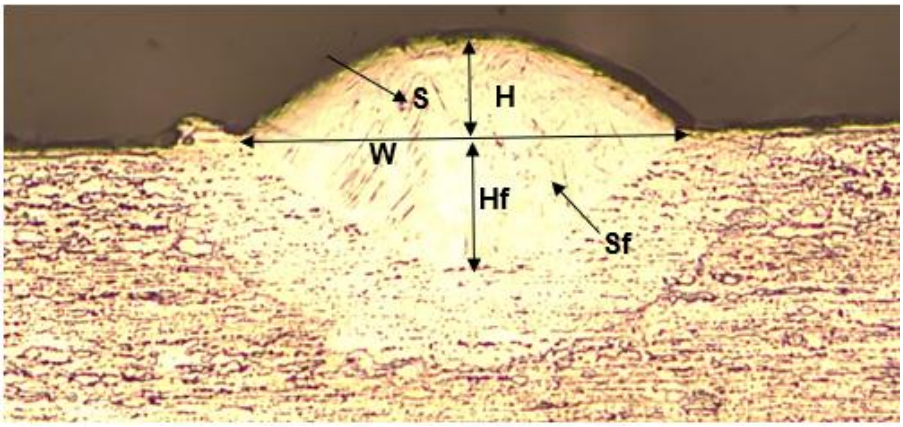

Figure 2.38 Geometric features of single tracks (Wang et al., 2018)

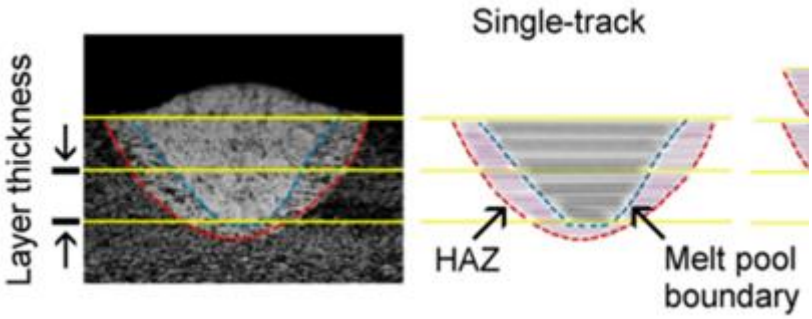

Figure 2.39 Single-track formation with HAZ indicated (Dilip et al., 2017)

The depth-to-width ratio allows for the categorisation of the melt pool as either in conduction mode, keyhole mode, or lack of fusion. The conduction mode is widely accepted as the desired feature in the formation of tracks. When the depth-to-width ratio is >1, then the melt pool is considered to be in the keyhole mode, as shown in

© Central University of Technology, Free State

Figure 2.40(a). The melt pool is in conduction mode (Figure 2.40(b)) when the depth-to-width ratio is 0.5, ensuring sufficient melting of previous layers and wide enough tracks to ensure the fabrication of fully dense parts. Insufficient bonding of layers (Figure 2.40(c)) leads to the formation of unfused pores; in this case, the depth-to-width ratio is <0.5 (Guo et al., 2023).

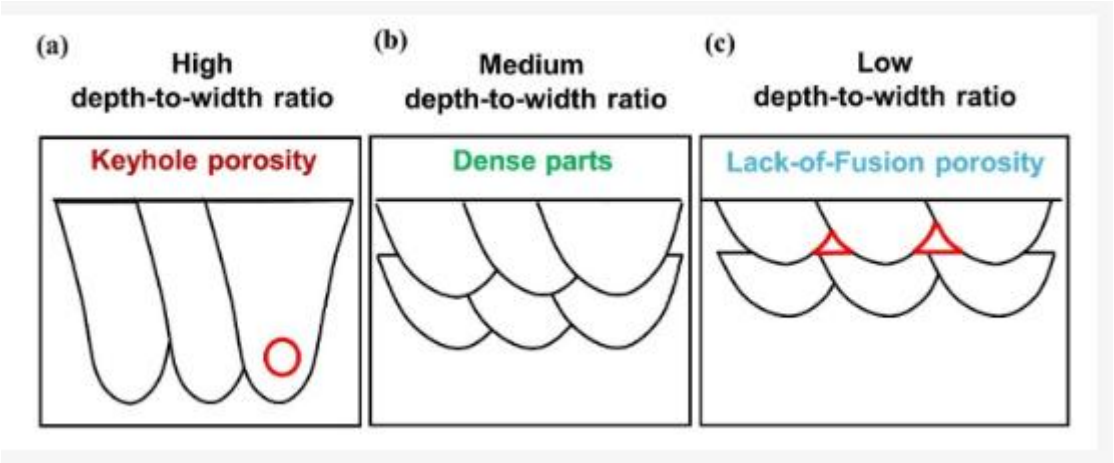

Figure 2.40 Illustration of melt pool formation in (a) keyhole mode, (b) conduction mode, and (c) lack-of-fusion mode (Guo et al. 2023)

Process parameters influence the formation of the melt pool, which subsequently influences the geometry, microstructure, and mechanical properties of the final part (Mohamad et al., 2021). A good surface finish has been attributed to powder layers with an adequate powder layer having the ability to be successfully melted by the laser beam. The laser power has been found to have more influence on SLM-processed parts than the laser scanning speed. Low scanning powers prevent the fast melting of powder material, while high scanning speeds lead to keyhole formation (Bakhtiarian et al., 2024). The right combination of laser scanning power and scanning speeds produces sufficient laser energy density to produce fully dense parts. Dilip et al. (2017) studied the influence of laser energy density on single tracks produced from Ti6Al4V pre-alloyed powder. The influence of laser energy density on track build at low laser energy densities produced irregular pores in the cross-sections, whilst high laser energy densities produced geometrical features with keyholes and circular pores (Dilip et al., 2017). Parameters, including the presence of gases such as oxygen and sulphur, also play a role in SLM-produced parts.

© Central University of Technology, Free State

Mohamad (2021) reviewed work by several authors on the influence that oxygen and sulphur have on melt pool geometry, more so on the melt pool depth. In one case in this work, a low sulphur sample was observed to lead to the production of a melt pool with a shallow depth and large width, whereas when the content of sulphur was increased, it led to the production of a melt pool with the opposite effects (Mohammad, 2021). Le and Lo (2019) studied the effect of sulphur content and Marangoni convection on the melt pool formation of SLM-produced CL20ES stainless steel. It was found that with high sulphur content an inward Marangoni takes place, leading to a deeper melt pool with lower porosity in the built part. The high sulphur content leads to a positive surface temperature gradient, which causes an inward Marangoni flow and a large increase in the melt pool depth (Le & Lo, 2019).

When producing single tracks in SLM, the Marangoni flow is dominant due to the intense heating at the melt surface. The Marangoni flow has a significant role in heat and mass transport for high-temperature processes (Dzogbewu, 2020). The Marangoni effect cannot be explained without surface tension at the melt surface. In the case of molten steel, the direction of flow of the melt is controlled by the gradient of the temperature-dependent coefficient of surface tension, which is affected by the contaminants, oxygen and sulphur. Figure 2.41(a) explains the Marangoni effect on the melt surface where the temperature gradient is parallel to the melt surface. In this case, the temperature changes uniformly at the melt surface. However, the surface temperature is lower than the temperature inside the melt. Figure 2.41(b) explains the Marangoni effect on the melt surface where the temperature gradient is normal to the surface; due to shear stress at the melt surface, the large surface tension pulls the smaller surface tension.

© Central University of Technology, Free State

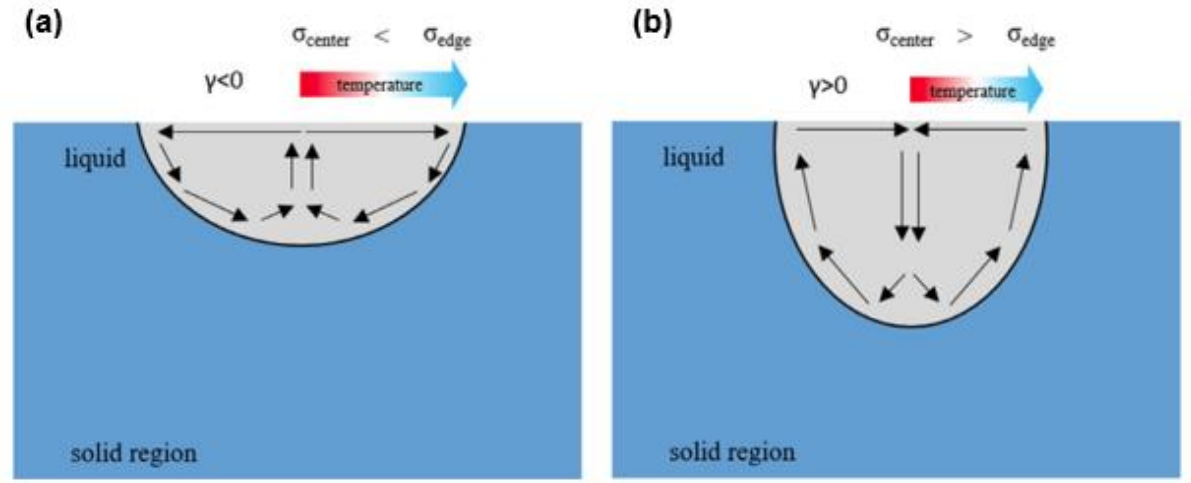

Figure 2.41 The Marangoni effect (a) temperature gradient normal to the surface of the melt, (b) temperature gradient parallel to the surface of the melt (Mohamad et al., 2021)

The shape and size of the tracks, as well as the aspect ratio of the molten pool, are dependent on the flow of liquid metal, which is driven predominantly by the spatial variation of interfacial tension known as the Marangoni effect. The Marangoni number (Ma) describes the magnitude of surface tension force relative to viscous force in the melt pool. The Ma is used to quantify the effects of the Marangoni stress on the velocity of the molten metal and measures the strength of the convective transport of heat. The Ma increases with increasing heat input. Higher values of Ma indicate higher velocities of the melt pool and result in a distinct increase in convective heat transfer, which produces a large melt pool (Mukherjee et al., 2017).

2.6.2 Additive Manufacturing and its Challenges in Manufacturing Nanocomposites

Nanocomposites offer the possibility of producing materials with enhanced mechanical properties. However, they exhibit poor interfacial adhesion and agglomeration. The agglomeration of nanoparticles reduces their dispersion and, therefore, their reinforcing effect, which may result in an inability to obtain the desired mechanical properties (Zare, 2016). Dorigato et al. (2017) studied the reinforcement of acrylonitrile-butadiene-styrene (ABS) polymer at concentrations of 1 wt.% to 8 wt.% CNTs, using FDM. The results showed that even with the smallest (1 wt.%) of CNTs, the electrical resistivity was significantly decreased. The FDM process led to partial losses of electrical conductivity, more especially in the horizontal and vertical build

© Central University of Technology, Free State

directions. The thermal properties of ABS were influenced by the addition of CNTs, with significant improvements observed at 6 wt.%. of CNTs. The thermal diffusivity increased by 55 %, and electrical conductivity increased by 30 %; however, it was gathered that the specific heat decreased by 11 % at this 6 wt.% of CNTs. The printing process largely affected the thermal conductivity of the nanocomposite with a loss of 21 %. (Dorigato et al., 2017). In separate works, Dul et al. (2018) used a twin-screw extruder to produce CNT/ABS filament nanocomposites for concentrations of 1–8 wt.%. CNTs were subsequently used to print FDM parts for testing. They found that the optimum reinforcement concentration was 6 wt.%. CNTs. The presence of CNTs in ABS promoted thermal stability in printed parts owing to the reduction in the CTE. There was a slight increase in electrical conductivity in 3D-printed parts, with a loss in conductivity due to the presence of CNTs. The resistivity of 3D-printed parts is largely dependent on build direction of reinforcements which leads to different surface temperature increases under applied voltages. Mechanical properties, including the tensile strength and elastic modulus of the printed nanocomposites, were also enhanced by the addition of CNTs in ABS (Dorigato et al., 2017). Polyamide-12 nanocomposites were produced using CNTs as reinforcement in the SLS process, and an increase in Young's modulus was reported. However, the cryogenic fracturing method used in the study proved difficult to produce powder with suitable morphology. If improved powder production can be achieved, the use of CNTs as reinforcements for SLS has a promising effect on the improvement of mechanical properties (Goodride et al., 2011). Aluminium alloy (AlSi10Mg) was reinforced with 0.5 wt.% CNTs and fully dense structures were produced using SLM. The results showed improved mechanical properties of microhardness, tensile strength and percentage elongation. The printed samples had ultrafine microstructures. The authors also determined that incorporating CNTs made it difficult to optimise SLM process parameters for the AlSi10Mg/CNTs nanocomposites (Gu et al., 2019). The incorporation of CNTs into metal matrices is a challenge due to their non-uniform dispersion caused by their high aspect ratios, large specific surface areas that support agglomeration, and weak interfacial reinforcement between the metal and CNTs. Moreover, inhomogeneous dispersion of CNTs may lead to non-homogeneity of the resulting composite and may affect the full melting of the aluminium alloy and lead to reduced wetting of CNTs (Azarniya et al., 2017).

© Central University of Technology, Free State

References

1. Abd-Elaziem, W., Khedr, M., Elsheikh, A. H., Liu, J., Zeng, Y., Sebae, T. A., Abd El-Baky, M. A., Darwish, M. A., Daoush, W. M. and Li, X., 2023. Influence of nanoparticles addition on the fatigue failure behavior of metal matrix composites: Comprehensive review. Engineering Failure Analysis, pp. 107751.

2. Abdulhameed, O., Al-Ahmari, A., Ameen, W. and Mian, S. H., 2019. Additive manufacturing: Challenges, trends, and applications. Advances in Mechanical Engineering, 11(2), pp. 1-7.

3. Aboulkhair, N. T., Simonelli, M., Parry, L., Ashcroft, I., Tuck, C. and Hague, R., 2019. 3D printing of Aluminium alloys: Additive Manufacturing of Aluminium alloys using selective laser melting. Progress in Materials Science. 106(July), pp. 100578. doi.org/10.1016/j.pmatsci.2019.100578

4. Adamos, L. and Loutas, T., 2021. Challenges in the fatigue crack growth characterization of metal/composite joints: A compliance-based investigation of a Ti/CFRP joint. International Journal of Fatigue, 148, pp. 106233. https://doi.org/10.1016/j.ijfatigue.2021.106233 (https://www.sciencedirect.com/science/article/pii/S0142112321000931).

5. Adegbola, T. A., Olorundaisi, E., Agboola, O. and Fayomi, O. S. I., 2020. WITHDRAWN: Influence of fillers particles on material toughness properties during processing. Materials Today: Proceedings. https://doi.org/10.1016/j.matpr.2020.01.464.

6. Agarwal, K.M., Singhal, A., Kapoor, A. and Bhatia, D., 2021. Simulated analysis of Ti-6Al-4V processed through equal channel angular pressing for biomedical applications. Materials Science for Energy Technologies, 4, pp. 290-295.

7. Ahmad, H., Markina, A. A., Porotnikov, M. V. and Ahmad, F., 2020, November. A review of carbon fibre materials in automotive industry. In IOP Conference Series: Materials Science and Engineering, 971(3), p. 032011. IOP Publishing.

© Central University of Technology, Free State

8. Alkahari, M. R., Furumoto, T., Ueda, T. and Hosokawa, A., 2014. Melt pool and single track formation in selective laser sintering/selective laser melting. In Advanced Materials Research, 933. Trans Tech Publications Ltd. pp. 196–201. doi.org/10.4028/www.scientific.net/AMR.933.196

9. Alkasasbeh, H., Swalmeh, M., Bani Saeed, H., Al Faqih, F. and Talafha, A., 2020. Investigation on CNTs-water and human blood based Casson nanofluid flow over a stretching sheet under impact of magnetic field. Frontiers in Heat and Mass Transfer (FHMT), 14, pp. 1-7.

10. AL-Nafeay, R. H., AL-Roubaiy, A. O. and Omidvar, H., 2021. Overview of joining and repairing techniques of ni-based superalloy for industrial gas turbine applications. In IOP Conference Series: Materials Science and Engineering,1094(1), p. 012141. IOP Publishing.

11. Amin, M. N., Ahmad, W., Khan, K. and Ahmad, A., 2022. A comprehensive review of types, properties, treatment methods and application of plant fibres in construction and building materials. Materials, 15(12), pp. 4362.

12. Anwer, A. H., Ahtesham, A., Shoeb, M., Mashkoor, F., Ansari, M. Z., Zhu, S. and Jeong, C., 2023. State-of-the-art advances in nanocomposite and bio-nanocomposite polymeric materials: A comprehensive review. Advances in Colloid and Interface Science, pp. 102955.

13. Ashby, M. F., 2012. Materials and the environment: eco-informed material choice. Elsevier.

14. Ashraf, M. A., Peng, W., Zare, Y. and Rhee, K. Y., 2018. Effects of size and aggregation/agglomeration of nanoparticles on the interfacial/interphase properties and tensile strength of polymer nanocomposites. Nanoscale Research Letters, 13(1), pp. 1–7. https://doi.org/10.1186/s11671-018-2624-0

15. ATI, T. D., (2012). Technical Data Sheet ATI Ti-6Al-*4V, Grade 5*. *1*, pp. 4–7. www.ATImetals.com

16. Azarniya, A., Safavi, M. S., Sovizi, S., Azarniya, A., Chen, B., Madaah Hosseini, H. R. and Ramakrishna, S., 2017. Metallurgical challenges in carbon nanotube-reinforced metal matrix nanocomposites. Metals, *7*(10), pp. 384.

© Central University of Technology, Free State

17. Badanayak, P. and Vastrad, J.V., 2021. Sol-gel process for synthesis of nanoparticles and applications thereof. Pharma Innov. J, pp.1023-1027.

18. Bakhtiarian, M., Omidvar, H., Mashhuriazar, A., Sajuri, Z. and Gur, C.H., 2024. The effects of SLM process parameters on the relative density and hardness of austenitic stainless steel 316L. Journal of Materials Research and Technology, 29, pp. 1616–1629.

19. Balbaa, M, Mekhiel, S, Elbestawi, M and McIsaac, J., 2020. On selective laser melting of Inconel 718: Densification, surface roughness, and residual stresses. Materials & Design, 193, pp. 108818. doi.org/10.1016/J.MATDES.2020.108818

20. Balla, V. K., Kate, K. H., Satyavolu, J., Singh, P. and Tadimeti, J. G. D., 2019. Additive manufacturing of natural fibre reinforced polymer composites: Processing and prospects. Composites Part B: Engineering, 174, pp.106956.

21. Baptista, A., Silva, F. J. G., Porteiro, J., Míguez, J. L., Pinto, G. and Fernandes, L., 2018. On the physical vapour deposition (PVD): evolution of magnetron sputtering processes for industrial applications. Procedia Manufacturing, 17, pp. 746–757.

22. Bhattacharyya, D., Subasinghe, A. and Kim, N. K., 2015. Natural fibres: Their composites and flammability characterizations. Multifunctionality of Polymer Composites, 1(1), pp. 102–143.

23. Bilisik, K., Kaya, G., Ozdemir, H., Korkmaz, M. and Erdogan, G., 2018. Applications of glass fibres in 3D preform composites. Advances in Glass Science and Technology, 207.

24. Bineli, A. R. R., Peres, A. P. G., Jardini, A. L. and Maciel Filho, R., 2011, April. Direct metal laser sintering (DMLS): Technology for design and construction of microreactors. In 6 Congress Obrasileiro De Engenharia De Fabrica ÇÃO.

25. Bokov, D., Turki Jalil, A., Chupradit, S., Suksatan, W., Javed Ansari, M., Shewael, I. H., Valiev, G. H. and Kianfar, E., 2021. Nanomaterial by sol-gel method: synthesis and application. Advances in Materials Science and *Engineering*, *2021*, pp. 1–21.

© Central University of Technology, Free State

26. Boyer, R. R., Cotton, J. D., Mohaghegh, M., and Schafrik, R. E., 2015. Materials considerations for aerospace applications. *MRS Bulletin*, *40*(12), pp. 1055–1066. https://doi.org/10.1557/mrs.2015.278

27. Budhe, S., Banea, M. D., and de Barros, S., 2018. Bonded repair of composite structures in aerospace application: a review on environmental issues. In *Applied Adhesion Science 6*(1), pp. 1–27. Springer International Publishing. https://doi.org/10.1186/s40563-018-0104-5

28. Cabeza, M., Feijoo, I., Merino, P., Pena, G., Pérez, M. C., Cruz, S. and Rey, P., 2017. Effect of high energy ball milling on the morphology, microstructure and properties of nano-sized TiC particle-reinforced 6005A aluminium alloy matrix composite. *Powder Technology*, *321*, pp. 31–43.

29. Camargo, E. A., Candido De Sousa, V., Sartorato, M., Oliveira, É., Camargo, E. A., Ambrosio, D. R., Candido De Sousa, V., Fernando Castillo, D., Sartorato, M., Costa, N. and Luiz Oliveira, E., 2024. Effect of rotational speed on the modal parameters of a helicopter blade based on Operational Modal Analysis approach. https://www.researchgate.net/publication/384243719

30. Callister Jr, W.D. and Rethwisch, D.G., 2020. *Materials science and engineering: an introduction*. John wiley & sons.

31. Casati, R. and Vedani, M., 2014. Metal matrix composites reinforced by nano-particles—a review. *Metals*, *4*(1), pp. 65-83. https://doi.org/10.3390/met4010065

32. Chong, Y., Bhattacharjee, T., Tian, Y., Shibata, A. and Tsuji, N., 2021. Deformation mechanism of bimodal microstructure in Ti-6Al-4V alloy: The effects of intercritical annealing temperature and constituent hardness. Journal of Materials Science & Technology, 71, pp.138-151.

33. Chaturvedi, A. and Deshmukh, P., 2022. A review on nanocomposites. *International Journal of Creative Research Thoughts (IJCRT)*, *10*(3), pp. 149–155.

© Central University of Technology, Free State

34. Chen, Y., Xu, S., Tebaldi, G. and Romeo, E., 2022. Role of mineral filler in asphalt mixture. Road Materials and Pavement Design, 23(2), pp. 247–286.

35. Cotton, J. D., Clark, L. P. and Phelps, H. R., 2002. Titanium alloys on the F-22 fighter airframe. Advanced Materials & Processes, 160(5), pp. 25.

36. Criales, L. E., Arısoy, Y. M., Lane, B., Moylan, S., Donmez, A. and Özel, T., 2017. Predictive modeling and optimization of multi-track processing for laser powder bed fusion of nickel alloy 625. Additive Manufacturing, 13, pp. 14–36.

37. Dandgaval, O. and Bichkar, P., 2016. Rapid prototyping technology-study of fused deposition modeling technique. International Journal of Mechanical and Production Engineering, 4(4), pp. 44–47.

38. Davis, J. R., 2001. Light Metals and Alloys-Aluminum and Aluminum Alloys. Alloying: Understanding the Basics, pp. 351–416. https://doi.org/10.1361/autb2001p351

39. Davoudinejad, A., Diaz-Perez, L. C., Quagliotti, D., Pedersen, D. B., Albajez-García, J. A., Yagüe-Fabra, J. A. and Tosello, G., 2018. Additive manufacturing with vat polymerization method for precision polymer micro components production. Procedia CIRP, 75, pp. 98–102.

40. Davoudinejad, A., Perez, L., Quagliotti, D., Pedersen, D., Albajez, J., Yagüe-Fabra, J. and Tosello, G., 2019. Geometrical and feature of size design effect on direct stereolithography micro additively manufactured components. European Structural Integrity Society, 13, pp. 1250–1255. doi.org/10.1016/j.prostr.2018.12.256

41. DeArmitt, C. and Hancock, M., 2003. Particulate-Filled Polymer Composites. https://www.researchgate.net/publication/236133079

42. Debnath, S., Ranade, R., Wunder, S. L., McCool, J., Boberick, K. and Baran, G., 2004. Interface effects on mechanical properties of particle-reinforced composites. *Dental Materials*, *20*(7), pp. 677–686.

43. Deshpande, P. K., Li, J. H. and Lin, R. Y., 2006. Infrared processed Cu composites reinforced with WC particles. Materials Science and Engineering: A, 429(1–2), pp. 58–65.

© Central University of Technology, Free State

44. De Vaucorbeil, A., Nguyen, V. P., Sinaie, S. and Wu, J. Y., 2020. Material point method after 25 years: theory, implementation, and applications. *Advances in Applied Mechanics*, *53*, pp. 185–398.

45. Dhotel, A., Chen, Z., Delbreilh, L., Youssef, B., Saiter, J. M. and Tan, L., 2013. Molecular motions in functional self-assembled nanostructures. *International Journal of Molecular Sciences*, *14*(2), pp. 2303–2333.

46. Diaham S (2021) Polyimide in Electronics: Applications and Processability Overview. Polyimide for Electronic and Electrical Engineering Applications. IntechOpen. Available at: http://dx.doi.org/10.5772/intechopen.92629.

47. Dilip, J. J. S., Zhang, S., Teng, C., Zeng, K., Robinson, C., Pal, D. and Stucker, B., 2017. Influence of processing parameters on the evolution of melt pool, porosity, and microstructures in Ti-6Al-4V alloy parts fabricated by selective laser melting. *Progress in Additive Manufacturing*, *2*, pp. 157–167.

48. Ding, X., Liu, D. D., Xu, Y. M., Ding, X.T., Yang, J. and Ma, Z. J., 2015. Utilizing the Plateau-Rayleigh instability with heat-driven nano-biosensing systems. *SLAS Technology. 20*(4), pp. 463–470. doi.org/10.1177/2211068215575688

49. Dorigato, A., Moretti, V., Dul, S., Unterberger, S.H. and Pegoretti, A., 2017. Electrically conductive nanocomposites for fused deposition modelling. *Synthetic Metals*, *226*, pp. 7–14.

50. Dul, S., Fambri, L. and Pegoretti, A., 2018. Filaments production and fused deposition modelling of ABS/carbon nanotube composites. *Nanomaterials*, *8*(1), pp. 49.

51. Dynamic Analysis of Modified Composite Helicopter Blade - Scientific Figure on ResearchGate. Available from: https://www.researchgate.net/figure/Modified-helicopter-blade-construction_fig1_265521009 [accessed 10 May 2024].

52. Dzogbewu, T.C., 2020. Laser powder bed fusion: evaluation of Ti15Mo single tracks. *J. Mech. Eng. Res. Dev*, *43*, pp. 487-496.

53. El-Bagoury, N., Ahmed, S. I., Ahmed Abu Ali, O., El-Hadad, S., Fallatah, A. M., Mersal, G. A. M., Ibrahim, M. M., Wysocka, J., Ryl, J., Boukherroub, R.

© Central University of Technology, Free State

and A. Amin, M., 2019. The influence of microstructure on the passive layer chemistry and corrosion resistance for some titanium-based alloys. *Materials*, *12*(8), pp. 1233.

54. Eliaz, N., 2019. Corrosion of metallic biomaterials: A review. Materials 12(3), MDPI AG. https://doi.org/10.3390/ma12030407

55. Esslinger, J., 1960. Titanium in Aero Engines. MTU Aero Engines, Munich, Germany.

56. Etemadi, R., Wang, B., Pillai, K. M., Niroumand, B., Omrani, E. and Rohatgi, P., 2018. Pressure infiltration processes to synthesize metal matrix composites – A review of metal matrix composites, the technology and process simulation. Materials and Manufacturing Processes, 33(12), pp. 1261–1290. https://doi.org/10.1080/10426914.2017.1328122

57. Everett, D. H., 2007. Basic Principles of Colloid Science. Royal Society of Chemistry.

58. Fakharifar, M., Chen, G., Lin, Z. and Woolsey, Z., 2014. Behavior and strength of passively confined concrete filled tubes. In The 10th US National Conference on Earthquake Engineering: July 21–25, 2014, Anchorage, AL.

59. Fan, Y., Tian, W., Guo, Y., Sun, Z. and Xu, J., 2016. Relationships among the microstructure, mechanical properties, and fatigue behavior in thin Ti6Al4V. Advances in Materials Science and Engineering, 2016.

60. Fang, Z. Z. and Wang, H., 2010. Sintering of ultrafine and nanosized particles. In Sintering of Advanced Materials, pp. 434-473. Woodhead Publishing.

61. Fatchurrohman, N., and Sulaiman, S., 2021. Metal matrix composites for automotive components in depth case study: Development of automotive brake disc. Encyclopedia of Materials: Composites, 1, pp. 540–556. https://doi.org/10.1016/B978-0-12-803581-8.10487-4

62. Fu, S. Y., Feng, X. Q., Lauke, B. and Mai, Y. W., 2008. Effects of particle size, particle/matrix interface adhesion and particle loading on mechanical properties of particulate–polymer composites. Composites Part B: Engineering, 39(6), pp. 933–961.

© Central University of Technology, Free State

63. Gajera, H. M., Dave, K. G., Darji, V. P., and Abhishek, K., 2019. Optimization of process parameters of direct metal laser sintering process using fuzzy-based desirability function approach. Journal of the Brazilian Society of Mechanical Sciences and Engineering, 41(3), pp. 124. https://doi.org/10.1007/s40430-019-1621-2

64. Ganeriwala, R.K., 2015. Multiphysics modeling of selective laser sintering/melting. University of California, Berkeley.

65. Gergely, V. and Degicsher, H. P., 2000. Comprehensive composite materials. Metal Matrix Composites, 3, https://cir.nii.ac.jp/crid/1130282272369457024

66. Ghaffar, S. H., 2017. Straw fibre-based construction materials. In Advanced High Strength Natural Fibre Composites in Construction, pp. 257–283. Woodhead Publishing.

67. Giner, E., Vercher, A., Marco, M. and Arango, C., 2015. Estimation of the reinforcement factor ξ for calculating the transverse stiffness E2 with the Halpin–Tsai equations using the finite element method. *Composite Structures*, *124*, pp. 402–408.

68. Gogia, A. K., 2005. High-temperature titanium alloys. Defence Science Journal, 55(2), pp. 149–173.

69. Gokuldoss, P. K., Kolla, S., and Eckert, J., 2017. Additive manufacturing processes: Selective laser melting, electron beam melting and binder jetting—Selection guidelines. Materials, 10(6). https://doi.org/10.3390/MA10060672

70. Gomes Souza Jr, F., Bhansali, S., Pal, K., Silveira Maranhão, F. D., Santos Oliveira, M., Valladão, V. S., Brandão e Silva, D. S. and Silva, G. B., 2024. A 30-year review on nanocomposites: Comprehensive bibliometric insights into microstructural, electrical, and mechanical properties assisted by artificial intelligence. Materials, 17(5), pp. 1088.

71. Gomez-Gallegos, A., Mandal, P., Gonzalez, D., Zuelli, N. and Blackwell, P., 2018. Studies on titanium alloys for aerospace application. In Defect and Diffusion Forum, 385, pp. 419–423. Trans Tech Publications Ltd.

© Central University of Technology, Free State

72. Goodridge, R. D., Shofner, M. L., Hague, R. J., McClelland, M., Schlea, M. R., Johnson, R. B. and Tuck, C. J., 2011. Processing of a polyamide-12/carbon nanofibre composite by laser sintering. Polymer Testing, 30(1), pp. 94–100.

73. Gopal, V. and Manivasagam, G., 2019. Zirconia-alumina composite for orthopedic implant application. In Applications of Nanocomposite Materials in Orthopedics, pp. 201–219, Woodhead Publishing.

74. Gu, D., Rao, X., Dai, D., Ma, C., Xi, L. and Lin, K., 2019. Laser additive manufacturing of carbon nanotubes (CNTs) reinforced aluminum matrix nanocomposites: Processing optimization, microstructure evolution and mechanical properties. Additive Manufacturing, 29, pp. 100801.

75. Gu, D., Chen, H., Dai, D., Ma, C., Zhang, H., Lin, K., Xi, L., Zhao, T., Hong, C., Gasser, A. and Poprawe, R., 2020. Carbon nanotubes enabled laser 3D printing of high-performance titanium with highly concentrated reinforcement. IScience, 23(9).

76. Güler, O., Cuvalci, H., Canakci, A. and Celebi, M., 2017. The effect of nano graphite particle content on the wear behaviour of ZA27 based hybrid composites. Advanced Composites Letters, 26(2), pp. 30-36.

77. Gulevich, D. G., Nabiev, I. R. and Samokhvalov, P. S., 2024. Machine learning–assisted colloidal synthesis: A review. *Materials Today Chemistry*, *35*, pp. 101837.

78. Guo, B., Chen, B., Zhang, X., Cen, X., Wang, X., Song, M., Ni, S., Yi, J., Shen, T. and Du, Y., 2018. Exploring the size effects of Al4C3 on the mechanical properties and thermal behaviors of Al-based composites reinforced by SiC and carbon nanotubes. Carbon, 135, pp. 224–235.

79. Guo, K., Ji, Y., Li, Y., Kang, X., Bai, H. and Ren, H., 2023. Numerical simulation of temperature field and melt pool characteristics of CP-Ti manufactured by laser powder bed fusion. Metals. 13(1). doi.org/10.3390/met13010011

80. Guo, Y., Jia, L., Kong, B., Wang, N. and Zhang, H., 2018. Single track and single layer formation in selective laser melting of niobium solid solution alloy.

© Central University of Technology, Free State

Chinese Journal of Aeronautics. 31(4) pp. 860–866. doi.org/10.1016/j.cja.2017.08.019

81. Halip, J. A., Hua, L. S., Ashaari, Z., Tahir, P. M., Chen, L. W. and Uyup, M. K. A., 2019. Effect of treatment on water absorption behavior of natural fibre–reinforced polymer composites. In Mechanical and Physical Testing of Biocomposites, Fibre-Reinforced Composites and Hybrid Composites, pp. 141–156. Woodhead Publishing.

82. Hanzl, P., Zetek, M., Bakša, T. and Kroupa, T., 2015. The influence of processing parameters on the mechanical properties of SLM parts. *Procedia Engineering,* *100*(January), pp. 1405–1413. https://doi.org/10.1016/j.proeng.2015.01.510

83. Hashmi, M. S. J., 2014. Comprehensive Materials Processing. Newnes.

84. Hench, L. and Jones, J., 2005. Biomaterials, artificial organs and tissue engineering. Elsevier.

85. Heydari, L., Lietor, P. F., Corpas-Iglesias, F. A. and Laguna, O. H., (2021). Ti(C,N) and WC-based cermets: A review of synthesis, properties and applications in additive manufacturing. Materials, 14(22). https://doi.org/10.3390/MA14226786

86. HG, P. K. and Xavior, A., 2018. Processing of graphene/CNT-metal powder. Powder Technology, Intechopen, pp. 45.

87. Ho J and Schroeder M (2021) Polyimides as High Temperature Capacitor Dielectrics. Polyimide for Electronic and Electrical Engineering Applications. IntechOpen. Available at: http://dx.doi.org/10.5772/intechopen.92643.

88. Idumah, C. I. and Obele, C. M., 2021. Understanding interfacial influence on properties of polymer nanocomposites. Surfaces and Interfaces, 22, pp. 100879.

89. Inagaki, I., Takechi, T., Shirai, Y. and Ariyasu, N., 2014. Application and features of titanium for the aerospace industry. Nippon steel & sumitomo metal technical report, 106(106), pp. 22-27.

© Central University of Technology, Free State

90. Jaiswal, M., Dudhe, R. and Sharma, P. K., 2015. Nanoemulsion: an advanced mode of drug delivery system. 3 Biotech, *5*, pp. 123–127. https://doi.org/10.1007/s13205-014-0214-0

91. James, J., Annamalai, A. R., Muthuchamy, A. and Jen, C. P., 2021. Effect of wettability and uniform distribution of reinforcement particle on mechanical property (tensile) in aluminum metal matrix composite—a review. Nanomaterials, 11(9), pp. 2230.

92. Jewell, S. and Kimball, S., 2017. Mineral Commodity Summaries 2017, U.S. Geological Survey. Available at: https://doi.org/10.1016/j.dss.2003.08.004

93. Jones, R. H., 2001. Environmental Effects on Engineered Materials. Marcel Dekker.

94. Jones, R. H., Henager Jnr, C. H. and Lewinsohn, C. A., Windisch Jnr, C. A., 2001. Environmental Effects on Engineered Materials, p. 372. Pacific Northwest National Laboratory, Richland, Washington.

95. Jong, L., 2019. Particle reinforced composites from acrylamide modified blend of styrene-butadiene and natural rubber. Polymer Composites, 40(2), pp. 758–765. https://doi.org/10.1002/PC.24734

96. Joshi, S. C. and Sheikh, A. A., 2015. 3D printing in aerospace and its long-term sustainability. Virtual and Physical Prototyping, 10(4), pp. 175–185.

97. Kalra, C., Tiwari, S., Sapra, A., Mahajan, S. and Gupta, P., 2018. Processing and characterization of hybrid metal matrix composites. Journal of Materials and Environmental Science, 9(7), pp. 1979–1986.

98. Kannan, C. and Ramanujam, R., 2018. Advanced liquid state processing techniques for ex-situ discontinuous particle reinforced nanocomposites: A review. Science and Technology of Materials, 30(2), pp. 109–119.

99. Kaplun, B. W., Zhou, R., Jones, K. W., Dunn, M. L. and Yakacki, C. M., 2020. Influence of orientation on mechanical properties for high-performance fused filament fabricated Ultem 9085 and electro-statically dissipative polyetherketoneketone. Additive Manufacturing, 36, pp. 101527.

© Central University of Technology, Free State

100. Ke, X., Wu, W., Wang, C., Yu, Y., Zhong, B., Wang, Z., Wang, T., Fu, J. and Guo, J., 2022. Material removal and surface integrity analysis of Ti6Al4V alloy after polishing by flexible tools with different rigidity. Materials, 15(5), pp. 1642. https://doi.org/10.3390/ma15051642

101. Khan, I., Saeed, K., and Khan, I., 2019. Nanoparticles: Properties, applications and toxicities. Arabian Journal of Chemistry, 12(7), pp. 908–931. https://doi.org/10.1016/j.arabjc.2017.05.011

102. Koczak, M. J., Khatri, S. C., Allison, J. E. and Bader, M. G., 1993. Metal-matrix composites for ground vehicle, aerospace, and industrial applications, pp. 297–326. Stoneham, MA: Butterworth-Heinemann.

103. Kontou, E., Christopoulos, A., Koralli, P. and Mouzakis, D. E., 2023. The effect of silica particle size on the mechanical enhancement of polymer nanocomposites. Nanomaterials, 13(6), pp. 1095.

104. Ku, H., Wang, H., Pattarachaiyakoop, N. and Trada, M., 2011. A review on the tensile properties of natural fiber reinforced polymer composites. Composites Part B: Engineering, 42(4), pp. 856–873.

105. Kumudinie, C., 2001. Polymer-Ceramic nanocomposites: Interfacial bonding agents. EMST, pp. 7574–7577. https://doi.org/10.1016/B0-08-043152-6/01356-5

106. Kundalwal, S. I., 2017. Review on Modeling of Mechanical and Thermal Properties of Nano- and Micro-Composites. http://arxiv.org/abs/1708.00764

107. Kundie, F., Azhari, C.H., Muchtar, A. and Ahmad, Z.A., 2018. Effects of filler size on the mechanical properties of polymer-filled dental composites: A review of recent developments. Journal of Physical Science, 29(1), pp.141-165.

108. Lagow, B. W., 2016. Materials selection in gas turbine engine design and the role of low thermal expansion materials. *Jom*, *68*(11), pp. 2770–2775. https://doi.org/10.1007/s11837-016-2071-2

109. Larimian, T., Kannan, M., Grzesiak, D., AlMangour, B. and Borkar, T., 2020. Effect of energy density and scanning strategy on densification, microstructure

© Central University of Technology, Free State

and mechanical properties of 316L stainless steel processed via selective laser melting. Materials Science and Engineering: A, 770, pp. 138455.

110. Lashgari, H. R., Ferry, M. and Li, S., 2022. Additive manufacturing of bulk metallic glasses: Fundamental principle, current/future developments and applications. Journal of Materials Science & Technology, 119, pp. 131–149.

111. Le, T. N. and Lo, Y. L., 2019. Effects of sulfur concentration and Marangoni convection on melt-pool formation in transition mode of selective laser melting process. Materials & Design, 179, pp. 107866.

112. Ligon, S. C., Liska, R., Stampfl, J., Gurr, M. and Mülhaupt, R., 2017. Polymers for 3D printing and customized additive manufacturing. Chemical Reviews, 117(15), pp. 10212–10290.

113. Liu, J., Zhang, H., Sun, H., Liu, Y., Liu, W., Su, B. and Li, S., 2021. The development of filler morphology in dental resin composites: a review. Materials, 14(19), pp. 5612.

114. Liu, S. and Shin, Y. C., 2019. Additive manufacturing of Ti6Al4V alloy: A review. Materials & Design, 164, pp. 107552. https://doi.org/10.1016/j.matdes.2018.107552

115. Liu, X. J., Xiao, M., Huang, W., Yang, X. and Zha, J. W., 2024. Overview of High-Temperature Polymers. High Temperature Polymer Dielectrics: Fundamentals and Applications in Power Equipment, pp. 1–19. https://doi.org/10.1002/9783527841059.ch1

116. Lorell, M. A., 1995. The gray threat: assessing the next-generation European fighters. United States Air Force, Project Air Force (U.S.), & Rand Corporation.

117. Mahato, S. S., Mahata, D., Panda, S. and Mahata, S., 2023. Perspective Chapter: Sol-Gel Science and Technology in Context of Nanomaterials–Recent Advances. Sol-Gel Method-Recent Advances. IntechOpen.

118. Mallick, P. K., 2010. Thermoplastics and thermoplastic–matrix composites for lightweight automotive structures. In Materials, Design and Manufacturing for Lightweight Vehicles, pp. 174-207. Woodhead Publishing.

© Central University of Technology, Free State

119. Manakari, V., Parande, G. and Gupta, M., 2016. Selective laser melting of magnesium and magnesium alloy powders: a review. Metals, 7(1), pp. 2.

120. Marghalani, H. Y., 2010. Effect of filler particles on surface roughness of experimental composite series. Journal of Applied Oral Science, 18, pp. 59–67.

121. Maringa, M., 2005. Introduction to Solid and St*ructural Mechanics – Volume 1*. 1st ed. Amazon Kindle Direct Publishing, Reprinted 2022.

122. Merupo, V. I., Velumani, S., Ordon, K., Errien, N., Szade, J. and Kassiba, A. H., 2015. Structural and optical characterization of ball-milled copper-doped bismuth vanadium oxide (BiVO 4). CrystEngComm, 17(17), pp. 3366–3375.

123. Moloi, T., Dzogbewu, T. C., Maringa, M. and Muiruri, A., 2024. Quasi-static tensile properties of DMLS TI6AL4V (ELI) specimens exposed to two different heat treatment processes and tested at different elevated temperatures. Results in Engineering, 22, pp. 102290.

124. Mounier, D., Poilâne, C., Bûcher, C. and Picart, P., 2012. Evaluation of transverse elastic properties of fibres used in composite materials by laser resonant ultrasound spectroscopy. Acoustics 2012.

125. Mumtaz, N., Li, Y., Artiaga, R., Farooq, Z., Mumtaz, A., Guo, Q. and Un-Nisa, F., 2024. Fillers and methods to improve the effective (out-plane) thermal conductivity of polymeric thermal interface materials–a review. Heliyon.

126. Mussatto, A., Ahad, I. U., Mousavian, R. T., Delaure, Y. and Brabazon, D., 2021. Advanced production routes for metal matrix composites. Engineering reports, 3(5), pp. e12330.

127. Narasimharaju, S. R., Zeng, W., See, T. L., Zhu, Z., Scott, P., Jiang, X. and Lou, S., 2022. A comprehensive review on laser powder bed fusion of steels: Processing, microstructure, defects and control methods, mechanical properties, current challenges and future trends. Journal of Manufacturing Processes, 75, pp. 375-414. https://doi.org/10.1016/j.jmapro.2021.12.033

© Central University of Technology, Free State

128. Negi, S., Dhiman, S. and Sharma, R. K., 2013. Basics, applications and future of additive manufacturing technologies: A review. Journal of Manufacturing Technology Research, 5(1/2), pp. 75.

129. Njoku, R. E., Okon, A. E. and Ikpaki, T. C., 2011. Effects of variation of particle size and weight fraction on the tensile strength and modulus of periwinkle shell reinforced polyester composite. Nigerian Journal of Technology, 30(2), pp. 87–93.

130. Ogin, S. L., Brøndsted, P. and Zangenberg, J., 2016. Composite materials: constituents, architecture, and generic damage. In Modeling Damage, Fatigue and Failure of Composite Materials, pp. 3-23. Woodhead Publishing.

131. Ogunleye, R. O. and Rusnakova, S., 2022. A review of prestressed fibre-reinforced polymer matrix composites. Polymers, 14(1). https://doi.org/10.3390/POLYM14010060

132. Okpala, C. C., 2013. Nanocomposites–an overview. International Journal of Engineering Research and Development, 8(11), pp. 17–23.

133. Oosthuizen, S., 2010. Titanium: the innovator's metal. Historical case studies tracing titanium process and product innovation. http://researchspace.csir.co.za/dspace/handle/10204/4747

134. Oyar, P., 2018. Laser sintering technology and balling phenomenon. Photomedicine and laser surgery, 36(2), pp.72-77. doi.org/10.1089/pho.2017.4311

135. Palmer, J., Jones, J., Whittaker, M. and Williams, S., 2020. An analysis of thermo-mechanical fatigue crack growth in the titanium alloy Ti-6246. In MATEC Web of Conferences, 321, p. 04002. EDP Sciences.

136. Papanicolaou, G. C., Portan, D. V. and Kontaxis, L. C., 2021. Interrelation between fibre–matrix interphasial phenomena and flexural stress relaxation behavior of a glass fibre–polymer composite. Polymers, 13(6). https://doi.org/10.3390/POLYM13060978

137. Park, S. J. and Seo, M. K., 2011. Interface science *and composites*, *18*. Academic Press.

© Central University of Technology, Free State

138. Parry, E. J., Best, J. M. and Banks, C. E., 2020. Three-dimensional (3D) scanning and additive manufacturing (AM) allows the fabrication of customised crutch grips. Materials Today Communications, 25, pp. 101225.

139. Peko, I., Krolo, J., Bagavac, P., Đurić, S., Kostić, N. and Bašić, A., 2017. Modeling and optimization of tensile strength of ABS parts manufactured by the fused deposition modeling process. In International conference, Mechanical Technologies and Structural Materials.

140. Pilipovic, A., Raos, P. and Sercer, M., 2011. Experimental testing of quality of polymer parts produced by laminated object manufacturing - LOM. Tehnicki Vjesnik, 18(2), pp. 253–260.

141. Poutord, A., Rossi, F., Poulachon, G., M'Saoubi, R. and Abrivard, G., 2013. Local approach of wear in drilling Ti6Al4V/CFRP for stack modelling. Procedia CIRP, 8, pp. 316–321. https://doi.org/10.1016/j.procir.2013.06.109

142. Pramanik, N. K., Haldar, R. S., Niyogi, U. K. and Alam, M. S., 2014. Development of an advanced engineering polymer from the modification of Nylon 66 by e-beam irradiation. Defence Science Journal, 64(3).

143. Ramakrishnan, T., Gift, M., Chitradevi, S., Jegan, R., Jose, H., Subha, P., Nagaraja, H. N., Sharma, R., Selvakumar, P. and Hailegiorgis, S. M., 2021. Study of numerous resins used in polymer matrix composite materials. Advances in Materials Science and Engineering, 2022(1), 1088926. https://doi.org/10.1155/2022/1088926

144. Rashid, A. B., Haque, M., Islam, S. M. and Labib, K. R. U., 2024. Nanotechnology-enhanced fibre-reinforced polymer composites: Recent advancements on processing techniques and applications. Heliyon. https://doi.org/10.1016/j.heliyon.2024.e24692

145. Rozhbiany, F. A. R. and Jalal, S. R., 2019. Reinforcement and processing on the machinability and mechanical properties of aluminum matrix composites. Journal of Materials Research and Technology, 8(5), pp. 4766–4777.

© Central University of Technology, Free State

146. Ruban, W., Vijayakumar, V., Dhanabal, P. and Pridhar, T., 2014. Effective process parameters in selective laser sintering. International Journal of Rapid Manufacturing, 4(2/3/4), pp. 148. https://doi.org/10.1504/ijrapidm.2014.066036

147. Saba, N., Jawaid, M. and Sultan, M. T. H., 2017. Thermal properties of oil palm biomass based composites. In Lignocellulosic Fibre And Biomass-Based Composite Materials, pp. 95–122. Woodhead Publishing.

148. Sachit, T. S., Sapthagiri Prasad, N. and Aameer Khan, M., 2018. Effect of particle size on mechanical and tribological behavior of LM4/SiCp based MMC. Materials Today: Proceedings, 5(2), pp. 5901–5907. https://doi.org/10.1016/j.matpr.2017.12.189

149. Sadeghi, B. and Cavaliere, P. D., 2023. Reviewing the integrated design approach for augmenting strength and toughness at macro- and micro-scale in high-performance advanced composites. Materials (Basel, Switzerland), 16(17), pp. 5745. https://doi.org/10.3390/ma16175745

150. Sadeghpour, E., Wang, H., Guo, Y., Chua, D. H. and Shim, V. P., 2020. A filler-matrix interaction model for the large deformation response of graphene nanocomposite–A PVA-GO nanocomposite example. Composites *Part A: Applied* Science and Manufacturing, 129, pp. 105729.

151. Saifuddin, N., Raziah, A. Z. and Junizah, A. R., 2013. Carbon nanotubes: a review on structure and their interaction with proteins. Journal of Chemistry, 2013(1), pp. 676815.

152. Salehabadi, A., Enhessari, M., Ahmad, M. I., Ismail, N., and Gupta, B. D., 2023. Fabrication of sensors. Metal Chalcogenide Biosensors, pp. 143–174. https://doi.org/10.1016/B978-0-323-85381-1.00008-8

153. Seetharaman, S. and Gupta, M., 2021. Fundamentals of Metal Matrix Composites. Encyclopedia of Materials: Composites, 1, pp. 11–29. Oxford: Elsevier. http://dx.doi.org/10.1016/B978-0-12-819724-0.00001-X

© Central University of Technology, Free State

154. Sen. M., 2020. Nanocomposite Materials. Nanotechnology and the Environment. IntechOpen. pp. 1-12. Available at: http://dx.doi.org/10.5772/intechopen.93047.

155. Sharma, A. K., Bhandari, R., Aherwar, A. and Rimašauskienė, R., 2020. Matrix materials used in composites: A comprehensive study. Materials Today: Proceedings, 21, pp.1559–1562.

156. Shirvanimoghaddam, K., Hamim, S. U., Akbari, M. K., Fakhrhoseini, S. M., Khayyam, H., Pakseresht, A. H., Ghasali, E., Zabet, M., Munir, K. S., Jia, S. and Davim, J. P., 2017. Carbon fibre reinforced metal matrix composites: Fabrication processes and properties. Composites Part A: Applied Science and Manufacturing, 92, pp. 70–96.

157. Shunmugasundaram, M., Praveenkumar, A., Sankar, L. P. and Sivasankar, S., 2021. Effect of tin oxide coatings by spray pyrolysis process on mechanical properties of aluminium, brass and mild steel. International Journal of Vehicle Structures & Systems, 13(2), pp. 195–199.

158. Shunmugavel, M., Polishetty, A. and Littlefair, G., 2015. Microstructure and mechanical properties of wrought and additive manufactured Ti-6Al-4V cylindrical bars. Procedia Technology, 20(July), pp. 231–236. https://doi.org/10.1016/j.protcy.2015.07.037

159. Sidambe, A. T., 2014. Biocompatibility of advanced manufactured titanium implants—A review. Materials, 7(12), pp. 8168–8188.

160. Sieniawski, J., Ziaja, W., Kubiak, K. and Motyka, M., 2013. Microstructure and mechanical properties of high strength two-phase titanium alloys. Titanium Alloys-Advances in Properties Control, Intechopen. pp.69-80.

161. Singh, R., Singh, S. and Hashmi, M. S. J., 2016. Implant materials and their processing technologies. Elsevier.

162. Singh, R. P., Singh, P. and Singh, K. R., 2021. Introduction to composite materials: Nanocomposites and their potential applications. In *Composite Materials,* pp. 1-28. CRC Press.

© Central University of Technology, Free State

163. Singh, N., Hameed, P., Ummethala, R., Manivasagam, G., Prashanth, K. G. and Eckert, J., 2020. Selective laser manufacturing of Ti-based alloys and composites: Impact of process parameters, application trends, and future prospects. Materials Today Advances, 8, pp. 100097.

164. Smith, J. C., 1976. Experimental values for the elastic constants of a particulate-filled glassy polymer. Journal of Research of the National Bureau of Standards. Section A, Physics and Chemistry, 80(1), pp. 45.

165. Spears, T.G. and Gold, S.A., 2016. In-process sensing in selective laser melting (SLM) additive manufacturing. Integrating Materials and Manufacturing Innovation, 5(1), pp.16-40.

166. Spruijt, E. and Biesheuvel, P. M., 2014. Sedimentation dynamics and equilibrium profiles in multicomponent mixtures of colloidal particles. Journal of Physics: Condensed Matter, 26(7), pp. 075101.

167. Staab, G., 2015. Laminar Composites. Butterworth-Heinemann.

168. Stalin, B., Meignanamoorthy, M. and Ravichandran, M., 2018, Synthesis of metal matrix composites and alloys by mechanical alloying: A Review. In IOP Conference Series: Materials Science and Engineering, 402(1), pp. 012097. IOP Publishing.

169. Sulima, I., Figiel, P., Sucœniak, M. and Œwitek, M., 2008. Sintering of TiB 2 - Al composites using HP-HT method. International Scientific Journal. October, 33(2), pp. 117–120.

170. Sunil, B. R., 2015. Developing surface metal matrix composites: A comparative survey. International Journal of Advances in Materials Science and Engineering, 4(3), pp. 9–16.

171. Sztorch, B., Brząkalski, D., Pakuła, D., Frydrych, M., Špitalský, Z. and Przekop, R. E., 2022. Natural and synthetic polymer fillers for applications in 3D printing—FDM technology area. Solids, 3(3), pp. 508–548.

172. Tanahashi, M., 2010. Development of fabrication methods of filler/polymer nanocomposites: with focus on simple melt-compounding-based approach without surface modification of nanofillers. Materials, 3(3), pp. 1593–1619.

© Central University of Technology, Free State

173. Taylor, R., 2000, Carbon matrix composites. Elsevier.

174. Teklal, F., Djebbar, A., Allaoui, S., Hivet, G., Joliff, Y. and Kacimi, B., 2018. A review of analytical models to describe pull-out behavior–fibre/matrix adhesion. Composite Structures, 201, pp. 791–815.

175. Thakur, A., Bandhu, D., Peshwe, D. R., Mahajan, Y. Y., Saxena, K. K. and Eldin, S. M., 2023. Appearance of reinforcement, interfacial product, heterogeneous nucleant and grain refiner of MgAl2O4 in aluminium metal matrix composites. Journal of Materials Research and Technology, 26, pp. 267-302.

176. Turowska, A. and Adamiec, J., 2015. Mechanical properties of WE43 magnesium alloy joint at elevated temperature. Archives of Metallurgy and Materials, (4).

177. Upadhyay, R. V., Pisuwala, M. S., Parekh, K. and Raj, K., 2020. Thermal conductivity of flake-shaped iron particles based magnetorheological suspension: Influence of nano-magnetic particle concentration. Journal of Magnetism and Magnetic Materials, 503, pp.166633.

178. Vahid, A., Hodgson, P. and Li, Y., 2017. Reinforced magnesium composites by metallic particles for biomedical applications. Materials Science and Engineering: A, 685, pp. 349–357.

179. Valino, A. D., Dizon, J. R. C., Espera Jr, A. H., Chen, Q., Messman, J. and Advincula, R. C., 2019. Advances in 3D printing of thermoplastic polymer composites and nanocomposites. Progress in Polymer Science, 98, pp. 101-162.

180. Vasile, B. S., Birca, A. C., Surdu, V. A., Neacsu, I. A. and Nicoară, A. I., 2020. Ceramic composite materials obtained by electron-beam physical vapor deposition used as thermal barriers in the aerospace industry. Nanomaterials, 10(2). https://doi.org/10.3390/nano10020370

181. Verma, D. and Senal, I., 2019. Natural fibre-reinforced polymer composites: Feasibiliy study for sustainable automotive industries. In Biomass,

© Central University of Technology, Free State

Biopolymer-Based Materials, and Bioenergy, pp. 103-122. Woodhead Publishing.

182. Viale, V, Stavridis, J, Salmi, A, Bondioli, F. and Saboori, A., 2022. Optimisation of downskin parameters to produce metallic parts via laser powder bed fusion process: an overview. International Journal of Advanced Manufacturing Technology, 123(7–8), pp. 2159–2182. doi.org/10.1007/S00170-022-10314-Z

183. Vinayaka, N., Bodukuri, A.K., Jadhav, G.K., Padmamalini, N., Pandey, S.K., Balasubramanian, M., Immanuel Durai Raj, J., Suresh Kumar, M. and Singh, B., 2023. Analyze the Mechanical Characteristics of Fabricated MMCs on Nanocarbon Influencing with Polymer Composites. Journal of Nanomaterials, 2023(1), pp.1-10.

184. Wang, J. H., Ren, J., Liu, W., Wu, X. Y., Gao, M. X. and Bai, P. K. 2018. Effect of selective laser melting process parameters on microstructure and properties of co-cr alloy. Materials. 11(9). doi.org/10.3390/ma11091546

185. Wanhill, R.J.H., 2017. Physical property significances for aerospace structural materials. Aerospace Materials and Material Technologies: Volume 2: Aerospace Material Technologies, pp.143-15

186. Wegner, A., 2016. New polymer materials for the laser sintering process: Polypropylene and others. Physics Procedia, 83, pp. 1003–1012.

187. Mark, Whittaker., 2011. Titanium in the Gas Turbine Engine, Advances in Gas Turbine Technology, Dr. Ernesto Benini (Ed.), ISBN: 978-953-307-611-9, InTech, Available from: http://www.intechopen.com/books/advances-in-gas-turbine-technology/titanium-in-the-gas-turbine-engine

188. Williams, J. C. and Boyer, R. R., 2020. Opportunities and issues in the application of titanium alloys for aerospace components. Metals, 10(6), pp. 705. 10.3390/met10060705.

189. Wiśniewska, A., Hernik, S., Liber-Kneć, A. and Egner, H., 2019. Effective properties of composite material based on total strain energy equivalence. Composites Part B: Engineering, 166, pp. 213–220.

© Central University of Technology, Free State

190. Wong, K. V. and Hernandez, A., 2012. A review of additive manufacturing. ISRN Mechanical Engineering, 2012, pp. 1–10. https://doi.org/10.5402/2012/208760

191. Wu, S. and Chen, B., 2023. Surface coatings of reinforcement phases in magnesium matrix composites: A review. Materials, 16(24), pp. 7560.

192. Yadroitsava, I., Els, J., Booysen, G. and Yadroitsev, I., 2015. Peculiarities of single track formation from TI6AI4V alloy at different laser power densities by selective laser melting. South African Journal of Industrial Engineering. 26(3), pp. 86–95. doi.org/10.7166/26-3-1185

193. Yadroitsev, I., Krakhmalev, P. and Yadroitsava, I., 2015. Hierarchical design principles of selective laser melting for high quality metallic objects. Additive Manufacturing, 7, pp. 45–56. doi.org/10.1016/j.addma.2014.12.007

194. Yehia, H. M., Hamada, A., Sebaey, T. A. and Abd-Elaziem, W., 2024. Selective laser sintering of polymers: process parameters, machine learning approaches, and future directions. Journal of Manufacturing and Materials Processing, 8(5), pp. 197.

195. Yu, M. F., Lourie, O., Dyer, M. J., Moloni, K., Kelly, T. F. and Ruoff, R. S., 2000. Strength and breaking mechanism of multiwalled carbon nanotubes under tensile load. Science, 287(5453), pp. 637–640.

196. Yu, M. F., Files, B. S., Arepalli, S. and Ruoff, R. S., 2000. Tensile loading of ropes of single wall carbon nanotubes and their mechanical properties. Physical Review Letters, 84(24), pp. 5552.

197. Zamora-Mendoza, L., Gushque, F., Yanez, S., Jara, N., Álvarez-Barreto, J. F., Zamora-Ledezma, C., Dahoumane, S. A. and Alexis, F., 2023. Plant fibres as composite reinforcements for biomedical applications. Bioengineering, 10(7), pp. 804.

198. Zare, Y., 2016. Study of nanoparticles aggregation/agglomeration in polymer particulate nanocomposites by mechanical properties. Composites Part A: Applied Science and Manufacturing, 84, pp. 158–164. https://doi.org/10.1016/J.COMPOSITESA.2016.01.020

© Central University of Technology, Free State

199. Zenani, A., Dzogbewu, T.C., Du Preez, W.B. and Yadroitsev, I., 2020. Optimum process parameters for direct metal laser sintering of Ti6Al powder blend. Univers. J. Mech. Eng, 8(4), pp. 170-182. doi.org/10.13189/ujme.2020.080402

200. Zhang, W., Hou, W., Deike, L. and Arnold, C., 2022. Understanding the Rayleigh instability in humping phenomenon during laser powder bed fusion process. International Journal of Extreme Manufacturing. 4(1) pp. 015201. doi.org/10.1088/2631-7990/AC466D

201. Zhang, X., Chen, Y. and Hu, J., 2018. Recent advances in the development of aerospace materials. Progress in Aerospace Sciences, 97, pp. 22–34.

202. Zhao, H., Zhou, F., Ma, C., Wei, Z. and Long, W., 2022. Bonding mechanism and process characteristics of special polymers applied in pelletizing binders. Coatings, 12(11), pp. 1618. https://doi.org/10.3390/COATINGS12111618

© Central University of Technology, Free State

CHAPTER 3 - RESEARCH METHODOLOGY

3.0 Summary

This chapter is divided into two sections. The first part addresses the different methods used to mix powders, and the second part discusses SLM printing of CNT/Ti6Al4V nanocomposites. Mixing of powder is tackled in the subcategories of primary mixing, secondary mixing, and tertiary mixing. The section on printing of single tracks includes details of the method used to optimise process parameters, wire-cutting, preparation of samples for metallographic analysis, and finally, the procedure used to carry out this analysis. Figure 3.1 gives an outline of the contents of the chapter.

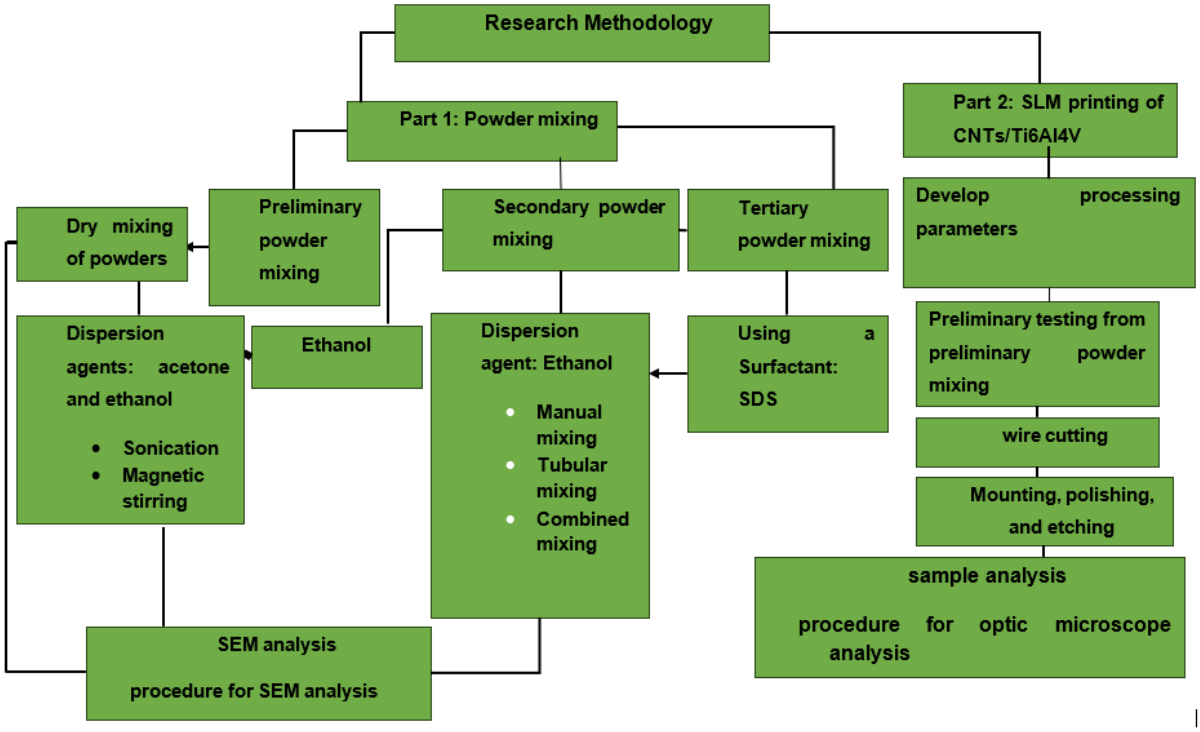

Figure 3.1 Detailed outline of the research methodology

© Central University of Technology, Free State

3.1 Introduction

Images of the powder samples described here are to be found in Appendix A. Mixing of CNTs and Ti6Al4V powders was carried out at volume fractions of 3 %, 8 %, 15 %, 20 %, 25 %, and 30 % CNTs. To calculate amount of powder required per volume fraction the following was obtained. The volume of powders required for carbon nanotubes and Ti6Al4V at 3% volume fraction was determined as follows:

$$Powder\ required\ per\ build = L \times W \times (t + 4)$$

$$Powder\ required\ per\ build = 40 \times 10{,}375 \times (5 + 4)$$

$$Powder\ required\ per\ build = 4150\ mm^3$$

The foregoing formula was arrived at by considering an E8 test build specimen. The high costs of CNTs necessitated adoption of such an approach.

The volumes of carbon nanotubes and Ti6Al4V powder required at 3% volume fraction were calculated as follows:

$\frac{3}{100} \times 4150mm^3 = 124.5\ mm^3$ (Carbon nanotubes)

$\frac{97}{100} \times 4150mm^3 = 4025.5\ mm^3$ (Ti6Al4V)

To calculate the quantities of required powder in mass, the following equation was used:

$$m = \rho . V$$

The known density of carbon nanotubes is 2.1 kg/m^3.

The mass (g) of carbon nanotubes (CNTS) that is required at 3% volume fraction was then calculated as:

$$m_{cnTs} = 0{,}00211 \frac{g}{mm^3} \times 124.5.5mm^3 = \mathbf{0.261g}$$

The known density of Ti6Al4V is 4.43 kg/m^3.

The mass (g) of Ti6Al4V that was required at 3% volume fraction wa calculated as:

$$m_{Ti6Al4V} = 0.00443 \frac{g}{mm^3} \times 4025.5.5mm^3 = \mathbf{17.314\ g}$$

© Central University of Technology, Free State

Table 3.1 Calculated mass of powders at six volume fractions

Carbon nanotubes volume fractions V_R	m_{cnTs} (g)	Volume CNTs (mm^3)	Ti6Al4V volume fractions V_m	Volume Ti6Al4V per volume fraction (mm^3)	m_{Ti64} (grams)
3%	0.261	124.5	97%	4025.5	17.310
8%	0.697	332	92%	3818	16.417
15%	1.307	622.5	85%	3527.5	15.168
20%	1.743	830	80%	3320	14.276
25%	2.179	1037.5	75%	3112.5	13.384
30%	2.6145	1245	70%	2905	12.492
Total	**8.802g**				**89.046g**

To determine the powder required for the single tracks, the number of single tracks that could be accommodated in the reduction unit used were first determined.

The dimensions of the machined Ti6Al4 base plates used for printing tracks were L x B = 50 mm x 50 mm. A layer thickness of 50 µm, was adopted with a laser spot size of 150 µm, which defined the track-width. The foregoing was used to determine the number of single tracks that could be accommodated on the reduction unit of 45 mm X 45 mm reduction unit. The track-lengths are set to 20 mm and an allowance of 1 mm is set between the single tracks.

The foregoing dimensions allowed a total of **30** single tracks ($[(45/20) \times (45/((30/1000) + 1]$ to be fitted the reduction unit.

The volume of a single track and from it that of 30 single tracks were calculated as follows:

© Central University of Technology, Free State

Volume of a single track = $L \times W \times t$

Volume of a single track = $= 20 \times 0.05 \times 0.15 = 0.09mm^3$

Volume of 30 single tracks $= 30 \times 0.09mm^3 = 2.7mm^3$

Table 3.2 The volume and mass of CNTs and Ti6Al4V(ELI) powder required for printing of 30 single tracks per volume fraction

Carbon nanotubes volume fractions V_R	Volume of carbon nanotubes for 30 single tracks per volume fraction (mm^3)	Mass of carbon nanotubes for 30 single tracks per volume fraction (g)	Ti6Al4V volume fractions V_m	Volume of Ti6Al4V for 30 single tracks per volume fraction (mm^3	Mass of Ti6al4V for 30 single tracks per volume fraction (g)
3%	0.081	0.00017	97%	2.619	11.6022
8%	0.216	0.000454	80%	2.16	9.5688
15%	0.405	0.000851	85%	2.295	10.1669
20%	0.54	0.001134	80%	2.16	9.5688
25%	0.675	0.001418	75%	2.025	8.97075
30%	2.646	0.005557	70%	1.89	8.3727
Total	**4.563 mm^3**	**0.018707g**		**13.149 mm^3**	**58.2501 g**

The total mass of carbon nanotubes required to print 30 single tracks for the six different volume fractions of CNT selected thus came to 0.018 g. Combining the total amount of powder required for the three-dimensional specimens required and that of

© Central University of Technology, Free State

the single tracks needed gave rise to a total of 8.802 g. The 10 g of CNT powder available was thus sufficient.

The range of volume fraction was advised by the literature that showed nanofibre-reinforced composite to be limited to 10 % at the most, which is greater than the value of 5 % for nanoparticles. The higher values of up to 30 % in the present work were used to investigate whether it was possible to exceed this upper limit (Kumar et al., 2022; Raza et al., 2024). Preliminary powder mixing was carried out to determine the effect of two common solvents, acetone and ethanol, as dispersion agents. Solvents can act as dispersion agents As is normally the case with low costs and simple methods using common solvents, it was resort to use sonication and a magnetic stirrer to agitate the nanoparticles further to enhance the deagglomeration and dispersion of the CNTs was taken (Khoza et al., 2012). This provided a basis for secondary mixing, which incorporated manual mixing, turbula mixing, and mechanical-turbula-manual mixing, which is referred to as combined mixing techniques. Tertiary mixing was carried out using a surfactant in addition to secondary mixing.

To successfully incorporate CNTs within a matrix, the attractive van der Waals forces between them that tend to keep them bundled up into agglomerates, thus minimising their dispersion and homogeneity of the resulting mixture, must be broken (Suzuki, 2013). To achieve uniform dispersion of nanoparticles within other particles, various methods of blending and dispersion are available, which include colloidal mixing, magnetic stirring, molecular-level mixing, nanoscale dispersion processing, particle composite system mixing, friction stir processing, layer stacking, ball milling, and roller mixing. Of the aforementioned processes, the most commonly used methods include molecular-level mixing, ball milling, and colloidal mixing (Suárez et al., 2016).

Dispersion agents are utilised in all these commonly used processes for mixing. In the case of ball milling, ethanol is used to prevent cold welding of the matrix and agglomeration of the particles of powder during ball milling. In molecular-level mixing, CNTs are first treated in an acid, such as nitric acid and sulphuric acid (Roy et al., 2018), then dispersed in a solvent using ultrasonic agitation. Colloidal mixing disperses material using an ultrasonic bath, homogeniser, or magnetic stirrer in a solvent (Suárez et al., 2016), as described by the schematic shown in Figure 3.2, for

© Central University of Technology, Free State

mixtures such as the present one, which makes use of dimethylformamide or ethylene glycol to achieve a stable dispersion of CNTs (Shojaeiarani, Bajwa and Holt, 2020).

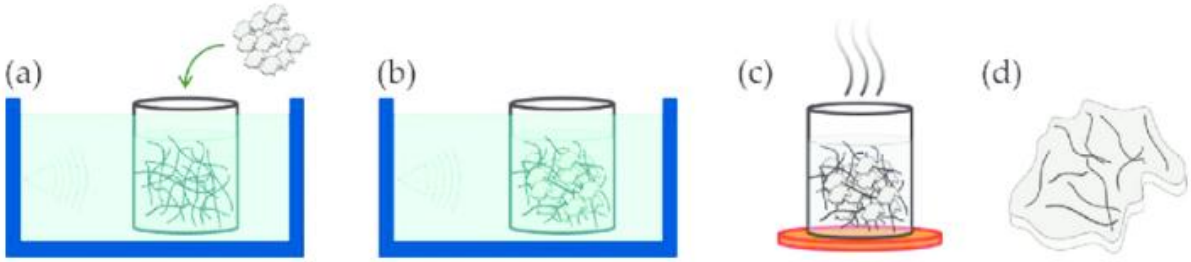

Figure 3.2 Schematic representation of colloidal mixing (Suárez et al., 2016)

In this figure, CNTs are first dispersed into a liquid solvent using ultra-sonication/sonication, after which (a) the metal powder is added, (b) the two materials are then mixed again using ultra-sonication, (c) the solvent is evaporated, and finally (d) a metal/CNT powder mixture is obtained (Suárez et al., 2016).

Mixtures can be agitated using screw mixers, ultrasonication, or other methods of blending (Ogunmefun et al., 2023). Several dispersion agents are available, including methanol, ethanol, glycol, butanol, ethylene glycol, ethanolamine, propanol, and ethylenediamine (Suárez et al., 2016).

3.1.1 Preliminary Powder Mixing

For the preliminary mixing, sonication and manual mixing (this low agitation would cause less deagglomeration of CNTs) were applied separately. A stationary magnetic stirrer was used separately in conjunction with the two dispersants, acetone and ethanol, in addition to sonication to disperse CNTs. Manual mixing was used alone to compare its effectiveness of dispersion with the previous method. A volume fraction of 3 % of CNTs was initially used in preliminary mixing, followed by an 8 % of CNTs in Ti6Al4V(ELI). It was proposed to use volume fractions of mixtures as a reference in order to relate the results obtained with the material in the literature that is predominantly presented in terms of volume fraction instead of weight fraction.

3.1.1.1 Equipment and Materials

The equipment used in the preliminary mixing is shown in Figure 3.3 and include an electronic scale, a box oven with a maximum temperature of 200 °C, a sonic bath from SCIENTECH, model 704, frequency of 35 Hz was employed to agitate the particles, a

© Central University of Technology, Free State

funnel flow meter for determining the apparent density (this was done by determining the mass of powder that fits into a specified volume under free-flow conditions applying the ASTM B212 standard. Five measurements were carried out and an average was taken) from the Ti6Al4V(ELI) powder, a magnetic stirrer, and a microscope for analysis of the powder mixtures. Mixing was done using spherical gas-atomised Ti6Al4V(ELI) (Figure powder and aligned multi-walled CNTs (data sheet in Appendix B) of purity: > 96%, outside diameter: 8–18 nm, surface area 30–300 m2/g. The health and safety concerns over handling of CNTs necessitated a health and safety data sheet (Appendix C)

Figure 3.3 Experimental equipment used for preliminary mixing of powder

3.1.1.2 Dispersion of Carbon Nanotubes in Ethanol

Dispersion of CNTs was carried out in 10 ml of ethanol in a plastic container (20 ml), with a measured weight of CNTs corresponding to a 3 % volume fraction of CNTs in the Ti6Al4V(ELI) powder to be added later. Sonication of the CNTs was then carried out for 10 min at a frequency of 35 Hz in a sonic bath from SCIENTECH, model 704, employed to agitate the particles. The CNTs in ethanol were then removed from the sonic bath, 9.92 g Ti6Al4V powder was added, and the mixture was sonicated as in

© Central University of Technology, Free State

the previous step. This was followed by oven-drying at 50 °C for 20 minutes. Lastly, the dried mixture was stirred magnetically for five minutes. Upon drying in an oven, the mixed sample of powder was placed in a plastic container and labelled according to the mixing process carried out. This was also done upon completion of the following two processes.

3.1.1.3 Dispersion of Carbon Nanotubes in Acetone

CNTs with a weight corresponding to a 3 % volume fraction in the Ti6Al4V(ELI) powder were added to 10 ml of acetone in a plastic container. The slurry that formed was then put in a sonic bath and sonicated for 10 minutes at a frequency of 33 Hz. After sonication, 9.92 g of Ti6Al4V powder was added to the slurry and the mixture sonicated as in the previous step. The resulting mixture was then oven-dried at 70 °C for 15 minutes to vaporise the acetone. Thereafter, the mixture was stirred magnetically for 10 minutes. It is noted that the degree to which the temperature for oven-drying is applied does not affect the mixture and is applied simply to vaporise the acetone. Hence the temperatures and times applied, which are different for both dispersion agents, are essentially carried out to vaporise the acetone.

3.1.1.4 Manual mixing

The CNTs were weighed and placed in a plastic container. Thereafter, Ti6Al4V(ELI) powder was added to the plastic container, and the mixture was blended manually using a manual mixing tool to stir the powders for 10 minutes.

Figure 3.4 presents three powder mixture samples in their plastic containers, from left to right, the samples where ethanol, acetone, and manual mixing were used.

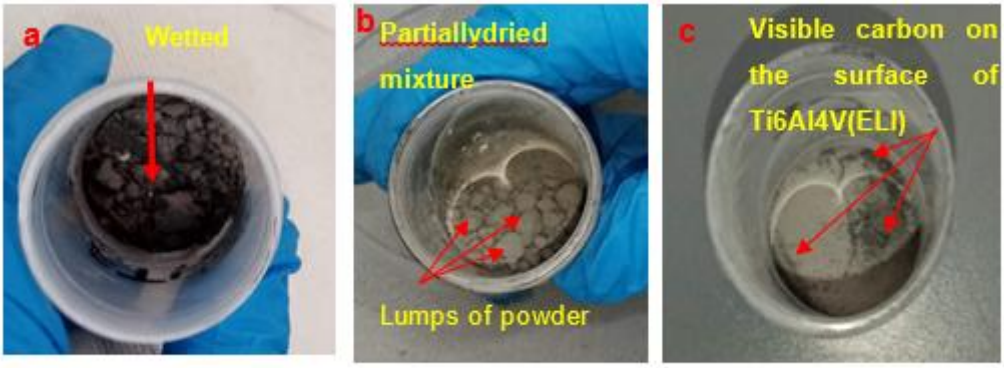

Figure 3.4 Powder samples of three different mixed powders

© Central University of Technology, Free State

Figure 3.4 presents CNT and Ti6Al4V(ELI) powder mixtures at various stages of mixing. In Figure 3.4(a), the powder samples consist of visible CNTs (black) and Ti6AlV (ELI) powders (grey), which form a wetted mixture as ethanol is still present. Figure 3.4(b) presents the powder mixture with visible lumps of powder mixture after partial oven-drying. Once the ethanol in the powder mixture is vaporised fully, the powder mixture remains in the form of loose particles, as seen in Figure 3.4(c). Visible carbon material inside the container, as shown in Figure 3.4(c), posed a health and safety issue. The red arrows in Figure 3.4(b & c) show the presence of CNTs on the surface of the mixture, which is thought to have been due to the density of CNTs being lower than that of Ti6Al4V(ELI). A health and safety standard was developed using the supplier details and research articles on the safe handling of CNTs and is presented in Appendix D.

3.1.2 Secondary Powder Mixing

This work was carried out using ethanol (which was found here to be a better dispersant than acetone) as a dispersant, and manual, turbula and combined mixing. was used to identify the most efficient method of mixing to produce a homogenous mixture of Ti6Al4V(ELI) and CNTs. To correct the shortcoming of the segregation of CNTs observed for turbula mixing, an approach was adopted first to apply manual mixing, followed by turbula mixing, and then further manual mixing. In this stage of mixing, the CNTs dispersed in ethanol were left for over a period of 48 hours. After this, Ti6Al4V powder was added to the CNTs slurry mixture, and both were mixed. Where manual mixing was employed, each sample was mixed manually for 30 minutes and then dried in a box oven.

3.1.2.1 Equipment and its use

The experiments were carried out in the powder room, where all powder material was kept. This is done to prevent and limit the exposure of other persons and equipment to the powders. Images of the experimental equipment used are presented in Figure 3.5.

© Central University of Technology, Free State

Figure 3.5 Equipment and area used for experiments on mixing of powder

© Central University of Technology, Free State

Figure 3.6(a) shows an image of the powder room. A sticky mat is placed at the entrance to the powder room to trap any powder material that might otherwise escape through persons stepping in and out of the room. There is also a designated bin used for disposing of personal protective equipment (PPE) that is contaminated with powder material. The samples (CNTs and Ti6Al4V) were weighed in the powder room using the KERN & SONH GmbH weighing machine shown in Figure 3.6(c), placed in respective containers bearing the different dispersion agents used and then carried in containers to the metallurgy lab for sonification. Sonication of powder samples was carried out using the sonic bath shown in Figure 3.6(b).

The tools depicted in Figure 3.6(i) and Figure 3.6(j) were used to carry out manual mixing. The tool shown in Figure 3.6(i) is made from steel but has a much smaller cross-section (10mm) compared to the tool used in Figure 3.6(j) (20mm diameter). It was initially used to carry out manual mixing for 12 samples. The tool shown in Figure 3.6(h) was then used on all other samples (It provided better mixing due to the large surface area compared to the tool with a smaller cross-section). Manual mixing of powders was carried out for 30 minutes for each sample.

The turbula mixer shown in Figure 3.5(e) was used to mix the powder in one of the three methods adopted in this work. It consists of a 3D mixer into which a container with the powder samples was inserted. A hood was then placed over the mixer to prevent powder material from flying out during mixing or in the unlikely event that the container escaped from its restraints on the mixer. A close-up of the 3D mixer is shown in Figure 3.5(f). The turbula mixer used had a motor that was supplied by SEW-Eurodrive and has a maximum revolution speed of 350 rpm (Figure 3.5(f)).

To dry the powders, the zirconia plates shown in Figure 3.6(h), which are non-reactive and therefore cannot react with the mixtures, were used. Upon completion of mixing, all the samples (emptied into the zirconia plates) were dried at 100 °C in the box oven shown in Figure 3.4(g), with a maximum temperature of 200 °C.

3.1.4 Tertiary Powder Mixing

A surfactant, SDS, was added to the powder mixtures to improve the dispersion of the CNTs in the Ti64-CNT powder mixtures. All three mixing method (mechanical only, turbula only, and combined mixing) were evaluated while using ethanol as a dispersion agent. Initially, a 1:1 ratio by mass of SDS: CNT was used with the SDS added to the

© Central University of Technology, Free State

6 vol% CNT-Ti64 mixture; however, this did not prove sufficient to fully de-agglomerate the CNTs and provide a homogenous mixture. Ultimately, a 10:1 SDS: CNT mass ratio resulted in producing a de-agglomerated CNT-Ti64 powder mixture, using ethanol as the solvent.

The three methods of mixing mentioned earlier in this chapter were applied to 6 vol.% of CNTs in Ti6Al4V(ELI) powder using SDS as a surfactant.

3.1.4.1 Experimental Method

Manual mixing was first carried out using a Ti6Al4V(ELI) hand tool with a diameter of 10 mm and a length of 15 cm. The length of the tool did not offer a good mechanical advantage, as the force exerted using the hand over the mixtures was limited by the grip strength (In this case the support grip over the tool was a disadvantage due to the short length thus the time and effort to apply a force over the powders was weakened and not effective), and a new tool (made of steel with a diameter of 20 mm and a length of 25cm, this gave an advantage over grip strength allowing longer operation times and good support.

Two images of the mixing tool are shown in Figure 3.6.

Figure 3.6 Images of a Ti6Al4V(ELI) tool used in manual mixing (a) length of tool, (b) diameter of tool

The powders were mixed in several steps. First, the CNTS were weighed, followed by the SDS weighing. Next, the two dry powders were mixed manually, followed by the addition of ethanol to the mixture and then further manual mixing. In this case, the SDS surfactant served to enhance the dispersion of CNTs when ethanol was added, followed by manual mixing. Thereafter, Ti6Al4V(ELI) powder was added to the mixture, followed by further manual mixing. This led to the formation of a slurry mixture. The mixture was then placed on zirconium plates and thereafter oven-dried at 200 °C.

© Central University of Technology, Free State

Following manual mixing, a turbula mixer was used to mix a fresh batch of powders (CNT+Ti6Al4V+SDS), and Ti6Al4V(ELI) spherical balls were added to the mixer to facilitate mixing. The spherical balls were additively manufactured using DMLS (Figure 3.7). Figure 3.8 shows the 10 spherical balls that were used for turbula mixing. The turbula mixing speed was set at 250 rpm for all the samples, as this allowed mixing to be carried out without spillage (Higher speeds at 350rpm caused powder to escape during rotation) of the powder and produced good mixtures.

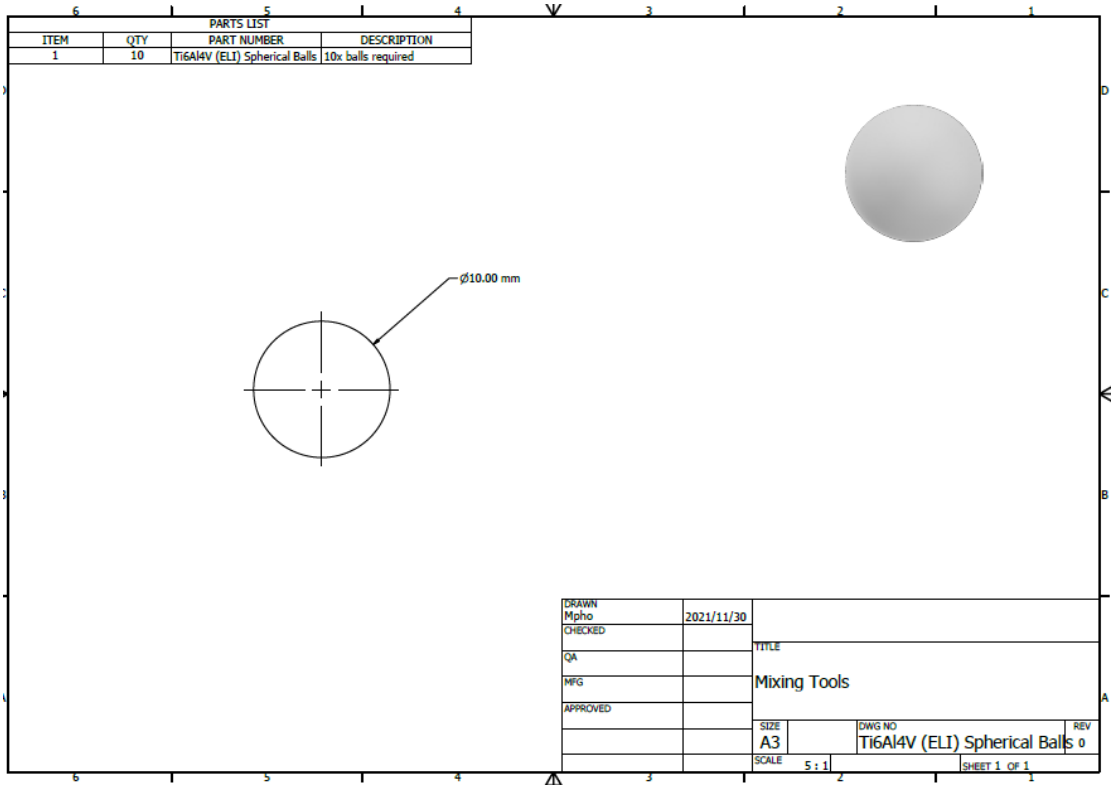

Figure 3.7 Design specification for steel balls

Spherical balls

of Ti6Al4V(ELI)

Figure 3.8 Ten Ti6Al4V (ELI) spherical balls

© Central University of Technology, Free State

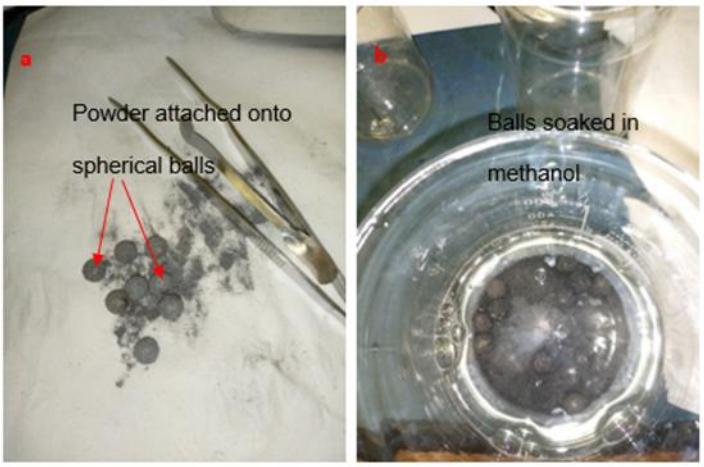

Figure 3.9 (a) Ti6Al4V(ELI) spherical balls with powder samples attached to their surfaces, (b) spherical balls soaked in methanol to remove powder residue from their surfaces

As the powder mixture attached to the Ti6Al4V(ELI) spherical balls during turbula mixing (this was caused by the rough finish surface due to support structures used during the AM process), as shown in Figure 3.9(a), the balls were soaked in methanol, as shown in Figure 3.9(b), to remove the powder and ensure that the mixing of other samples would not be affected by the left-over residue.

Turbula mixing was carried out in various steps, as depicted in Figure 3.10(a–c). First, the five spherical balls were placed one at a time inside the powder mixture, as shown in Figure 3.9(a & b). Then, each containers containing the powder samples with the Ti6Al4V(EI) balls were placed inside a larger container, which was then attached to the turbula mixer using cable ties, as shown in Figure 3.10(c). The turbula mixer was then set to run at a mixing speed of 250 rpm for 20 minutes.

Figure 3.10 Steps carried out to mix powder samples using a turbula mixer

© Central University of Technology, Free State

For all the different powders used that were mixed with different mixing techniques and at different volume fractions of CNTs, an analysis of the mixed powders was carried out upon completion of the mixing and drying process to determine the quality of the mixing. SEM was used to determine the homogeneity of the mixture and identify CNT fibres and agglomeration of CNTs in the powder samples. Analysis with EDX was used to identify various elements in the mixed powder samples. For all the SEM analyses conducted, the same magnification was utilised throughout to enable comparison of the different powder samples.

3.2 Developing a Test Matrix for Determining the Best Critical Process Parameters for CNT/Ti6AL4V(ELI) Composites

A simple experimental approach based on the known optimum critical process parameters of Ti6Al4V(ELI) on an M2 LaserCusing® machine from Concept Laser GmbH was used in developing a matrix for optimisation of the critical process parameters for the CNT/Ti6Al4V(ELI) composite. In this approach, first, the laser power was kept constant, and the scanning speed varied above and below the optimum value for Ti6Al4V(ELI). Then, the scanning speed was kept constant, and the laser power varied above and below the optimum value for Ti6Al4V(ELI). Table 3.3 represents the matrix that was developed from this approach for each laser power with varying scanning speeds below and above the optimum value.

Table 3.3 A matrix for use to determine the optimum process parameters of laser power and scanning speed based on an optimum area energy density of the alloy

Power (P) (W)	Scanning speed (v) (m/s)	Layer thickness (t) (µm)	Laser spot diameter (d) (µm)	Area Energy density $(E_v = P/vt)$ (J/mm^2)
60	0.2	50	150	10
	0.3	50	150	6.67
	0.4	50	**150**	5
	0.5	50	150	4
	0.6	50	150	3.33
80	0.3	50	150	8.89
	0.4	50	150	6.67
	0.5	50	**150**	5.33
	0.6	50	150	4.44

© Central University of Technology, Free State

	0.7	50	150	3.81
100	0.4	50	150	8.33
	0.5	50	150	6.67
	0.6	50	**150**	5.55
	0.7	50	150	4.76
	0.8	50	150	4.17
120	0.5	50	150	8
	0.6	50	150	6.67
	0.7	50	**150**	5.71
	0.8	50	150	5
	0.9	50	150	4.55
140	0.7	50	150	6.67
	0.8	50	150	5.83
	0.9	50	**150**	5.18
	0.1	50	150	4.67
	1.1	50	150	4.24
160	0.8	50	150	6.67
	0.9	50	150	5.92
	0.1	50	**150**	5.33
	1.1	50	150	4.84
	1.2	50	150	4.44
180	0.9	50	150	6.67
	1	50	150	6
	1.1	50	**150**	5.54
	1.2	0.05	150	5
	1.3	0.05	150	4.61

The known optimum process parameters of laser power, scanning speed, and powder layer thickness for Ti6Al4V(ELI) produced with an M2 LaserCusing® of 100 W, 0.6 ms^{-1}, and 50 μm, respectively, were used to calculate the optimum area energy density of the alloy (since single tracks are built, the hatch spacing is not taken into account). The layer thickness was adjusted to 50 μm, as the layer thickness of 30 μm was deemed insufficient based on tests carried out for levelling the powder. The optimum area energy density was then used to calculate values of scanning speed for each selected value of laser power in the range of 60 W and 180 W. The scanning speeds in the matrix were then set to vary by 0.1 ms^{-1} in two stages, above and below the calculated values of scanning speed, for each value of laser power. Values of volumetric energy density were then calculated for each value of scanning speed, with the results shown in Table 7.2.

For the optimum laser power for Ti6Al4V(ELI) of 100 W, values of laser power between 60 W and 180 W were selected. Five scanning speeds were varied between the extreme values of 0.2 ms^{-1} and 1.2 ms^{-1} m based on the optimum scanning speed for

© Central University of Technology, Free State

Ti6Al4V(ELI) of 0.6 ms^{-1}. Values of linear power density for each combination of laser power and scanning speed were calculated and inserted in the table.

In Table 3.3, the starting values of scanning speeds for the composite at different values of laser power are presented in bold. Tracks of the composites printed using the process parameter sets in this table were then analysed to determine which set amongst them led to the best acceptable track.

The test matrix developed from this approach was then used to print single tracks, whose surface and cross-sectional features were then studied. The outcome of these studies was then used to identify the best scanning speeds and laser powers for the additively manufactured CNT/Ti6Al4V(ELI) nanocomposite with a volume fraction CNTs of 3% in the first run. The results from this first run were then used to optimise the test matrices of the remaining volume fractions of reinforcement, and the foregoing process was repeated to determine the best critical process parameters for each volume fraction of CNTs.

3.3 Other Equipment and Analysis

The other equipment used in the present work included an M2 LaserCusing® SLM machine for printing the single tracks, an electrical discharge machine for wire-cutting the built tracks into cross-sections for analysis, as well as an optical microscope (OM) for analysing the top surfaces of tracks and their cross-sections.

3.3.1 The AM Machine Used to Build Single Tracks

The specifications of the M2 LaserCusing® SLM machine used to produce single tracks are described in Table 3.2. Figure 3.10 and Figure 3.11 depict the M2 LaserCusing® machine's exterior and interior build platform, respectively.

Table 3.4 Specifications of the M2 LaserCusing® machine

Build volume	250 x 250 x 280 mm (x,y,z)
Selectable powder layer thickness	0.02 mm (20 µm) to 0.05 mm (50 µm)
Print speed	2–20 cm^3/h (depending on the material)
Laser system	Fibre laser 200 W
Maximum scanning speed	7000 mm/s
Focus diameter of the laser beam	70–200 µm
Materials that can be built with the machine	Ti6Al4V, stainless steel 316, Maraging steel
Type of inert gas used in the machine	Nitrogen or argon

© Central University of Technology, Free State

Figure 3.11 Laser M2 LaserCusing® machine

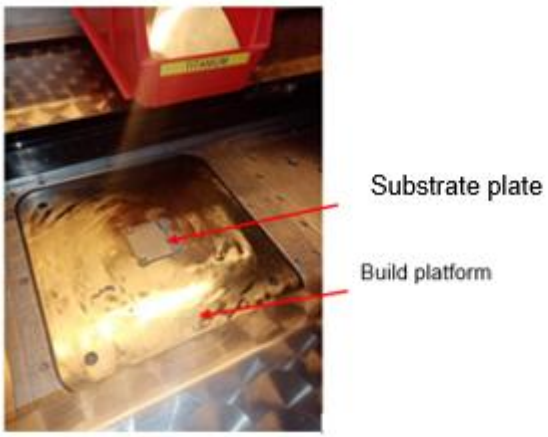

Figure 3.12 M2 LaserCusing® machine build platform with a substrate plate

3.3.2 Wire-Cutting to Avail Cross-Sections of the Built Tracks for Inspection

Cross-sections of the single tracks that were printed were cut out using the Accutex 500iA wire electric discharge machine (EDM), making use of a 0.25 mm brass wire to cut through metals by means of an electrical erosion process. An image of the wire cutting machine is presented in Figure 3.12.

© Central University of Technology, Free State

Figure 3.13 Accutex 500i wire cutting machine

The procedure that was used for wire cutting of the built single tracks in this work is shown in Figure 3.13 (1–3).

1. Separate the substrate into two pieces (1 & 2), along the red line, as shown in Figure 3.14(a).

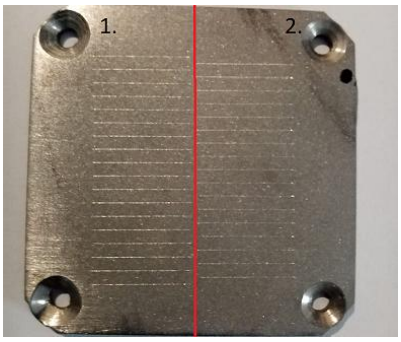

2. Cut pieces 1 & 2 into two halves each, along the orange and green lines shown in Figure 3.14(b), respectively. Make sure that the cuts are done in-between the printed tracks. Also ensure that the length (L) of each resultant quadrant cut out is less than 30 mm long.

© Central University of Technology, Free State

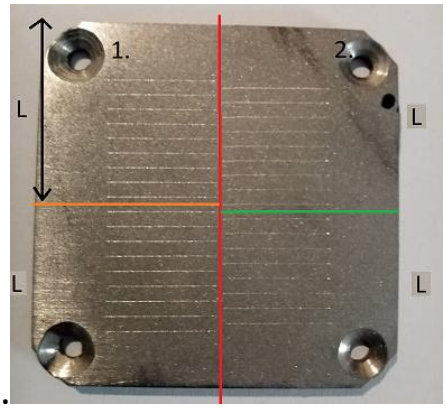

3. Lastly section each quadrant along the half length of the single tracks in each one of them, as shown by the black lines in Figure 3.14(c).

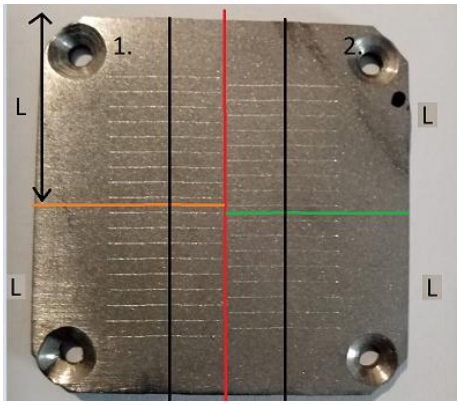

Figure 3.14 Sectioning of the single tracks built on substrates

3.3.3 Sample preparation for metallographic preparation

Preparation of samples for the purpose of the metallographic analysis was carried out using first, hot mounting of specimens, followed by polishing of their top surfaces and finally, etching of these surfaces. Hot mounting was carried out using a Struers CitoPress-1 machine (Figure 3.15). The specifications of the Clarofast resin used for this mounting are presented in Table 3.5. Other resins, including ConduFast, DuroFast, IsoFast, LevoFast, and MultiFast can be used on this machine for the same purpose. As none of them were used in this work, their specifications were left out of Table 3.5.

Table 3.5 Specification for hot mounting of specimens using ClaroFast resin

Diameter of the cylinder (inches)	Type of resin	Heating	Cooling	Time

© Central University of Technology, Free State

1 ¼	Type	Quantity (ml)	Time [min]	Temp. [°C]	Pressure [bar]	Time [min]	Rate	Total time [min]
	Clarofast	20	4	180	350	6.5	Low	10.5

Mounting of the specimens was carried out as follows:

- The sectioned specimens were placed on the base, with the diameter specified in Table 3.5, as indicated in Figure 3.14(b)
- The base was then lowered slightly to allow for pouring of the resin
- The base was lowered completely thereafter, and the heating and cooling parameters were set according to the details shown in Table 3.5
- Upon completion of the hot mounting process, the specimens were removed from the base.

Figure 3.15 shows a specimen on the base, after hot mounting.

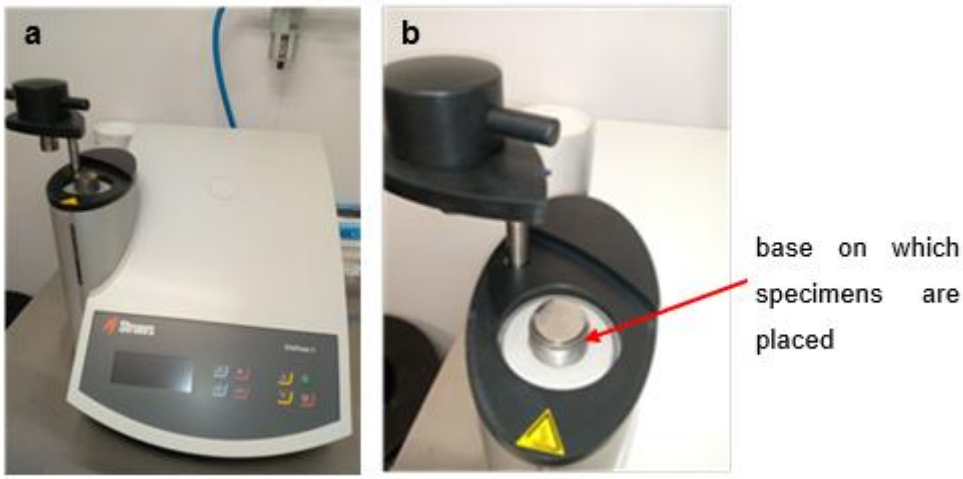

Figure 3.15 Struers CitoPress machine for hot mounting

Figure 3.16 presents several specimens after completion of hot mounting.

© Central University of Technology, Free State

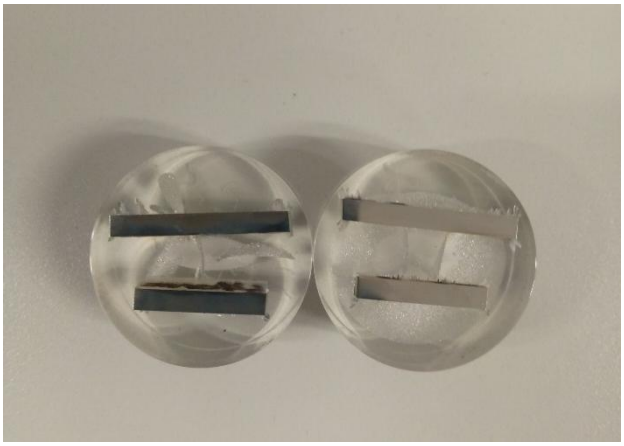

Figure 3.16 Specimens after hot mounting

Following the hot mounting process, the specimens were ground and polished according to the procedure presented in Table 3.6.

Table 3.6 Specifications for grinding and polishing of specimens

		Plane grinding	Fine grinding	Chemical polishing
Surface		Foil/paper	MD-Largo	MD-Chem
Abrasive	**Type**	SiC	Diamond	Colloidal silica
	Grain Size	320	9 µm	0.04 µm
Suspension/lubricant		Water	Diapro Allegro/Diapro-9	Diapro Allegro/Diapro-9
Speed (rpm)		300	150	150
Force [N]/specimen		15	20	20
Time (min)		10	5	5

The equipment used in this procedure is the Struers Tegramin-ZS shown in Figure 3.17 (a, b), an automatic microprocessor-controlled machine for grinding and polishing on a 300 mm diameter MD-disc. The head, indicated by the red arrow in Figure 3.17(a), is able to accommodate a maximum of six specimens. Firstly, plane grinding of specimens was carried out, followed by fine grinding. For plane grinding, silicon carbide paper was used, the MD largo disc was used for fine grinding, and the MD Mol and MD Chem discs were used for chemical polishing. The different discs for grinding and polishing are presented in Figure 3.17(c). The settings for plane grinding were used with the MD Mol disc.

© Central University of Technology, Free State

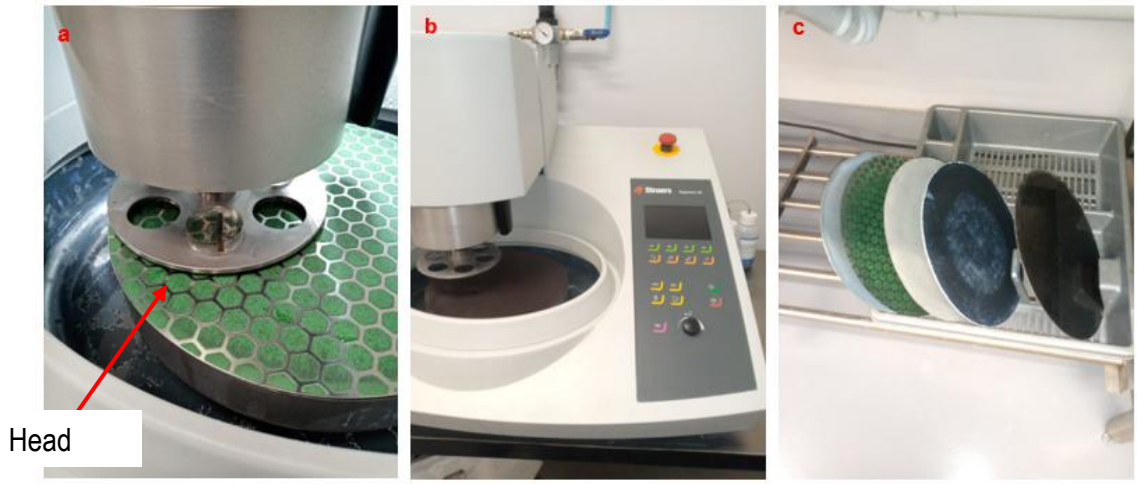

Figure 3.17 Equipment used for the preparation of metallographic specimens

Etching of the samples to reveal their features for cross-sectional analysis was carried out using Kroll's reagent (Figure 3.18(b)) under an Esco Ascent·MAX ventilated hood (Figure 3.18(a)).

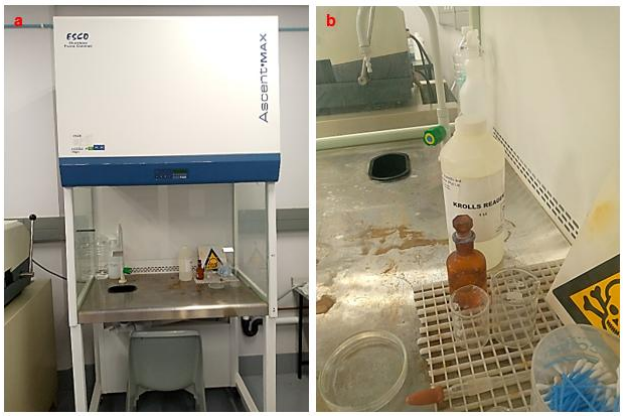

Figure 3.18 Equipment and material used for etching of specimens

3.3.4 Optical Microscope for Analysis of the Top Surfaces of Tracks and Their Cross-Sections and for SEM Analysis of the Mixtures of Powder

The Zeiss Merlin field emission (FE) SEM equipment (Figure 3.19) combines ultra-fast analytics, high-resolution imaging and specifications of voltage of 20 V to 30 kV, beam currents of 7 pA to 40 nA, as well as resolutions of up to 0.6 nanometres at 30kV and 1.6 nanometres at 1kV. It has a number of detectors for imaging, including in-lens and chamber secondary (SE) detectors (nano and micron-scale imaging), an in-column energy selective backscattered (ESB) electron detector, a retractable 5-diode backscattered electron detector (BSD) (nano-BSE & 5-diode detector nano to micron

© Central University of Technology, Free State

imaging), cathodoluminescence (CL) detector and a scanning transmission electron microscopy (STEM) detector with a resolution of 0.6 nanometre.

Figure 3.19 ZEISS (FE SEM) machine

Sample preparation for SEM analysis was carried out as follows:

- Stubs were cleaned using a sonic bath cleaner to remove dirt from their surfaces
- Thin strips of carbon paper were then placed on the stubs
- Thereafter, the strips of carbon were coated with powder from the mixture, which was then placed in a plastic container to prepare for analysis.

The SEM equipment allows the insertion of up to 12 stubs, which allows for faster processing of many samples.

Figure 3.20 presents the prepared stubs for the mixtures prepared in the initial experiments: for dispersion with acetone and ethanol and for manual mixing of dry powders.

© Central University of Technology, Free State

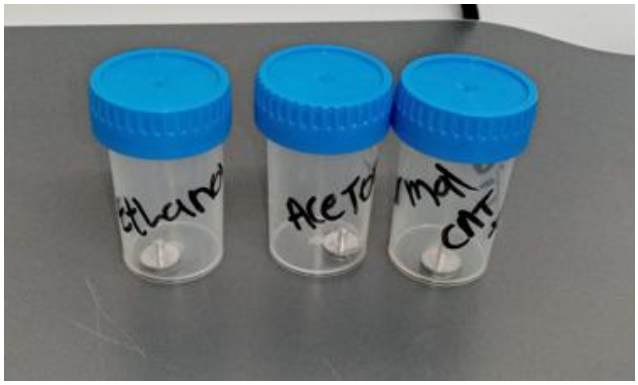

Figure 3.20 Stubs for SEM analysis

The ZEISS AXIO optical microscope A.1, shown in Figure 3.21, was used to obtain images of the top views and cross-sections of the built single tracks. The microscope has magnifications of 5x, 10x, 20x, and 50x.

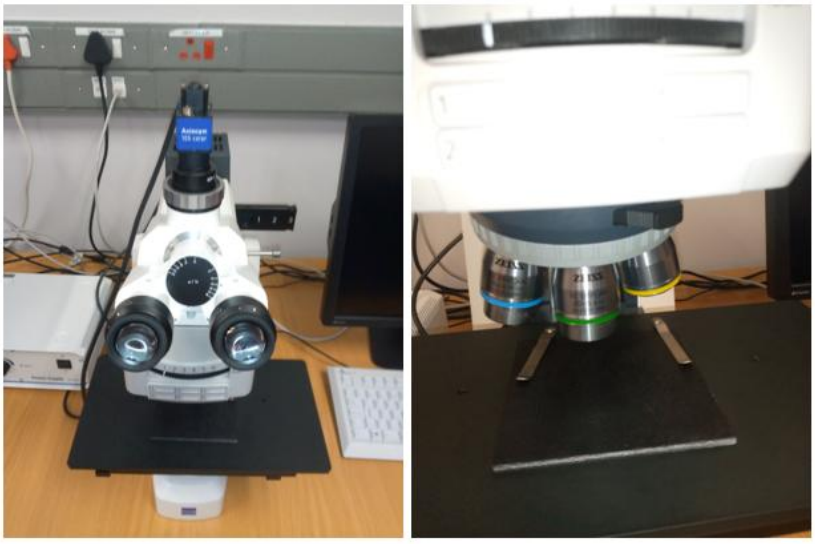

Figure 3.21 ZEISS AXIO optic microscope

3.4 Conclusion

This chapter detailed the methodology pertaining to preliminary, secondary, and tertiary mixing. It briefly discussed the process of obtaining preliminary best critical process parameters. The procedure used to prepare samples for metallographic examination was also discussed, and the details of the equipment used were presented.

© Central University of Technology, Free State

References

1. Khoza, P.B., Moloto, M.J. and Sikhwivhilu, L.M., 2012. The effect of solvents, acetone, water, and ethanol, on the morphological and optical properties of ZnO nanoparticles prepared by microwave. *Journal of Nanotechnology*, *2012*(1), pp 1-6. https://doi.org/10.1155/2012/195106
2. Shojaeiarani, J., Bajwa, D. and Holt, G., 2020. Sonication amplitude and processing time influence the cellulose nanocrystals morphology and dispersion. *Nanocomposites, 6*(1), pp. 41–46.
3. Suárez, S., Reinert, L. and Mücklich, F., 2016. Carbon Nanotube (CNT)-Reinforced Metal Matrix Bulk Composites: Manufacturing and Evaluation, in Diamond and Carbon Composites and Nanocomposites. InTech. Available at: https://doi.org/10.5772/63886.
4. Suzuki, S. ed., 2013. Physical and Chemical Properties of Carbon Nanotubes. *Bod — Books on Demand*.
5. Liu, K.G., Abbasi, A.R., Azadbakht, A., Hu, M.L. and Morsali, A., 2017. Deposition of silver nanoparticles on polyester fiber under ultrasound irradiations. *Ultrasonics sonochemistry*, *34*, pp.13-18.
6. Roy, S., Petrova, R. S. and Mitra, S., 2018. Effect of carbon nanotube (CNT) functionalization in epoxy-CNT composites. *Nanotechnology Reviews*, *7*(6), pp. 475–485. https://doi.org/10.1515/ntrev-2018-0068
7. Kumar, M. S., Selvan, C. P., Santhanam, K., Kadirvel, A., Chandraprabu, V. and SampathKumar, L., 2022. Effect of nanomaterials on tribological and mechanical properties of polymer nanocomposite materials. *Advances in Materials Science and Engineering*, *2022*(*1*), pp. 2165855.
8. Raza, A., Salmi, A., El Ouni, M. H., Shabbir, F., Ghazouani, N., Ahmed, B., Ali, M. R. and Hendy, A. S., 2024. A comprehensive review on material characterization and thermal properties of geopolymers: potential of various fibres. *Case Studies in Construction Materials*, pp. e03519.
9. Ogunmefun, O. A., Bayode, B. L., Jamiru, T. and Olubambi, P. A., 2023. A critical review of dispersion strengthened titanium alloy fabricated through spark plasma sintering techniques. *Journal of Alloys and Compounds*, *960*, pp. 170407.

© Central University of Technology, Free State

CHAPTER 4 - PRELIMINARY MIXING OF CNTS AND TI6AL4V(ELI) POWDERS

Some of the material contained in this chapter has been published in peer-reviewed conference proceedings as follows:

1. **Mpho Mashabela, Maina Maringa and Thywill Dzogbewu**, "Examining Various Mixing Techniques and their Effect on the Uniform Dispersion of Carbon Nanotubes within a Ti6Al4V (ELI) Matrix", Rapid Product Development Association of South African (RAPDASA)-RobMech-PRASA) 22nd Annual International Conference, Pre-Conference Seminar on Design and Additive Manufacturing of Titanium Parts, 02-05 November 2021, Hosted by the Central University of Technology, Free State (CUT), Venue: CSIR International Convention Centre, Pretoria Tuesday 2nd November 2021, Japie van Lill Hall, Central University of Technology, Free State, South Africa, https://site.rapdasa.org/pre-conference-seminar/. Accepted for publication in the IEEE Xplore edition of March 2022.

4.0 Summary

Mixing of CNTs and Ti6Al4V(ELI) powders at a 3 % and 8 % vol. of CNTs in Ti6Al4V(ELI) was done to test three different methods of mixing in order to determine their suitability. These were the manual mixing of dry powders and the use of two dispersants, acetone and ethanol, used separately, with sonication and magnetic stirring applied. Sonication, ethanol, and acetone, as well as manual mixing and magnetic stirring, were all used to facilitate the deagglomeration and dispersion of CNTs in order to improve the homogenisation of the two powders. The study showed that the use of ethanol and acetone as dispersants provided better dispersion of CNTs in Ti6Al4V(ELI) than manual mixing (of dry powders without the use of ethanol and acetone). on its own. The use of acetone led to slightly fewer CNT agglomerates that were also smaller in size compared to ethanol. The formation of agglomerates for all three methods of mixing used here implied that more vigorous agitation techniques would be required to break down the strong van der Waal forces between CNTs in order to achieve effective dispersion.

4.1 Introduction

The literature shows that no single technique can be used on its own to achieve dispersion of CNTs in a matrix. In most cases, a combination of techniques is used to achieve dispersion of reinforcements and homogeneity of powder mixtures. Dispersion agents are usually low-molecular-weight materials that strongly adsorb onto particles and thus form a repulsive barrier against the attraction forces that exist between all particulate materials. Though solvents cause some dispersion of CNTs, this is of little effect, and other techniques are also required.

© Central University of Technology, Free State

4.2 Scanning Electron Microscopy Images of 3 % vol. of CNTs in Ti6Al4V(ELI) That Were Mechanically Mixed

Figure 4.1 (a–b) presents SEM images for a 3 % vol. of CNTs in TI6AI4V(ELI) that were mixed mechanically.

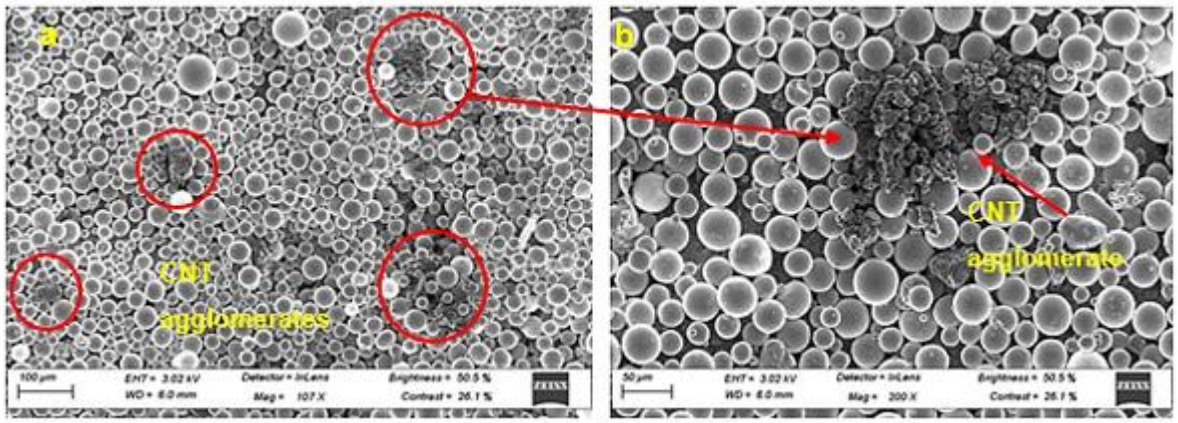

Figure 4.1 Scanning electron microscope image of 3 % vol. CNTs in Ti6Al4V(ELI) where only manual mixing was applied

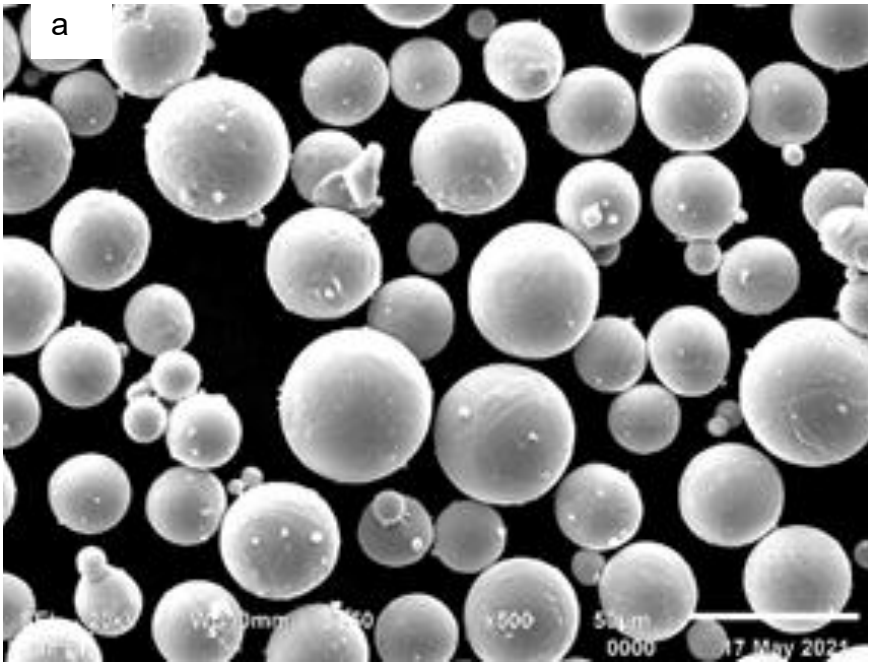

© Central University of Technology, Free State

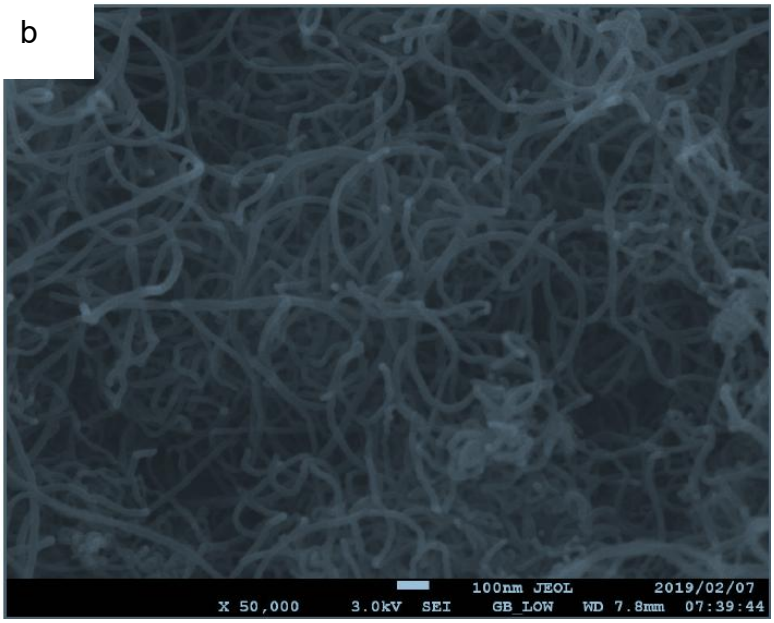

Figure 4.2 Scanning electron microscopy of un-mixed powders of (a) Ti6Al4V(ELI) particles at 5000x and (b) CNTs at 50 000x

Figure 4.1 shows the morphology of powders that were mixed manually in the present work. It shows that this mixing technique achieved poor dispersion and that 10 minutes of mixing did not suffice. This is thought to be a result of the strong van der Waals forces between the CNTs, which would not allow them to disperse within the Ti6Al4V(ELI) (spherical particles in the figures). The presence of dispersed CNT agglomerates in Ti6Al4V(ELI) is indicated by the red circles in Figure 4(a), while Figure 4(b) shows a magnified view of one such CNT agglomerate in the mixture. The presence of CNT agglomerates in certain parts of the mixture shows that effective dispersion using manual mixing was not achieved. From the micrographs in Figure 4.1(a and b), it was impossible to determine whether the CNTs within the agglomerates were separated or remained entangled after manual mixing. It is evident, therefore, that this mixing technique was not successful in achieving the de-agglomeration of the CNTS and in delivering dispersion of CNTs in Ti6Al4V to achieve a homogenous mixture.

Figure 4.2 (a-b) provides SEM images of un-mixed Ti6Al4V powders and CNTs. From Figure 4.2(a) it is observed that irregular and satellite particles are present in Ti6l4V(ELI) spherical particles. It is also observed in Figure 4.2 (b) that CNT tubes are visible at high magnifications, in this case at 50 000x.

© Central University of Technology, Free State

The area and perimeter of the agglomerate shown in Figure 4.1(b) were measured using the method of continuous analysis in an image analysis software with an area and perimeter of $823.008\ \mu m^2$ and $121.678\ \mu m$, respectively, now shown in a zoomed-in image in Figure 4.3. This was the largest agglomerate in the sample.

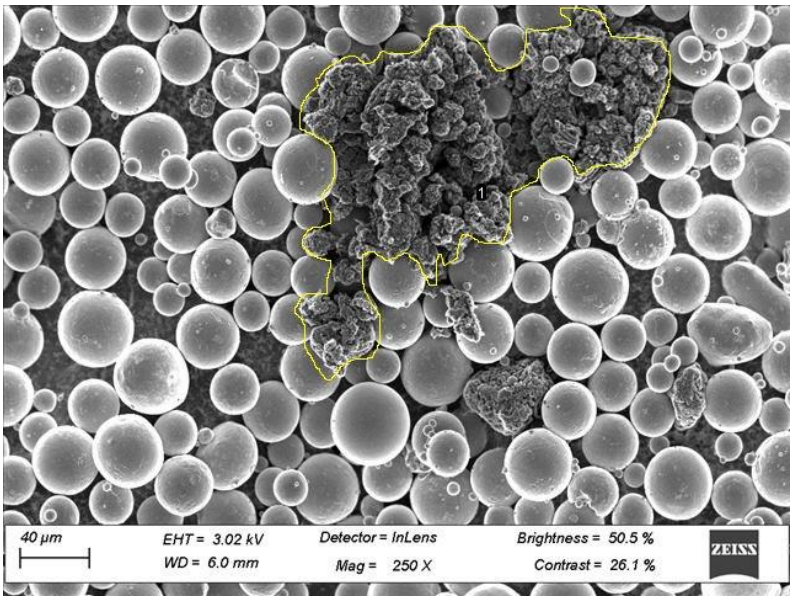

Figure 4.3 Zoomed-in image for measurements of length and perimeter of the CNT agglomerate shown in Figure 4.1(b)

However, measurements of the areas and perimeters of eight other agglomerates, shown in Figure 4.4 using the method of continuous analysis in an image analysis software, obtained from elsewhere in the mixture, generated the values shown in Table 4.1, amongst which the largest agglomerate measured an area and perimeter of 12640.055 μm^2 and 577.277 μm, respectively. The table also contains values of average (Avg), standard deviation (Stdev), and coefficient of variance (CoV) for the measured values of area and perimeter. The rightmost column in the table gives values of the ratios of diameters calculated from circles with equal areas and perimeters to those given in the table.

© Central University of Technology, Free State

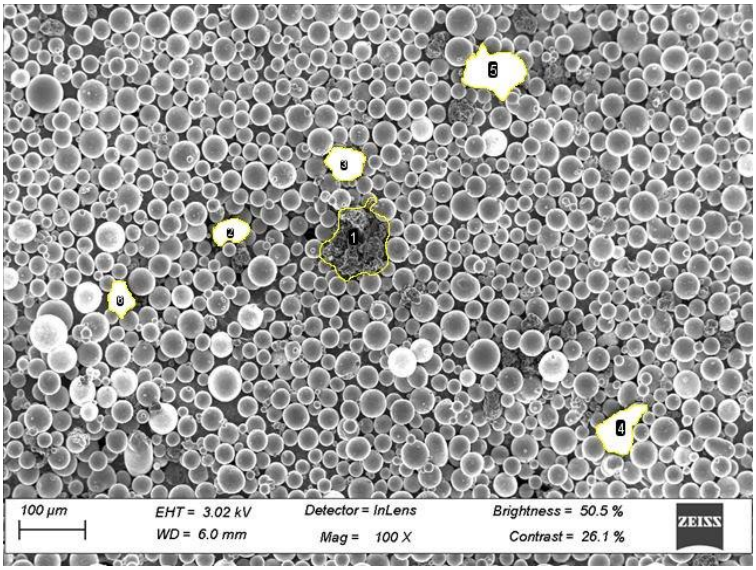

Figure 4.4 Agglomerates of CNTs whose lengths and perimeters were measured

Table 4.1 Measured areas and perimeters of eight CNT agglomerates with a 3 % vol. of CNTs in Ti6Al4V(ELI) manual mixed sample

Area (μm^2)	Perimeter (μm)	Diameter – D_a (μm)	Diameter – D_p (μm)	Ratio of diameters (D_p/D_a)	
8552	405	104	129	1.237	
1581	161	44	51	1.146	
2257	186	53	59	1.105	
3191	246	63	78	1.233	
4862	307	78	97	1.243	
1466	170	43	54	1.253	
3652	246	64	78	1.203	Avg
2709	95	23	30	0.062	Stdev
74	38	36	38	5.124	CoV

* Subscripts *a* and *p* in this table refer to cross-sectional area and perimeter, respectively, while the symbol *D* stands for diameter.

Figure 4.5 shows the curve of measured values of the area of agglomerates versus their perimeters.

© Central University of Technology, Free State

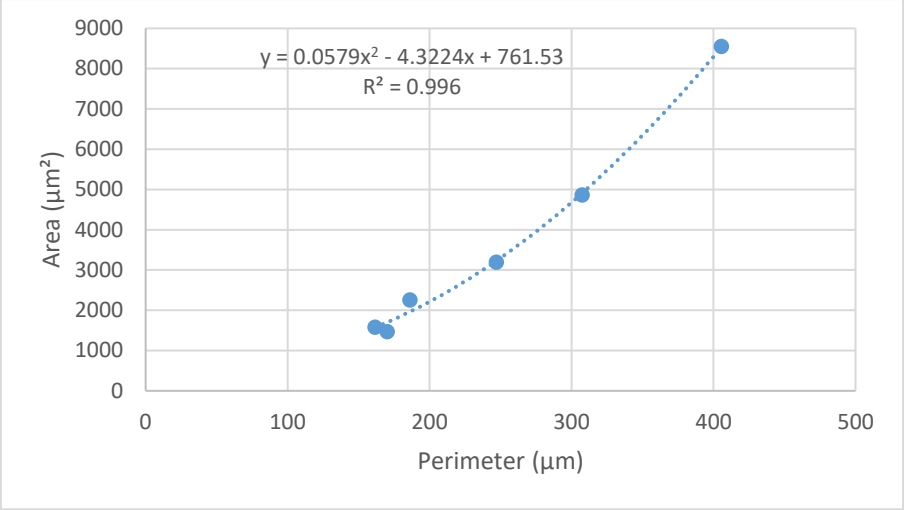

Figure 4.5 Plotted values of perimeter versus area of CNT agglomerates

The values of area and perimeter have an average, standard deviation and coefficient of variance (CoV) of 3652, 2709 and 74 for the area, respectively and for the perimeter of 246, 95 and 38, respectively. The very large values of CoV for the values of area and perimeter indicate a large dispersion of the two parameters from the means, which reduces the reliability of the calculated statistical values of the mean. The ratios of the diameters given in the rightmost column of the table are all greater than unity with an average, standard deviation and CoV of 1.203, 0.062 and 5.124. That the ratios of diameter are all greater than unity is a result of the irregularity of the perimeters of the agglomerates. The low value of CoV indicates good clustering of the data points around the mean, thus implying that the mean is a good statistic.

The correlation coefficient of 0.996, seen in Figure 4.5, is very high and denotes a good correlation between the plotted values and the fitted curve. Visual observation of the figure shows clustering of CNT agglomerates at the lower magnitudes of areas and perimeters and a wide spread of single values at the higher magnitudes of areas and perimeters.

4.3 Scanning Electron Microscopy Images of a 3 % vol. of CNTs in Ti6Al4V(ELI), in Which the CNTs Were Dispersed in Ethanol

Figure 4.5 (a-b) shows micrographs of mixed CNTs and Ti6Al4V(ELI) powders, the former of which were dispersed in ethanol, sonified, and stirred magnetically.

© Central University of Technology, Free State

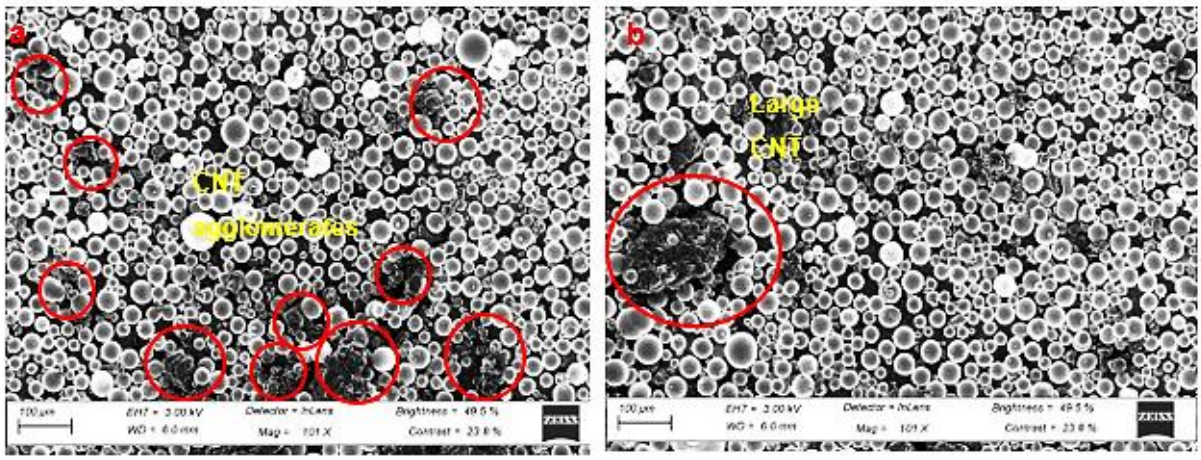

Figure 4.6 SEM micrographs of a 3 % vol. of CNTs in Ti6Al4V(ELI), in which the CNTs were dispersed in ethanol

Ethanol was used as a dispersion agent to aid in separating the CNTs, followed by sonication. Thereafter, magnetic stirring was applied to the mixture. The micrographs show the presence of agglomerated CNTs within the Ti6Al4V and imply that the process was not effective in breaking down the CNT bundles as was desired. Measurements of the areas and perimeters of some of the CNT agglomerates in Figure 4.5a, shown in Figure 4.6, were obtained using the continuous analysis method in an image analysis software for comparison with similar measurements for the agglomerates found in the previous case of manual mixing. These measured values, as well as calculated values of Avg, Stdev and CoV, are shown in Table 4.2. The table also shows calculated values of the diameter of the agglomerates for circles with equal values of area and perimeter to those given in the table and their ratios.

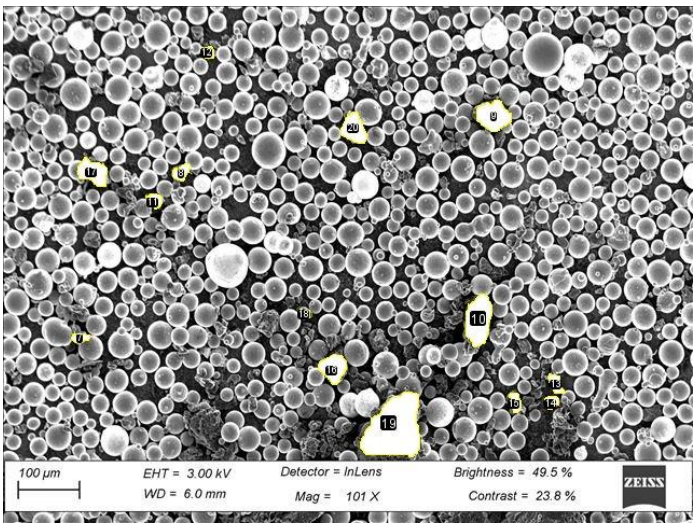

Figure 4.7 Agglomerates of CNTs whose values of area and perimeter were measured

© Central University of Technology, Free State

Table 4.2 Measured values of areas and perimeters of CNT agglomerates for a 3 % vol. of CNTs in Ti6Al4V(ELI), mixed as detailed above

Area (μm^2)	Perimeter (μm)	Diameter – D_a (μm)	Diameter – D_p (μm)	Ratio of diameters (D_p/D_a)	
1466	170	43	54	1.253	
344	77	20	24	1.180	
526	97	25	31	1.205	
2063	175	51	55	1.088	
2799	214	59	68	1.145	
369	87	21	28	1.277	
338	69	20	22	1.068	
522	107	25	34	1.324	
344	73	20	23	1.111	
404	87	22	28	1.230	
1511	147	43	47	1.066	
1514	158	44	50	1.148	
165	51	14	16	1.124	
7531	350	98	111	1.138	
1466	153	43	49	1.132	
1421	131	45	43	1.102	Avg
1931	78	25	21	0.266	Stdev
130	57	57	50	6.261	CoV

The values shown in Table 4.2 were plotted in Figure 4.8 to explore the manner in which the two values are related to one another.

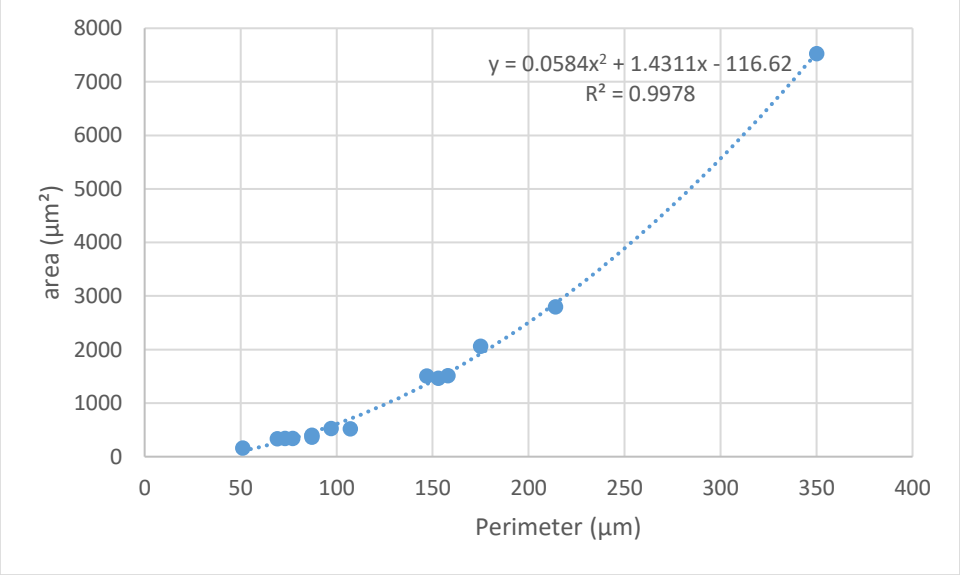

Figure 4.8 Plotted values of perimeter versus area of CNT agglomerates

The values of area and perimeter in Table 4.2 have an Avg, Stdev and CoV of 1421, 1931 and 113 for the area, respectively and for the perimeter of 131, 78 and 57, respectively. The very large values of CoV for the area and perimeter indicate large

© Central University of Technology, Free State

dispersions from the mean for the two parameters, which reduces the reliability of the calculated statistical values of the mean. The ratios of the diameters given in the rightmost column of the table are all greater than unity with an Avg, Stdev and CoV of 1.405, 0.073 and 6.261. The fact that the ratios of diameter are all greater than unity is a result of the irregularity of the perimeters of the agglomerates. The low value of CoV indicates good clustering of the data points around the mean, thus implying that the mean is a good statistic.

Figure 4.8 shows clustering of values of area and perimeter of the agglomerates towards the lower magnitudes of both parameters and a wide spread of single values for the higher magnitudes of area and perimeter. The high correlation coefficient of 0.9879 in this figure denotes a good correlation between the plotted points and the curve fitted to them.

4.4 Scanning Electron Microscopy Images of a 3 % vol. CNTs in Ti6Al4V(ELI), in Which the CNTs Were Dispersed in Acetone

Figure 4.8 (a–d) shows micrographs of mixed CNTs and Ti6Al4V(ELI) powders, in which the CNTs were dispersed in acetone, then sonified and stirred magnetically.

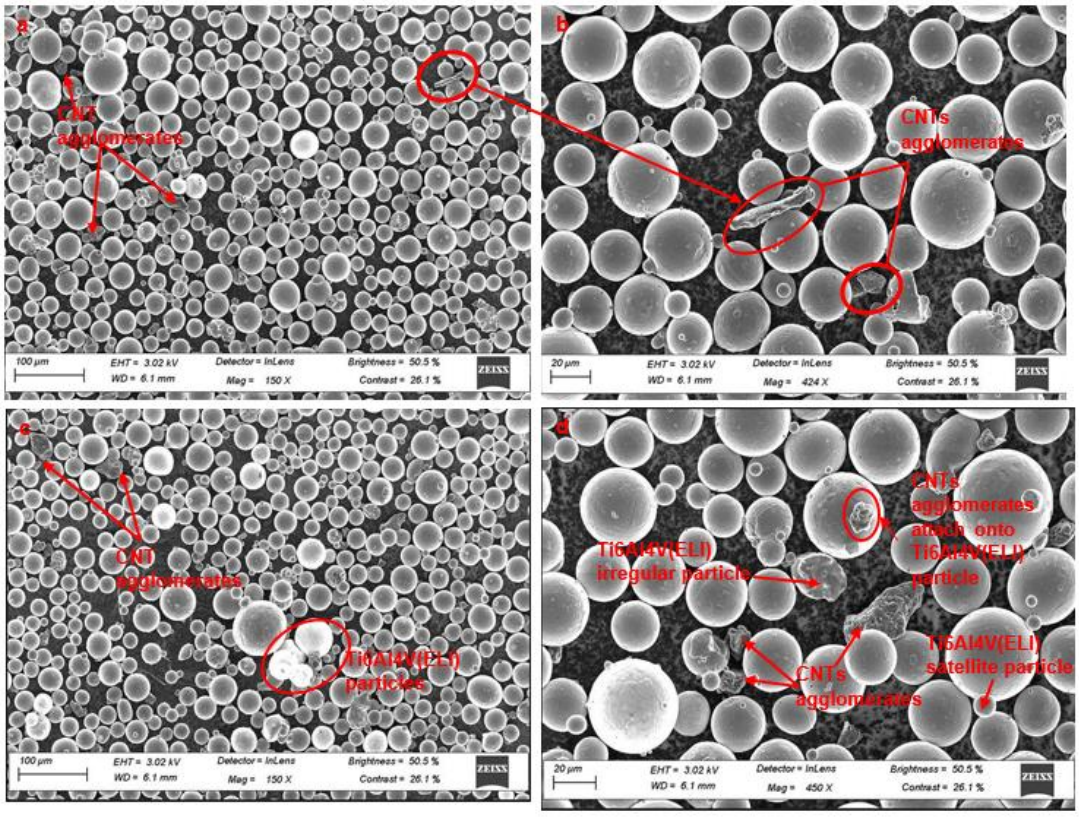

Figure 4.9 SEM micrographs of a CNTs/Ti6Al4V(ELI) powder mixture where acetone was used to disperse the CNTs

© Central University of Technology, Free State

In Figure 4.9(a), not much detail can be observed apart from the CNT agglomerates (circled in red), which is further magnified in Figure 4.9(b,) and other agglomerates are shown. In Figure 4.9(b), the CNT agglomerate that is shown has an almost rectangular shape, which is different from the other agglomerates in the sample. In Figure 4.9(b and c), Ti6Al4V(ELI) satellite particles, CNT attachment on Ti6Al4V(ELI) particle, and three Ti6Al4V(ELI) particles (circled in red) are visible.

Measurements of the areas and perimeters of some of the CNT agglomerates in Figure 4.9(a), shown in Figure 4.10, were obtained using the method of continuous analysis in an image analysis software, for comparison with similar measurements for the agglomerates found in the previous case of ethanol and manual mixing. These measured values, as well as calculated values of Avg, Stdev and CoV, are shown in Table 4.3. The table also shows calculated values of the diameter of the agglomerates for circles with equal values of area and perimeter to those given in the table and their ratios.

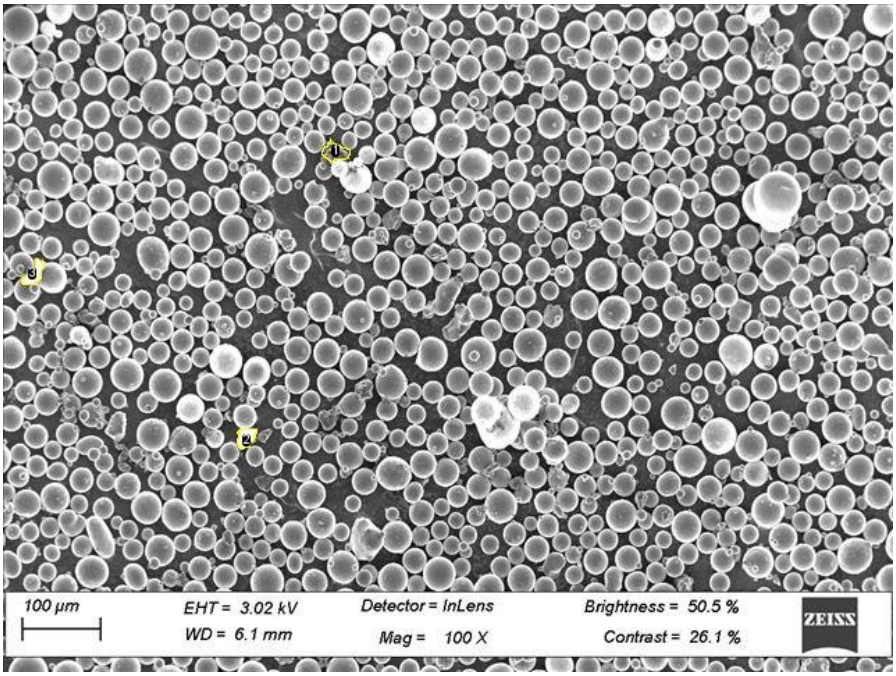

Figure 4.10 SEM micrographs of a CNT/Ti6Al4V(ELI) powder mixture, with three identified agglomerates

The values of the areas and perimeters of the three agglomerates identified in Figure 4.8(c) were obtained using the continuous analysis image software and areas presented in Table 4.3. Figure 4.10 presents a plot of these values.

© Central University of Technology, Free State

Table 4.3 Measured areas and perimeters of CNT agglomerates for 3 % vol. of CNTs in Ti6Al4V(ELI), mixed as detailed above

Area (μm^2)	Perimeter (μm)	Diameter – D_a (μm)	Diameter – D_p (μm)	Ratio of diameters (D_p/D_a)	
589	105	27	33	1.219	
465	90	24	28	1.176	
468	98	24	31	1.276	
508	97	25	31	1.224	Avg
70.898	7	1	2	0.050	Stdev
13.954	7	6	7	4.080	CoV

The values shown in Table 4.3 were plotted in Figure 4.10 to explore how the two values are related. The measured values of perimeter and area are also plotted in Figure 4.10 to tease out any trends in them.

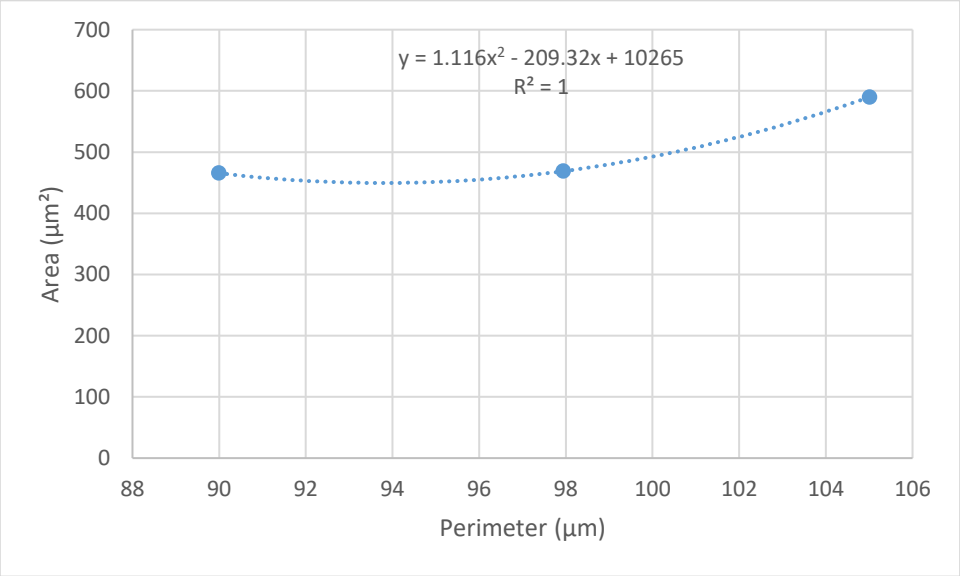

Figure 4.11 Plotted values of perimeter versus area for CNT agglomerates

The values of area and perimeter in Table 4.3 have an Avg, Stdev and CoV of 508.078, 70.898 and 13.954 for the area, respectively and a perimeter of 97.643, 7.511 and 7.693, respectively. In comparison to the values for the same parameters in the previous two tables, these values are modest. The much lower values of CoV for the area and perimeter in this table indicate lower dispersions from the mean for the two parameters and, thus, higher reliability of the calculated statistical values of the mean in this case. The ratios of the diameters given in the rightmost column of the table are

© Central University of Technology, Free State

all greater than unity with an Avg, Stdev and CoV of 1.224, 0.050 and 4.080. Ratios of diameters that are higher than unity denote irregularity of the perimeters of the agglomerates. The low value of CoV indicates good clustering of the data points around the mean, thus implying that the mean is a good statistic.

The small data set is not enough to draw trends from the sample. However, the differences in the values of area and perimeter for the three agglomerates are small.

4.4.1 Comparative Analysis of the three Methods of Mixing

Figure 4.12 is a representation of the methods of mixing discussed in section 4.2, 4.3, and 4.4 for manual, ethanol and acetone respectively.

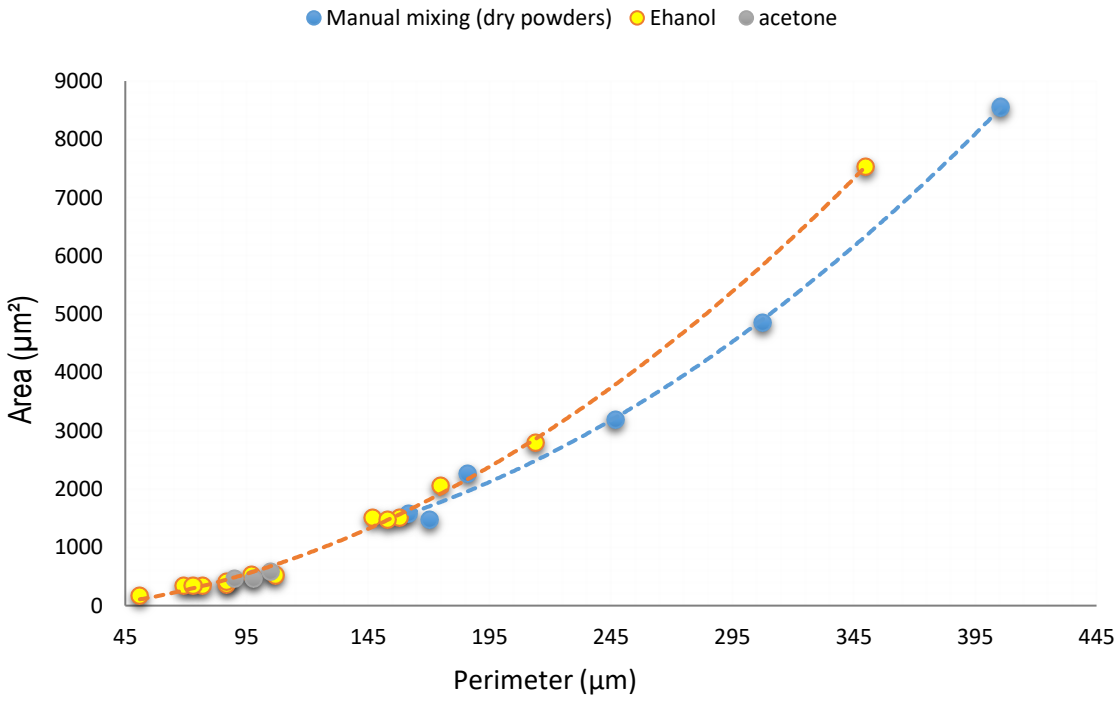

Figure 4.12 Comparison of the three methods of mixing

Figure 4.12 shows that for acetone and ethanol there is good dispersion and a decrease in agglomeration of CNTs. It is also observed that mechanical mixing produced larger agglomerates compared to the two other methods. This was a preliminary test with fewer data sets and would need to be expanded to arrive at fool proof conclusions.

© Central University of Technology, Free State

4.5 Scanning Electron Microscopy Images of an 8 % vol. CNTs in Ti6Al4V(ELI), in Which the CNTs Were Dispersed in Ethanol

The resulting SEM images, given in Figure 4.13(a and b), investigated the effectiveness of ethanol as a dispersant at an 8 % vol.% of CNTs in Ti6Al4V(ELI).

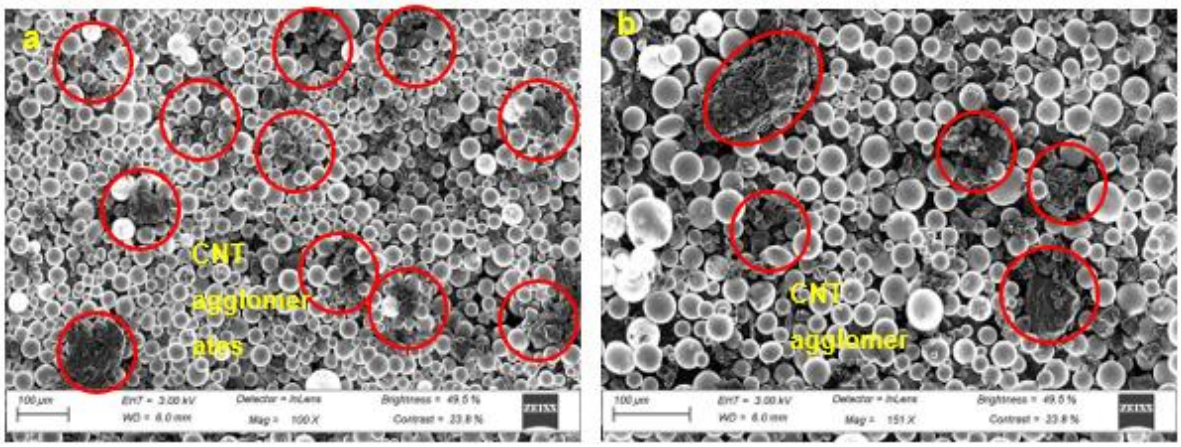

Figure 4.13 Scanning electron microscope image of an 8 % vol. CNTs in Ti6Al4V(ELI), in which the CNTs were dispersed in ethanol

It is evident from Figure 4.13(a) that there was an increased dispersion of CNT agglomerates in the powder mixture, given the high incidence of agglomerates indicated by the red circles. Figure 4.13(b) shows that these agglomerates were embedded between Ti6Al4V(ELI) particles.

The measured values of the areas and perimeters of the agglomerates shown in Figure 4.14 were taken from Figure 4.13(b) using the continuous analysis method in image analysis software. The measured values are shown in Table 4.4.

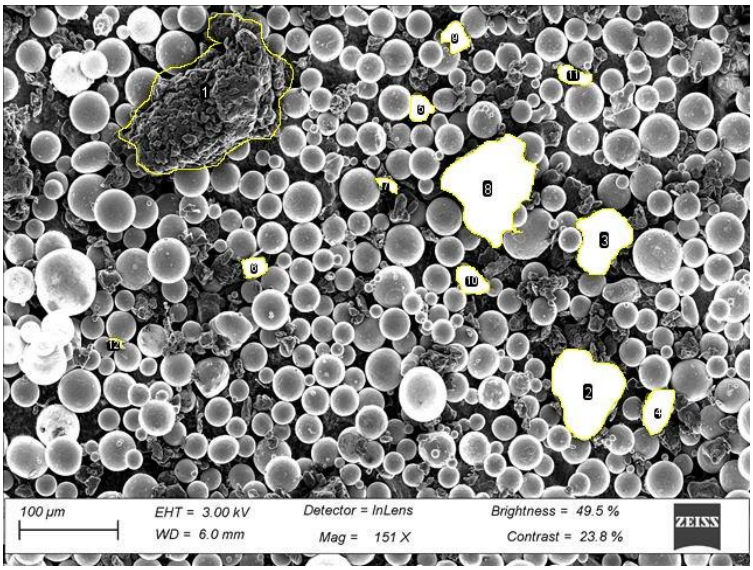

Figure 4.14 Agglomerates whose areas and perimeters were measured

© Central University of Technology, Free State

Table 4.4 shows the measured areas and perimeters of 12 CNT agglomerates identified in Figure 4.14.

Table 4.4 Measured areas and perimeters of 12 CNT agglomerates for an 8 % vol. of CNTs in Ti6Al4V(ELI)

	Area (μm^2)	Perimeter (μm)	Diameter – D_a (μm)	Diameter – D_p (μm)	Ratio of diameters (D_p/D_a)	
CNT_1	17077	579	147	184	1.251	
CNT_2	4669	275	77	87	1.138	
CNT_3	2652	218	58	69	1.195	
CNT_4	1086	137	37	43	1.176	
CNT_5	486	86	24	27	1.110	
CNT_6	412	78	22	25	1.094	
CNT_7	187	62	15	19	1.278	
CNT_8	6595	371	91	118	1.289	
CNT_9	587	103	27	32	1.202	
CNT_{10}	681	102	29	32	1.113	
CNT_{11}	460	91	24	29	1.199	
CNT_{12}	105	42	11	13	1.165	
	2916	179	47	56	1.184	Avg
	4904	159	40	50	0.065	Stdev
	168	89	84	89	5.470	CoV

The largest area measured was 17077.979 µm2, and the perimeter was 579.575 µm. The smallest area measured was 105.331 µm2, and the perimeter was 42.397 µm.

The values of area and perimeter in Table 4.4 have an Avg, Stdev and CoV of 2916, 4904 and 168 for the area, respectively, and a perimeter of 179.119, 159.568 and 89, respectively. The standard deviation for the areas is higher than the average and in the same range as the average for the perimeter. This implies a very high dispersion of data away from the average, as evidenced by the very high values of CoV. Therefore, the statistical measure of mean in this case is not of much value. The ratios of the diameters given in the rightmost column of the table are all greater than unity with an Avh, Stdev and CoV of 1.184, 0.065 and 5.470. The fact that the values of this ratio are all greater than unity is a result of the irregularity of the perimeters of the agglomerates. The low value of CoV indicates good clustering of the data points around the mean, thus implying that the mean is a good statistic.

© Central University of Technology, Free State

The results shown in Table 4.4 are plotted in Figure 4.15 to tease out trends of the measured values.

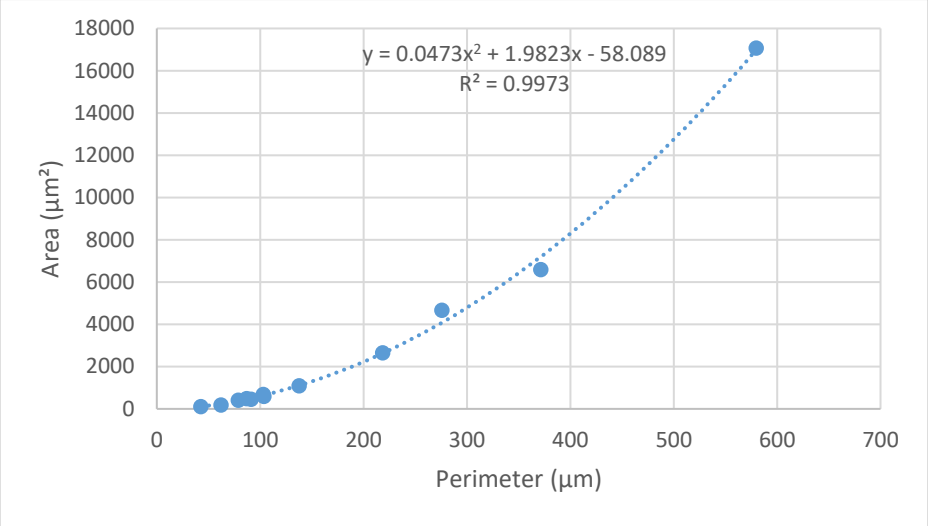

Figure 4.15 Plotted values of perimeter versus area for CNT agglomerates

This figure shows the clustering of the agglomerates' area and perimeter values towards the lower magnitudes of both parameters and a wide spread of single values for the higher magnitudes of area and perimeter. The high correlation coefficient of 0.9973 implies that there is a good correlation between the plotted points and the curve fitted to them.

4.6 Conclusions

Three methods were used in the effort to achieve a homogenous mixture between CNTs and Ti6Al4V(ELI) powders. It was not possible from pure visual observation of the SEM micrographs of the mixed powders to tell from the study which method was superior from a perspective of homogeneity of the mixture and degree of agglomeration of CNTs. However, it was clear that an 8 % CNT/Ti6Al4V(ELI) mixture using ethanol followed by sonication and magnetic stirring gave rise to higher multiplicity of CNT clusters in this instance. Comparison of the size of CNT agglomerates showed the smallest average area of agglomerates to have resulted from the 3 % CNT/Ti6Al4V(ELI) mixture dispersed with acetone, with average areas that were about 7.2, 4.1 and 4.8 times lower than the prevailing average areas for dry manual mixing at 3% CNTs, using ethanol at 3 % CNTs and at 8% CNTs, respectively. Dry manual mixing yielded significantly larger average areas of agglomerates than the

© Central University of Technology, Free State

other methods. It is also clear that increasing the percentage of CNTs from 3 % to 8 %, using ethanol as a dispersant, led to a marginal increase in the average areas of agglomerates, but with the emergence of a higher number of small clusters of CNTs that were more widely dispersed. It can be concluded that while using acetone as a dispersant lowered the average area of agglomerates, the use of ethanol led to a wider dispersion of CNTs with a marginal increase in the average areas of CNT agglomerates at increased %vol. CNTs and was thus preferable.

© Central University of Technology, Free State

CHAPTER 5 - INVESTIGATING THE EFFECTIVENESS OF THREE DIFFERENT MIXING TECHNIQUES USING ETHANOL AS A DISPERSION AGENT

5.0 Summary

Three mixing techniques were utilised with one dispersion agent in an attempt to achieve homogenous mixtures of CNTs and Ti6Al4V(ELI). CNTs at volume fractions of 3 %, 8 %, 15 %, 20 %, 25 %, and 30 % in Ti6Al4V(ELI) were dispersed in ethanol and then sonicated using a sonic bath. The slurries of CNTs were then mixed with Ti6Al4V(ELI) powders, first using manual mixing, then turbula mixing, and finally turbula-mechanical- and further manual mixing, which is referred to as combined mixing.

Samples from the final powder mixtures were analysed and studied using an SEM. The results obtained from manual mixing showed poor dispersion of CNTs within the Ti6Al4V(ELI) particles, with large agglomerates present throughout the mixture. Attachment of CNTs to Ti6Al4V(ELI) particles was seen on a few particles of Ti6Al4V(ELI) that appeared to be substantially covered by CNTs. No attachment of CNTs to Ti6Al4V(ELI) particles was visible in this case, but rather, several damaged particles of Ti6Al4V(ELI) were observed. Where combined mixing was used, SEM images showed improved dispersion throughout the samples, with the CNT agglomerates broken down into smaller sizes. However, this mixing technique led to more defects in the Ti6Al4V(ELI) particles. This was thought to have been due to the additional round of manual mixing used to correct the centrifugal separation of particles caused by turbula mixing. At 30 % vol. of CNTs, there were fewer particle defects compared to those of the lower volume fractions for this last combined mixing technique. Turbula mixing produced large clusters of CNTs across the volume fractions. These increased with an increase in volume fraction, especially the large CNT clusters, which were more prominent at 30 % vol. of CNTs in Ti6Al4V(ELI). These powder samples did not produce any single CNTs, and there were no particle attachments. Only a large cluster of CNTs was observed to be in physical contact with a Ti6Al4V(ELI) particle; however, this was not an attachment. Particle defects were detected at 20 % and 25 % vol. of CNTs in Ti6Al4V(ELI), and no other defects arose from the other volume fractions. Research has shown that even at a 1 % vol. of CNTs,

© Central University of Technology, Free State

reinforcement will still occur (Kim & Lee, 2014). However, some studies have shown an increase in mechanical properties at 12 % reinforcement (Goutianos & Peijs, 2021). In this study, the reinforcement followed the study of Kim and Lee, where reinforcement occurred at a low volume fraction of 3 %, and opposite to the studies of Goutianos and Pejis, where in this case, a rise in volume fraction resulted in a decrease in reinforcement and not an increase. It was concluded from the work carried out here that the best mixing technique was combined mixing.

5.1 Analysis of Scanning Electron Microscopy of Mixed Samples of Powder

SEM was performed on all powder samples to study the various characteristics of the powder particles. It was also done to determine, amongst other things, the degree of dispersion of CNTs, attachment of CNTs to Ti6Al4V(ELI) particles, and the level of deterioration of Ti6Al4V powder particles for the various mixing processes and dispersion agents used. The exercise was intended to help determine the best method for mixing CNTs and Ti6Al4V(ELI) between mechanical, turbula and combined turbula and manual mixing, using ethanol as a dispersion agent. Various SEM images were obtained at different magnifications to facilitate this study.

5.1.1 Analysis of Dispersion and Agglomeration of CNTs for Manual Mixed Powder Samples of Different Volume Fractions of CNTs in Ti6Al4V(ELI), using Ethanol as Dispersion Agent

The following images were obtained at different magnifications, with higher magnifications used to identify specific features in the samples. To guide the analysis in this chapter the SEM images of the un-mixed powders in Chapter 4, Figure 4.1 (a-b) were used as a reference for the observations, and conclusions arrived at in each mixing method. Preliminary mixing reported in Chapter 4 did highlight the presence of irregularly shaped Ti6Al4V(ELI) particles together with spherically shaped Ti6Al4V(ELI) particles. In the preceding work in this chapter, particle defects were presented largely in the form of deformed shapes and surface damage. In a few cases, particles were seen to be smeared onto others.

© Central University of Technology, Free State

Figure 5.1 is a representation of CNT/Ti6Al4V(ELI) powder samples at (a) 3 %, (b) 8 %, (c) 15 %, (d) 20 %, (e) 25 % and (f) 30 % vol. of CNTs in Ti6Al4V(ELI). Detailed descriptions are provided in Appendix E

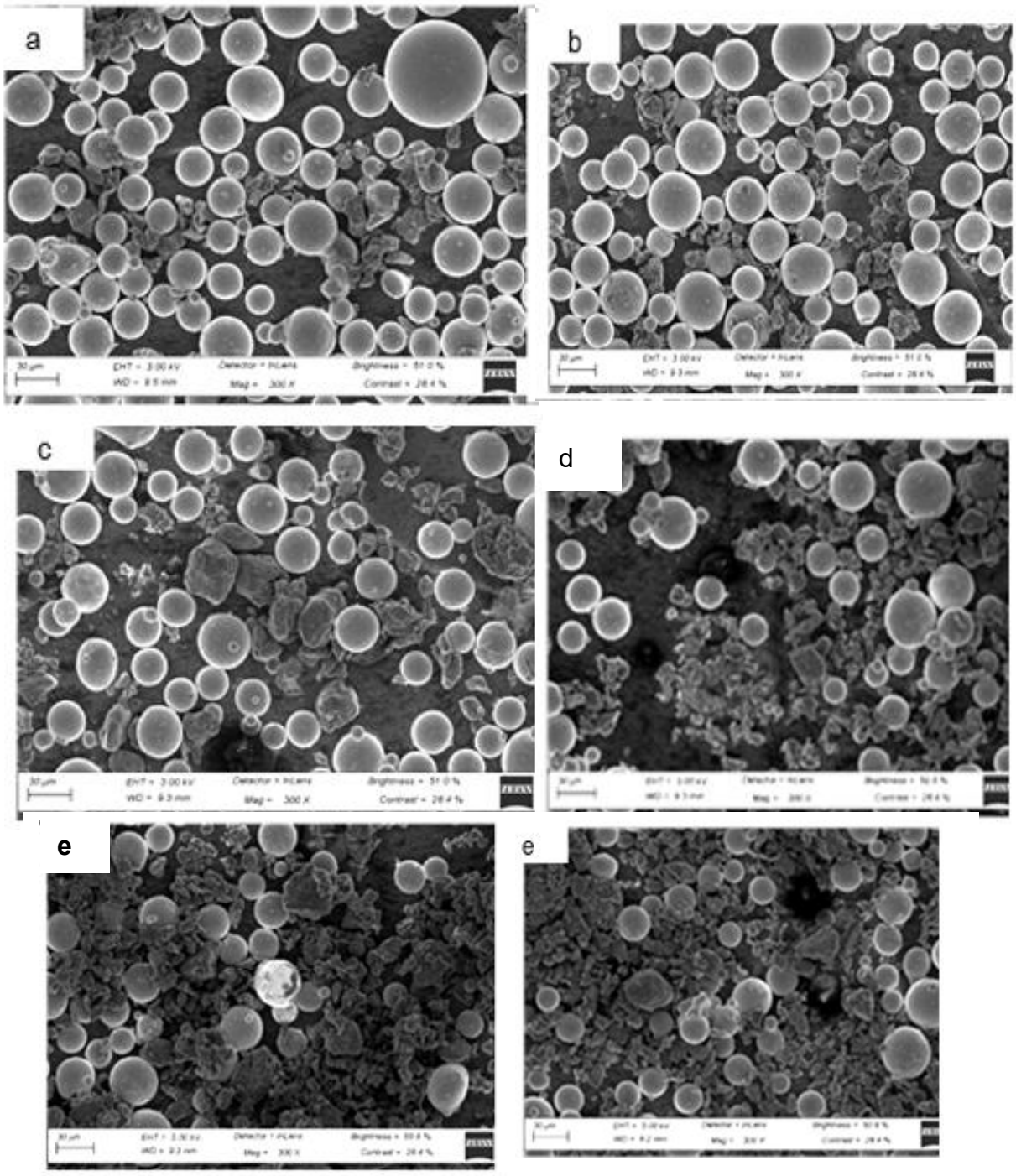

Figure 5.1 Scanning electron microscope images of CNT/Ti6AL4V(ELI) powder mixtures at (a) 3 %, (b) 8 %, (c) 15 %, (d) 20 %, (e) 25 % and (f) 30 % vol. of CNTs in Ti6Al4V(ELI)

© Central University of Technology, Free State

A detailed description of the images is provided in Appendix E, the discussion in this section points to the detailed description of the images provided in Figure 5.1.

The SEM image for the 3 % vol. CNTs dispersed in ethanol (Figure 5.1(a)) shows CNT clusters that do not appear as large as was the case in previous studies (Chapter 4, section 4.2). This is in reference to Figure 4.1(b) in Chapter 4, in which one large CNT agglomerate is visible. This is possibly due to the different tools used and increased periods of manual mixing in the present case, where manual mixing was applied for a maximum of 30 minutes, whereas previously (Chapter 4), it was only applied for ten minutes. Some CNTs attached themselves to the Ti6Al4V(ELI) matrix particles in this figure.

Figure 5.1(b) shows a SEM image of an 8 % vol. of CNTs in Ti6Al4V(ELI). The CNT clusters are more visible than at 3 % vol. of CNTs in Ti6Al4V(ELI), possibly because of the increased content of CNTs. The arrows point to a few of the CNT clusters amongst the Ti6Al4V(ELI) particles and incidences of CNTs attached to Ti6Al4V(ELI) particles, as well as numerous incidences of stand-alone clusters of CNTs. Increasing the concentration of CNTs to 15 % vol. (Figure 5.1(c)) showed a further increase of clusters of CNTs, which are more prominent in this sample compared to the 3 % and 8 % vol. CNT samples shown in Figure 13(a) and (b), respectively. It appears that increasing the concentration of CNTs this far prevents the dispersion of the CNTs, which may possibly require the application of larger mechanical forces for longer periods to break down the van der Waal forces between the nanotubes. Of interest is the surface morphology of the Ti6Al4V(ELI) particles that show discontinuities (roughness), possibly due to the impact of the tool (steel rod) for manual mixing. Also visible in this image are several irregularly shaped Ti6Al4V(ELI) particles. Two particles of Ti6Al4V(ELI) appear fused together, possibly due to the forces impacted on them during mixing. This is an observation of Figure 4.2 (a) of the un-mixed Ti6Al4V particles in which the feature observed in this case is not found in the sample. Taking into effect the steel rod used which has a strength greater than Ti6Al4V (ELI), with the increased force applied by the hand, the yield strength of the material can be exceeded leading to particle defects. Figure 5.1(d), with a 20 % mixture of CNTs in Ti6Al4V(ELI), shows clusters of CNTs that are more prominent in the powder mixture than in Ti6Al4V(ELI) particles. This is a sign of Ti6Al4V(ELI) particles that are covered up by

© Central University of Technology, Free State

the clusters of CNTs, given the fact that the latter only constitutes 20 % by volume fraction of the mixture.

Increasing the concentration to 25 % vol. of CNTs leads to an increase in the size of CNT clusters compared to the case for lower CNT volume fractions of 3 %, 8 %, and 15 %. These clusters are distributed randomly in the powder mixture. At the 25 % vol. CNTs, there is increased dispersion of CNTs, and very few vacant spaces between the particle interstices are evident. The predominance of CNTs here is even greater than 20 % vol. CNTs. One Ti6Al4V(ELI) particle in this image is seen to have a CNT agglomerate partially covering its surface. The rest of the image shows large clusters of CNTs between Ti6Al4V(ELI) particles. The darkened faces of the Ti6Al4V(ELI) are likely due to CNTs over their surfaces as was the case for the 20 % vol. CNT mixtures discussed previously.

At 30 % vol. of CNTs, the micrograph in Figure 5.1(f) shows numerous CNT agglomerates of different sizes in Ti6Al4V(ELI). There is a lower tendency for the CNTs to disperse in ethanol; effectiveness of deagglomeration is expected to diminish with increasing volume fraction of CNTs, thus an attendant increase in the number and size of clusters of CNTs and, therefore, in Ti6Al4V(ELI) at this volume fraction of CNTs compared to the case at 3 %, 8 % and 15 % CNTs in Ti6Al4V(ELI). At increased concentrations the interactions between CNT tubes are at proximity which leads to re-agglomeration even after initial deagglomeration decreasing their reinforcing effect (Ramezani et al., 2022). Comparing this case to the ones at 20 % and 25 % vol. of CNTs in Ti6Al4V(ELI) particles, dispersion here is less, with little or no clusters of CNTs seen in large areas of the micrograph. From the foregoing observations and those arising for the other volume fractions of CNTs, it is evident that as the vol. CNTs is increased, the efficiency of reinforcement decreases. Some loss of powder occurred at the higher rotational speed of 350 rpm used in the case of the 30 % vol. CNTs in Ti6Al4V(ELI). However, this was minimal and is believed not to have affected the final mixture significantly. Here, as for the last two volume fractions of CNTs, the particles of Ti6Al4V(ELI) appear darkened, which points to the presence of CNTs on their surfaces.

© Central University of Technology, Free State

5.1.1.1 Visual Analysis of Attachments of CNTs on Ti6Al4V(ELI) Particles for Manual Mixed Powder Samples of CNTs in Ti6Al4V(ELI)

Incidences of attachment of CNTs on Ti6Al4V(ELI) particles were observed at the different volume fractions of CNTs.

Figure 5.2 presents a magnified SEM image with CNT attachments at 3 %, 8%, 15%, 20%, 25%, and 30% vol. of CNTs in Ti6AL4V(ELI).

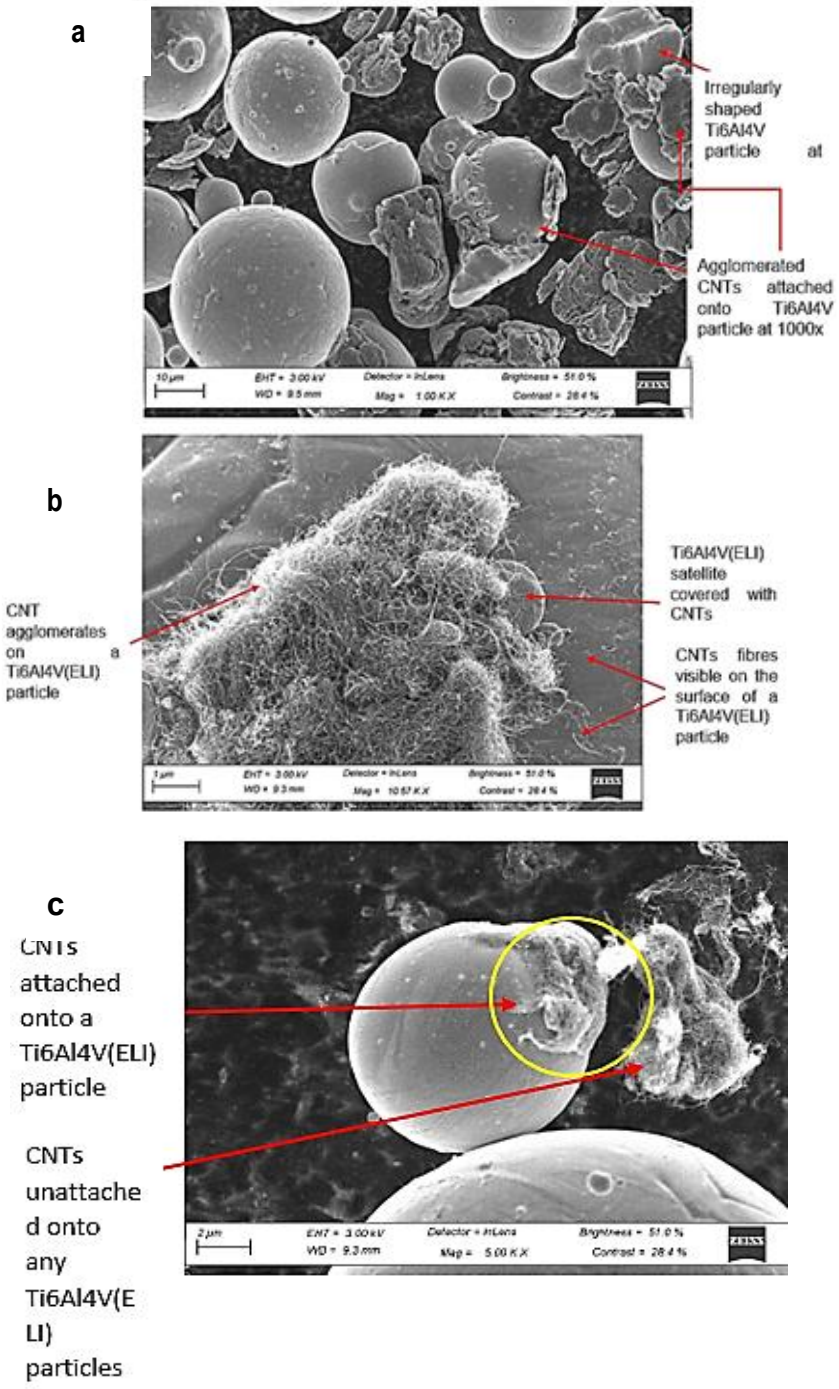

© Central University of Technology, Free State

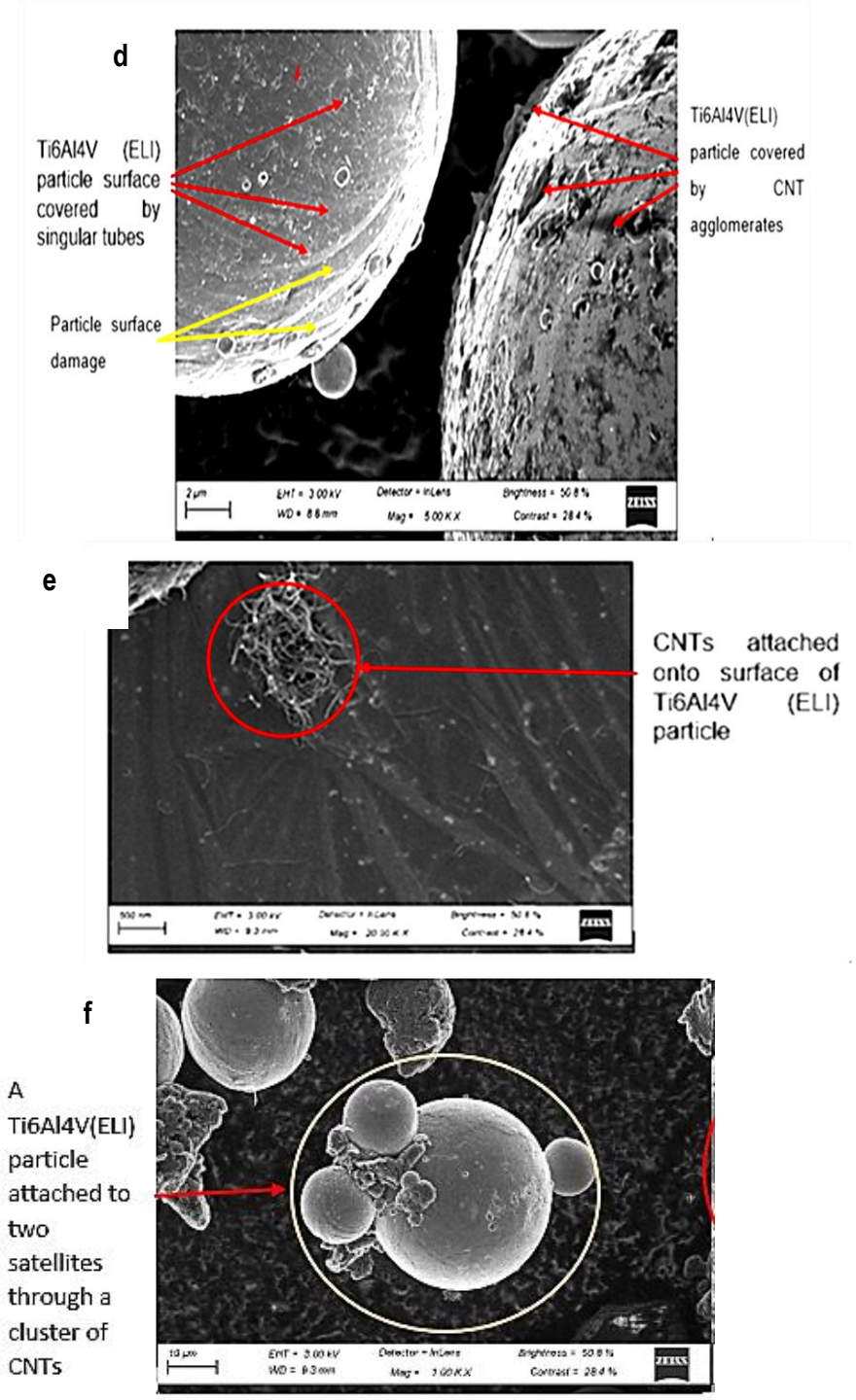

Figure 5.2 Attachments of CNTs observed on Ti6Al4V(ELI) particles at (a) 3% (b) 8% (c) 15% (d) 20% (e) 25 and (f) 30% % vol. of CNTs in Ti6Al4V(ELI)

At 1000x magnification (Figure 5.2a), at 3% vol. the attachment of CNT agglomerates to the surfaces of some Ti6Al4V(ELI) particles is clearly visible in Figure 5.2 (a). Some

© Central University of Technology, Free State

irregularly shaped Ti6Al4V particles are also seen. Satellites and stand-alone agglomerates of CNTs are also present.

The sample at 8 % vol. of CNTs (Figure 5.2 b) in Ti6Al4V(ELI), at 10570x magnification shown in Figure 5.2(b), displays CNTs agglomerates that have attached to a Ti6Al4V(ELI) particle much more clearly. In this magnified image, the CNTs are seen to be entangled with one another in the cluster. Also, visible are single CNT fibres that are attached to the surface of the Ti6Al4V (ELI) particle, a sign that some CNTs were able to separate from the agglomerates, possibly due to increased manual mixing together with the use of ethanol as a dispersion agent.

Figure 5.2(c) shows the attachment of CNTs at 15% vol. to a Ti6Al4V(ELI) particle. One end of the CNTs is attached to a Ti6Al4V(ELI) particle, while the other end is left floating freely without any attachment. Charged CNTs (which appear white in colour in the image) have strands of nanotubes protruding from the CNT agglomerate. The agglomerate of CNTs comprises numerous entangled nanotubes. Satellite particles and scarring are also seen on the surfaces of two large particles of Ti6Al4V(ELI) in the image.

In Figure 5.2(d), at 20 % vol. of CNTs in Ti6A4V(ELI), CNTs attached to the bottom right particle of Ti6Al4V(ELI) (indicated by red arrows) were spread all over its surface. The top left Ti6Al4V(ELI) particle showed single CNT fibres attached (indicated by red arrows) to its surface. The surface damage observed on the bottom right Ti6Al4V(ELI) particle is thought to have been caused by the manual mixing process.

In Figure 5.3(e), at 25 % vol. of CNTs in Ti6Al4V(ELI), a CNT agglomerate, clearly showing entangled CNTs in an area with a width of about 750 nm and breadth of about 1250 nm, attached itself to the surface of a Ti6Al4V(ELI) particle. Several stand-alone nanotubes are visible all over the surface of the Ti6Al4V(ELI) particle.

The SEM image of a 30 % vol. of CNTs in Ti6Al4V(ELI), shown in Figure 5.3(f), had one satellite and two small Ti6Al4V(ELI) particles attached to it through a cluster of CNTs.

No trend in the attachment of CNTs to particles of Ti6Al4V(ELI) was identified with respect to their volume fraction.

© Central University of Technology, Free State

5.1.1.2 Qualitative Visual Analysis of Defects on Ti6Al4V(ELI) Particles at 3 %, 8 %, 15 %, 20 %, 25 %, and 30 % vol. CNTs in Ti6Al4V(ELI) for Mechanically Mixed CNTs and Ti6AL4V(ELI) Powder Samples

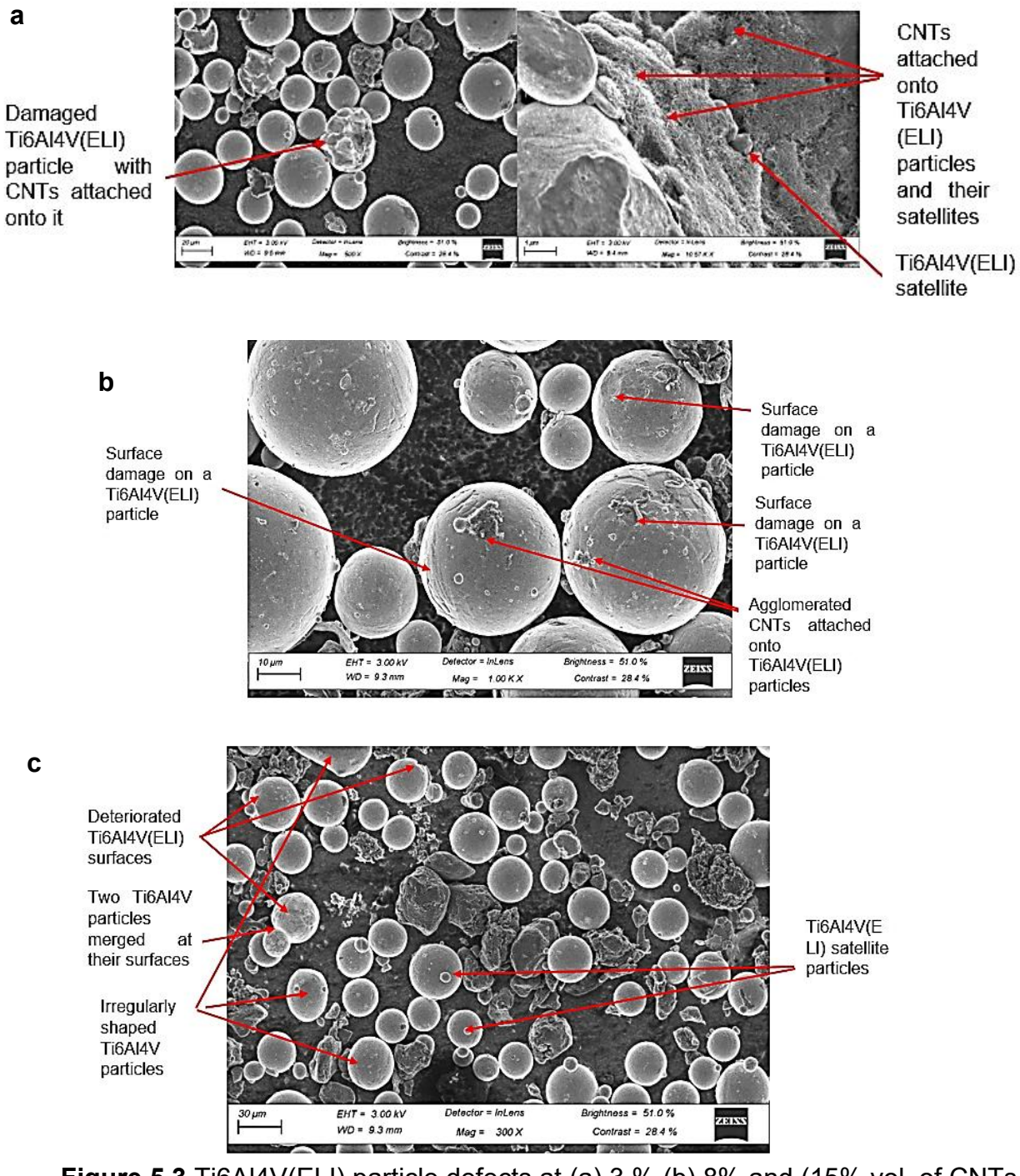

Figure 5.3 Ti6Al4V(ELI) particle defects at (a) 3 % (b) 8% and (15% vol. of CNTs in Ti6Al4V(ELI)

© Central University of Technology, Free State

At a magnification of 500x, a damaged Ti6Al4V (ELI) particle in a 3 % vol. of CNTs in the Ti6AL4V(ELI) mixture was observed to have CNT attachments (Figure 5.3a). CNT clusters were located in between Ti6Al4V particles as well as satellite particles.

The SEM image of an 8 % vol. of CNTs in the Ti6Al4V(ELI) mixture, shown in Figure 5.3b, exhibits clear signs of surface damage to Ti6Al4V(ELI) particles, possibly due to impact during manual mixing. Also observed were satellites, a CNT cluster attached to one particle of Ti6Al4V(ELI) and agglomerates of CNTs in between the particles of Ti6Al4V(ELI).

At a magnification of 200x at 15 % vol. of CNTs in Ti6Al4V(ELI) (Figure 5.3c), several irregularly shaped Ti6Al4V(ELI) particles were seen, as well as a number of satellite particles. The irregularities in these particles were likely to have been caused by the manual mixing process.

The particle defects at 20 % and 25 % vol. of CNTs in Ti6Al4V(ELI) were discussed in the previous subsection, where the attachment of CNTs was covered and will not be repeated here. No particle defects were detected in the 30 % vol. of CNTs in Ti6AL4V(ELI). This points to a possible threshold above which the predominance of CNTs in the mixture acted to protect the particles of Ti6Al4V(ELI) from damage, a fact that should be investigated further in future work.

5.1.1.3 Conclusions

The SEM images of CNT vol. % at 3 %, 8 %, 15 %, 20 %, 25 %, and 30 % in Ti6Al4V(ELI) showed good dispersion of CNT agglomerates at 3 %, 8 %, 15 % vol. CNTs and poor dispersion at 20 %, 25 %, and 30 % vol. CNTs, the latter due to increased aggregation of CNT at these volume fractions. A number of Ti6Al4V(ELI) particles had attachments of CNT fibres and agglomerates on their surfaces, with a few having their entire surfaces covered with CNTs. While the samples of mechanically mixed powder at the macro-scale (Appendix A, section A.2.1.1) indicated that they were well blended, observations at the micro-scale in this section showed that manual mixing was not effective in breaking the forces holding CNT fibres together and, therefore, led to the formation of agglomerates. Incidences of surface damage on and deformation of Ti6Al4V(ELI) particles were recorded. This was thought to be a

© Central University of Technology, Free State

result of impact during manual mixing and indicates the need for a better method of mixing.

5.2 Qualitative Visual Analysis of Dispersion and Agglomerations of Turbula Mixed Samples for Different Volume Fractions of CNTs in Ti6Al4V(ELI), Using Ethanol as a Dispersion Agent

The following images were taken at different vol.% of CNTs to show the characteristics of the mixed powders (the scale was superimposed due to image quality)

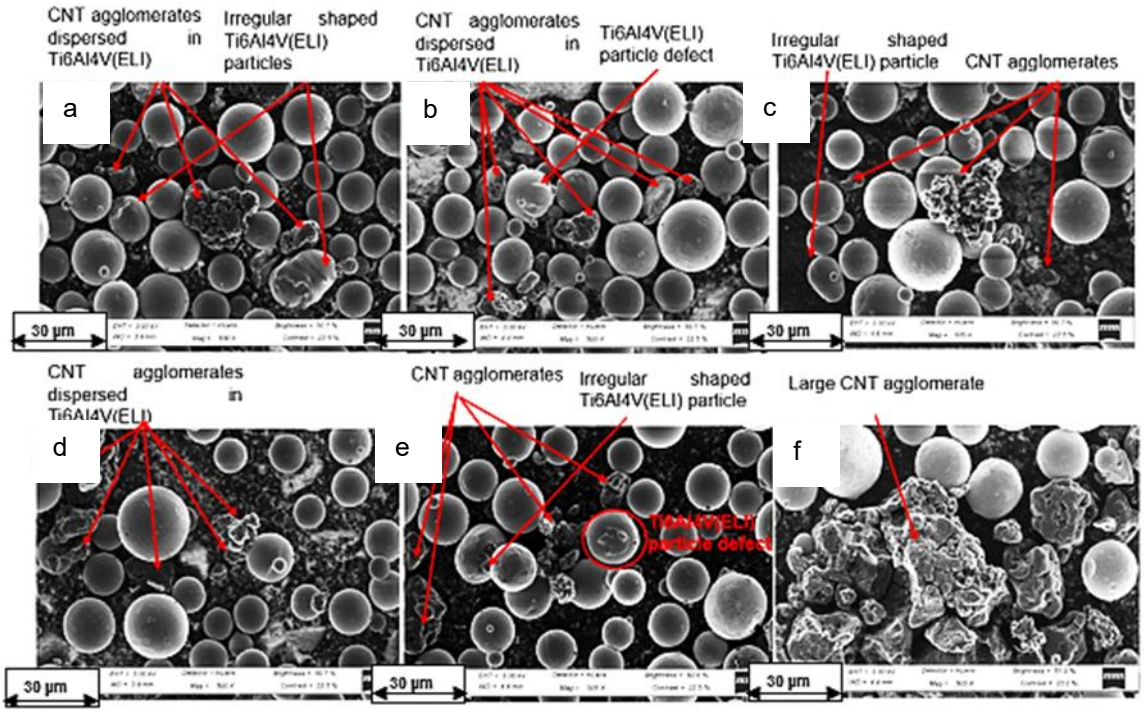

Figure 5.4 Scanning electron microscope images at (a) 3 %, (b) 8 %, (c) 15 %, (d) 20 %, (e) 25 %, (f) 30 % vol. of CNTs in Ti6AL4V(ELI) using turbula mixing

At 3 % vol. of CNTs in Ti6Al4V(ELI), the CNTs were not dispersed throughout the sample but rather occurred in the form of agglomerates in certain areas, as is evident in Figure 5.4(a). The agglomerates are as large as those seen in the mechanically mixed samples at the same volume fraction of CNTs. The same characteristic was found in the mixed sample of 8 % vol. of CNTs in Ti6Al4V(ELI) (Figure 5.4(b)). The agglomerates in the powder sample occurred in between Ti6Al4V(ELI) particles, as at 3 % vol. CNTs, with no visible attachment to the particles either. At 15 % vol. of CNTs (Figure 5.4(c)), there were CNTs agglomerates of different sizes throughout the image, as was the case for the other two lower volume fractions of CNTs. At 20 % vol. of CNTs (Figure 5.4 (d)), large agglomerates were visible compared to the case at 15 % vol. of CNTs in Figure 5.4(c). The mixed sample at 25 % vol. of CNTs (Figure 5.4(e))

© Central University of Technology, Free State

showed smaller agglomerates compared to the previous three volume fractions of CNTs. Higher revolving speeds were used in this sample due to the increased concentration, which could explain the smaller agglomerates. At 30 % vol. of CNTs (Figure 5.4(f)), a very large aggregation of agglomerates was seen.

Compared to manual mixing, the samples obtained from turbula mixing produced fewer defects and deformations of Ti6Al4V(ELI) particles. A few incidences of attachments of CNTs to particles of Ti6Al4V(ELI) were seen at all volume fractions of CNTs in Ti6Al4V(ELI), far lower than in manual mixing.

5.2.1 Qualitative Visual Analysis of Defects and Attachments on Ti6Al4V(ELI) Particles at 3%–30%vol. CNTs in Ti6Al4V(ELI) for Turbula Mixed CNT/Ti6AL4V(ELI) Powder Samples

In a powder sample at 15 % vol. CNTs in Ti6Al4V(ELI), the agglomeration of CNTs and their attachment to particles of Ti6Al4V(ELI) are shown in Figure 5.5. The figure is presented in magnifications of 2000x and 5000x in Figure 5.5 (a, b) to observe better the CNT agglomerates in it. Damage on the surfaces of Ti6Al4V(ELI) particles is indicated in the figure.

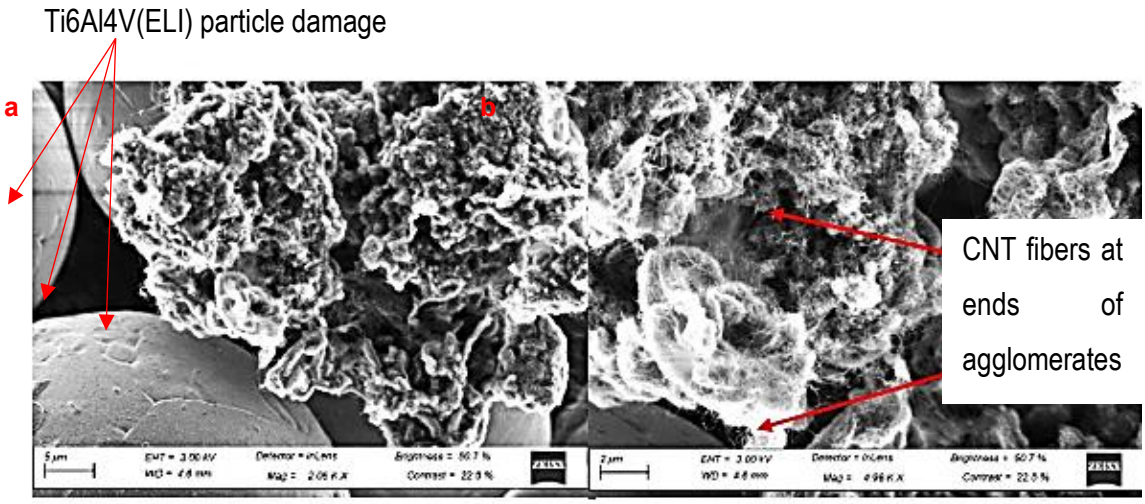

Figure 5.5 Scanning electron microscope image of 15 % vol. CNTs powder sample in Ti6Al4V(ELI)

Figure 5.5 (a-c), with a magnification of 1000x, shows a CNT agglomerate that appears to be attached to the surface of a Ti6Al4V(ELI) particle in a 20 % vol. CNTs in Ti6Al4V(ELI) powder sample.

© Central University of Technology, Free State

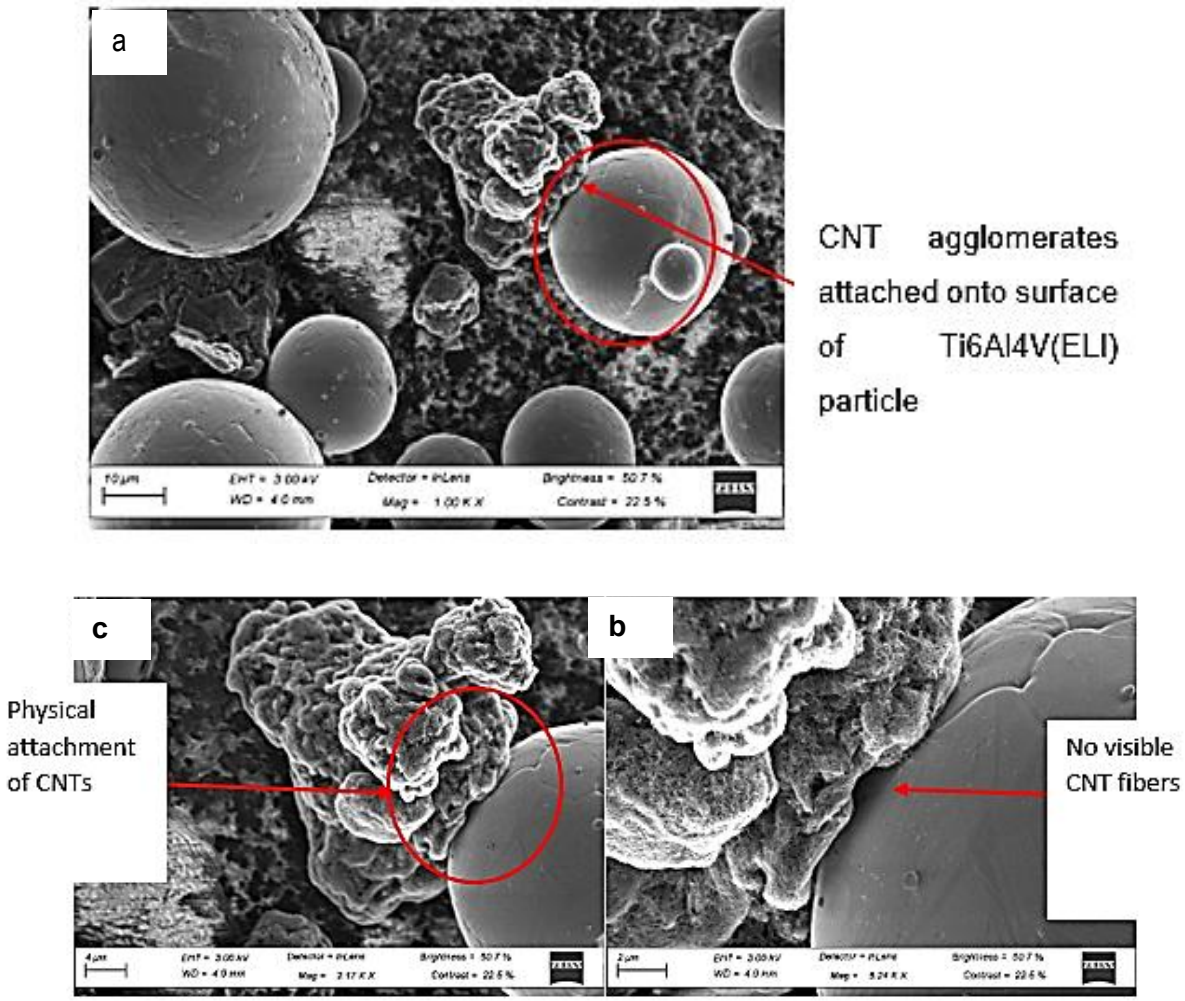

Figure 5.6 Scanning electron microscope image of 20 % vol. CNTs powder sample in Ti6Al4V (ELI) at (a) 2170x and (b) 5240x

Further magnification (Figure 5.6(a)) of this apparent attachment showed it to be mere physical contact and not attachment, as is evident in Figure 5.5(b & c). Defects on the surfaces of the Ti6Al4V(ELI) particles were also evident in the figure.

At 25% vol. of CNTs Figure 5.7(a) showed several CNT agglomerates lodged in between Ti6Al4V(ELI) particles and apparently attached to them. Particles of Ti6Al4V(ELI) with surface defects were also apparent in the figure. Magnification of this image to 1000x around one of the locations showing apparent attachment revealed these to be cases of physical contact and not attachment, as is evident in Figure 5.7(b), similar to that observed at the lower volume fraction of CNTs of 20 %,

© Central University of Technology, Free State

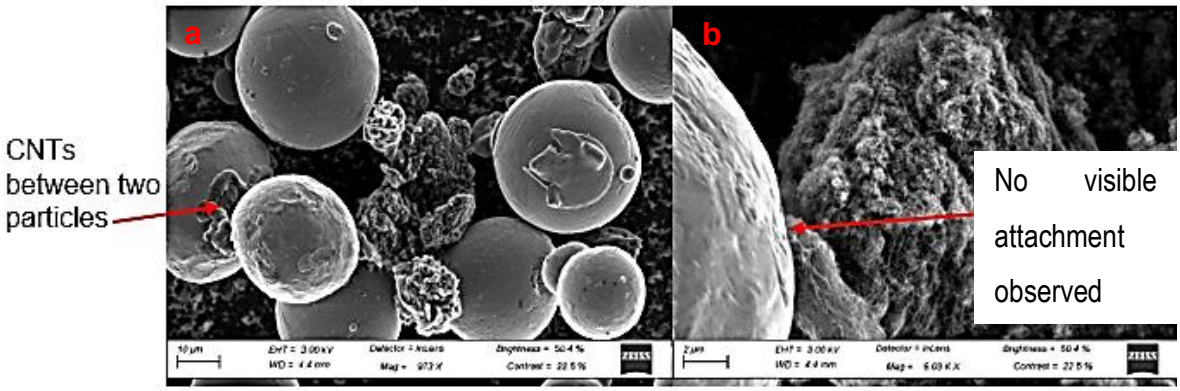

Figure 5.7 Scanning electron microscope image of 25 % vol. CNTs powder sample dispersed in ethanol and turbula mixed with Ti6Al4V(ELI) at 1000x

The SEM image in Figure 5.8(a) of a mixed powder sample at 30 % vol. of CNTs in Ti6Al4V(ELI) showed a small particle of Ti6Al4V(ELI) lodged in an agglomerate of CNTs. Magnification of this image (Figure 5.8(b) to 3460x, around the lodged particle of Ti6Al4V(ELI), showed no signs of attachment of the agglomerate to the particle.

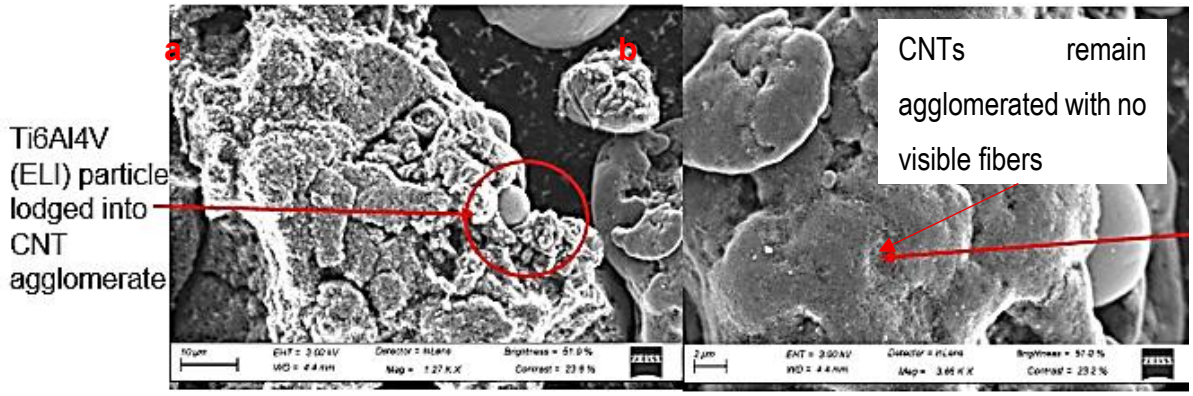

Figure 5.8 Scanning electron microscope image of 30 % vol. CNTs powder sample in Ti6Al4V(ELI)

5.2.2 Conclusions

The SEM images of CNT vol. % at 3 %, 8 %, 15 %, 20 %, 25 %, and 30 % in Ti6Al4V(ELI) showed poor dispersion between 3–20 %, and 30 % vol. of CNTs in Ti6Al4V(ELI). Better dispersion of CNTs was observed at 25 % vol. of CNTs in Ti6Al4V(ELI). This method of mixing depicted fewer attachments of CNTs on Ti6Al4V(ELI) particles compared to the case for manual mixing. Defects on the surfaces of particles of Ti6Al4V(ELI) were seen at 20 %, 25 %, and 30 % vol. of CNTs in Ti6Al4V(ELI). No individual CNT fibres were seen for all the concentrations of CNTs in this case.

© Central University of Technology, Free State

5.3 Qualitative Visual Analysis of Dispersion and Agglomeration of CNTs for Combined Mixing, for Different Volume Fractions of CNTs in Ti6Al4V(ELI), using Ethanol as Dispersion Agent

The SEM images in this section show samples of CNT/Ti6Al4V(ELI) mixtures for various volume fractions and magnifications. Figure 5.9 shows SEM images of these mixtures at a low magnification of 300x. A more detailed description of the SEM images is provided in Appendix E.

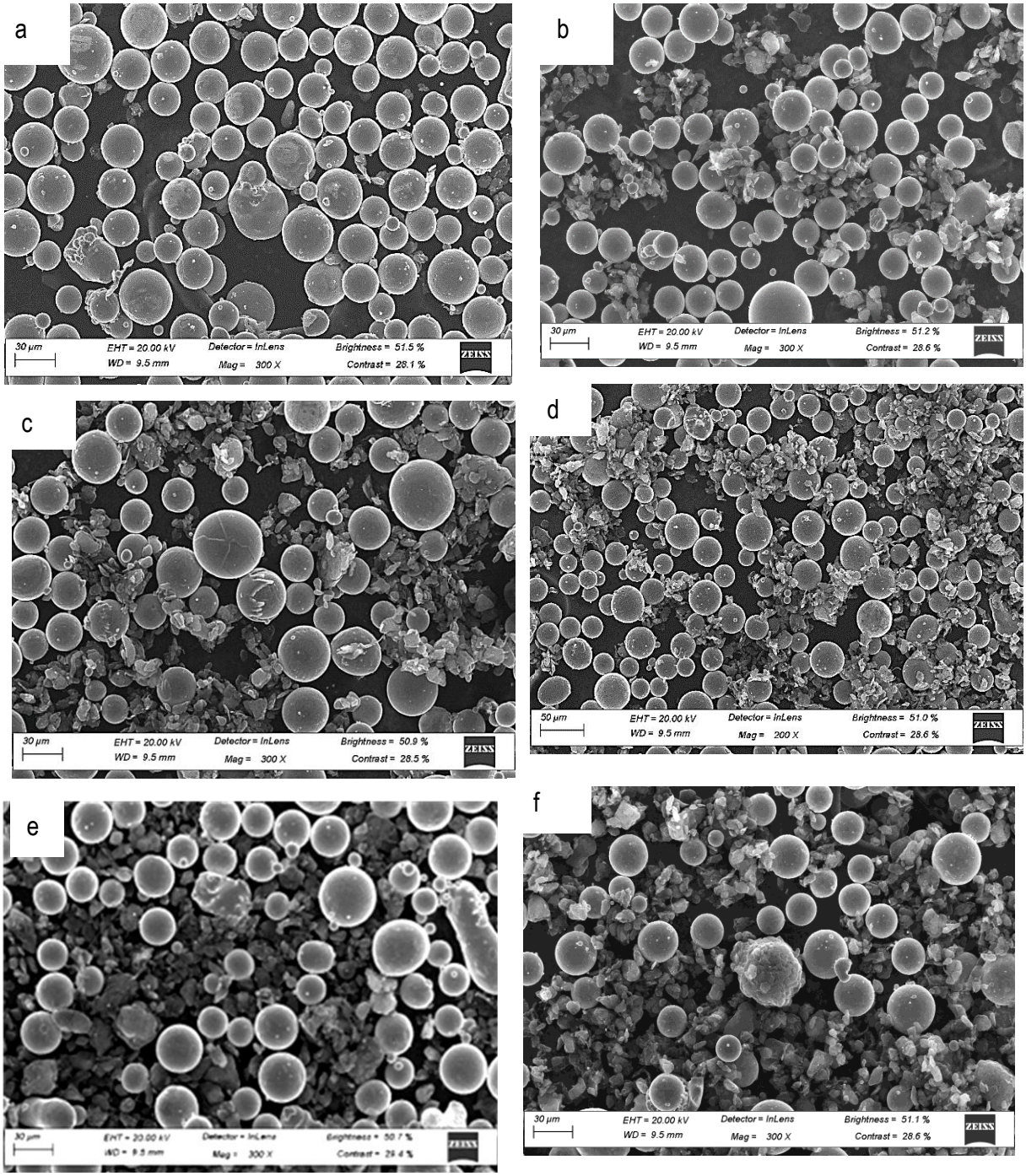

Figure 5.9 Scanning electron microscope images at (a) 3 %, (b) 8 %, (c) 15 %, (d) 20 %, (e) 25 %, (f) 30 % vol. of CNTs in Ti6AL4V(ELI) using combined mixing

© Central University of Technology, Free State

At 3 % vol. of CNTs in Ti6AL4V(ELI), the CNTs appear as significantly smaller agglomerates (Figure 5.9(a)). The presence of large CNT agglomeration that was previously observed in the mechanically mixed samples is not apparent in this sample; rather, many smaller clusters that have a lighter shading. Two damaged Ti6Al4V(ELI) particles are visible near the centre of this image. In both cases, it appears that one Ti6Al4V(ELI) particle merged with another smaller one.

Figure. 5.9(b) for 8 % vol. CNTs in Ti6Al4V(ELI) shows the presence of many small clusters of CNT agglomerates within groups of Ti6Al4V(ELI) particles (circled in red) that are more in number than in the case of manual mixing increased at the same percentage volume fraction of CNTs. There is also an increase in the number of attachments of CNTs to Ti6Al4V(ELI) particles compared to the case for manual mixing at the same volume fraction of CNTs. The areas circled in red also appear to be clusters of CNTs linking several particles of Ti6Al4V(ELI) to one another. At this low magnification, it was not possible to determine the nature of the bond between these CNT clusters and the adjacent Ti6Al4V(ELI) particles.

The mixed powder sample for 15 % vol. of CNTs (Figure 5.9(c)), exhibited an increase in the number of dispersed agglomerates when compared to the 3 % and 8 % volume fractions of CNTs due to the increased vol.% of CNTs in Ti6Al4V (ELI). At 15% vol. of CNTs in Ti6Al4V(ELI), the SEM image showed more details of the powder sample than for the two previous, lower volume fractions of CNTs. The image highlighted the presence of an uneven distribution of CNTs in the powder sample, with some areas exhibiting more, less, and no CNTs. The sample also had Ti6Al4V(ELI) particles with defects. Statically charged CNTs were visible, appearing lighter than the rest of the CNTs.

The powder sample for 20 % vol. of CNTs in Ti6Al4V(ELI) showed a much higher presence of dispersed CNT clusters in the Ti6Al4V(ELI) than at previous, lower volume fractions of CNTs (Figure 5.9(d)).

The predominance of CNTs at a 25% vol. fraction of CNTs is apparent in Figure 5.9(e), which rather shows a more or less continuous mass of well-dispersed CNTs instead of the clusters seen at lower volume fractions. Like in the previous images, satellite particles were observed, as well as damaged and merged Ti6Al4V(ELI) particles.

© Central University of Technology, Free State

There was also one particle that appeared very elongated or possibly a merger of several particles.

The SEM image of the powder sample for 30 % vol. of CNTs in Ti6Al4V(ELI), shown in Figure 5.9(f), exhibited a large presence of CNTs that were dispersed between the Ti6Al4V(ELI) particles. Several spaces without either one of the two particles in the mixture were also evident, denoting a drop in the degree of dispersion from the case at the immediately lower volume fraction of CNTs, 25 % vol. In one instance, CNT agglomerates were attached to the surface of a Ti6Al4V(ELI) particle. The sample also had damaged particles of Ti6Al4V(ELI).

5.3.1 Qualitative Visual Analysis of Defects onTi6Al4V(ELI) Particles at 3 %–30 % Vol. CNTs in a Ti6Al4V(ELI) Matrix for Combined Mixed CNTs and Ti6Al4V(ELI) Powder Sample

Figure 5.10 shows Ti6Al4V(ELI) particle defects in 3 % vol. CNTs in Ti6Al4V(ELI), which were not detected in the samples that were only mixed mechanically or by turbula mixing. These defects were, therefore, taken to have been caused by further manual mixing, which was done to reverse the undesirable separation of the two powders caused by turbula mixing. Three different types of particle defects were detected in Figure 5.10. These include (a) a particle with morphology and shape not observed before. It is not clear how this morphology and shape was formed, and further research is required to provide answers to this unknown. Secondly, (b) a particle that had surface damage and cracks that were visible on its surface and finally, (c) a particle showing surface damage, and which appeared to have another particle stuck to part of its surface.

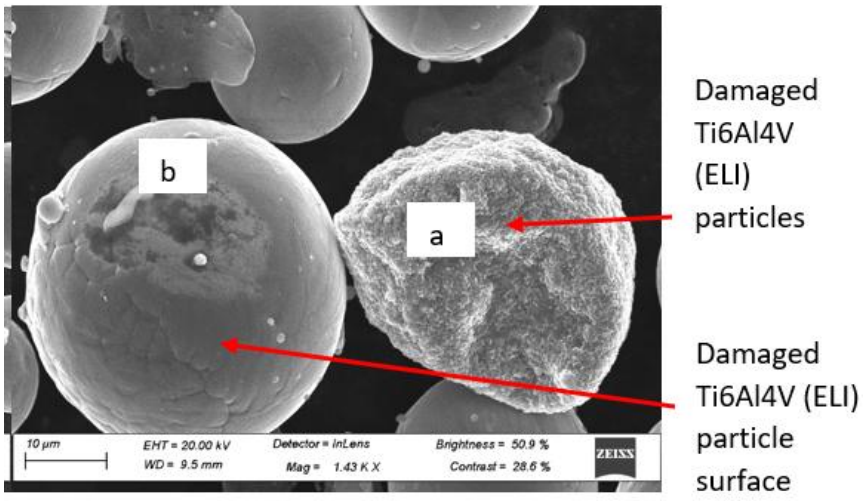

© Central University of Technology, Free State

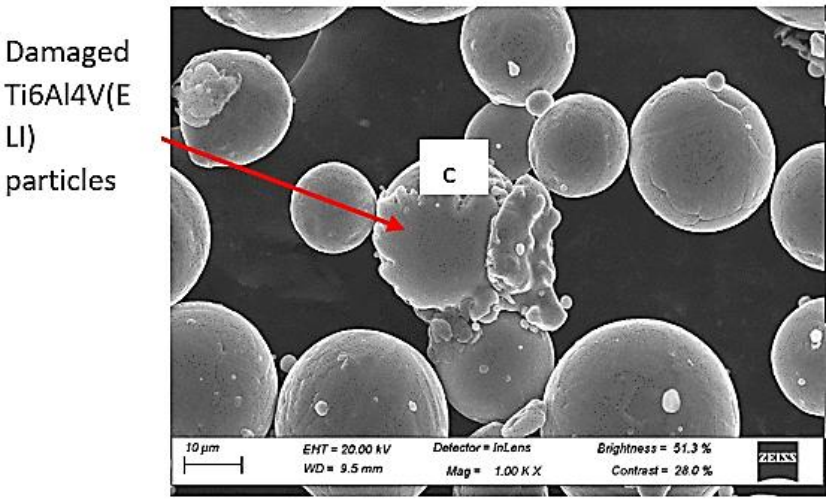

Figure 5.10 Scanning electron microscopy image of Ti6Al4V(ELI) particle defects at 1000x and 1470x, left and right images, respectively

The areas with surface defects on the two Ti6Al4V(ELI) particles labelled a and b in Figure 5.10 above were magnified and compared, as shown in Figure 5.11, at magnifications of 20 000x and 5000x, respectively. Both figures showed surface damage, with the left side showing the granular structure of the surface of the left side image being more evident due to its higher magnification".

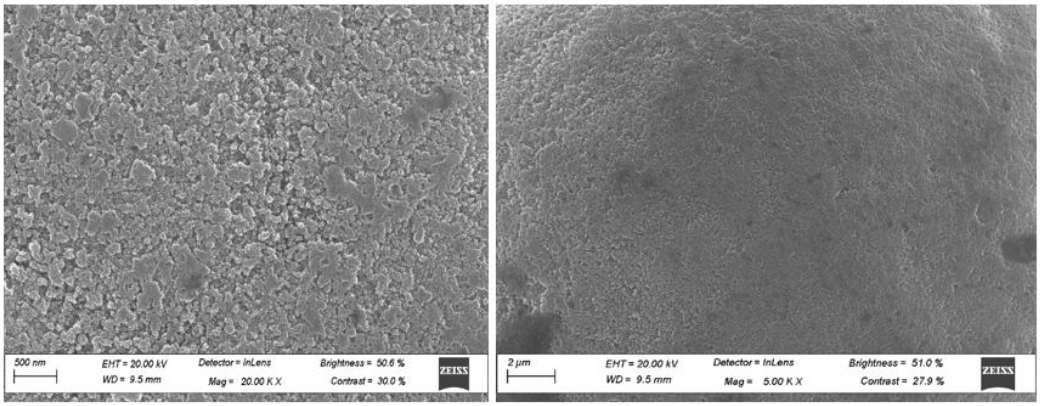

Figure 5.11 Scanning electron microscope image of a Ti6Al4V(ELI) particle defect at 20 000x and 5000x

At 1000x magnification in Figure 5.12, several details in the sample shown in Figure 5.9(a) became clearer. The CNTs that were not visible in Figure 5.9(a) at 300x magnification appeared clearly at this magnification. They appeared translucent and not black, as seen in previous samples, which made it difficult to observe the details on them at a lower magnification. The Ti6Al4V(ELI) particles which were observed to

© Central University of Technology, Free State

have merged (within the area labelled A in Figure 5.9(a) in the 3 % vol. of CNTs sample), were also seen in this figure, where it was clear that the larger one was an irregularly shaped particle, whilst the smaller one was a spherically shaped particle.

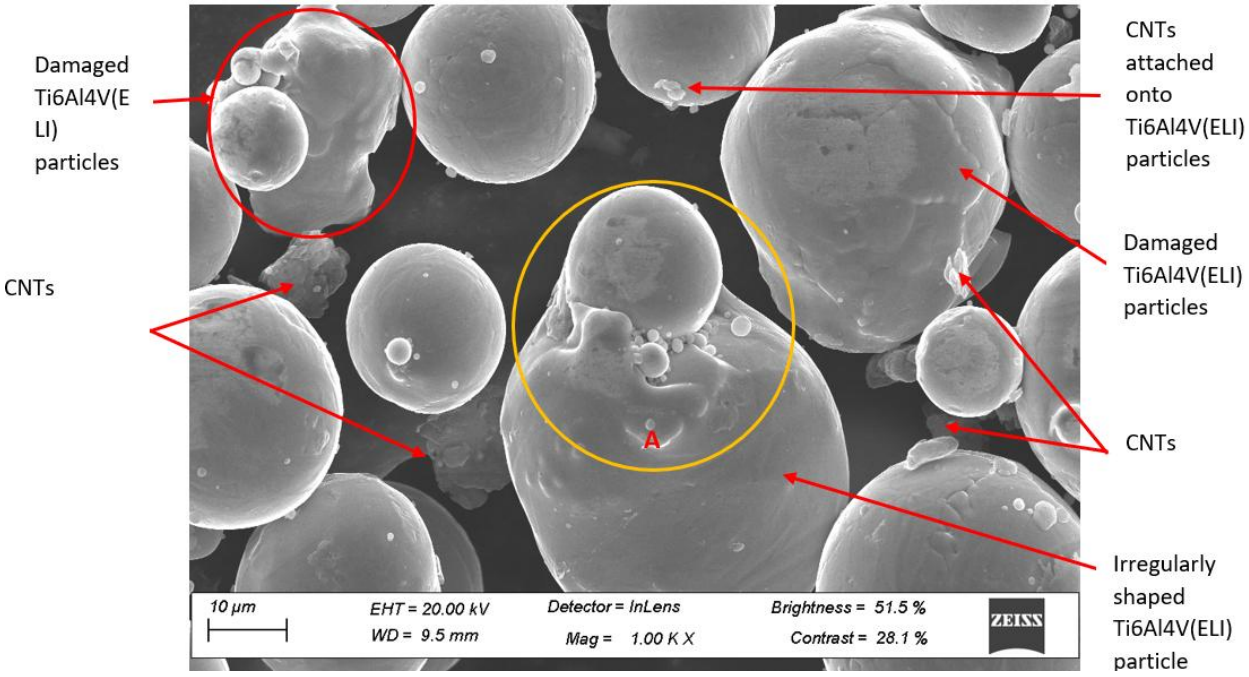

Figure 5.12 Scanning electron microscope image of 3 % vol. CNTs powder sample for combined mixing at 1000x

A closer look at the merged Ti6Al4V(ELI) particles within the area labelled A in Figure 5.12 showed numerous smaller Ti6Al4V(ELI) particles around them. This was seen better in Figure 5.13(a–b) at a much higher magnification.

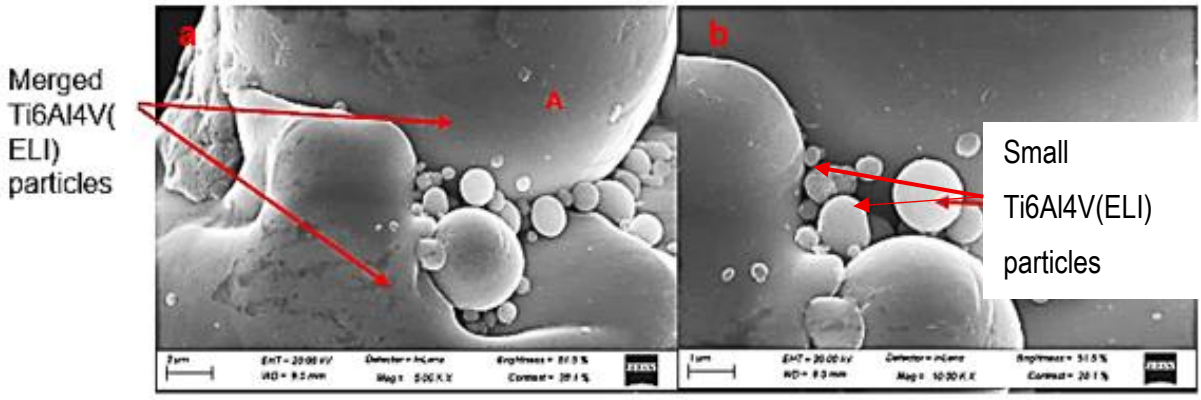

Figure 5.13 Scanning electron microscopy image of merged Ti6Al4V(ELI) particles with many smaller Ti6Al4V(ELI) particles around them, at 5000x and 20 000x

© Central University of Technology, Free State

In Figure 5.14, at 20 000x magnification, single CNT fibres were seen on the surfaces of the large deformed Ti6Al4V(ELI) particle shown in Figure 5.13.

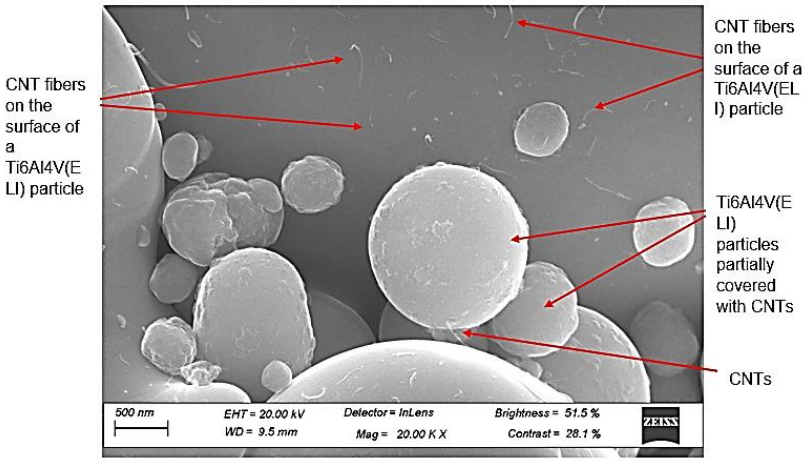

Figure 5.14 Scanning electron microscope image of 3 % vol. CNTs powder sample at 20 000x

There were no particle defects in the sample at an 8 % vol. CNTs; however, there were surface attachments.

At 500x and 1000x magnification, Figure 5.15 (left and right), respectively, showed a cluster of CNTs linking several particles of Ti6Al4V(ELI) to one another. It was not possible at these magnifications to determine the nature of the bond between the CNT clusters and Ti6Al4V(ELI) particles.

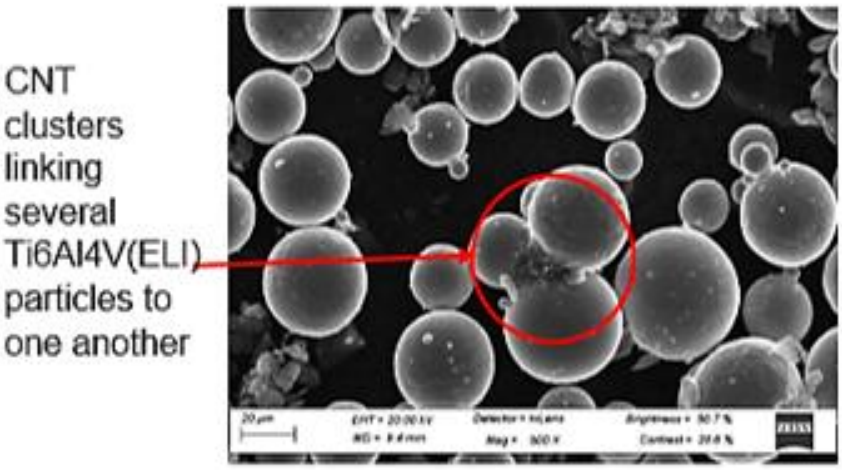

© Central University of Technology, Free State

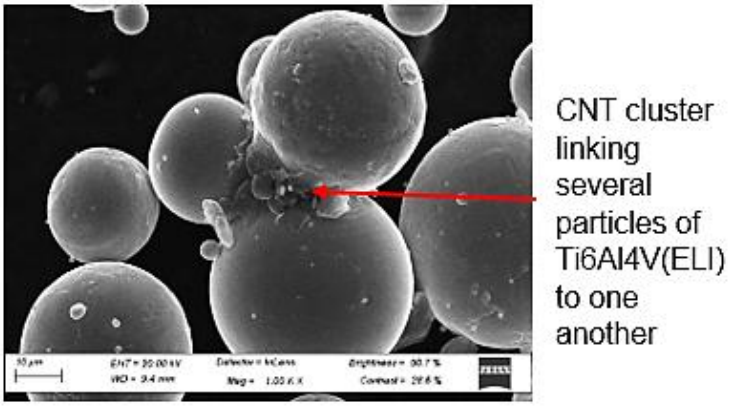

Figure 5.15 Scanning electron microscope image of 8 % vol. of CNTs in Ti6Al4V(ELI) powder sample with combined mixing applied

Further magnification around the cluster in Figure 5.15 (left and right) to link several particles of Ti6Al4V(ELI) led to the images in Figure 5.16 (left and right). At 5000x magnification (Figure 5.16 (left)), it was seen that this cluster of CNTs contained smaller particles of Ti6Al4V(ELI) trapped inside it. Figure 5.16 (right) showed a dimpled Ti6Al4V(ELI) particle surface morphology whose cause is unknown. A CNT agglomerate was attached to the surfaces of the two adjacent particles of Ti6Al4V(ELI).

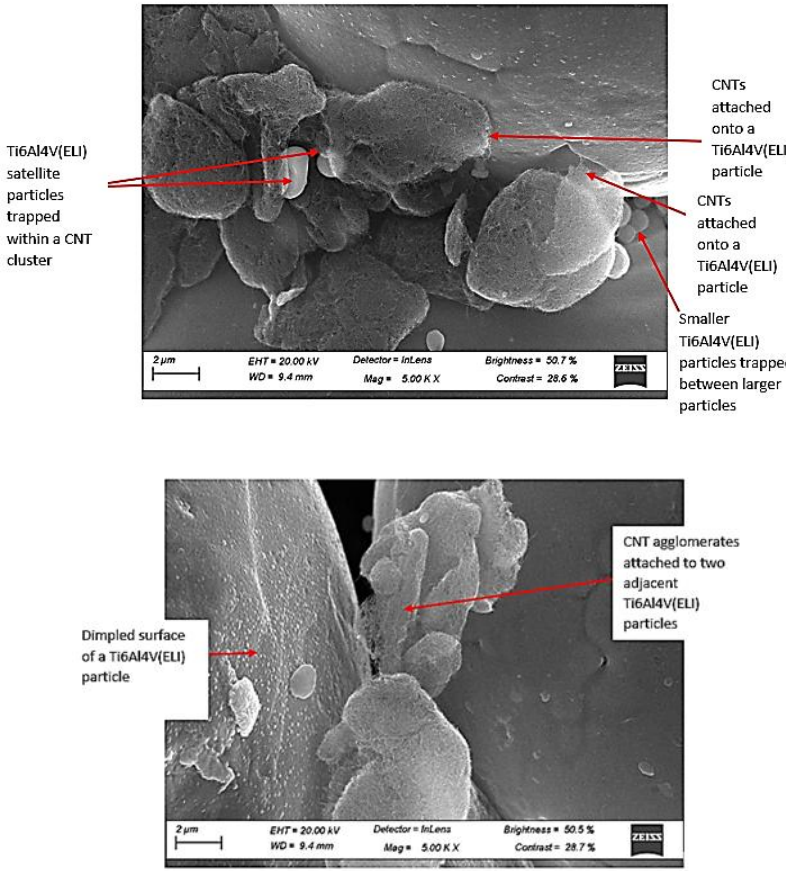

Figure 5.16 Attachments of CNTs to the surfaces of adjacent Ti6Al4V(ELI) particles at 5000x

© Central University of Technology, Free State

The attachment of CNTs in Figure 5.16 (right) was examined at a magnification of 5000x and within a smaller area, as shown in Figure 5.17. The attachment was viewed from a different position and was seen to be lodged between two adjacent Ti6Al4V(ELI) particles.

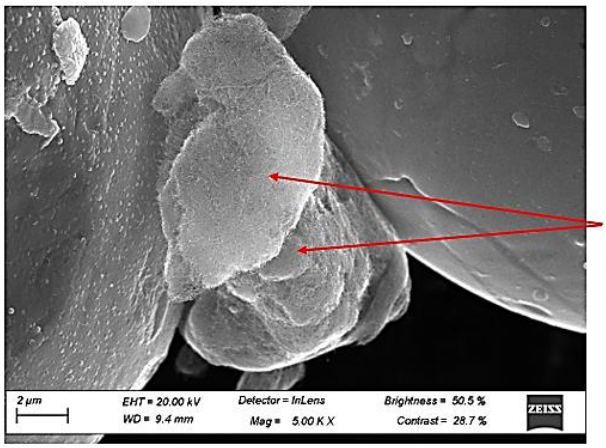

Figure 5.17 CNT cluster lodged between two Ti6Al4V(ELI) particles at 5000x

Several particles of Ti6Al4V(ELI) in a sample of 15 % vol. CNTs in Ti6Al4V(ELI) revealed defects at this volume fraction of CNTs in Ti6Al4V(ELI). In Figure 5.18(a), the particle circled in red showed an acorn-like structure. Figure 5.18(b) shows what appears to be a particle smeared on the surface of another particle, with damage on its surface and located next to another particle with surface damage. The presence of satellites on and agglomerates of CNTs around the particles of Ti6Al4V(ELI) was noted.

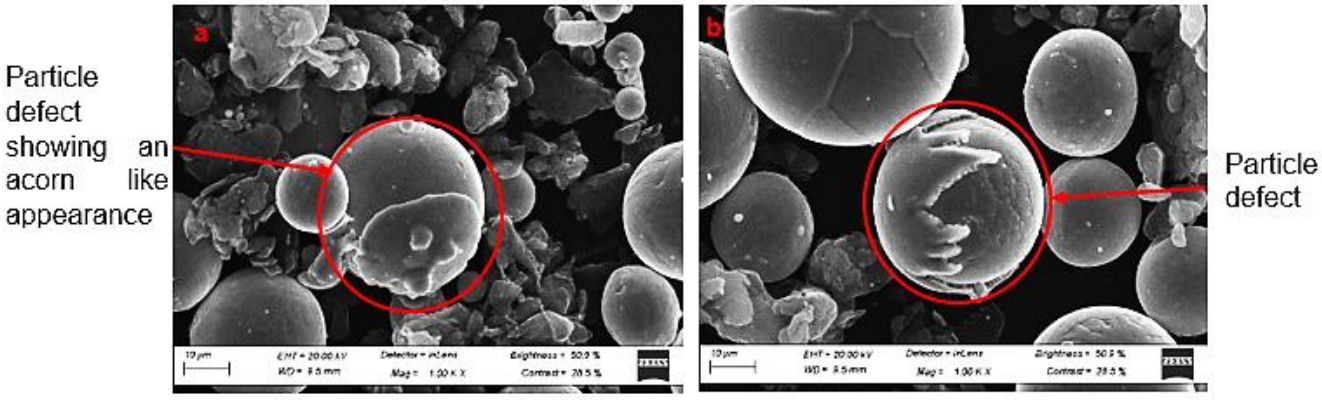

Figure 5.18 Scanning electron microscope image of a Ti6Al4V(ELI) particle defects at 1000x

The particle defect in Figure 5.18(b) was magnified to 5000x, with the result shown in Figure 5.19(a), which highlighted the presence of smaller particles trapped beneath

© Central University of Technology, Free State

the particle that was smeared on the surface of the particle below it. In Figure 5.19(b), a similar particle defect to the one in Figure 5.18(a) was observed, also having an irregular edge and carrying another smeared particle on top of it. Several satellite particles were also seen in the figure.

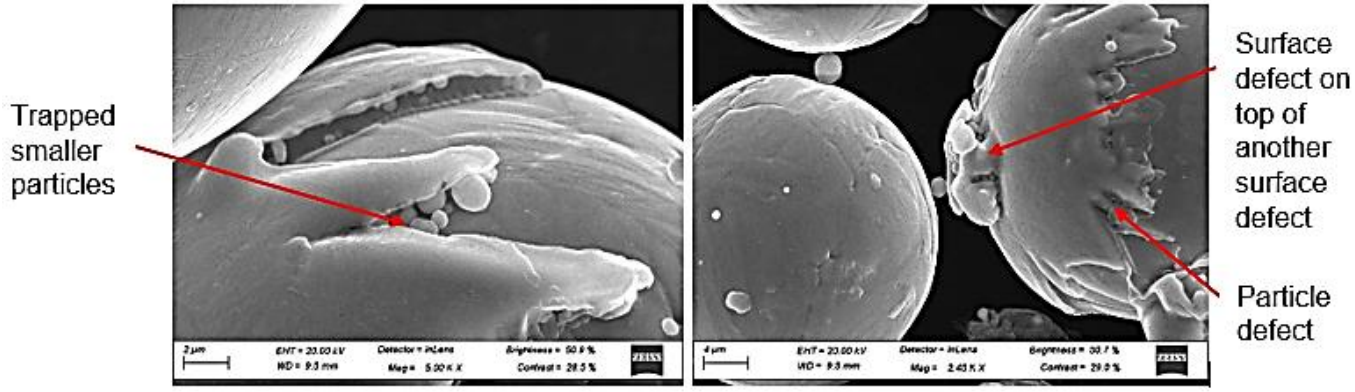

Figure 5.19 Scanning electron microscope image of a Ti6Al4V(ELI) particle defect at 5000x

In Figure 5.20 (at 20% vol. of CNTs), a Ti6Al4V(ELI) particle defect was found, showing a ripple collapse, possibly due to the impact of the steel tool used in manual mixing. The end of the particle with ripples was thought to have been the one impacted by the mixing tool, while the other end showed signs of surface damage. Three particles located near the particle with ripple failure also showed signs of surface damage. Several free-standing agglomerates of CNTs and one that appeared attached to two Ti6Al4V(ELI) particles were noted.

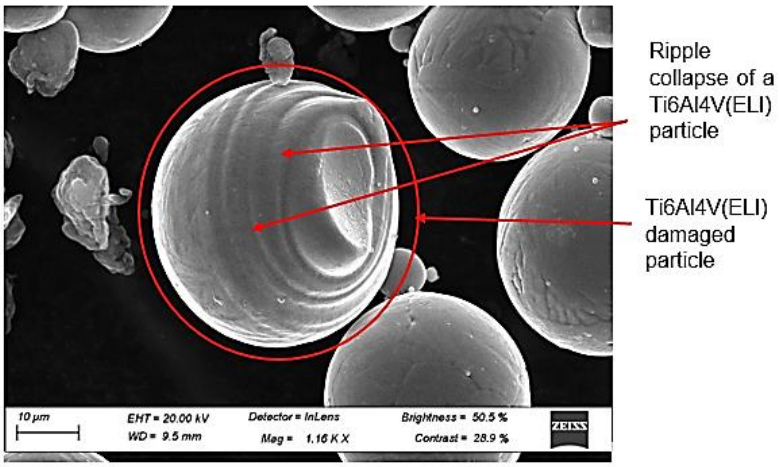

Figure 5.20 Scanning electron microscope image showing damaged Ti6Al4V(ELI) particles

© Central University of Technology, Free State

At 1000x magnification, surface damage was seen on a large number of Ti6Al4V(ELI) particles in the 25 % vol. CNTs in the Ti6Al4V(ELI) sample shown in Figure 5.21. This is thought to have been caused by increased manual mixing in this process.

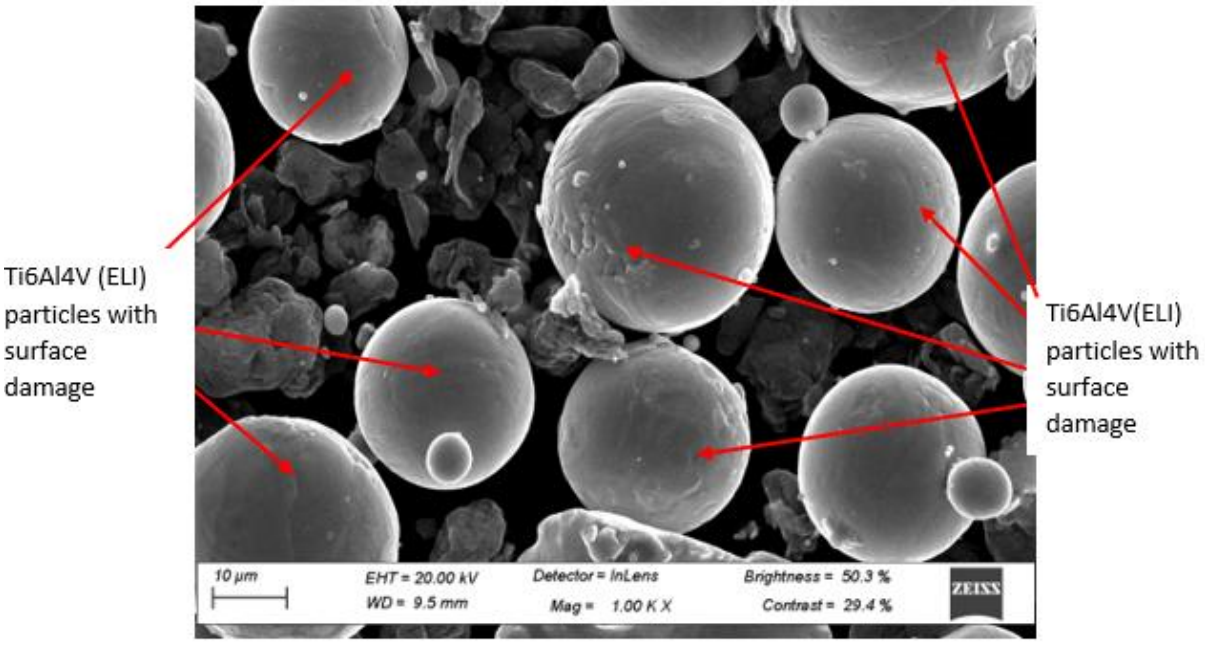

Figure 5.21 Scanning electron microscope image of 25 % vol. CNTs powder sample in Ti6Al4V(ELI) at 1000x

In Figure 5.22(a), some Ti6Al4V(ELI) particles appeared to have merged. The merged particles were of different sizes, and the smaller one of the two had a satellite particle on top of it. The SEM image in Figure 5.22(b) gives closer details of the CNT agglomerate occurring in between three adjacent Ti6Al4V(ELI) particles shown in Figure 5.35(a). The agglomerate attached itself to the lower surface of the larger particle and to the upper surface of the particle below it and the right.

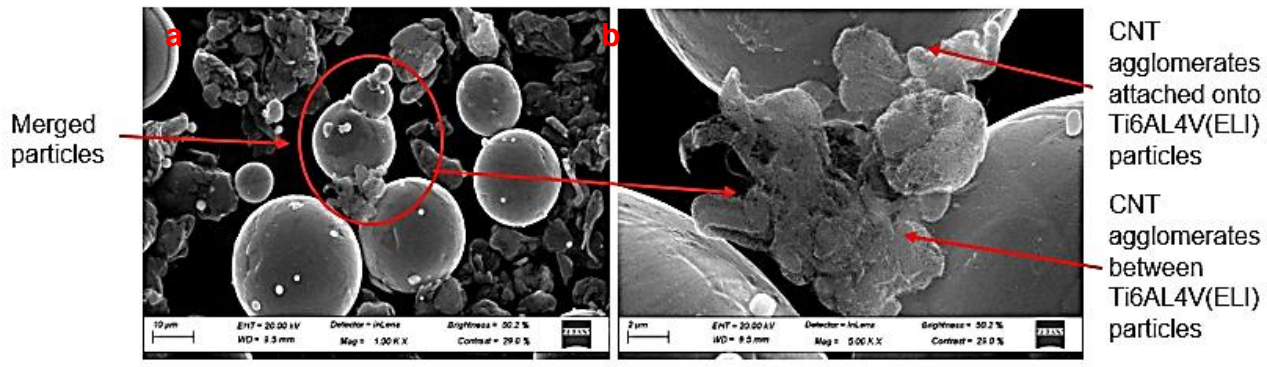

Figure 5.22 Scanning electron microscope image of 25 % vol. CNTs powder sample in Ti6Al4V(ELI) 1000x

In Figure 5.23(a), a particle defect (highlighted in yellow). However, in this sample, there were defects completely different from the foregoing ones, showing extreme

© Central University of Technology, Free State

deformation and damage over the entire surface, which appeared broken up into little pieces, as is evident in Figures 5.36(a & b).

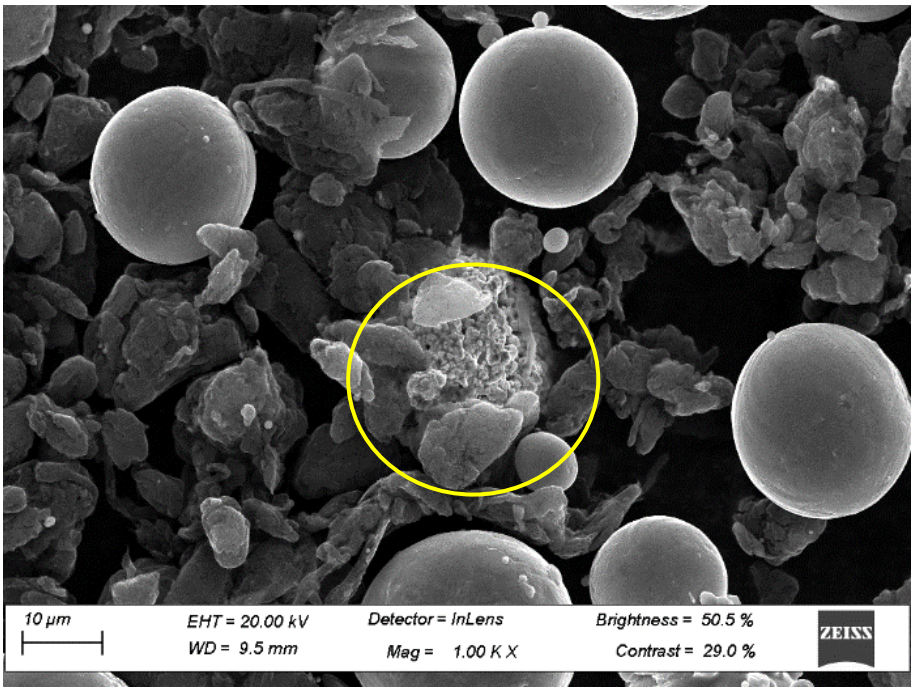

Figure 5.23 Scanning electron microscope image of 25 % vol. CNTs powder sample in Ti6Al4V(ELI) 500x

Magnifying the damaged particle, circled in Figure 5.23, 10 times to 5000x generated the image shown in Figure 5.24(a). The figure shows that the particle has shattered into small pieces on its surface and body. Figure 5.24(b) further provides a magnified view of this anomaly. This is thought to have been a result of excessive impact due to the extra round of manual mixing used.

© Central University of Technology, Free State

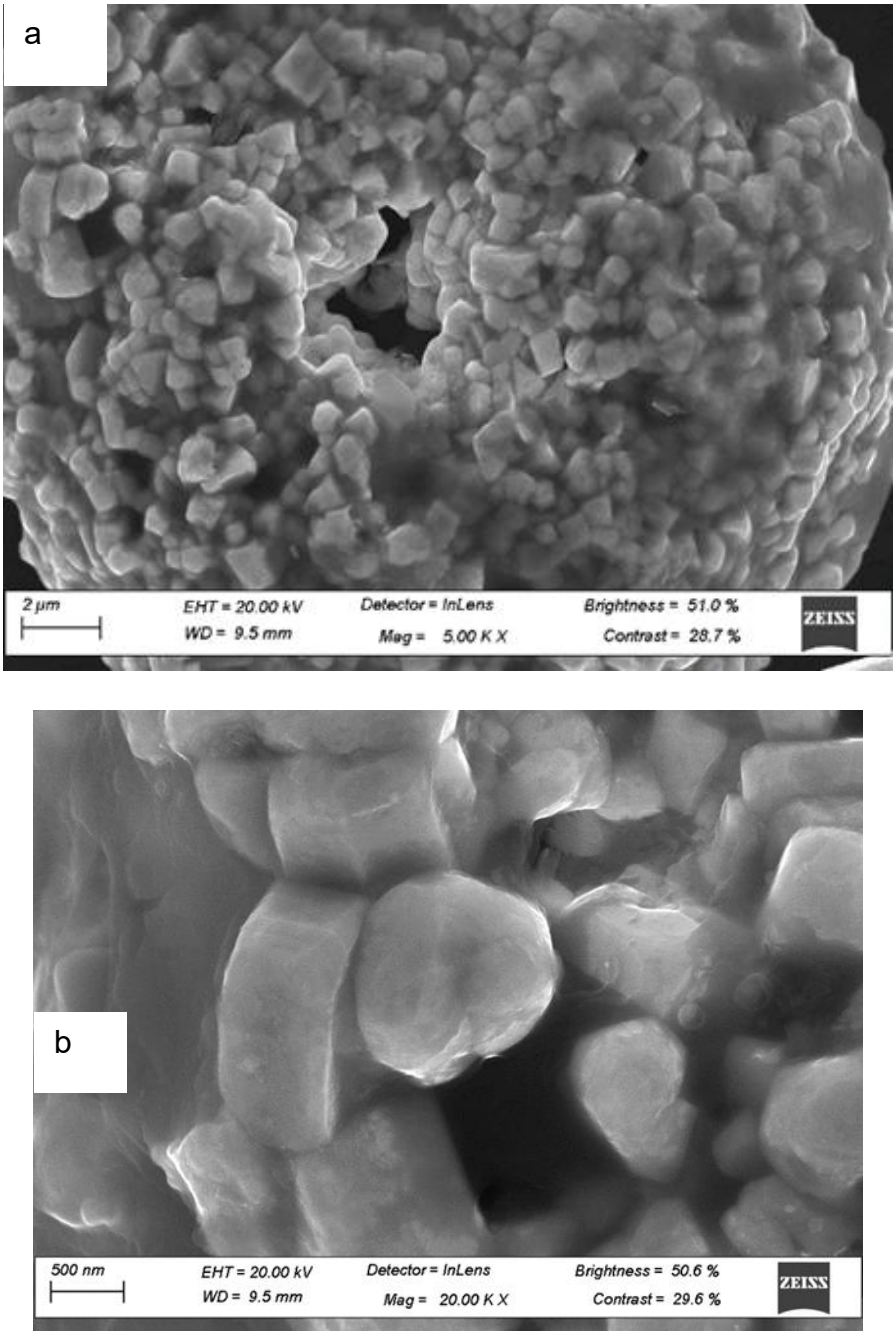

Figure 5.24 Scanning electron microscope image of 25 % vol. CNTs powder sample in Ti6Al4V(ELI) 5000x

To ascertain the presence of the particle defect in Figure 5.24 (a-b) similar defects were obtained at 8% vol. of CNTs as shown in Figure 5.25 (highlighted in yellow).

© Central University of Technology, Free State

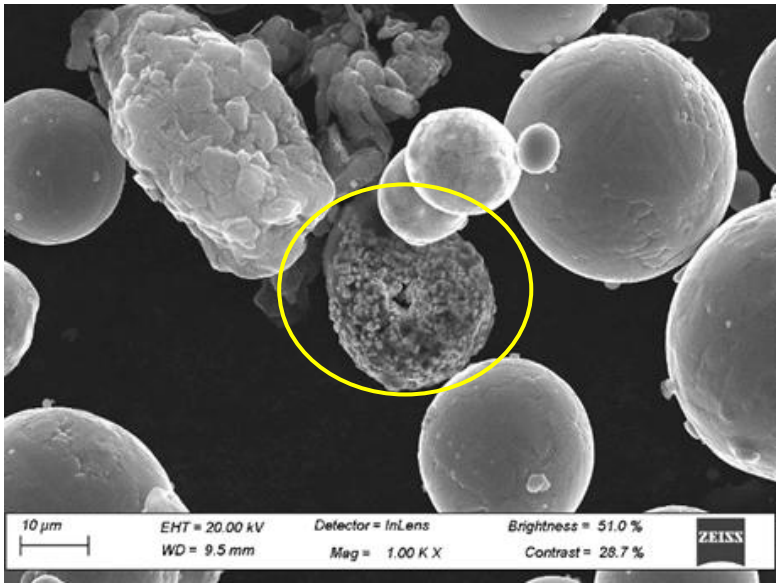

Figure 5.25 Observed particle defect in 8% vol. of CNTs in Ti6Al4V

At 1000x magnification, Figure 5.26 showed the presence of four deformed Ti6Al4V(ELI) particles with surface damage that appeared fused together in a cluster, with one of them showing ripple failure similar to the one observed in Figure 5.26. This was attributed to the increased time of manual mixing applied to compensate for the increased vol.% of CNTs in the Ti6Al4V(ELI) to increase dispersion and reduce agglomeration.

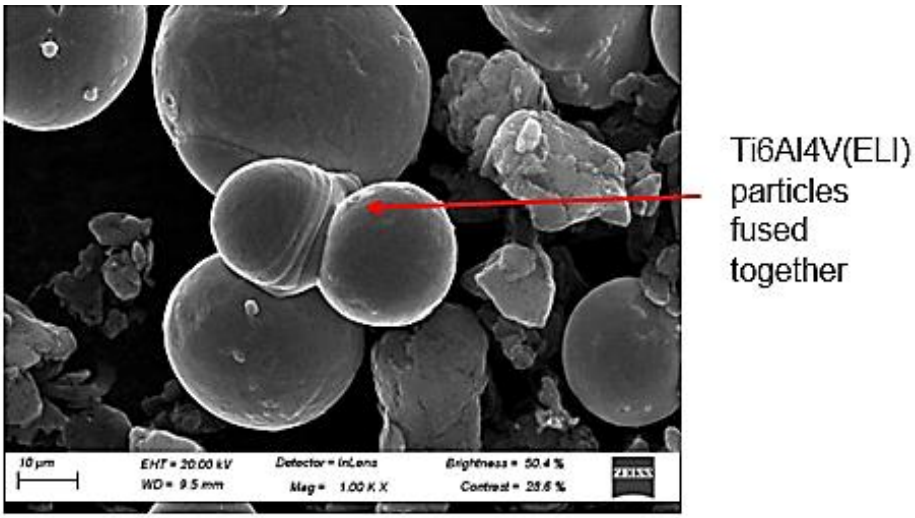

Figure 5.26 Scanning electron microscope image of particle damage at 25 % vol. CNTs powder sample in Ti6Al4V(ELI) at 1000x

To support the conclusions arrived at regarding the influence of the mixing tool on the damage impact of Ti6Al4V(ELI) particles Figure 5.27 was analysed.

© Central University of Technology, Free State

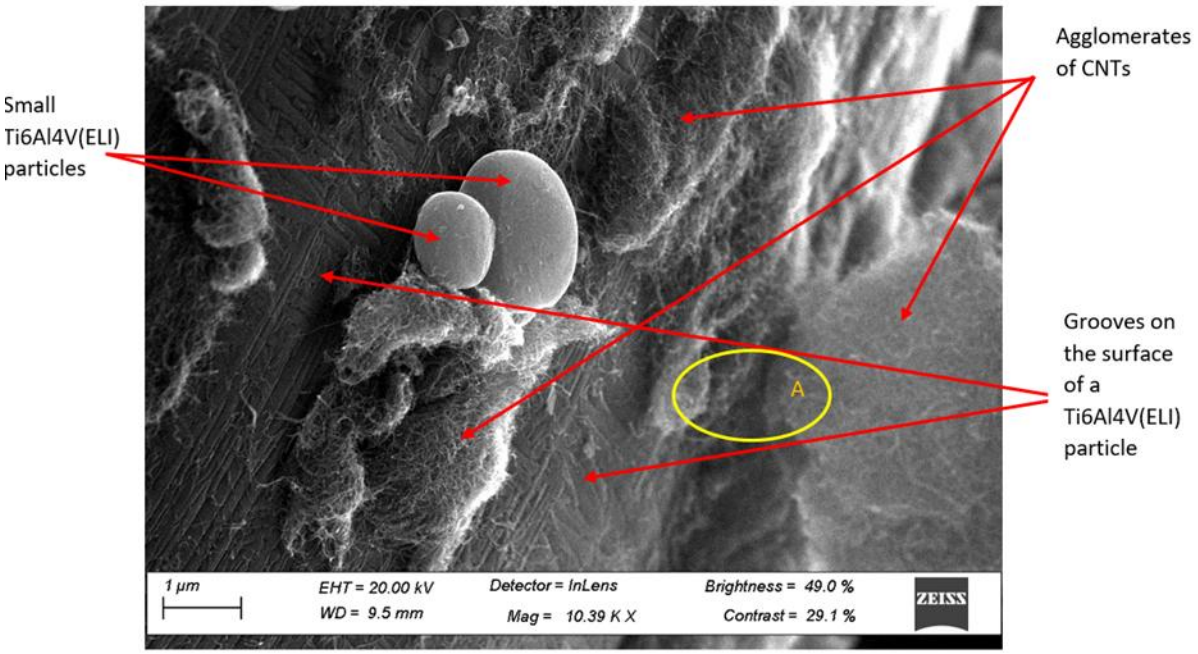

Figure 5.27 Impact of mixing tool of Ti6Al4V(ELI) particle surface

From Figure 5.27 the presence of grooves which are not consistent with normal Ti6Al4(ELI) particles are present. Also, the presence of defects was not observed in the preliminary samples due to shorter mixing times (10min) versus with secondary mixing where longer mixing times (30min) were applied. This allows the conclusion that the tool used caused these defects.

5.4.3.2 Conclusions

Dispersion of CNTs was achieved at all the volume fractions of CNTs. However, the size and number of agglomerates increased with increasing volume fraction of CNTs. The analysis showed that dispersion is effective at low-volume fractions of reinforcement. Although this method of mixing provided better results with better dispersion and less tendency of CNTs to aggregate, it exhibited a higher number of deformed Ti6Al4V(ELI) particles, some of which had ripple failure and others that were broken up with very severe damage. This is thought to have been caused by the increased time for manual mixing carried out following turbula mixing in an effort to correct the segregation of powders caused by turbula mixing. Numerous cases of Ti6Al4V(ELI) particles appearing to be linked to one another by CNTs were observed, as well as others that appeared fused to one another. Clearly, manual mixing that minimises impact needs to be sought to minimise such damage and deformation. In

© Central University of Technology, Free State

this case, more damage is seen in the Ti6Al4V(ELI) spherical particles than in manual mixing. This is thought to be a result of the further manual mixing carried out in this case. There also appears to be increased attachment of CNTs to the Ti6Al4V(ELI) particles, less aggregation of CNTs and improved dispersion of the CNT agglomerates in this combined method of mixing of the two powders than for manual mixing.

References

1. Kim, W. J. and Lee, S. H., 2014. High-temperature deformation behavior of carbon nanotube (CNT)-reinforced aluminum composites and prediction of their high-temperature strength. *Composites Part A: Applied Science and Manufacturing*, *67*, pp. 308–315. https://doi.org/10.1016/j.compositesa.2014.09.008
2. Goutianos, S. and Peijs, T., 2021. On the low reinforcing efficiency of carbon nanotubes in high-performance polymer fibres. *Nanocomposites*, *7*(1), pp. 53–69. https://doi.org/10.1080/20550324.2021.1917815
3. Ramezani, M., Dehghani, A. and Sherif, M.M., 2022. Carbon nanotube reinforced cementitious composites: A comprehensive review. *Construction and Building Materials*, *315*, pp.125100.

© Central University of Technology, Free State

CHAPTER 6 - INVESTIGATING THE USE OF THREE DIFFERENT METHODS OF MIXING CNTS AND TI6AL4V(ELI) POWDERS WITH SDS AS A SURFACTANT

Some of the material contained in this chapter has been presented at conference proceedings as follows:

M. Mashabela, M. Maringa, T.C. Dzogbewu, "Investigating the effect methanol and ethanol have on the dispersion of carbon nanotubes in Ti6Al4V(ELI)", The Sustainable Research and Innovation Conference, College of Engineering and Technology, Jomo Kenyatta University of Agriculture and Technology (JKUAT), Juja, 4th– 5th October 2023, https://sri.jkuat.ac.ke/ (accepted and presented).

.

6.0 Summary

The work presented in this chapter is a continuation of previous work on the use of different methods of mixing CNTs and Ti6Al4V(ELI) powders using different processing agents, as discussed in Chapters 4 and 5. In this chapter, an SDS surfactant was used to enable dispersion of CNTs in Ti6Al4V(ELI) at volume fractions of 3 %, 8 %, 15 %, 20 %, 25 %, and 30% of the CNTs. Dispersion of CNTs was effective at the low-volume fractions of 3 % and 8 %, which is where individual CNT fibres were detected (Figure 6.15 and Figure 6.18). Increasing the volume of CNTs in Ti6Al4V(ELI) with this surfactant caused the formation of CNT sheets. This resulted in the potential reduction of the effectiveness of reinforcement of Ti6Al4V(ELI) with CNTs due to a reduction in the surface areas available for interfacial bonding between CNTs and Ti6Al4V(ELI) vis-a-vis the case of a single CNT. Clusters of CNT and Ti6Al4V(ELI) particles were found at all volume fractions of CNTs. There was an increase in the size of clusters or agglomerates with an increasing volume fraction of CNTs. The presence of a surfactant was expected to reduce the surface tension of Ti6Al4V(ELI) particles and, in this way, allow for easy attachment of CNTs. There were higher incidences of attachments across all samples using SDS than in the cases reported in previous chapters without it, regardless of the mixing technique, pointing to the effectiveness of SDS as a surfactant. However, the formation of CNT agglomerates was expected to minimise this effect as not all the available surfaces of each CNT would be available for interfacial bonding with particles of Ti6Al4V(ELI). The presence of large agglomerates of CNTs was also expected to affect AM of the composite during levelling of layers of powder and fusion, the latter due to the different thermal properties of CNTs and Ti6Al4V(ELI).

© Central University of Technology, Free State

6.1 Introduction

Three mixing techniques were used to achieve homogenous powder mixtures of CNTs and Ti6Al4V(ELI) matrix. SDS was used as a surfactant to coat the CNTs, thus reducing their surface tension and that of Ti6Al4V(ELI) particles, allowing easier attachment to one another. Part of the reason for the use of this surfactant was to try and achieve effective dispersion of individual CNTs in Ti6Al4V(ELI). Attaining good interfacial adhesion and large surface areas between CNTs and matrices, which supports effective load transfer, is a prerequisite to obtaining materials with enhanced mechanical properties.

The effects of the separate use of acetone and ethanol together with sonication for mixing CNTs and Ti6Al4V(EI) particles, as well as the manual mixing of the dry powders on their own, were reported and discussed in Chapter 4. It was shown that manual mixing on its own led to the formation of large agglomerates of CNTs. The use of acetone and sonication resulted in the formation of smaller clusters of CNTs, while the use of ethanol and sonication led to the formation of the smallest clusters of CNTs with the best dispersion.

In Chapter 5, the outcome of using ethanol as a dispersion agent was reported, together with the three methods of mixing: mechanical, turbula, and combined mixing. The mixtures obtained with ethanol as a dispersion agent were generally seen to have the lowest dispersion and largest CNT agglomerates for turbula mixing. The best dispersion and smaller clusters of CNTs were found in the case of combined mixing.

The reported presence of agglomerates of CNTs using acetone and ethanol as dispersion agents and for the three methods of mixing in these two chapters indicated the need to explore further avenues of increasing the separation and dispersion of CNTs. This led to the use of SDS, a surfactant, to further enhance dispersion.

A major obstacle to the dispersal of CNTs in aqueous solutions using surfactants, for instance, is the fact that CNTs aggregate into bundles because of van der Waals forces, which results in poor dispersion of CNTs within most aqueous media (Yang et al., 2023). It has been shown in the literature that in aqueous media, ultrasonication leads to enough SDS molecules penetrating gaps between CNTs in a bundle. WFurther congregation of the surfactant at such gaps, they become enlarged until

© Central University of Technology, Free State

dispersion of the nanotubes is achieved (Duan et al., 2011). Mechanical agitation by ultrasonication produces temporary dispersal of CNTs in aqueous media but is, however, often followed by agglomeration of the dispersed CNTs due to the presence of van der Waal forces (Pillari et al., 2023).

Surfactants disperse CNTs in aqueous solutions mainly through hydrophobic/hydrophilic interactions, in which the hydrophobic tail of a surfactant molecule adsorbs on the surface of CNT bundles, while its hydrophilic head associates with water for dissolution (Yang et al., 2023). Strano et al. (2003) visualised a three-stage surfactant dispersion mechanism starting with (i) the initial bundles of CNTs before the application of any surfactant. This is followed by (ii) ultrasonication that provides high local shear to fray the CNT bundle ends and hence create a gap between CNTs. Then comes (iii) the adsorption of the molecules of the surfactant into the gap created, thus keeping any two adjacent CNT entities partially separated in what is also referred to as unzippering of the CNTs. Finally, as the individual CNTs move relative to one another in a bundle through Brownian motion, (iv) the surfactant continues to progress along the length of CNTs until their complete separation occurs. This is visualised using the schematics shown in Figure 6.1. From an energy point of view, there are three distinct statuses in terms of the interaction between SDS molecules and CNTs in this visualisation, namely the bundle, micelle, and unzippering statuses. In the bundle status, CNTs are aggregated in a bundle in which tube-tube interaction is dominant. In the micelle status, the individual CNTs are coated with SDS molecules, and the interaction between SDS molecules and CNTs becomes important. In the unzippering status, CNT bundles are unzipped with the adsorption of SDS molecules around the gaps between CNT bundles caused by ultrasonication. Both ultrasonic energy and adsorption energy between the SDS molecules and CNTs are required, leading to a final dispersion of the CNT bundle (Strano et al., 2003).

© Central University of Technology, Free State

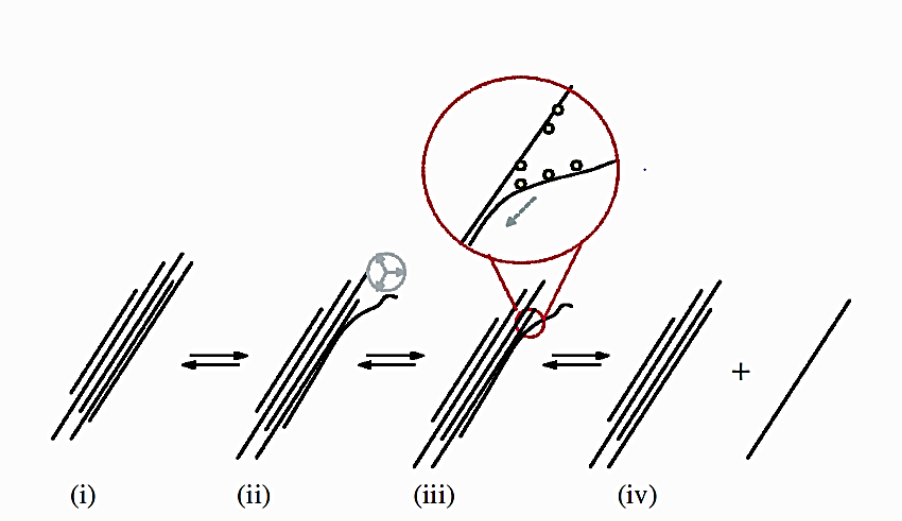

Figure 6.1 Proposed mechanism of the dispersion of CNTs upon the application of a surfactant showing stages (i)–(iv) of the process on the site of fraying and (iv) release of isolated, surfactant-coated nanotube (Strano et al., 2003)

6.2 Results and Analysis

The ensuing material uses SEM images to discuss the results for the three methods of mixing at 3 %, 8 %, 15 %, 20 %, 25 %, and 30 % CNT/Ti6Al4V(ELI) mixtures.

6.3 Analysis of Dispersion and Agglomeration of CNTs for Mechanically Mixed Powder Samples of Different Volume Fractions of CNTs in Ti6Al4V(ELI), using SDS as a Surfactant

Analysis of SEM images of samples that were mixed mechanically for volume fractions of CNTs of 3 %, 8 %, 15 %, 20 %, 25 %, and 30 % in Ti6Al4V(ELI), carried out to determine the dispersion of CNTs and homogeneity of powder mixtures, and to identify defects on and attachment of CNTs to Ti6Al4V(ELI) particles is now presented. The SEM images were captured from these samples at the same magnification of 300x. Figure 6.2(a–f) represents the mixed samples of powder at different volume fractions of CNTs in Ti6Al4V(ELI) from 3 %–30 %.

© Central University of Technology, Free State

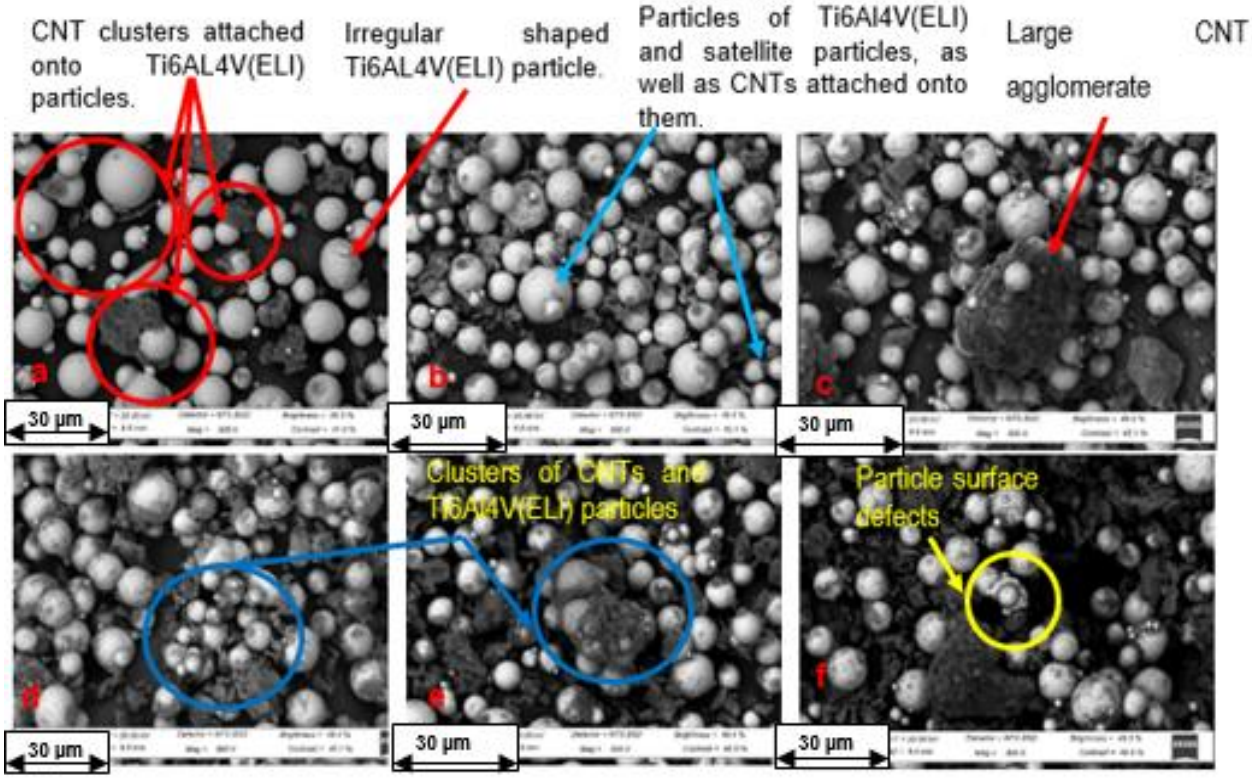

Figure 6.2 Dispersion of CNTs in Ti6Al4V(ELI) at (a) 3 % vol. of CNTs, (b) 8 % vol. of CNTs, (c) 15 % vol. of CNTs, (d) 20 % vol. of CNTs, (e) 25 % vol. of CNTs, and (f) 30 %

The micrographs in this figure showed good dispersion of CNTs agglomerates in Ti6Al4V(ELI), except for 3 % vol. of CNTs in Ti6Al4V(ELI), where very few CNTs agglomerates occurred, and there were many areas with no particles. With the exception of the sample of 3 % vol. CNTs mixed in Ti6Al4V(ELI), the samples of all the other volume fractions showed particles of Ti6Al4V(ELI) coated with CNTs. Clusters of CNTs and Ti6Al4V(ELI) particles were also observed for all volume fractions of CNTs, whose incidence appeared to increase with increasing volume fraction of CNTs. This is a concern for AM as it is likely to lead to uneven spreading and packing density of powder. It is also expected to affect the melting of powder, as some particles of Ti6Al4V(ELI) will receive different quantities of power depending on the amount of CNTs surrounding them. The result is a rise in the presence of defects in printed parts. Compared to the cases reported in Chapters 4 and 5, where acetone and ethanol were used as dispersants, the use of SDS as a surfactant here, in addition to ethanol as a dispersant, did lead to increased dispersion of CNTs and increased coating of Ti6A4V(ELI) particles with CNTs. These two phenomena were expected to

© Central University of Technology, Free State

have been a result of the function of the SDS surfactant of reducing the surface tension of both types of particles, thus promoting better dispersions and adherence of CNTs to the surfaces of Ti6Al4V(ELI) particles and enabling their dispersion and easy attachment to Ti6Al4V(ELI) particles. However, the presence of CNT agglomerates in the CNT/Ti6Al4V(ELI) mixtures at all volume fractions of CNTs shows that even after the dispersion of CNTs with the addition of SDS powder, they did re-agglomerate as reported in the literature. This calls for further research into ways of minimising this occurrence.

6.3.1 Visual Analysis of Particle Defects at Different Volume Fractions of CNTs in Manual Mixed Sample

In the following section, the particle defects are discussed. In the cases where other volume fractions are not mentioned, no particle defects were detected in those volume fractions of CNTs. Figure 6.3 (a–c) highlights Ti6Al4V(ELI) particle defects at different volume fractions of CNTs.

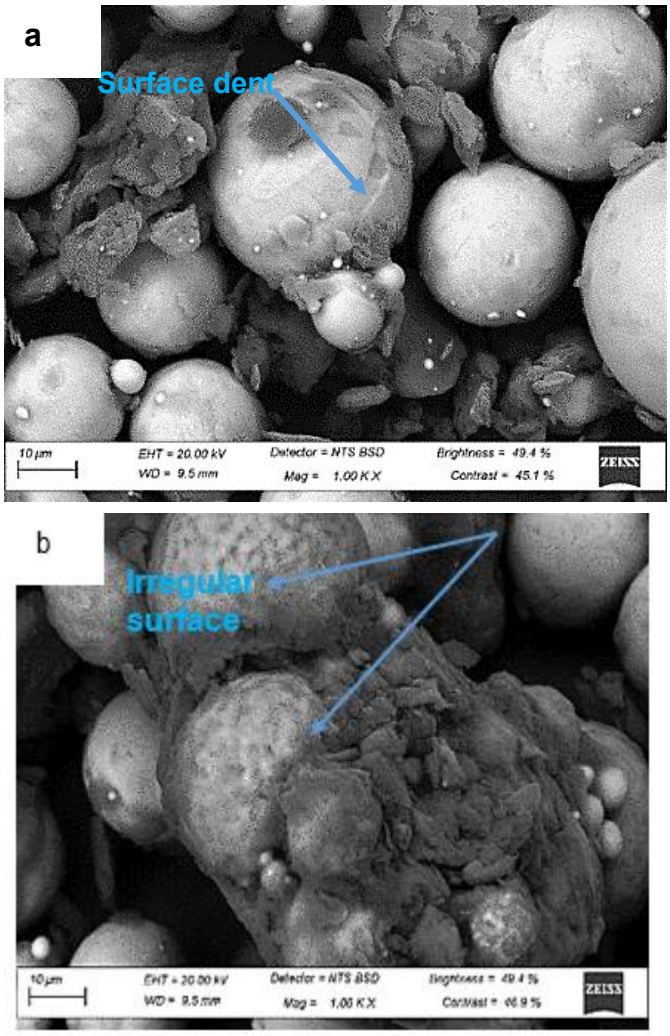

© Central University of Technology, Free State

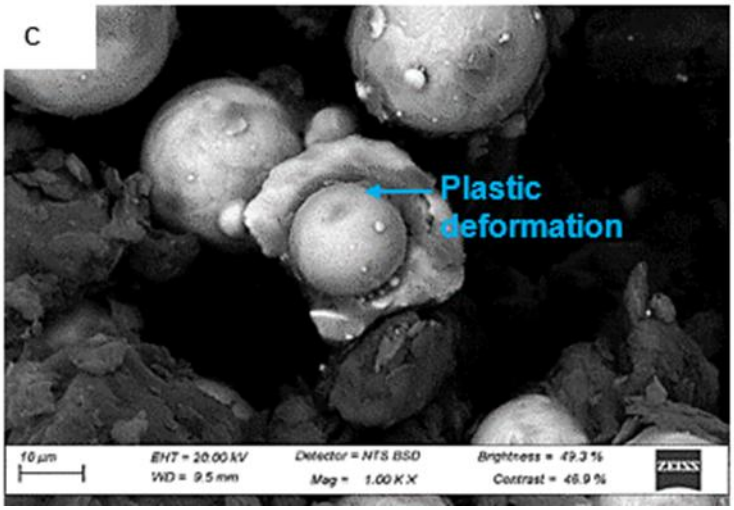

Figure 6.3 Defects in Ti6Al4V(ELI) particles at (a) 8 % vol. of CNTs (b) 25 % vol. of CNTs (c) 30 % vol. of CNTs

In Figure 6.3(a), a particle defect was observed at 8 % vol. of CNTs in Ti6Al4V(ELI) in the form of a surface dent that is likely to have occurred during the mixing process. Particle defects were seen in Figure 6.3(b) at 25 % vol. of CNTs in Ti6Al4V (ELI), which appear in the form of irregular surface morphologies. In Figure 6.3(c), a severely deformed particle was observed at 30 % vol. of CNTs in Ti6Al4V(ELI).

The nature of the defect in Figure 6.3(a) was likely due to the force applied to the surface during mixing. The irregular surface morphologies in Figure 6.3(b) were thought to be indications of shattering of the surfaces of Ti6Al4V(ELI) particles due to impact. The severely deformed Ti6Al4V(ELI) particle in Figure 6.3(c), which is semi-wrapped around another particle of regular spherical shape, likely arose from sustaining the pressure of the mixing tool during manual mixing.

The same severely deformed particle shown in Figure 6.3(c) was examined further at magnifications of 5000x and 10 000x, as shown in Figure 6.4 (a–b), respectively. Satellite particles occurred in between two Ti6Al4V(ELI) particles, a clear sign of no contact between them in this area. The presence of sheets of CNTs over all the particles of Ti6Al4V(ELI) was considered a good sign of the effectiveness of the SDS surfactant in reducing the surface tension of both types of particles in the mixture of powder.

© Central University of Technology, Free State

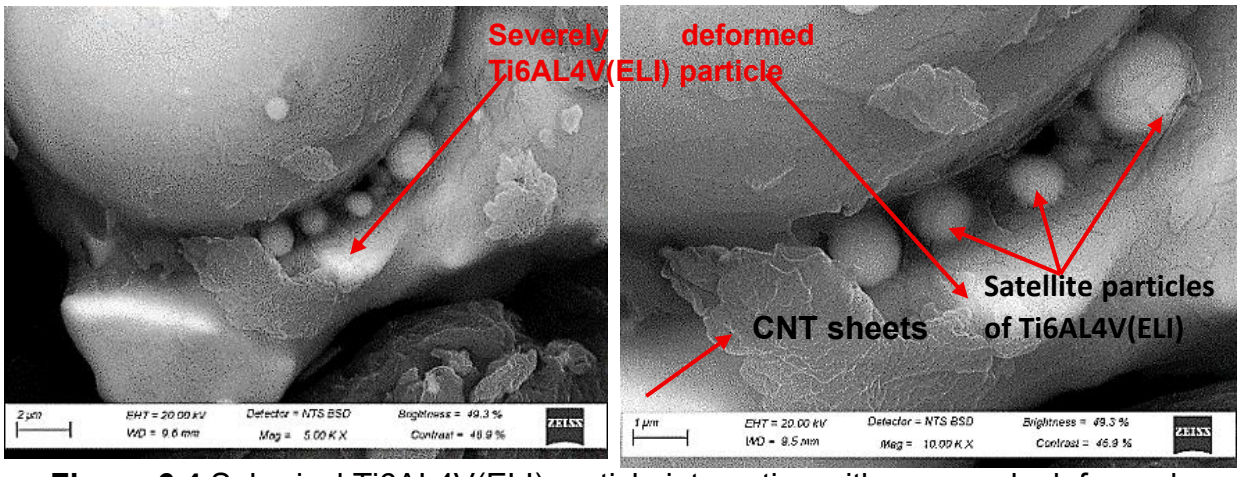

Figure 6.4 Spherical Ti6AL4V(ELI) particle interacting with a severely deformed Ti6Al4V(ELI) particle, with some satellite particles trapped in between the two, all covered by CNTs.

6.3.1.1 Visual Analysis of Attachments of CNTs to the Surfaces of Ti6Al4V(ELI) Particles at 3 % vol. of CNTs

The interaction between Ti6Al4V(ELI) particles and CNT agglomerates was examined for various volume fractions of CNTs, wherever it occurred. Micrographs for the 3 % vol. CNTs in Ti6Al4v(ELI), magnified to 10 000x and 20 000x, are presented in Figure 6.5(a–b).

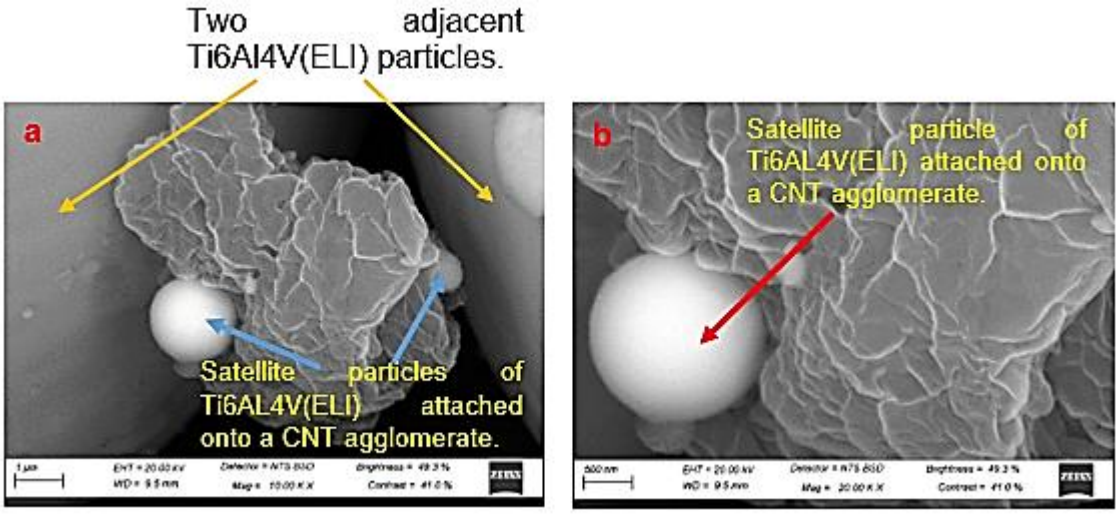

Figure 6.5 Surface attachment of a Ti6Al4V (ELI) satellite particle to a CNT agglomerate at 3 % vol. of CNTs in Ti6l4V(ELI)

In Figure 6.5(a), the surface of the large Ti6Al4V(ELI) particle on the left was seen to touch the adjacent CNT agglomerate that partially surrounded a small satellite particle of Ti6Al4V(ELI). The agglomerate occurring in between the two particles of

© Central University of Technology, Free State

Ti6Al4V(ELI) only touched the surface of the one on its left side. In Figure 6.5(b), the satellite particle is attached to a CNT agglomerate. At this magnification, the type of interaction between the two cannot be determined, and higher magnification would lead to an image with poor clarity.

Figure 6.6(a–c) shows cases of CNTs' attachment to particles of Ti6Al4V(ELI) at 3 % vol. of CNTs in Ti6Al4V(ELI).

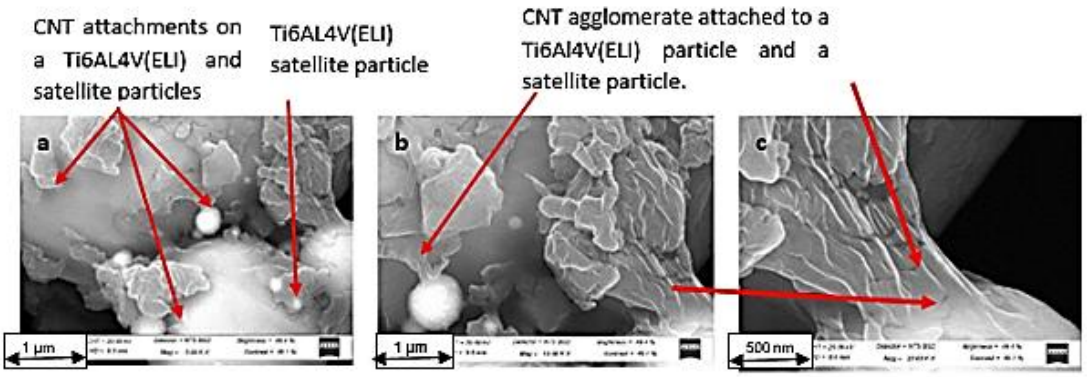

Figure 6.6 (a, b) Attachment of CNT agglomerates to Ti6Al4V(ELI) and satellite particles (c) CNT agglomerate attached between two Ti6Al4V(ELI) particles

In Figure 6.6(a–c), there were several incidences of close interaction/attachment between CNTs and Ti6Al4V(ELI) particles, as well as their satellites. In certain cases, CNT agglomerates were seen to bridge between two adjacent Ti6Al4V(ELI) particles.

6.3.1.2 Visual Analysis of Attachments of CNTs Onto the Surfaces of Ti6Al4V(ELI) Particles at 15 % vol. of CNTs

At 15 % vol. of CNTs in Ti6Al4V(ELI), a CNT agglomerate with a TI6Al4V(ELI) particle on top of it and others around it is circled in red in Figure 6.7(a), at 500x magnification. Several small particles of Ti6Al4V(ELI) on this CNT agglomerate can be seen. All the Ti6Al4V(ELI) particles appeared to have surface coatings of CNT agglomerates, a good sign confirmed in literature that the use of SDS caused CNTs to attach to Ti6Al4V(ELI) particles by reducing the surface tension on the surfaces of both types of particles.

© Central University of Technology, Free State

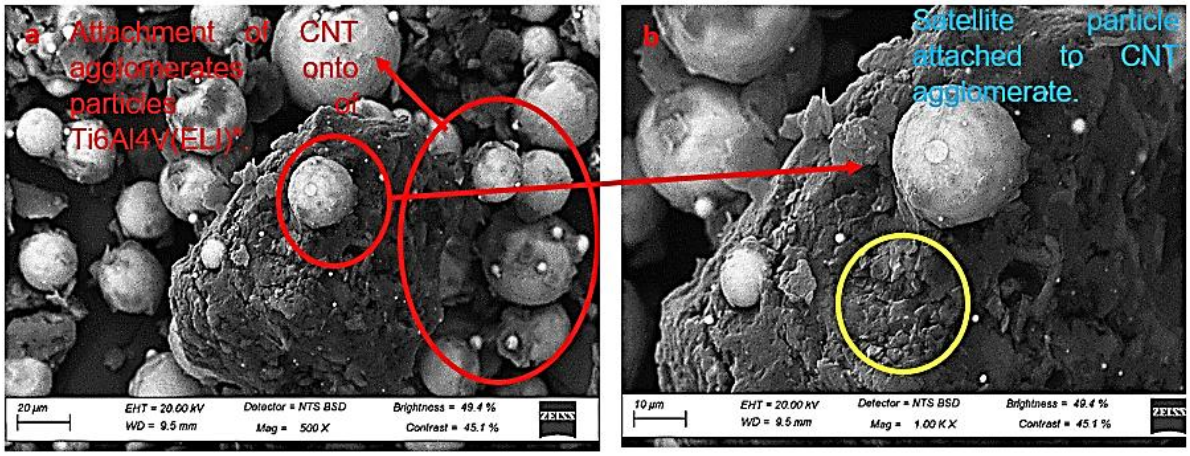

Figure 6.7 Attachments of CNT agglomerates to the surfaces of Ti6Al4V(ELI) particles at 15 % vol. of CNTs in Ti6Al4V(ELI)

Further magnification of the area indicated in Figure 6.7(b) by the yellow circle at a magnification of 20 000x gave rise to the image shown in Figure 6.8. In this figure, no individual fibres were visible, but CNTs appeared as wrinkled sheets. Clearly, the use of SDS and manual mixing did not lead to the separation of individual nanotubes from the agglomerate but rather the formation of these wrinkled sheets.

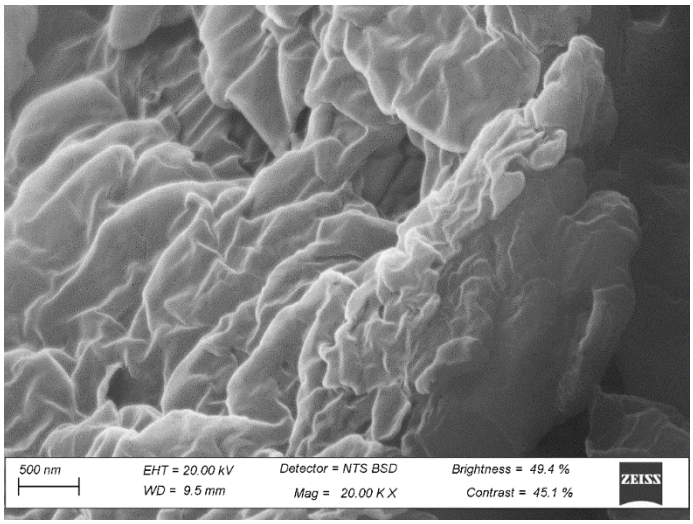

Figure 6.8 Appearance of wrinkled carbon sheets at a magnification of 20 000x at 15 % of CNTs in Ti6Al4V(ELI)

6.3.1.3 Visual Analysis of Attachments of CNTs to the Surfaces of Ti6Al4V(ELI) Particles at 20 % vol. of CNTs

In Figure 6.9, attachments of CNT agglomerates covering a Ti6Al4V(ELI) particle and satellite particles were found at 20 % vol. of CNTs in Ti6Al4V(ELI). Satellites that were not visible at a lower magnification of 300x in Figure 6.2d were visible in Figure 6.9 (a and b) at the higher magnification of 5000x and 10 000x, respectively. CNTs covered

© Central University of Technology, Free State

the particles of Ti6Al4V(ELI) in the form of folded sheets. At the highest magnification of 20 000x (Figure 6.9c), CNTs appear as crumpled sheets.

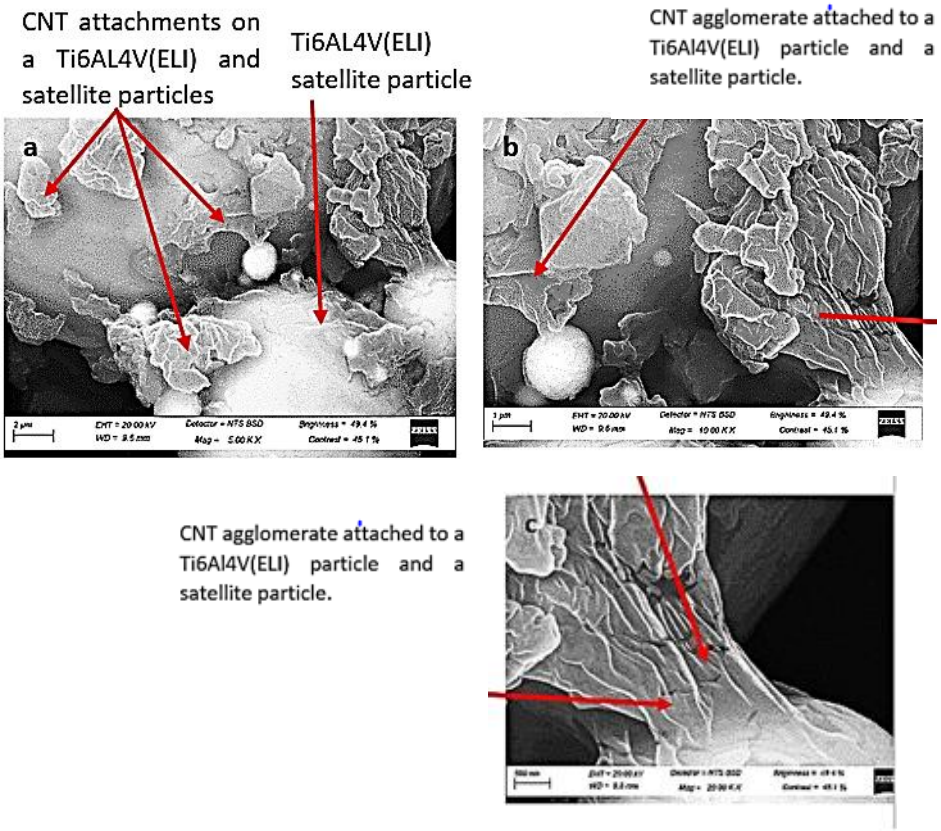

Figure 6.9 Carbon sheets covering particles of Ti6Al4V(ELI)

6.4 Visual Analysis of SEM Images at Different Volume Fractions of CNTs for Turbula Mixed Samples

Samples mixed using a turbula mixer were analysed for volume fractions of CNTs of 3 %, 8 %, 15 %, 20 %, 25 %, and 30 % in Ti6Al4V(ELI) matrices. SEM images were captured at the same magnification of 300x and analysed to facilitate comparison of dispersion and homogeneity of CNTs, as well as particle defects in the mixtures.

Figure 6.10(a–f) represents the mixed powder samples for different volume fractions of CNTs in Ti6Al4V(ELI).

© Central University of Technology, Free State

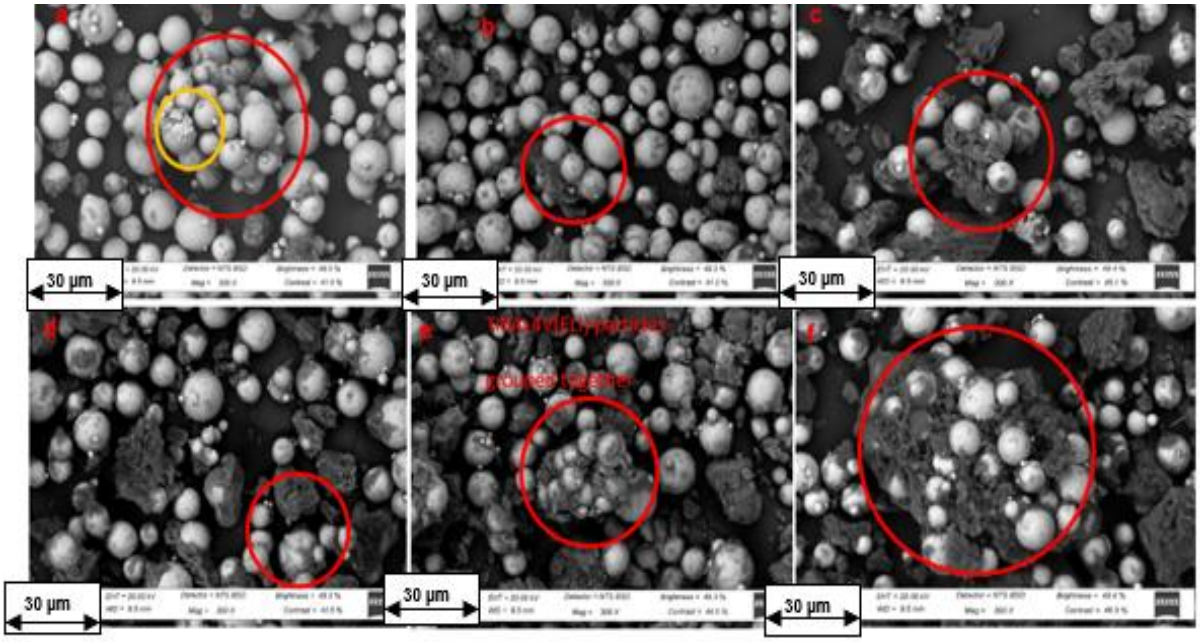

Figure 6.10 Dispersion of CNTs in Ti6Al4V(ELI) at (a) 3 % vol. of CNTs, (b) 8 % vol. of CNTs, (c) 15 % vol. of CNTs, (d) 20 % vol. of CNTs, (e) 25 % vol. of CNTs, and (f) 30 % (vol. of CNTs

The SEM images in Figure 6.10 show the presence of CNT agglomerates on the surfaces of all Ti6Al4V(ELI) particles, except at 3 % vol. of CNTs in Ti6Al4V(ELI) (Figure 6.10(a)), where the phenomenon was limited to a much smaller number of particles. Clusters of CNT agglomerates and Ti6Al4V(ELI) particles were seen in the micrographs for all CNT volume fractions except at 3 %, some of which are indicated within red circles in Figure 6.10. The CNT clusters increased in number and size as the volume fraction of CNTs in Ti6Al4V(ELI) increased. This tendency was expected to affect both levelling and packing of powder, as well as laser melting, as discussed in the previous section. The tendency of grouping of CNT agglomerates together with Ti6Al4V(ELI) particles was the lowest at 20 % vol. of CNTs in Ti6Al4V(ELI) and highest at 25 % and 30 % vol. of CNTs in Ti6Al4V(ELI).

During turbula mixing, the rotation speed of the mixer was the only factor affecting the interaction of CNTs and Ti6Al4V(ELI) particles. From the foregoing images and related discussions, as well as the contents of the previous subsection, the use of SDS and ethanol combined with turbula mixing was not as successful in dispersing CNTs as the use of SDS, ethanol and manual mixing.

© Central University of Technology, Free State

6.4.1. Visual Analysis of SEM Images to Study the Interaction Between Ti6Al4V(ELI) Particles and Between Them and CNTs for Different Volume Fractions of CNTs

The mixtures of CNTs and Ti6l4V(ELI) particles were analysed through visual inspection of their mixtures to determine if any attachments of CNTs to and interaction between particles of Ti6Al4V(ELI) of Ti6Al4V(ELI) could be found.

The interactions are shown in Figure 6.11 for all volume fractions of CNTs considered in this subsection.

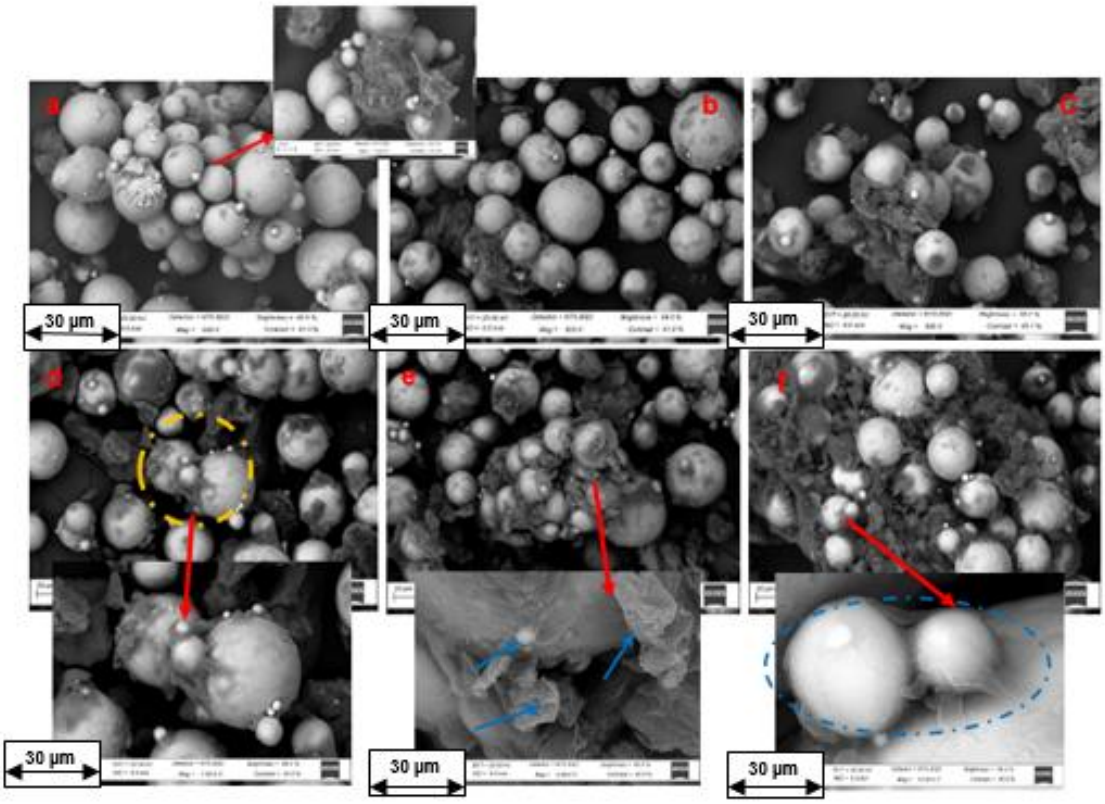

Figure 6.11 Interaction between CNTs and Ti6Al4V(ELI) particles, and Ti6Al4V(ELI) particle-to-particle interaction at (a) 3 % vol. of CNTs, (b) 8 % vol. of CNTs, (c) 15 % vol. of CNTs, (d) 20 % vol. of CNTs, (e) 25 % vol. of CNTs, and (f) 30 % vol. of CNTs

In Figure 6.11(a), at 3 % vol. of CNTs in Ti6Al4V(ELI), the Ti6l4V(ELI) particles appeared closely packed together, with some of them coated with CNT agglomerates. These particles formed a cluster likely held together by CNTs. In the same figure, an arrow designates an area that was then magnified to show individual strands of CNTs within the CNT agglomerate. This was a positive observation as it confirmed that SDS did work to separate the fibres within the agglomerate. In Figure 6.11(b), at 8 % vol.

© Central University of Technology, Free State

of CNTs in Ti6Al4V(ELI), the Ti6Al4V(ELI) particles had patches of CNT agglomerates on their surfaces. At a 20 % vol. of CNTs in a Ti6Al4V(ELI) matrix (Figure 6.11(d)), two Ti6Al4V(ELI) particles were seen to have CNTs agglomerates between them that appeared to link them and to a satellite particle right above and between them. Large clusters of CNTs and Ti6Al4V(ELI) particles were evident at volume fractions of CNTs in Ti6Al4V(ELI) of 25 % and 30 %, which was thought to have been due to the increased vol.% of CNTs and SDS in the mixture. The magnified image in Figure 6.11(e) shows the attachment of carbon sheets on a Ti6Al4V(ELI) particle. The magnified image of Figure 6.11(f) for a 30 % vol. of CNTs in Ti6Al4V(ELI) shows two satellite particles covered by CNTs while on top of a Ti6Al4V(ELI) particle.

6.4.1.1 Visual Analysis of Particle Defects at 3 % and 8 % vol. of CNTs in Ti6Al4V(ELI)

Particle defects were only detected at 3 % and 30 % vol. of CNTs in Ti6Al4V(ELI) matrices. A SEM image of particle defects at a 3 % vol. of CNTs in the Ti6Al4V(ELI) matrix is shown in Figure 6.12.

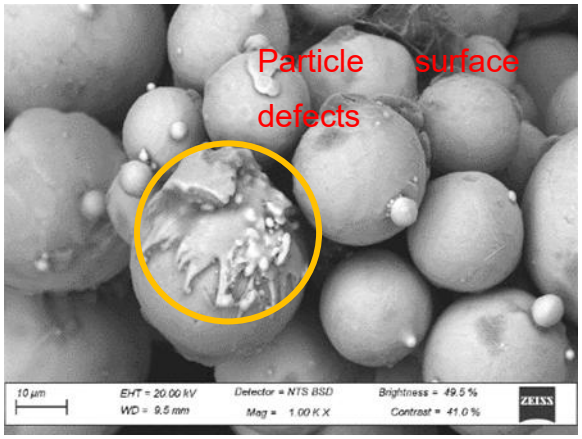

Figure 6.12 Smeared Ti6Al4V(ELI) particle on a spherical Ti6Al4V(ELI) particle at 3 % vol. of CNTs in Ti6Al4V(ELI)

The particle defect at 3 % vol. of CNTs in Ti6Al4V(ELI) appeared more like a melt spread onto the surface of a spherical Ti6Al4V(ELI) particle. The particle above it has a smaller “melt” on its surface. The presence of these “melts” would indicate applied localised forces during mixing that were high enough to cause softening of the particles resulting in plastic flow leading to these “melts”. Such severity of damage is not desirable, and consideration should be given to reducing the mixing forces without compromising dispersion and break-up of CNT agglomerates.

© Central University of Technology, Free State

Figure 6.13 represents particle surface defects at 30 % vol. of CNTs in Ti6AL4V(ELI).

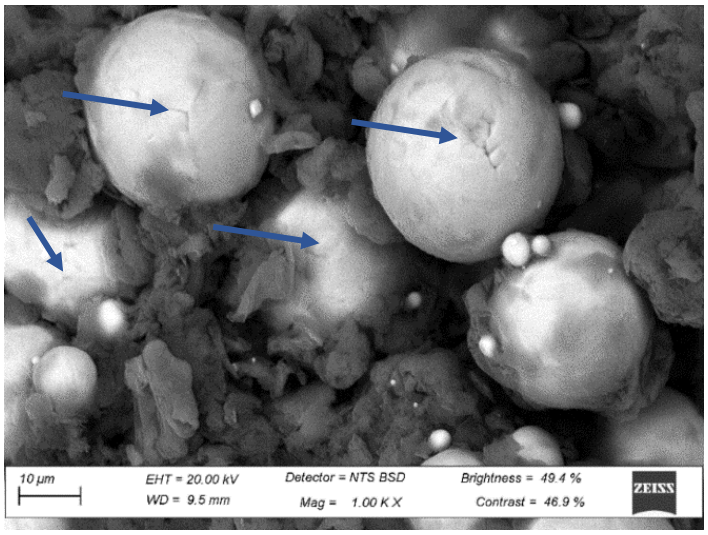

Figure 6.13 Surface defects on Ti6Al4V(ELI) particles at 30 % vol. of CNTs in Ti6Al4V(ELI)

At 30 % vol. of CNTs in Ti6Al4V(ELI), five particles with surface defects were observed, indicated by the blue arrows. During turbula mixing, the rotational speed of the mixer was increased to accommodate the increased presence of CNTs in the matrix. This may have resulted in an increased severity of collision between particles, thus leading to such a multiplicity of surface defects at the highest volume fraction of CNTs.

6.4.1.2 Visual Analysis of Different Forms of CNTs in Different Volume Fractions of CNTs where Turbula Mixing was Applied

To determine if single CNT strands were present when this method of mixing was applied, SEM images of 3 %, 8 %, 15 %, 20 %, and 25 % vol. CNTs in Ti6Al4V(ELI) were analysed with the results shown in Figure 6.14 (a–e), respectively. Where no images are shown implies that no defects and/or forms of CNTs were seen in that sample. At 30% vol. of CNTs in Ti6Al4V(ELI), using a higher magnification led to an unclear image.

© Central University of Technology, Free State

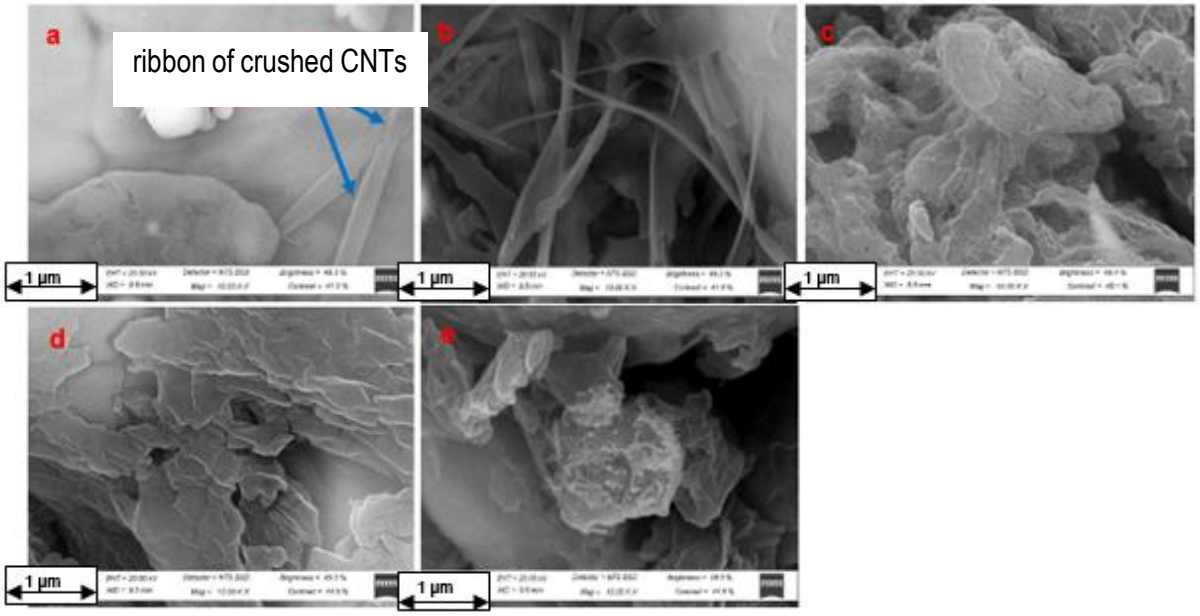

Figure 6.14 Different forms of CNTs in Ti6Al4V(ELI) at (a) 3 % vol. of CNTs, (b) 8 % vol. of CNTs, (c) 15 % vol. of CNTs, (d) 20 % vol. of CNTs, and (e) 25 % vol. of CNTs

In Figure 6.14(a), at 3 % vol. of CNTs in Ti6Al4V(ELI), two single CNT strands of CNTs were observed. It is thought that the low-volume fraction of CNTs allowed these strands to zip away from CNT agglomerates during mixing. There were a larger number of single CNT strands at 8% vol. of CNTs in Ti6Al4V(ELI) - Figure 6.14(b). This was thought to be for the same reasons as for the 3 % vol. of CNTs in Ti6Al4V(ELI). As the vol. of CNTs in Ti6Al4V(ELI) increased to 15 %, 20 %, and 25 %, the CNTS were in the form of entangled masses, as well as sheets of CNTs at the lower, higher as well as middle volume fraction, respectively. Clearly, the effectiveness of the SDS decreased with increasing volume fraction of CNTs, which is thought to have been a result of increasing van der Waal forces with increasing content of CNTs. As the load transfer mechanisms in composites are a function of the available reinforcing surface, the foregoing trend implied a reduced reinforcing effect with an increasing volume fraction of CNTs above 8% vol. CNTs in Ti6Al4V(ELI).

6.5 Visual Analysis of SEM Images at Different Volume Fractions of CNTs for Samples Mixed Using Combined Mixing

The analysis of samples mixed by combined mixing was carried out for volume fractions of CNTs of 3 %, 8 %, 15 %, 20 %, 25 %, and 30 % in Ti6Al4V(ELI). SEM images were captured at a magnification of 300x and analysed to compare the

© Central University of Technology, Free State

dispersion and homogeneity of CNTs, as well as particle defects. Figure 6.15 (a–f) represents the mixed powder samples at the different volume fractions of CNTs in Ti6Al4V(ELI).

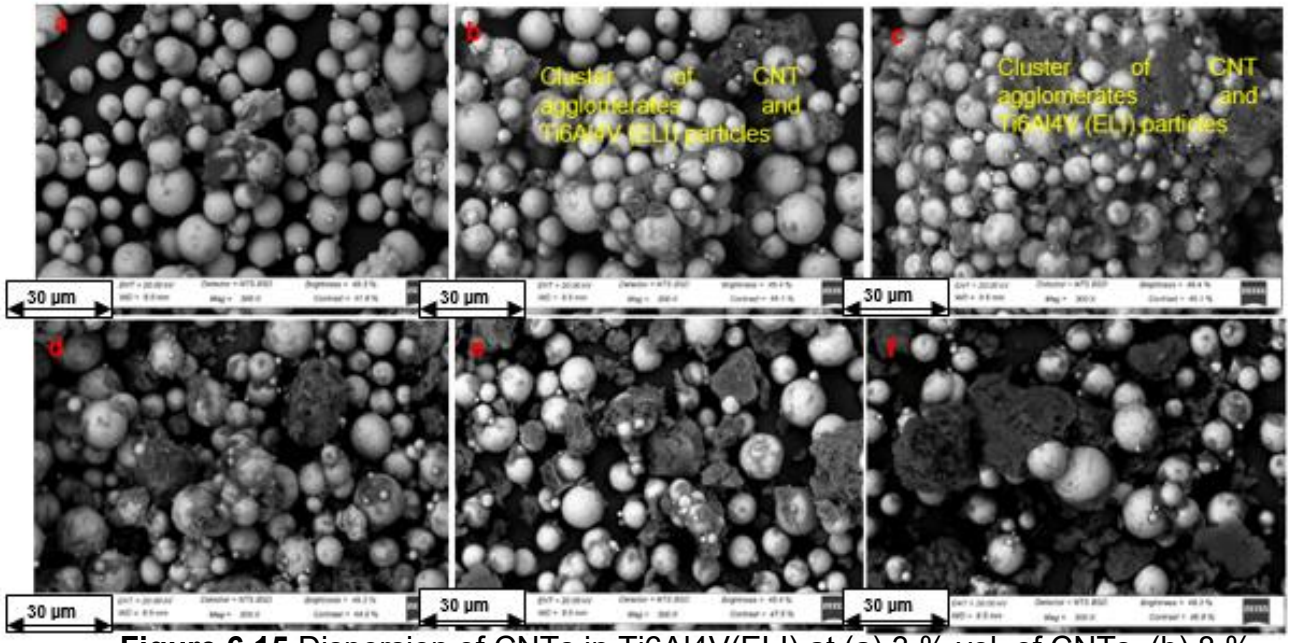

Figure 6.15 Dispersion of CNTs in Ti6Al4V(ELI) at (a) 3 % vol. of CNTs, (b) 8 % vol. of CNTs, (c) 15 % vol. of CNTs, (d) 20 % vol. of CNTs, (e) 25 % vol. of CNTs and (f) 30 % vol. of CNTs

The powder mixtures in the figure all showed the presence of clusters of CNTs and Ti6Al4V(ELI) particles, the ones at 8% and 15% vol. of CNTs in Ti6Al4V(ELI) being significantly larger than the other volume fractions of CNTs. From the trends seen in the preceding sections on mechanically and turbula mixed powders, it was expected that this trend would become more prevalent with increasing volume fraction of CNTs. The images showed that the presence of CNT agglomerates was higher at 25% and 30% vol. of CNTs in Ti6Al4V(ELI) than at the lower volume fractions of CNTs. Also, as noted previously, higher volume fractions of CNTs lead to a higher number and larger sizes of agglomerates, which was not so in this case due to the effectiveness of the method of mixing used to achieve some extent of de-agglomeration of CNTs.

6.5.1 Visual Analysis of Particle Defects at Different Volume Fractions of CNTs for Combined Mixed Samples

Micrographs of the particle defects in samples of powder at 3 %, 8 %, 20 %, 25 %, and 30 % vol. of CNTs in Ti6Al4V(ELI) are shown in Figure 6.16. No particle defects were observed at 15 % vol. of CNTs in Ti6AL4V(ELI).

© Central University of Technology, Free State

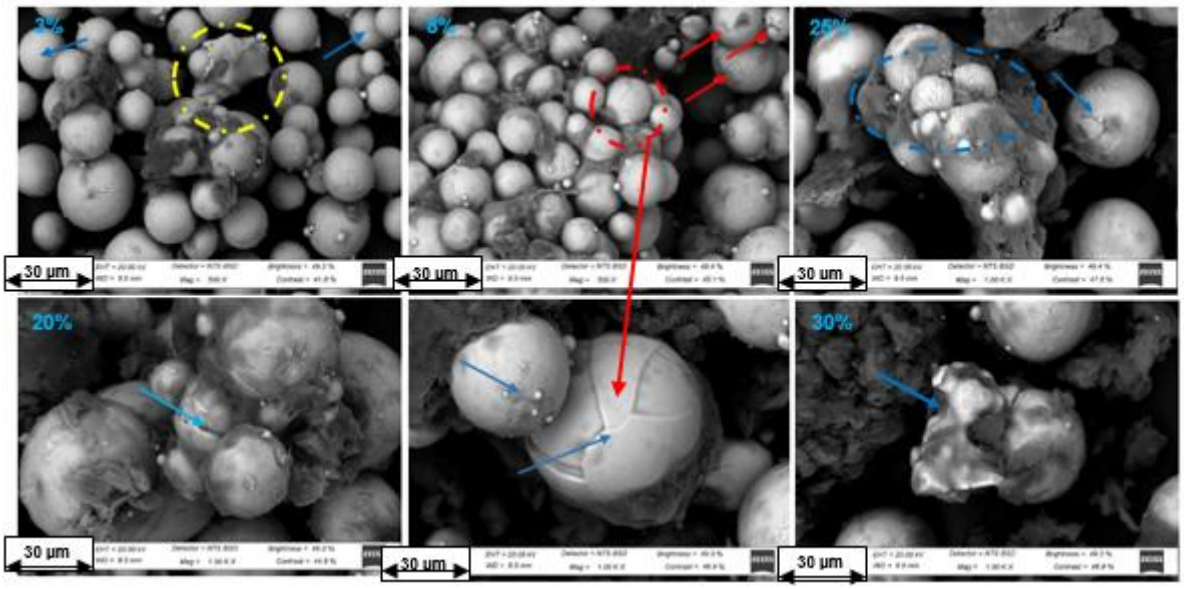

. **Figure 6.16** Particle defects at (a) 3 % vol. of CNTs, (b) 8 % vol. of CNTs, (c) 25 % vol. of CNTs, (d) 20 % vol. of CNTs, (e) 25 % vol. of CNTs, and (f) 30 % in Ti6Al4V(ELI)

In Figure 6.16, at 3 % vol. of CNTs in Ti6Al4V(ELI), evidence of extreme plastic deformation of Ti6Al4V(ELI) particle(s) is circled in yellow, where parts of Ti6Al4V(ELI) particle(s) have been extruded around a particle of Ti6Al4V(ELI). This is likely to be a result of force applied by the mechanical mixer and is similar to other occurrences in the case of pure manual mixing discussed earlier in this document. It is significant to note that the Ti6Al4V(ELI) particles indicated by blue arrows have deformed plastically into oval shapes. A Ti6Al4V(ELI) particle at 8 % vol. of CNTs with surface defects is circled in red in Figure 6.16(b), and other Ti6Al4V(ELI) particles with surface defects are indicated by red arrows. Surface defects on Ti6Al4V(ELI) particles were found at 25 % vol. of CNTs shown within the blue ellipsoid and with a blue arrow in Figure 6.16. Another Ti6Al4V(ELI) particle defect was seen at 20 % vol. of CNTs in Figure 6.16. This defect had a sharp depression running along part of the visible surface of the particle. The SEM image in Figure 6.16, at 30 % vol. of CNTs, had surface defects on two adjacent particles of Ti6Al4V(ELI). One of these particles showed parts of its surface chipped or peeled off. Several Ti6Al4V(ELI) particles at 30 % had surface depressions, while one on the left end of the micrograph suffered very severe plastic deformation, with some bits of it partially broken up away. The micrographs denote an increase of damaged particles and severity of damage with increasing volume fraction of CNTs. To facilitate effective dispersion of CNTs in the Ti6Al4V(ELI), more rigorous

© Central University of Technology, Free State

mixing was applied at increasing vol.% of CNTs to counteract the increasing strong van der Waal forces tending to keep the CNTs together. However, the trend of damaged particles and severity of damage with increasing volume fraction of CNTs would indicate that this led to increased particle defects due to the increased force applied and particle-particle interaction.

6.5.1.1 Visual Analysis of Different Forms of CNTs at Different Volume Fractions of CNTs for Combined Mixed Samples

To determine whether single CNT bundles were separated from the CNT agglomerates with this process of mixing, SEM images were analysed at 3 %, 8 %, 15 %, 20 %, 25 %, and 30 % and are presented in Figure 6.17(a–f), respectively. The typical outside diameter of CNTs used in this work was in the range of 8–11 nm. For the given scale in Figure (a), the measured average diameter of the strands was 0.168 µm. This implied a total of about 15–21 nanotubes for this average diameter of CNT strand.

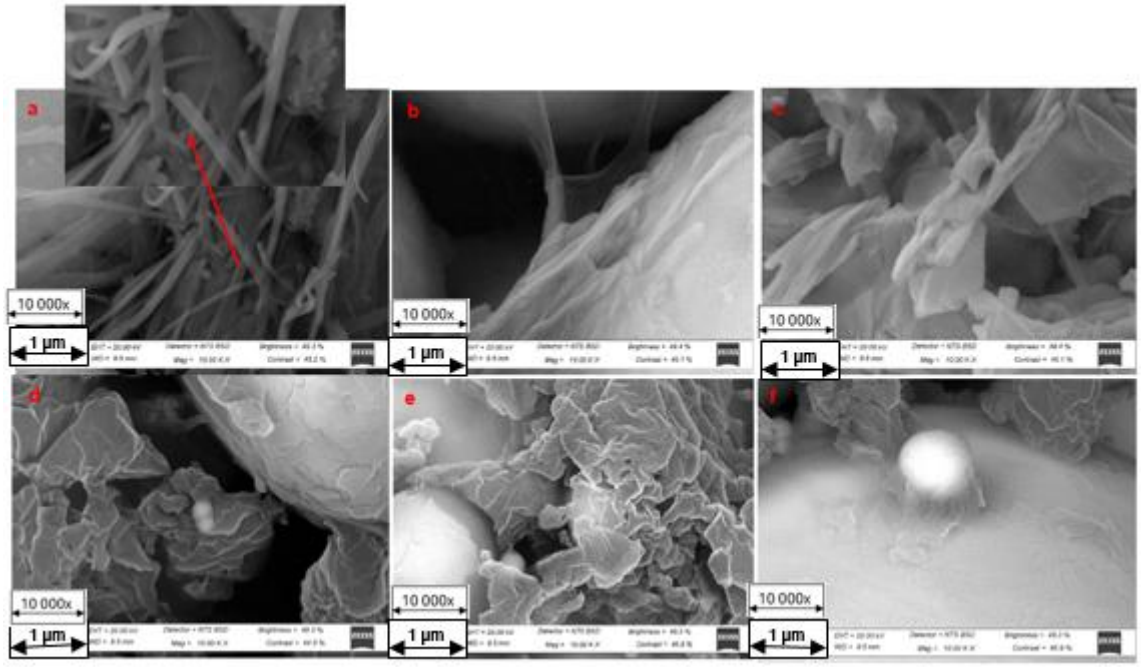

Figure 6.17 Different forms of CNTs in Ti6Al4V(ELI) at (a) 3 % vol. of CNTs, (b) 8 % vol. of CNTs, (c) 15 % vol. of CNTs, (d) 20 % vol. of CNTs, (e) 25 % vol. of CNTs, and (f) 30 % vol. of CNTs.

There were single entangled strands of CNTs at 3 % vol. of CNTs in Ti6Al4V(ELI). Thin sheets of CNTs covered several strands of CNTs at 8 % vol. of CNTs in Ti6Al4V(ELI). At 15% vol. of CNTs in Ti6Al4V(ELI), the CNTs were in the form of both

© Central University of Technology, Free State

strands and sheets. When the volume fraction was increased to between 20–30 % CNTs in Ti6Al4V(ELI), no CNT strands were visible but rather folded CNT sheets. Clearly, the trend was from single strands of CNTs to folded sheets of CNTs as the content of CNTs increased. Increasing the vol.% of CNTs is expected to have led to an increase in van der Waal forces between them, making it difficult to separate them into individual strands, and hence, sheets of CNTs were formed.

6.6 Conclusion

SDS was used as a surfactant for CNTs in three mixing techniques, including mechanical, turbula, and combined mixing. In manual mixing, the use of SDS achieved dispersion of CNTs in Ti6l4V(ELI). However, re-agglomeration of CNTs occurred at 8% and 30% vol. of CNTs. Re-agglomeration at 8% vol. of CNTs was surprising to see, as this was expected at higher contents of CNTs. The tendency for CNTs to re-tangle occurs at increased concentrations due to the proximity of tubes to interact between themselves. This mixing technique produced particle defects at 8%, 25%, and 30% vol. of CNTs in Ti6Al4V(ELI). There were surface defects at 8% and 25% vol. of CNTs in Ti6Al4V(ELI), while at 30% vol. of CNTs in Ti6l4V(ELI), a Ti6l4V(ELI) particle appeared merged with a spherical Ti6l4V(ELI) particle.

When turbula mixing was used, there was a high incidence of CNT agglomerates at 15% to 30% vol. of CNTs in Ti6Al4V(ELI). The number of clusters and sizes of CNTs and Ti6Al4V(ELI) particles increased from 15% to 30% vol. of CNTs in Ti6Al4V(ELI), likely due to the combination of SDS and increased rotational speeds of the mixer, which provided more Ti6Al4V(ELI) particle-particle and CNT interaction. The powder samples associated with this mixing technique also showed increased Ti6Al4V(ELI) particles to CNT interaction through surface attachment of CNTs on Ti6Al4V(ELI) particles for all CNT volume fractions. An analysis of the different forms of CNTs at the various volume content showed the presence of CNT strands at 3% and 8% vol. of CNTs in Ti6Al4V(ELI). This was thought to be due to the low content and effectiveness of SDS at these low-volume fractions of CNTs. As the volume of CNTs in Ti6Al4V(ELI) increased, the individual strands of CNTs were replaced with entangled masses at 15% and 25% vol. of CNTs in Ti6Al4V(ELI), and sheets of CNTs at 20% vol. of CNTs in Ti6Al4V(ELI), while no data could be collected for the 30% CNT sample as it led to a distortion of the image at the same magnification. This trend was noted to imply a decreased potential efficiency of reinforcement with increasing volume of CNTs in

© Central University of Technology, Free State

Ti6Al4V(ELI). Two defects on Ti6Al4V(ELI) particles were observed, one at 3% vol. of CNTs in Ti6Al4V(ELI), where a severely deformed Ti6Al4V(ELI) particle was smeared onto another spherical Ti6Al4V(ELI) particle and the other at 30% vol. of CNTs in Ti6Al4V(ELI), where surface defects were seen on several particles of Ti6Al4V(ELI).

Combined mixing produced clusters of tightly packed Ti6Al4V(ELI) particles and CNTs, which were most prominent at 8% and 15% vol. of CNTs in Ti6Al4V(ELI). At 20%, 25%, and 30% vol. of CNTs in the Ti6Al4V(ELI) matrix, re-agglomeration of CNTs was seen. This mixing technique produced more particle defects in the three methods of mixing used here, seen in different forms at 3%, 8%, 20%, 25%, and 30% vol. of CNTs in the Ti6Al4V(ELI) matrix. The defects occurred on the surfaces of Ti6Al4V(ELI) particles. The most severe defects were at 3% and 30% vol. of CNTs in Ti6Al4V(ELI). Strands of CNTs occurred at 3% CNTs in Ti6Al4V(ELI), while sheets of CNTs were seen at 8% CNTs in Ti6Al4V(ELI). There were more CNT sheets at 15% CNTs in Ti6Al4V(ELI), while agglomerated bundles of CNTs were found at 25% and 30% vol. of CNTs in Ti6Al4V(ELI).

The presence of single strands of CNTs at 3% and 8% vol. of CNTs in Ti6Al4V(ELI) indicated the possibility of efficient reinforcement at these low-volume contents. Increasing the volume fraction of CNTs in Ti6Al4V(ELI) led to the re-agglomeration of CNTs, irrespective of the mixing technique(s) used and a reduction in the possibility of efficient reinforcement. The use of SDS as a surfactant achieved good dispersion with agglomerates of CNTs on each particle of Ti6Al4V(ELI) at all volume fractions. However, this came with the disadvantage of increasing clusters of CNTs and Ti6Al4V(ELI) particles, which is expected to affect the levelling of powder on the powder bed and lead to an increase of porosity in parts that are built additively. In order to reduce the effectiveness of dispersing CNTs, the three methods of mixing can be graded as combined mixing, followed by mechanical and finally, turbula mixing.

References

1. Yang, H., Neal, L., Flores, E. E., Adronov, A. and Kim, N. Y., 2023. Role and impact of surfactants in carbon nanotube dispersions and sorting. *Journal of Surfactants and Detergents*, *26*(5), pp. 607–622.

© Central University of Technology, Free State

2. Duan, W. H., Wang, Q. and Collins, F., 2011. Dispersion of carbon nanotubes with SDS surfactants: a study from a binding energy perspective. *Chemical Science*, *2*(7), pp. 1407–1413.
3. Pillari, L. K., Lessoway, K. and Bichler, L., 2023. Carbon nanotube and graphene reinforced magnesium matrix composites: a state-of-the-art review. *Journal of Magnesium and Alloys*, 11(6), pp.1825-1905.
4. Strano, M. S., Moore, V. C., Miller, M. K., Allen, M. J., Haroz, E. H., Kittrell, C., Hauge, R. H. and Smalley, R. E., 2003. The role of surfactant adsorption during ultrasonication in the dispersion of single-walled carbon nanotubes. *Journal of Nanoscience and Nanotechnology*, *3*(1–2), pp. 81–86.

© Central University of Technology, Free State

CHAPTER 7 - DETERMINING THE OPTIMUM PROCESS PARAMETERS FOR ADDITIVELY MANUFACTURED SLM CNT/TI6AL4V(ELI) COMPOSITES

7.0 Summary

In this chapter, preliminary testing to determine the best process parameters was carried out for 35 single tracks printed from a mixture of 3% vol. CNTs in Ti6Al4V(ELI) from mixtures obtained in Preliminary powder mixing (ethanol used as a dispersion agent). Process parameters influence the formation of the melt pool, which subsequently influences the geometry, microstructure, and mechanical properties of the final part (Mohamad et al., 2021). A matrix for the optimisation of the two critical process parameters of laser power and scanning speed was developed. In this approach, the optimum laser power for processing Ti6Al4V(ELI) using SLM on an M2 LaserCusing® machine was selected as the starting point and values below and above it were placed in the matrix. Different scanning speeds above and below a calculated value for Ti6Al4V(ELI) were then selected for each value of power and entered into the matrix. This process was necessary as the different thermophysical properties of the CNT/Ti6Al4V(ELI) composites implied different optimum values of laser power and scanning speed for each volume fraction of CNTs.

7.1 Determining the Best Process Parameters of Laser Power and Scanning Speed for CNT/Ti6Al4V(ELI) Nanocomposites

Titanium alloy Ti6Al4V(ELI) has different optimum processing parameters depending on the LBPF method and type of machine used, as is evident in Table 7.1.

Table 7.1 Optimum values of three process parameters for SLM of Ti6Al4V(ELI) on different machines

Author	Machine used	Laser scanning speed (mm/s)	Laser power (W)	Layer thickness (μm)
Simonelli, M., Tse, Y. Y. and Tuck, C. (2014)	Renishaw AM250	225	157	50
Gong, H., Rafi, K., Gu, H., Starr, T. and Stucker, B. (2015)	EOS M270	120–1560	40–160	30
Xu, W., Brandt, M., Sun, S., Elambasseril, J., Liu, Q., Latham, K., Xia, K. and Qian, M. (2015)	SLM 250HL	686	375	30

© Central University of Technology, Free State

Liu, Q. C., Elambasseril, J., Sun, S. J., Leary, M., Brandt, M. and Sharp, P. K. (2014)	SLM 250HL	710	175	30
Leuders, S., Thöne, M., Riemer, A., Niendorf, T., Tröster, T., Richard, H. A. and Maier, H.J. (2013)	SLM 250HL	450	100	30
Song, B., Dong, S., Zhang, B., Liao, H. and Coddet, C. (2012)	Realiser 250	200–1600	110	30
Edwards, P. and Ramulu, M. (2014)	MTT 250	200	200	50
Qiu, C., Adkins, N. J. E. and Attallah, M. M. (2013)	M2 LaserCusing	800–1500	150–200	20
Li, Z., Kucukkoc, I., Zhang, D. Z. and Liu, F. (2018)	EOS M280	950–1550	150–190	30
Ran, Q., Yang, W., Hu, Y., Shen, X., Yu, Y., Xiang, Y. and Cai, K. (2018)	EOS M280	700	400	20

In selecting CNTs as a reinforcement, their thermal properties were examined to ensure that they did not melt to form a compound with Ti6Al4V(ELI) upon melting of the latter but rather a composite as desired. It was necessary to ensure that the mechanical properties were high enough to provide reinforcement as well. Table 7.3 shows the thermal, physical and mechanical properties of CNTs and Ti6Al4V(ELI) identified from the literature.

The flow of heat in a material is determined by its thermal diffusivity and conductivity. The importance of these two properties is that they determine how rapidly a material is penetrated and conducts thermal energy, respectively, and consequently influence the distribution of temperature in the part as it is being built (Zheng et al., 2021). A material with a low thermal diffusivity limits the penetration of heat into it. The specific heat and latent heat of a material determines how much of the heat is consumed to raise its temperature and phase changes, respectively (Miao et al., 2014). The thermal conductivity of loose powder is primarily determined by its packing density and less by the properties of the powder material. The thermal conductivity of CNTs is higher than that of Ti6Al4V(ELI); the higher the vol.% of CNTs in Ti6Al4V(ELI), the higher the thermal conductivity of the composite (Sillani et al., 2021). A similar reasoning applies to the other thermal properties discussed in this paragraph.

Table 7.2 Thermophysical and mechanical properties of Ti6Al4V(ELI) and CNTs

Property	**Ti6Al4V (grade 23)**	**CNTs**

© Central University of Technology, Free State

Density, Kgm^{-3}	4430	1200–2100
Melting point, °C	1604–1660	3550
Specific heat, $J{\cdot}kg^{-1}K^{-1}$	526.3	740–800
Thermal conductivity, $Wm^{-1}K^{-1}$	6.7×10^{-6}	0.613
Thermal diffusivity, m^2s^{-1}	7.15×10^{-6}	4.6
Boiling point, °C	289.85	4027
Ultimate tensile strength, MPa	860	11000– 63 000
Yield strength, MPa	790	20 000–90 000
Elasticity modulus, GPa	113.8	1000
Elongation at break, %	15	16
Hardness, Vickers (HV)	341	1210

From Table 7.3, it is evident that the melting point and specific heat of CNTs are higher than those for Ti6Al4V(ELI), which ensures that the CNTs reach faster equilibration of temperatures than in Ti6Al4V(ELI). It is also clear from the data that the mechanical properties of strength, stiffness, hardness and percentage elongation for CNTs are well above those of Ti6Al4V(ELI) expected in the case of the property. This confirms that the CNTs will serve their purpose of reinforcement.

The thermal conductivity of CNTs in Table 7.3 is 9.149×10^4 times that of Ti6Al4V(ELI) and the thermal diffusivity 6.434×10^5 times that of Ti6Al4V(ELI). This implies that CNTs are much more effective in transmitting heat than Ti6Al4V(ELI). In a case where the size of the source of energy is less than the particles, CNTs attain temperature equilibrium faster than Ti6Al4V(ELI). However, this trend does apply in the present case, as the M2 LaserCusing® beam diameter of 150 µm is 18.75 and 3.75 times larger than the average diameters of the CNT and Ti6Al4V(ELI) particles, respectively. The density of Ti6Al4V(ELI) decreases with temperature from 4430 kgm^{-3} at room temperature to about 3852 kgm^{-3} at the melt temperature of 1660 °C (Tchuindjang et al., 2021). This gives a percentage range of density of 29–51%, even at melting, though the density of CNTs is much less than that of Ti6Al4V(ELI). Therefore, upon melting of the Ti6Al4V(ELI), the particles of CNTs are likely to float on the surface of

© Central University of Technology, Free State

the Ti6Al4V(ELI) melt. However, the process of SLM does not lead to laminar flow of the melt and occurs in very short time intervals, so short that it is not expected that aggregation of the CNTs at the surface of the melt would occur. In cases of complete turbulence of the melt, the spatial distribution of the CNTs will be completely random. Where complete turbulence does not occur throughout the melt, the spatial distribution of the CNTs will assume patterns that conform to the flow of the Ti6Al4V(ELI) melt. These are some features that should be investigated in the built single tracks.

7.2 Results and Discussion

The tracks discussed were produced on an M2 LaserCusing® machine using the process parameters in the process parameter test matrix shown in Table 7.2 in the previous section. The reference LED of 166.67J/m of Ti6Al4V(ELI) calculated from its optimum processing parameters was used.

7.2.1 Single Tracks of 3 % CNTs in Ti6Al4V(ELI), Built With a Laser Power of 60 W and Scanning Speeds Between 200 mm/s–600 mm/s

Figure 7.1 shows the top surfaces of single tracks produced at a laser power of 60 W and scanning speeds between 200 mm/s–600 mm/s.

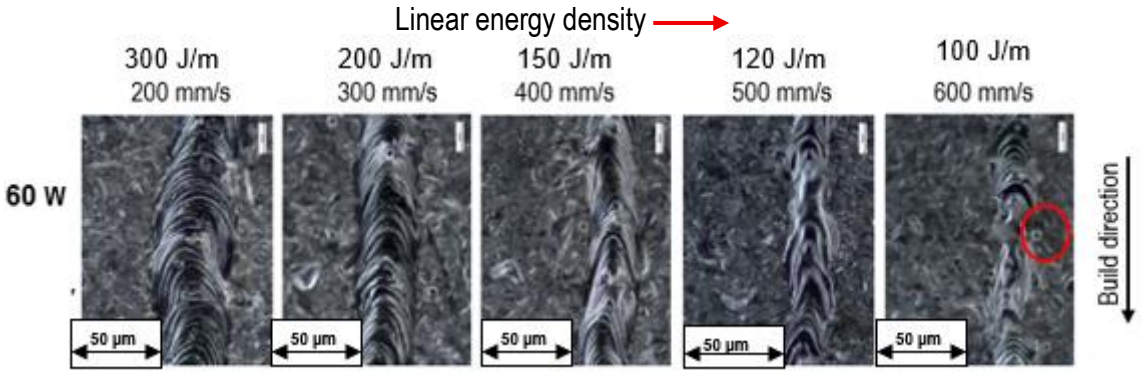

Figure 7.1 Optical micrographs of track builds at 60 W constant laser power and scanning speeds between 200–600 mm/s

600 mm/s

© Central University of Technology, Free State

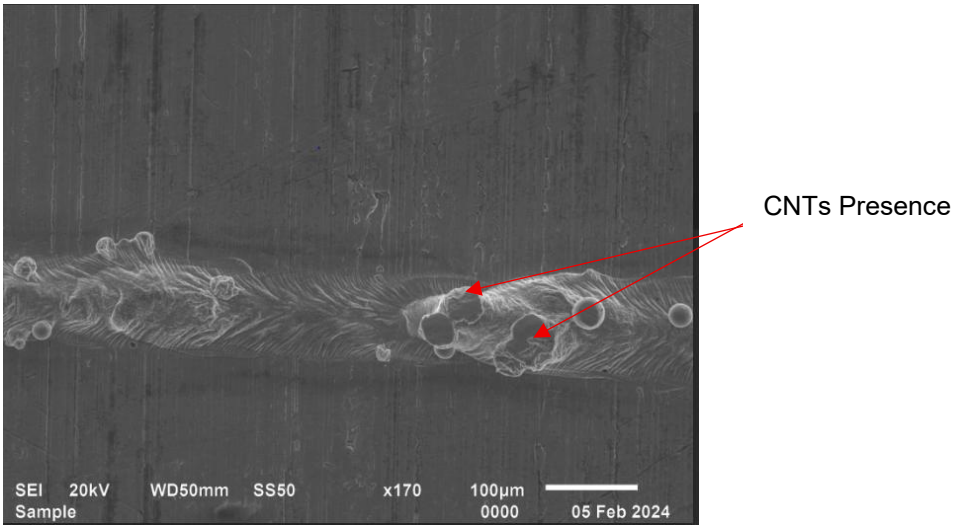

Figure 7.1 (600 mm/s) Depiction of un-melted CNTs in Track

The magnitude of the laser power and laser scanning speed influenced the tracks produced. The laser spot size and layer thickness were kept constant during processing. At the low scanning speeds of 200 mm/s and 300 mm/s, continuous tracks with more or less even widths were formed. When the scanning speed was increased to between 400–600 mm/s tracks, the widths of the tracks decreased and became irregular. From the equation for linear energy density (W/m/s), for the same value of laser power, low scanning speeds lead to high LED values and vice versa. The high LEDs prevailing at low scanning speeds cause higher melt temperatures and the attendant reduction of viscosity and surface tension. The former allows easier flow and mass transfer of the melt, while the latter creates a greater gradient of the surface tension from the lowest values at the centre of the melt pool, where the LED is highest, to the edges. This, in turn, causes Marangoni positive thermal capillary flow of the melt from the centre to the edges of the tracks. The foregoing leads to the formation of wide tracks with stable widths. The irregular tracks formed at scanning speeds between 400–600 mm/s were thought to have been a result of the related reduction of LEDs and, therefore, reduced surface tension gradient and viscosity that caused a reduction of the lateral rate of mass transfer of the melt pool and the formation of narrow tracks with irregular widths. The figure shown for a scanning speed of 600 mm/s shows un-melted CNTs in the track, pointing to the formation of a nanocomposite. No discontinuity of tracks was observed; however, in Figure 7.1, the ripple effect that arises from creation of shear stress gradients in a melt (Balhara et al., 2021) was seen with more regular and shallower ripples at the two lowest scanning speeds (200 mm/s

© Central University of Technology, Free State

and 300 mm/s), as well as less regular and deeper ripples at the three highest scanning speeds.

The deeper ripples at higher scanning speeds point to higher speeds of the longitudinal flow of the melt at the centre of the tracks as a result of the higher scanning speeds. Though unavoidable during SLM, ripples have a great influence on the structure of the surface and reflectivity of products. Ripple marks between layers could evolve into cracks that can lead to failure of structures during fatigue loading (Wang et al., 2018). Thus, post-surface treatment is needed to remove or minimise them.

7.2.1.1 Observed Peculiarities

Unmelted Ti6Al4V(ELI) powder (indicated by red circles) was found at 600 mm/s. These unmelted particles occurred due to incomplete melting of Ti6Al4V(ELI) powder in the circumferential or peripheral zone of the laser spot. Spatter particles are formed from small droplets of Ti6Al4V(ELI) that are expelled from the melt pool (oxidising in-flight), which then land on the powder bed. These small droplets can land on the part being fabricated and then get trapped if not completely melted during the re-melting of subsequent layers (Zenani et al., 2020). The presence of unmelted powder leads to the formation of uneven surfaces of subsequent layers of powder that may act as centres of failure of parts during use.

7.2.1.2 Cross-Sectional Analysis of Tracks Built at a Laser Power of 60 W and Scanning Speeds of 200–600 mm/s

Further analysis of the built tracks, shown in Figure 7.1, was carried out on the basis of their cross-sections (an average of 5 measurements were taken), whose OM images are shown in Figure 7.2.

© Central University of Technology, Free State

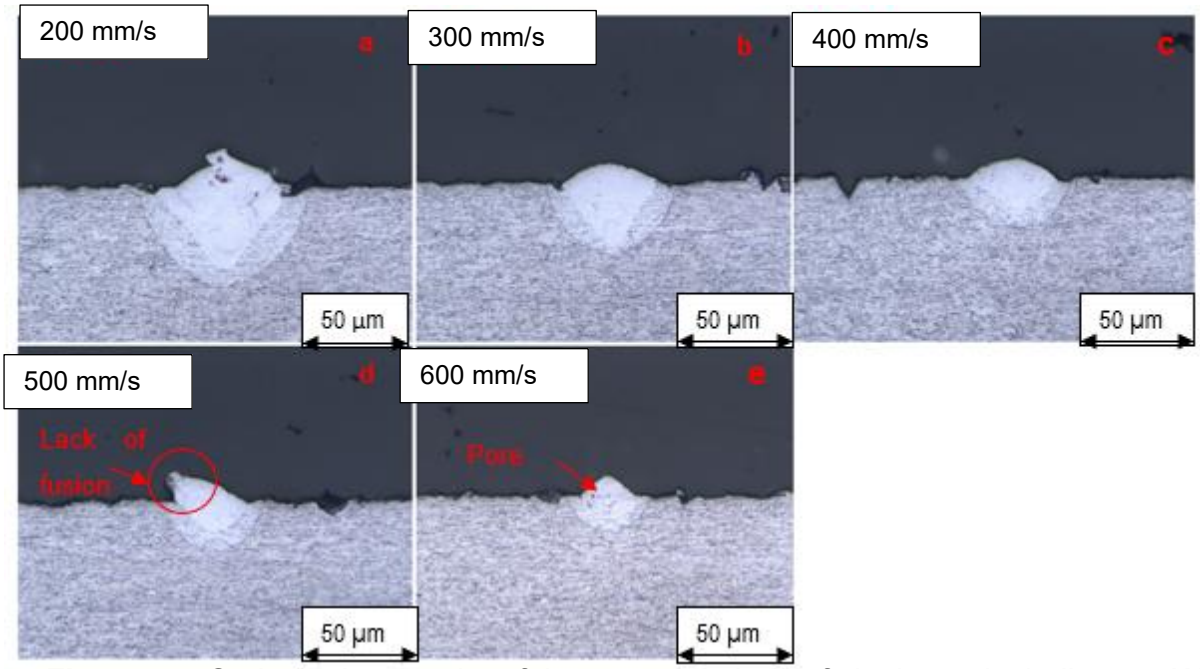

Figure 7.2 Optical micrographs of the cross-sections of single tracks built at 60 W laser power and scanning speeds between 200–600 mm/s

Melt pools and the resultant tracks are defined by their depths of penetration, widths and lengths. Irregularities of the height cause the formation of uneven or discontinuous build surfaces. Shallow tracks cause debonding of layers and the formation of interlayer cracks in built parts. Very deep depths of penetration result in the formation of keyholes in a process that causes porosity. The melt pool is described as being in conduction mode when the melt pool depth to width ratio is less than 0.5. The melt pool is said to be in keyhole mode when the ratio of depth to width is greater than 0.5. A good track should exhibit sufficient depth of penetration with a semi-circular U-shaped cross-section. Excessively high energy input leads to the keyhole mode, whilst significantly low energy input leads to a lack of fusion or the balling phenomena (Guo et al., 2022).

The characteristics of the cross-sections of the track builds can be further analysed using Figures 7.3, 7.4 and 7.5, whose values are extracted from Table 7.4.

© Central University of Technology, Free State

Table 7.3 Geometrical features for track built at 60 W scanning power and 400–800 mm/s (50µm layer thickness)

Track width (µm)	Track height (µm)	Track depth (µm)	Aspect ratio	Scanning speed (mm/s)	Linear energy density (J/m)
149.65	43.144	82.44	0.55	200	300
117.07	21.321	63.74	0.54	300	200
103.22	19.23	33.92	0.33	400	150
80.95	32.96	31.71	0.39	500	120
73.785	22.86	23.22	0.31	600	100

The characteristics of the cross-sections of the tracks built at 60 W laser power and scanning speeds between 200–600 mm/s are further analysed using the plots in Figures 7.3, 7.4 and 7.5

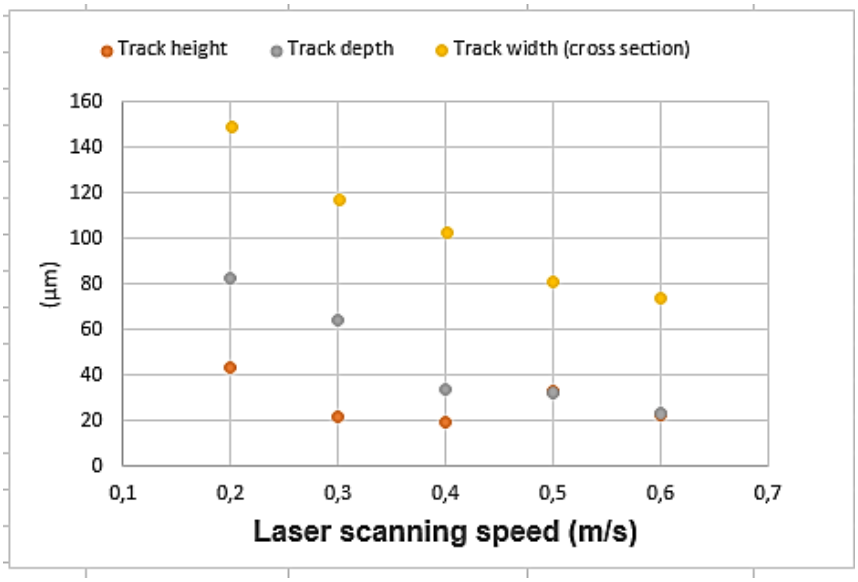

Figure 7.3 Plotted geometrical characteristics of depth, height and width of built tracks at 60 W laser power and scanning speeds of 200–600 mm/s

Figure 7.3 shows the variation in width, depth and height of tracks with increasing scanning speed. The widths of the tracks plotted in Figure 7.3 decreased as the laser scanning speed increased, which is thought to have been a result of the attendant reduction of the LED. A track with "jagged" melt flow was observed in Figure 7.2(d), as well as black zones at the edges of the tracks on the substrate and near the top areas of the tracks that are likely to be agglomerates of CNTs, in addition to undercutting. The layer thickness largely influences the heights of the tracks. The heights of the

© Central University of Technology, Free State

tracks decreased with increasing scanning speed, which is thought to have been a result of the decreased lateral flow of melt due to decreased LED. The depths of penetration followed a similar trend of reduction with increasing scanning speed, which was also due to decreasing LED.

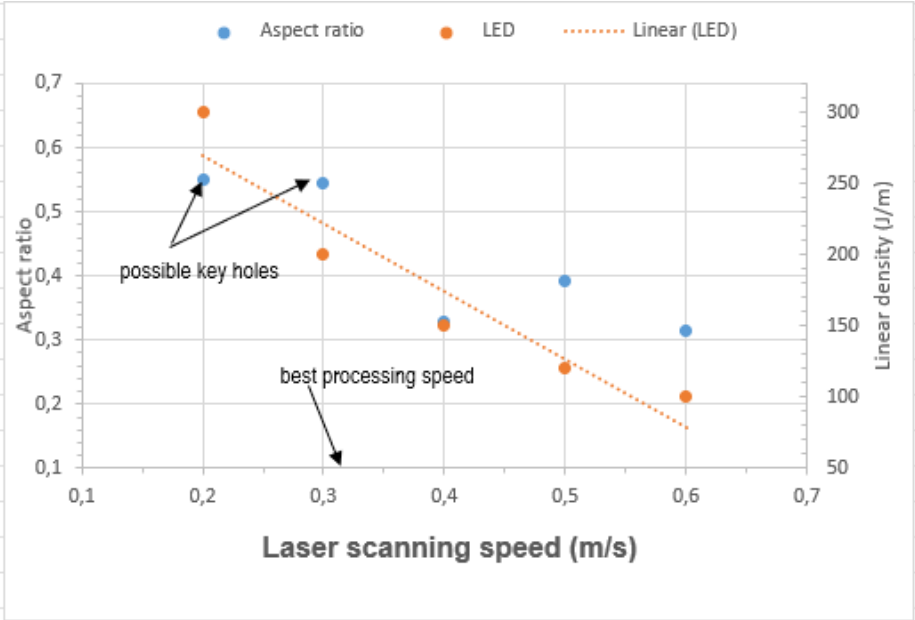

Figure 7.4 Plotted geometrical characteristics of aspect ratio (depth/width) and LED at 200–600 mm/s

Figure 7.4 shows the variation in the aspect ratio of tracks and LED with increasing scanning speed. While the laser scanning speed defines the time of interaction between the laser beam and powder material, the LED defines the transverse temperature gradient across the width of tracks. Keyhole modes were found at scanning speeds of 200 mm/s and 300 mm/s, for which aspect ratios of 0.55 and 0.54, respectively, were calculated. The aspect ratio calculated at the optimum processing speed of 400 mm/s from Table 7.2 is 0.33. This value falls outside the expected value required to form a melt pool in conduction mode. This is a deviation from the predicted optimum value, which is largely due to limited experimental data. A close examination of the depth-to-width ratios plotted in Figure 7.4 and assuming a polynomial (best-fit curve of the third order) of their variation with scanning speed, using the known threshold depth-to-width ratio of 0.5 as a reference, produced an optimum scanning speed of 320 mm/s. The difference between this predicted value of best scanning speed and the one given in Table 7.2 of 400 mm/s implied that the presence of CNTs in Ti6Al4V(ELI) facilitates the heat of flow and reaches equilibrium faster than the alloy; thus, a lower LED is required compared to the predicted optimum value in Table 7.2.

© Central University of Technology, Free State

Since the values calculated in Table 7.2 are predicted from the alloy's optimum values of processing and taking into consideration the low thermal conductivity of CNTs, a lower scanning speed is thus required for processing the composite compared to the optimum value for processing the alloy. It is expected that the LED follows a linear trend with respect to the laser scanning speed. However, this does not occur in this case. Similar trends were observed at 60–140 W scanning powers with linearity approaching at higher scanning powers of 160–180 W. Work by Zenani et al. (2019) had nonlinear LED curves for titanium aluminide (TIAL) produced via DMLS for scanning powers between 150–350 W. However, they did not explain the non-linearity of these results. Further research is necessary to explore this trend in scanning powers.

The influence of the LED on the width and depth of built tracks is presented in Figure 7.5

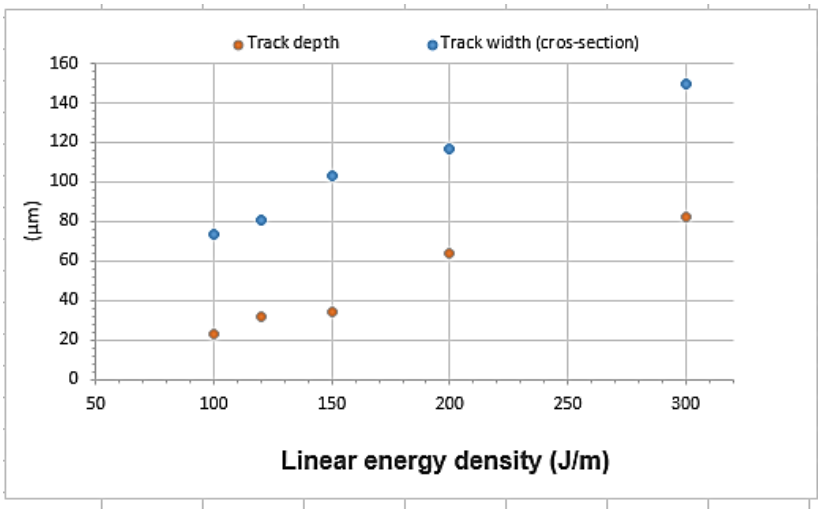

Figure 7.5 Influence of linear energy density on geometrical features at a laser power of 60 W and scanning speeds between 200–600 mm/s

Figure 7.5 shows the variation in width and depth of penetration of tracks with increasing LED. The influence of the LED on the depth and width of built tracks shows an increase in both as the LED increases. The foregoing is explained by the earlier mention that the linear energy density defines the transverse temperature gradient of the melt pool and, therefore, the transverse surface tension, which largely influences the width of the melt pool. Increasing LED also increases the penetration of the laser beam and, therefore, the depth of penetration of tracks.

© Central University of Technology, Free State

7.2.2 Single Tracks of 3 % CNTs in Ti6Al4V(ELI), Built with a Laser Power of 80 W and Scanning Speeds Between 300–700 mm/s

Figure 7.6 shows the top surfaces of single tracks built at a laser power of 80 W and scanning speeds between 300–700 mm/s (50µm layer thickness).

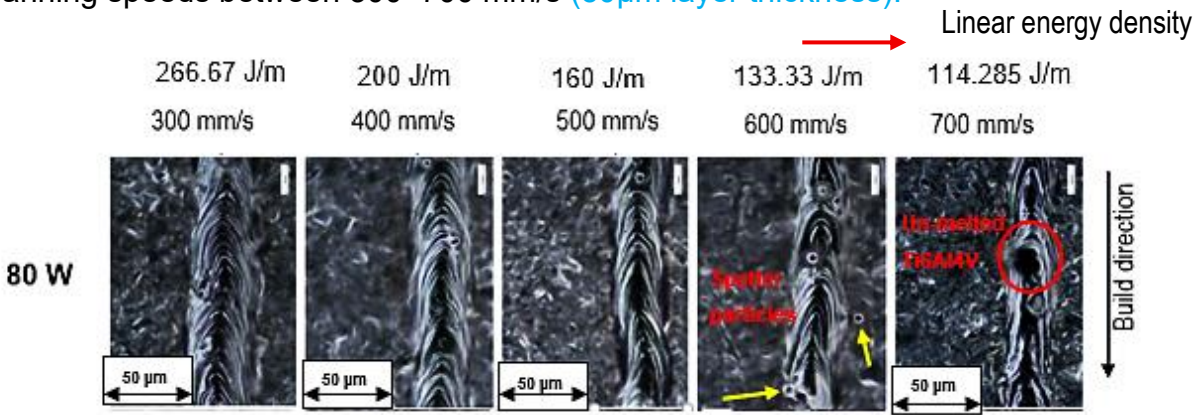

Figure 7.6 Optical micrographs of track builds at a laser power of 80 W and scanning speeds between 300–700 mm/s

The tracks built at a laser power of 80 W were continuous, with even widths for scanning speeds between 300–500 mm/s. The widths of tracks built at scanning speeds between 600 mm/s and 700 mm/s were irregular. There was a decrease in the widths of the tracks with increasing laser scanning speed, which is known to arise from a reduction of the LED. The track built at a scanning speed of 600 mm/s exhibited spatter particles, some of which are indicated by yellow arrows in the figure, and unmelted particles (red circle) also occurred in the track built at a scanning speed of 700 mm/s. There were ripples along all the tracks but with different characteristics, with tracks built at the three highest scanning speeds having the lowest occurrence and greatest depth.

7.2.2.1 Geometric Analysis of Tracks Built at a Laser Power of 80 W and Scanning Speeds of 300–700 mm/s

Further analysis of the built tracks, shown in Figure 7.6, was carried out on the basis of their cross-sections, whose OM images are shown in Figure 7.7.

© Central University of Technology, Free State

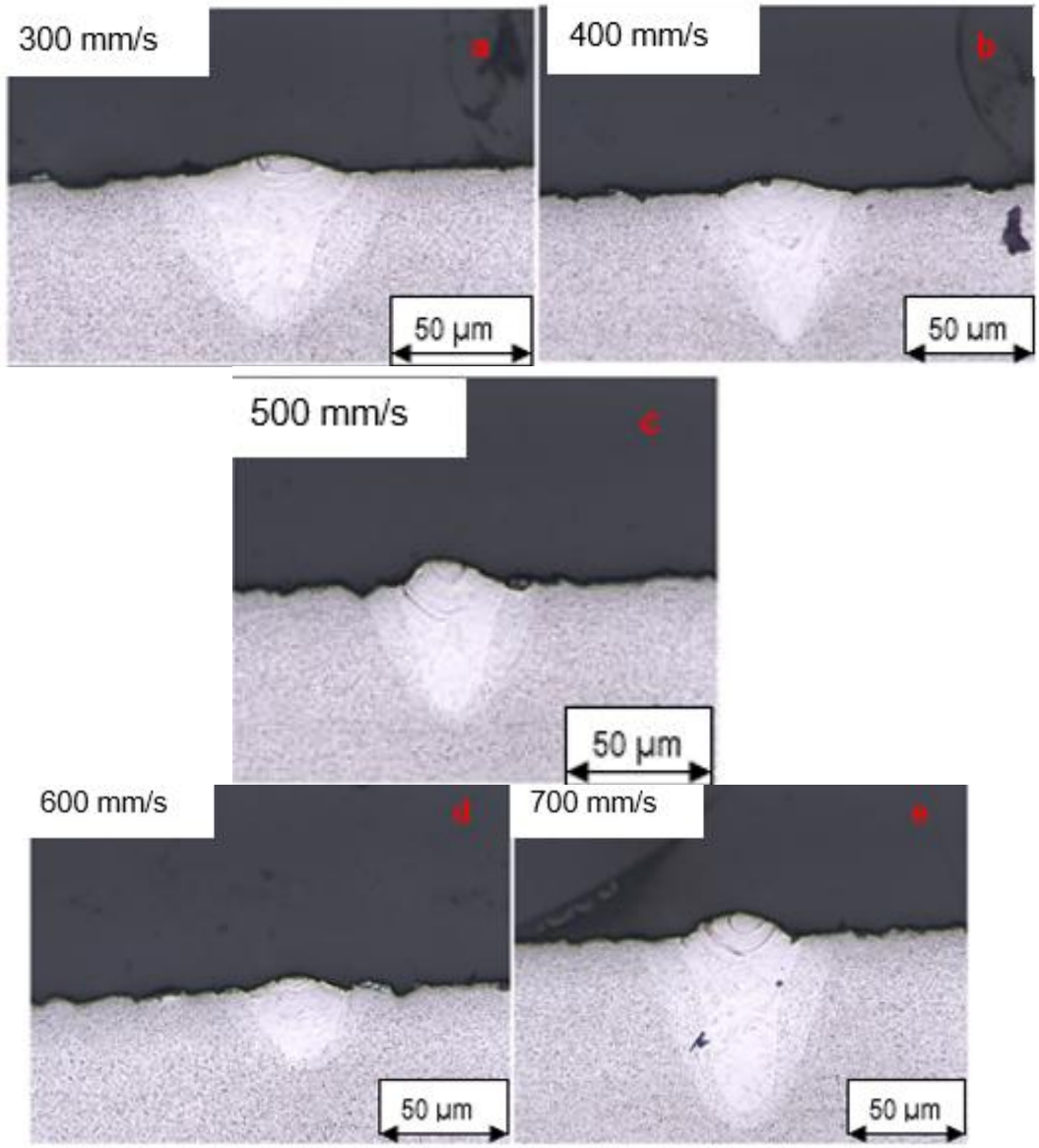

Figure 7.7 Optical micrograph of the cross-sections of single tracks built at a laser power of 80W and scanning speeds between 300–700 mm/s

A visual observation of Figure 7.7 points to the formation of keyhole modes between scanning speeds of 300–500mm/s. A much higher aspect ratio is observed at the final scanning speed of 700 mm/s, which is an anomaly as the highest scanning speed in this series should result in the lowest LED and, therefore, the lowest depth of penetration.

The characteristics of the cross-sections of the track builds can be further analysed using Figures 7.8, 7.9 and 7.10, whose values are extracted from Table 7.5.

© Central University of Technology, Free State

Table 7.4 Geometrical features for track builds at laser power of 80 W and scanning speeds of 300–700 mm/s

Track width (µm)	Track height (µm)	Track depth (µm)	Aspect ratio	Scanning speed mm/s	Linear energy density (J/m)
144.45	20.78	133.69	0.92	300	266.67
115.52	14.43	139.33	1.21	400	200.00
103.22	22.55	105.12	1.01	500	160.00
100.5	15.24	58.71	0.59	600	133.33
128.34	24.59	15.90	1.22	700	114.29

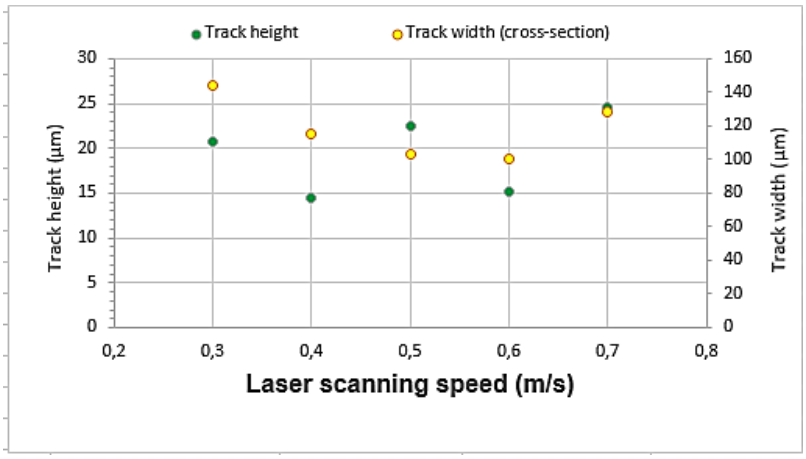

Figure 7.8 Plotted geometrical characteristics of depth, height, and width of tracks at a laser power of 80 W and scanning speeds of 300–700 mm/s

Figure 7.8 shows the effect of scanning speed on the width and height of the built tracks. The heights of the tracks did not show any clear trend with changing scanning speed and increased or decreased randomly with each change of scanning speed. The widths of the tracks decreased as the scanning speed increased to a speed of 600 mm/s and then increased at the highest scanning speed of 700 mm/s. This last trend is an anomaly that cannot be explained.

© Central University of Technology, Free State

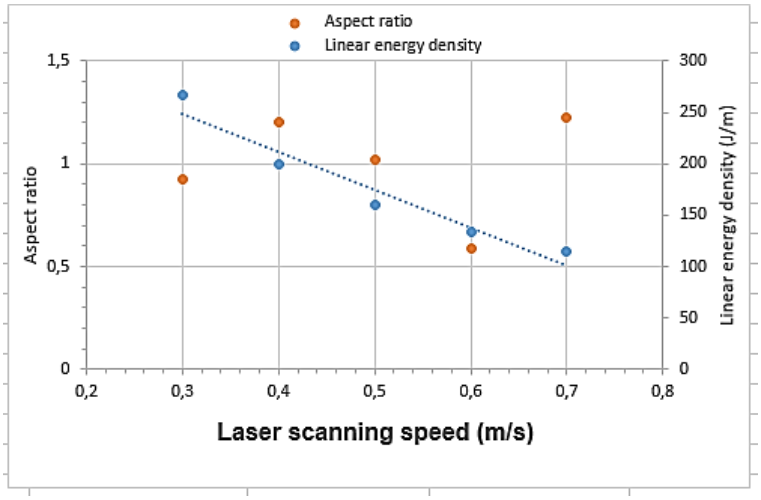

Figure 7.9 Plotted geometrical characteristics of aspect ratio and LED at 200–600 mm/s

Figure 7.9 shows the effect of scanning speed on the aspect ratio of tracks and LED. The plotted aspect ratios point to the formation of keyholes at all speeds in this case. Using the data for ratios of depth-to-width, deep keyholes were present at scanning speeds of 300 mm/s, 400 mm/s, 500 mm/s and 700 mm/s. The ratio of depth-to-width at a scanning speed of 600 mm/s in the same figure pointed to the presence of a shallower keyhole. The depths of penetration showed an increase between scanning speeds of 300 mm/s and 400 mm/s, then a sustained decrease till a scanning speed of 600 mm/s followed by an increase till a scanning speed of 700 mm/s. The initial increase in depth of penetration is likely to be the result of a very high ratio of laser power to scanning speed, at the lowest value of scanning speed, that promotes a large lateral flow of the melt to create a wide track. The subsequent continuous reduction in aspect ratio is a result of the continuous reduction of LED. The final increase in the aspect ratio cannot be explained and should be studied further in future work.

The effect of LED on the widths and depths of penetration of tracks in Figure 7.10 showed a sustained decrease from a scanning speed of 300 mm/s to 600 mm/s, followed by an increase to a scanning speed of 700 mm/s.

© Central University of Technology, Free State

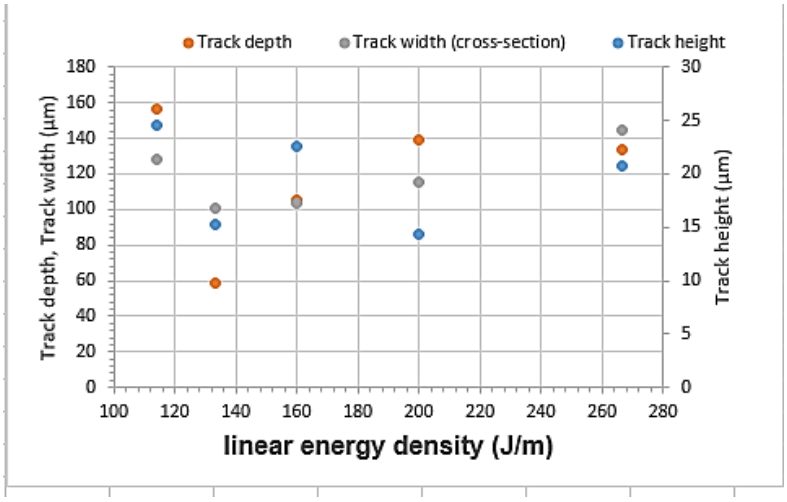

Figure 7.10 Influence of laser energy density on geometrical features at a laser power of 80 W and scanning speeds between 300–700 mm/s

The influence of the laser energy density on the height of tracks followed a similar trend to that in Figure 7.9.

The presence of keyholes in all the tracks built at a laser power of 80 W implied that none of these parameter sets were good for building 3D parts, as the keyholes would lead to structural defects in such parts.

7.2.3 Single Tracks of 3 % CNTs in Ti6Al4V(ELI), Built With a Laser Power of 100 W and Scanning Speeds between 400–800 mm/s

Figure 7.11 shows the top surfaces of single tracks built at a laser power of 100 W and scanning speeds between 400–800 mm/s (50µm layer thickness).

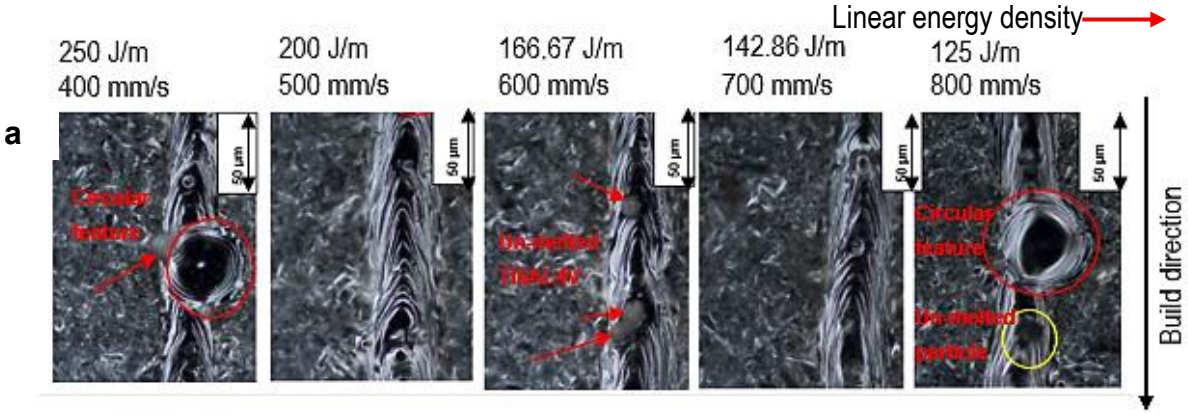

Figure 7.11 Optical micrographs of the cross-sections of single-track builds at a laser power of 100 W and scanning speeds between 400–800 mm/s

© Central University of Technology, Free State

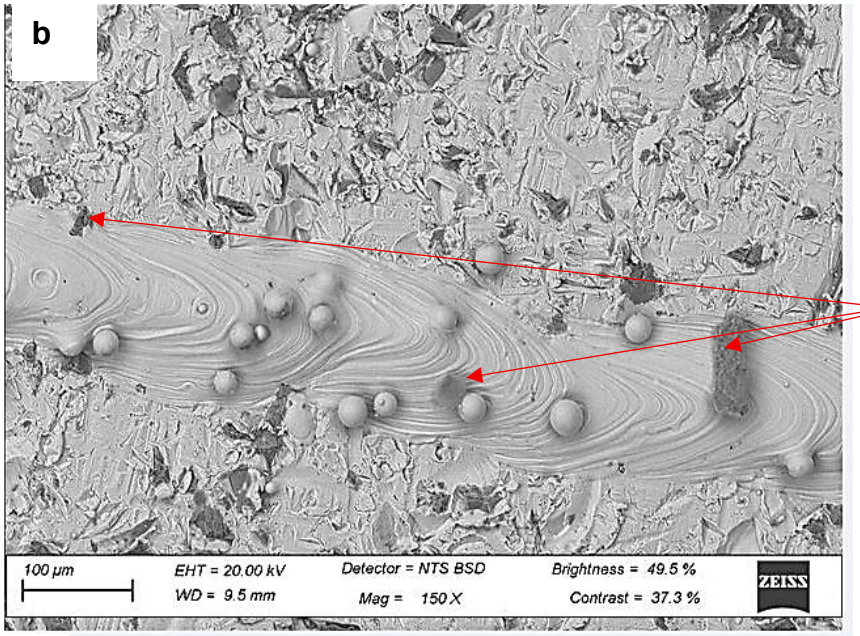

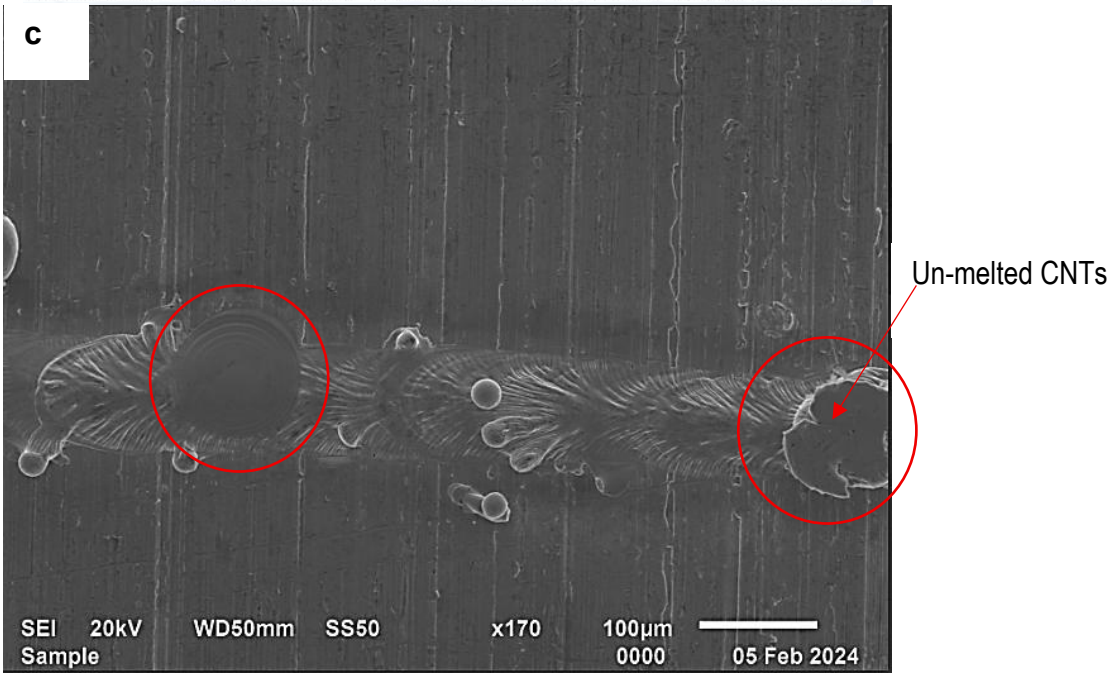

© Central University of Technology, Free State

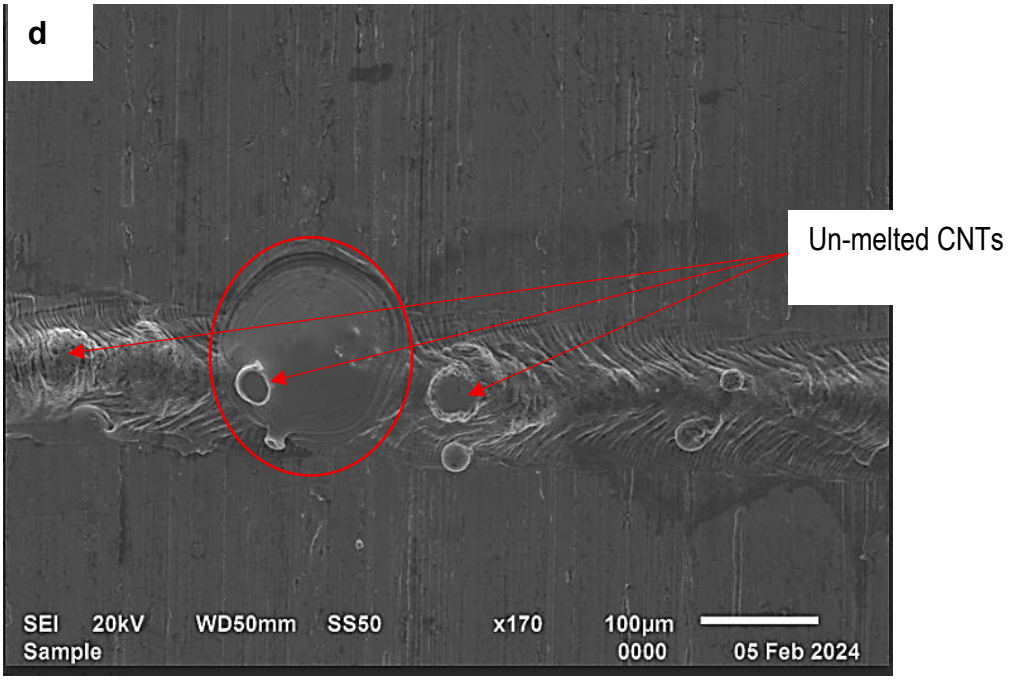

Figure 7.11 (b-d) SEM images of Single track pointing to the presence of CNTs

In Figure 7.11, the spots circled in red occurred at scanning speeds of 400 mm/s and 800 mm/s. From considerations of density and specific heat of the composite constituents of Ti6Al4V(ELI) and CNTs shown in Table 7.3, it is evident that the same volume of CNTs requires between 0.381–0.720 times the heat supplied to an equal volume of Ti6Al4V(ELI) to attain the same rise in temperature. The thermal conductivity of CNTs of 0.613 $Wm^{-1}K^{-1}$, shown in Table 7.3, is 91 493 times higher than that of Ti6Al4V(ELI) of 6.7 x 10^{-6} $Wm^{-1}K^{-1}$. Therefore, for the same power and dwell time, CNTs will heat up 2.625–1.389 times faster and experience equilibration of temperature 91 493 times faster than Ti6Al4V(ELI). In such a case, CNTs become a heat source to the surrounding particles of Ti6Al4V(ELI), creating a temperature gradient away from them and the attendant gradients of viscosity and surface tension, that, in turn, cause a flow of melt away from them. The foregoing may explain the black spots as large clusters of CNTs and the circular features around them as ripples created by the radial flow of Ti6Al4V(ELI) melt away from them. Figure 7.11 (b-d) depicts the black spots observed (red circles) which further confirms this observation due to the distinction between the Ti6Al4V spatter particles which are different from the black spots. It is also indicated that the presence of un-melted CNTs in the track is found.

© Central University of Technology, Free State

Unmelted Ti6Al4V(ELI) particles (indicated by red arrows in Figure 7.11) were observed at the lower energy scanning speeds (400 mm/s and 600 mm/s) where the LED was high (250 J/m and 200 J/m). This was surprising as this was expected to occur at higher scanning speeds, where the linear energy density was lower, thus leading to incomplete melting of powder particles caused by decreased periods of interaction between the laser beam and mixture of powder. At a scanning speed of 800 mm/s, a cluster of unmelted CNTs in the track is indicated by the yellow circle. The tracks were continuous with even widths for all the scanning speeds, apart from the sections with dark spots. There were very few spatter particles in this figure, and the trends of decreasing width of the tracks and increasing depths of ripples with increasing scanning speed were not observed.

7.2.3.1 Geometric Analysis of Single-Track Built at a Laser Power of 100 W and Scanning Speeds Between 400–800 mm/s

The dimensions of the cross-sections shown in Figure 7.12 were measured and then used to carry out further analysis of the tracks built with the foregoing process parameters.

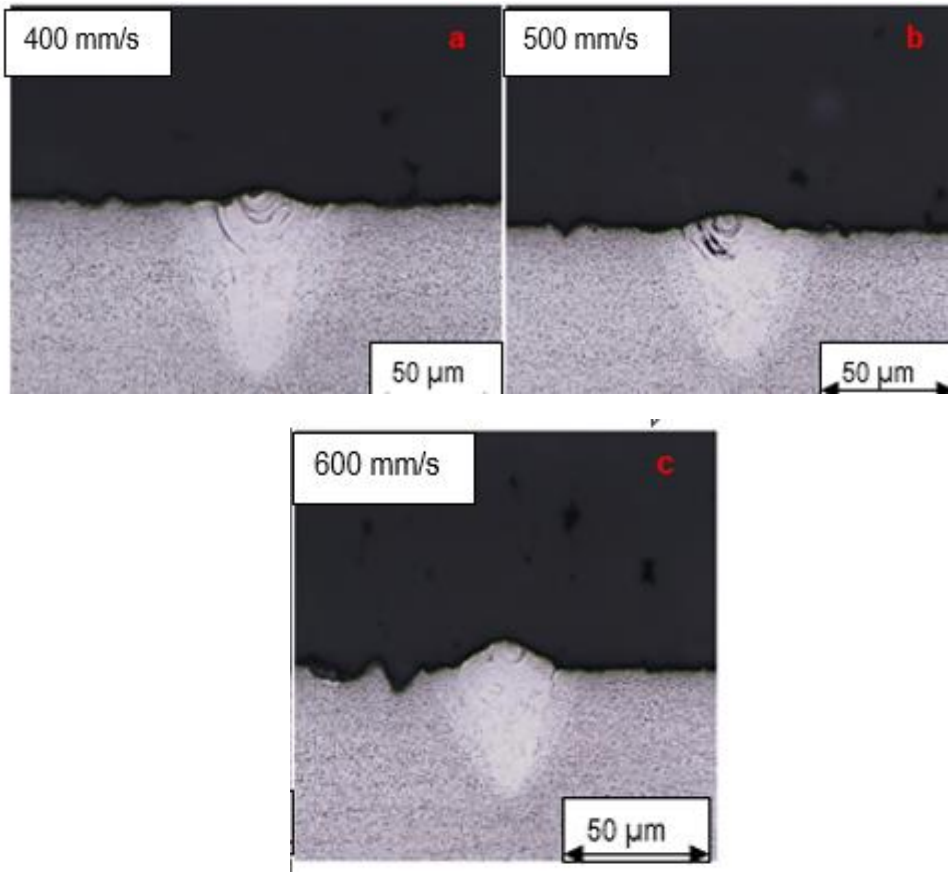

© Central University of Technology, Free State

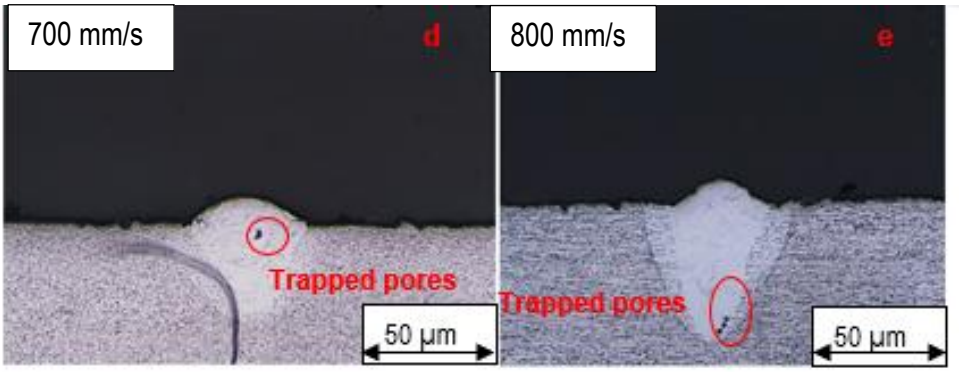

Figure 7.12 Optical micrographs of the cross-sections of single-track builds at a laser power of 100 W and scanning speeds between 400–800 mm/s

The images in Figure 7.12 all showed the presence of keyholes. The heat-affected zone (HAZ) was high at the highest scanning speed of 400 mm/s, where the LED is high due to the increased heat input into the substrate. The HAZ decreases with a decrease in the laser scanning speed due to a decrease in LED. The arc top surfaces of the tracks increase steadily from 600–800 mm/s. In general, the deposition height is directly proportional to the scanning speed (Ayalew et al., 2023). The shapes of the track heights are also influenced by the inclination angle. At an angle of 0° the melt pool spreads symmetrically due to surface tension and viscous forces around the centre of the laser beam. At this angle, a symmetrical track height profile is formed because the gravitational force is acting perpendicular to the surface of the deposition. As the inclination increases, the melt pool spreads; however, the gravitational force has a component acting in the lateral direction of the slope. This causes asymmetry in the profile of the track height (Alya et al., 2019). The study of the inclination angle on the geometric profile of the track will be examined in future studies and is not included in the current studies. Pores occurred at scanning speeds of 700 mm/s and 800 mm/s (red circles). Gas pores are formed from trapped gases and are normally spherical in shape, as are those formed at the latter scanning speed. The formation of pores due to trapped gases in SLM-produced parts depends on the processing parameters (Zhang et al., 2017).

The measured geometrical values for the scanning speeds between 400–800 mm/s are presented in Table 7.6.

© Central University of Technology, Free State

Table 7.5 Geometrical features for track builds at a laser power of 100 W and 400–800 mm/s (50 µm layer thickness).

Track width (µm)	Track height (µm)	Track depth (µm)	Aspect ratio	Scanning speed (mm/s)	Linear energy density (J/m)
128.33	13.68	141.49	1.10	400	250.00
115.51	14.72	109.80	0.95	500	200.00
114.14	23.55	91.61	0.80	600	166.67
111.02	28.05	80.01	0.72	700	142.86
125.56	19.75	148.42	1.18	800	125.00

The data presented in Table 7.6 shows reducing widths and depths of penetration, as well as increasing heights of the track with an increase in the laser energy density, except at the scanning speed of 800 mm/s.

The data presented in Table 7.6 was plotted in Figures 7.13–7.15.

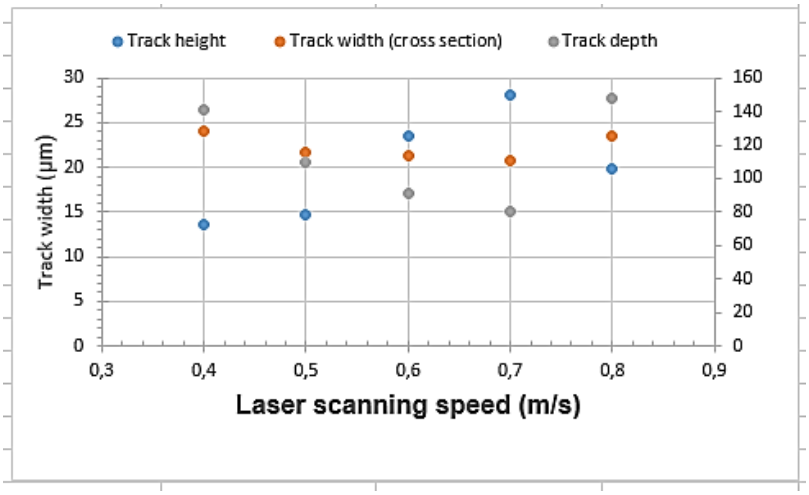

Figure 7.13 Plotted geometrical characteristics of depth, height, and width of tracks at a laser power of 100 W and scanning speeds of 400–800 mm/s

The graph in Figure 7.13 shows the relationships between scanning speeds and the width, depth of penetration and height of tracks. The depth of penetration, width and height of tracks in Figure 7.13 exhibited a similar trend of a continuous respective decrease and increase of values with increasing scanning speed and a reversal at 800 mm/s. The cause of the reversal at 800 mm/s is not clear and would require further testing and analysis. The trends for the depths of penetration, widths, and heights of the tracks for the four lowest scanning speeds were due to a decrease in the LED.

© Central University of Technology, Free State

This resulted in a decrease in temperature and surface tension and an increase in viscosity of the melt pool that limited the lateral flow of the melt pool, and thus the formation of narrower tracks with greater heights. The lower linear energy density also limited the ability of the laser beam to penetrate the layer of powder and the substrate, showing a decreasing trend of the depth of penetration of the tracks with increasing scanning speed.

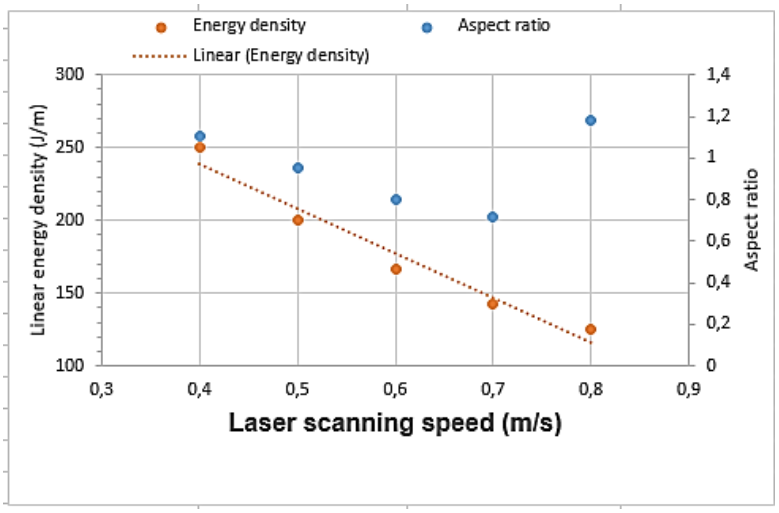

Figure 7.14 Plotted geometrical characteristics of aspect ratio and linear energy density at scanning speeds between 400–800 mm/s

In Figure 7.14, the plotted values of LED and aspect ratio show that as the laser energy density decreased, the aspect ratio also decreased; however, an outlier was identified at 800 mm/s where the aspect ratio increased, even as the LED decreased. This trend also occurred at a laser power of 80 W but not at 60 W. The aspect ratio at all scanning speeds, in this case, is above the threshold of 0.5, thus implying the formation of keyholes. Therefore, none of the process parameter sets in this case are suitable for further building of tracks and layers.

© Central University of Technology, Free State

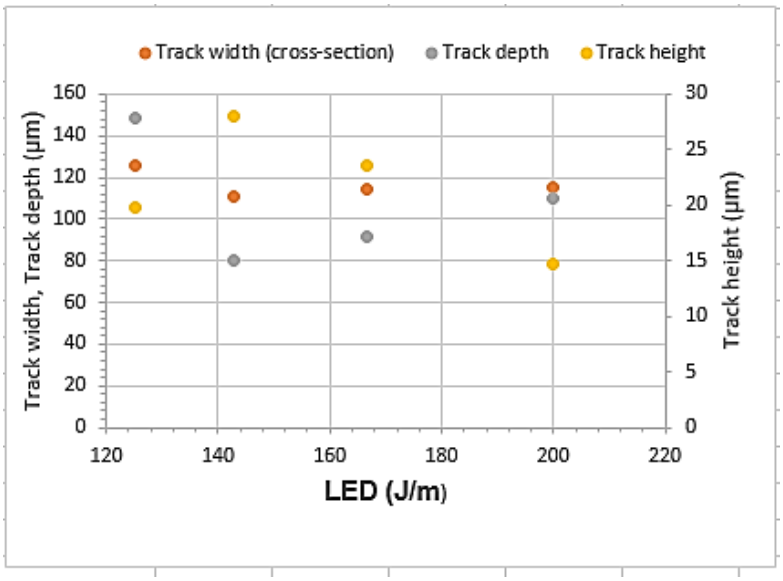

Figure 7.15 Influence of LED on geometrical features at a laser power of 60 W and scanning speeds between 400–800 mm/s

Plotting the data for width, depth and height of tracks against the LED in Figure 7.15 shows a similar reverse trend to that of the plots of the same factors against laser scanning speed. This reverse trend is not altogether surprising as the laser power is constant, and the LED is defined as the ratio of laser power to scanning speed.

In Table 7.2, the optimum scanning speed at a laser power of 100 W was predicted to be 600 mm/s, which in Figure 7.15 is seen to have produced tracks with an aspect ratio of 0.8. This high aspect ratio is expected to lead to the formation of keyholes, thus implying the scanning speed is not optimum.

7.2.4 Single Tracks of 3% CNTs in Ti6Al4V(ELI), Built with a Laser Power of 120 W and Scanning Speeds between 500–900 mm/s

Figure 7.16 shows the top surfaces of single tracks built at a laser power of 120 W with scanning speeds between 500–900 mm/s.

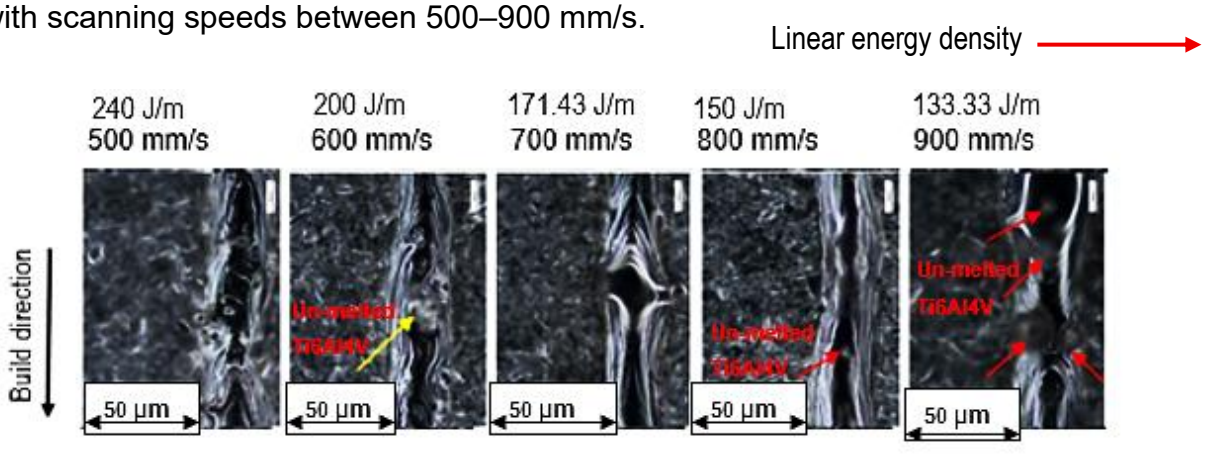

Figure 7.16 Optical micrographs of track builds at a laser power of 120 W and scanning speeds between 500–900 mm/s

© Central University of Technology, Free State

The built tracks in this figure were stable, with reasonably even widths and with no discontinuities. They did not have any ripples, as was the case for the previously discussed tracks in this section. The track at the two highest scanning speeds (800 mm/s and 900 mm/s) had unmelted Ti6Al4V(ELI) particles (indicated by red arrows). This was likely due to the reduced volumetric energy density at this scanning speed. There were unmelted Ti6AL4V(ELI) particles at 600 mm/s.

Further analysis of the built tracks, shown in Figure 7.16, was carried out on the basis of their cross-sections, whose OM images are shown in Figure 7.17.

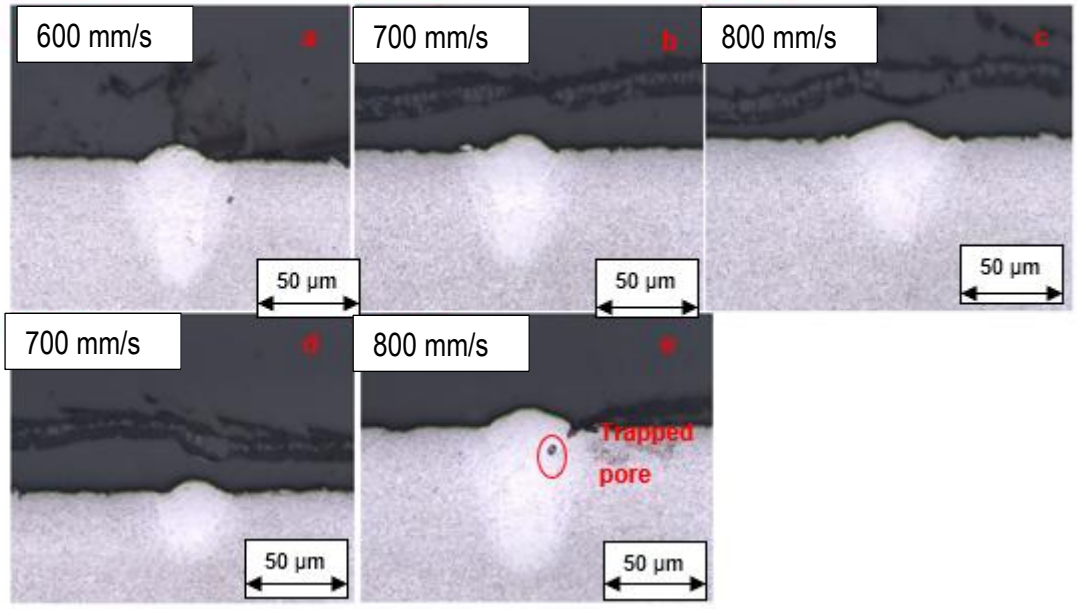

Figure 7.17 Optical micrographs of the cross-sections of single tracks built at a laser power of 120 W and scanning speeds between 400–800 mm/s

Visual observation of Figure 7.17 identifies keyhole formations at scanning speeds of 600 mm/s, 700 mm/s, 800 mm/s, and 1000 mm/s. The deeper keyholes at the lower scanning speeds of 700 mm/s and 800 mm/s were expected due to the higher LED at these scanning speeds. However, the much deeper keyhole formed at 1000 mm/s was not expected due to the higher scanning speed and, thus, lower LED, which was not expected to have a deeper penetration into the substrate. What appears to be a trapped pore (red circle) was also observed in the keyhole of the track built at a scanning speed of 1000 mm/s.

The measured geometric features of Figure 7.17 are presented in Table 7.7

© Central University of Technology, Free State

Table 7.6 Measured dimensions of the cross-sectional features of the single tracks, shown in Figure 7.17 (50 µm layer thickness).

Track width (cross section) (µm)	Track height (µm)	Track depth (µm)	Aspect ratio	Scanning speed (mm/s)	Linear energy density (J/m)
117.09	19.75	128.67	0.91	500	240.00
109.80	20.78	115.16	0.95	600	200.00
120.71	20.09	100.44	1.20	700	171.43
104.46	19.89	68.53	1.52	800	150.00
122.96	24.42	154.99	0.79	900	133.33

The arising trends following a similar analysis for tracks built at values of laser power of 60 W, 80 W, and 100 W, will only be mentioned in short as detailed information has been provided in sections 7.2.1, 7.2.2, and 7.2.3.

The values presented in Table 7.7 are plotted in Figures 7.18–7.20

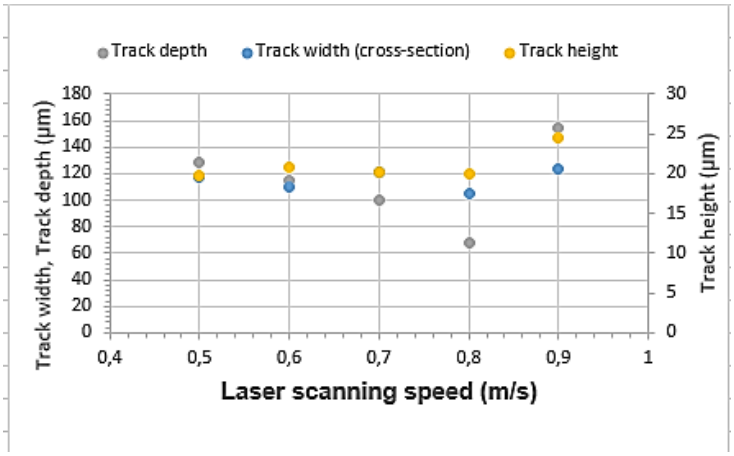

Figure 7.18 Plotted geometrical characteristics of depth, height, width of tracks at a laser power of 120 W and scanning speeds of 500 mm/s

The graphs for the depths of penetration, widths and heights of the tracks in Figure 7.18 showed a general continuous decrease for the first two and an increase for the last one, with increasing scanning speed. This was a result of decreasing LED with increasing scanning speed, leading to a decrease of temperature (and thus lower penetration of the laser beam), with an attendant increase of viscosity and surface tension that limited the lateral flow of the melt. However, the increase in depth and width of the track built at the highest scanning speed of 1000 mm/s was an anomaly that needed further investigation.

© Central University of Technology, Free State

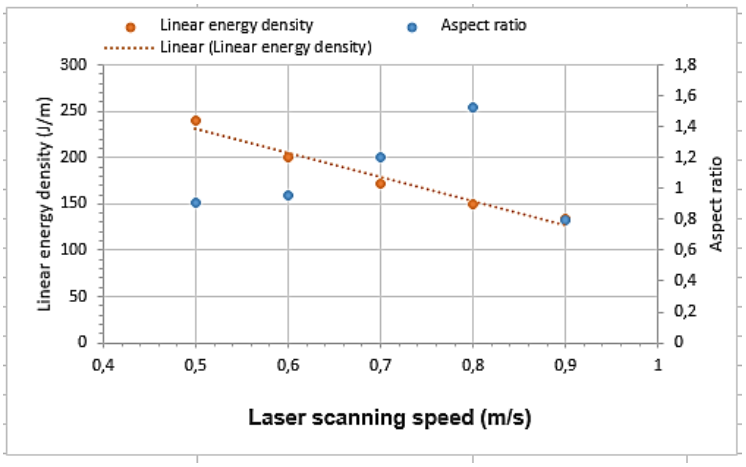

Figure 7.19 Plotted geometrical characteristics of aspect ratio and LED at 500–900 mm/s

The plotted depth-to-width ratios (Figure 7.19) were all greater than the threshold value of 0.5, which indicated the presence of keyholes for all these scanning speeds. The presence of keyholes indicates that the process parameters used to build them are non-optimal and could not be used to build good multiple tracks or multiple layers.

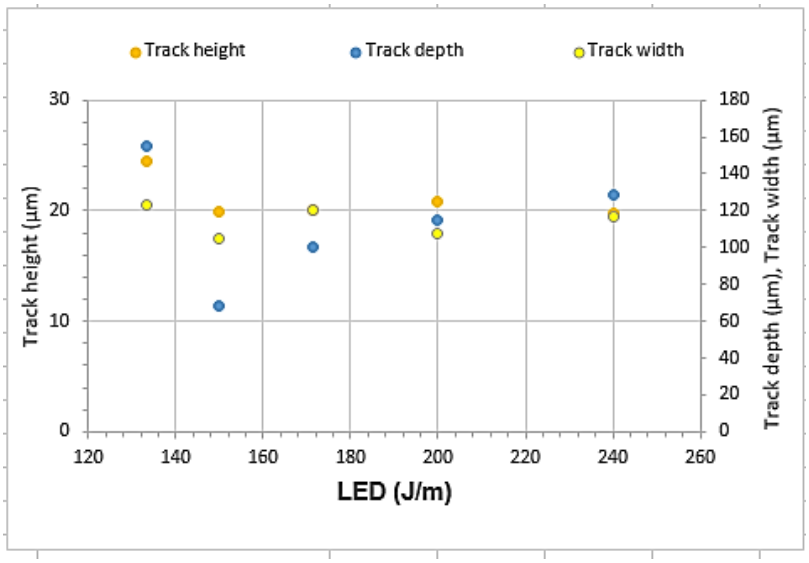

Figure 7.20 Influence of LED on geometrical features at a laser power of 60 W and scanning speeds between 500–800 mm/s

The widths and depths of penetration of the tracks in Figures 7.19 and 7.20 decrease and increase with increasing scanning speed and LED, respectively. The trends in Figures 7.19 and 7.20 are reversed to one another as expected due to the definition of the LED. The reasons for the reverse trend for the last value of scanning speed compared to the others in both graphs are not clear, which calls for further

© Central University of Technology, Free State

investigations. The aspect ratio in Figure 7.19 increases first and then decreases for the last scanning speed. The initial increase may be explained by the reduced lateral flow of the melt with the reduced dwell time of the laser beam, which accompanies an increase in scanning speed. The final increase in the aspect ratio cannot be explained, and further research is required.

7.2.5 Single Tracks of 3% CNTs in Ti6Al4V(ELI) Built with a Laser Power of 140 W and Scanning Speeds Between 700–1100 mm/s

Figure 7.21 shows the top surfaces of single tracks built at a laser power of 140 W and scanning speeds between 700–1100 mm/s.

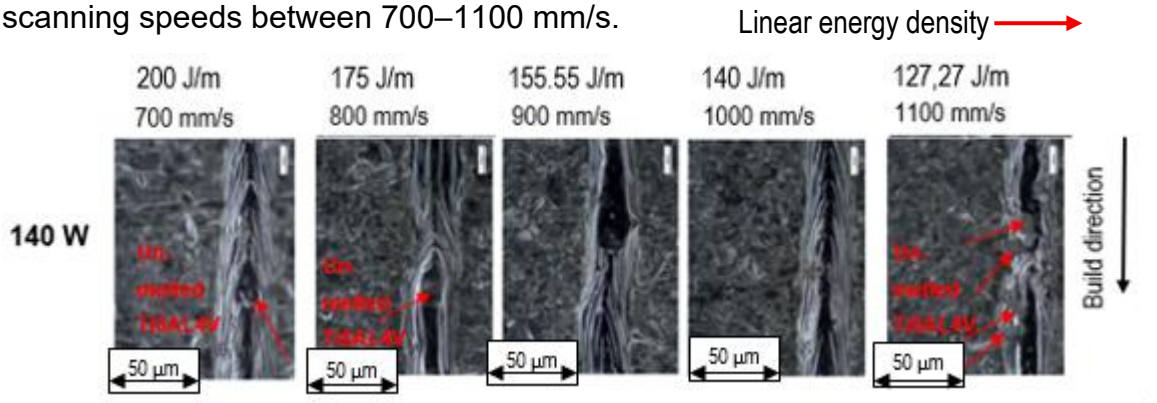

Figure 7.21 Optical micrographs of track builds at a laser power of 140 W and scanning speeds between 700–1100 mm/s

Figure 7.21 shows that the built tracks were all continuous and stable, with substantially even widths. The tracks exhibited ripples that were opened up at the centres and which appeared to run parallel to one another along the longitudinal directions of the tracks, as was seen in the tracks discussed in the previous subsection. The opening up of ripples is attributed to the much higher velocities. Unmelted Ti6Al4V(ELI) particles were seen in all the built tracks except at a scanning speed of 900 mm/s and at the highest scanning speed of 1100 mm/s, where the laser energy density was lowest.

Further analysis of the built tracks in Figure 7.2 was carried out on the basis of their cross-sections, whose OM images are shown in Figure 7.22.

© Central University of Technology, Free State

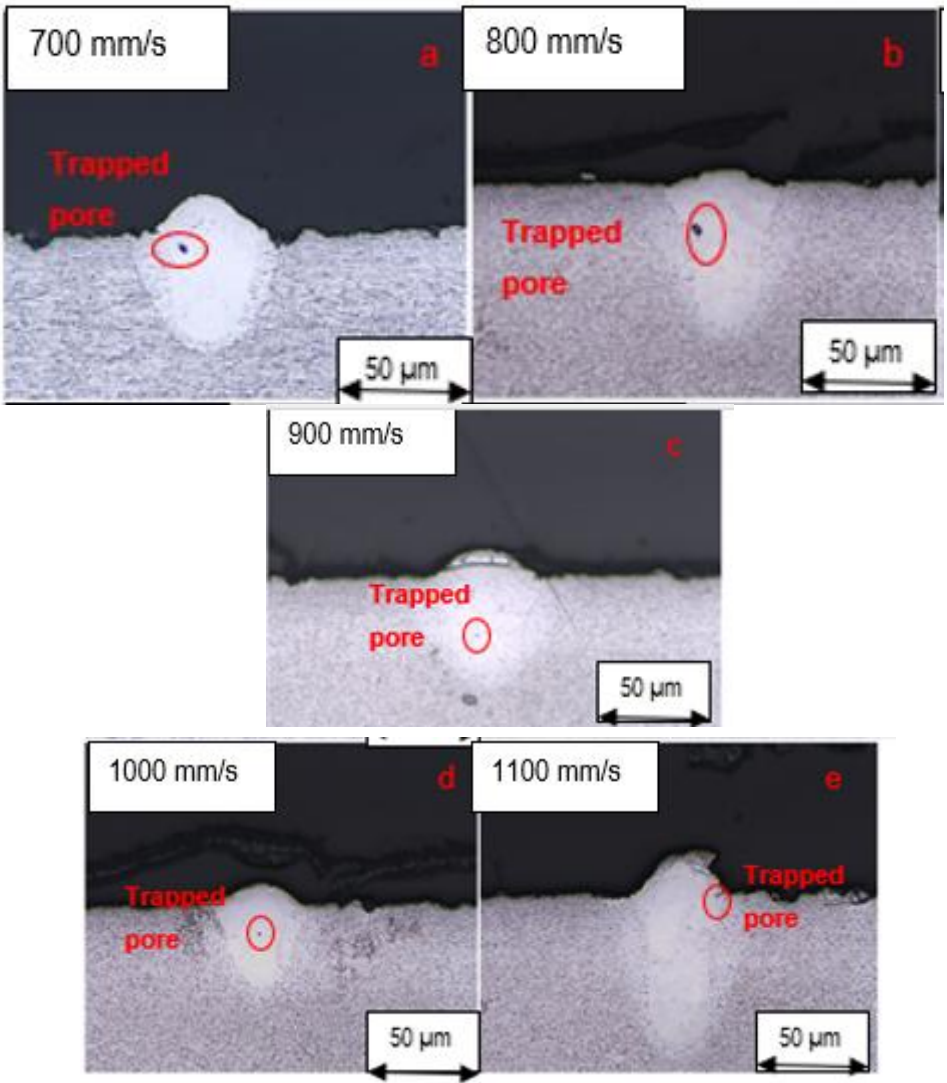

Figure 7.22 Optical micrographs of the cross-sections of single-track builds at a laser power of 140 W and scanning speeds between 700–1100 mm/s

All the cross-sections of the tracks shown in this figure exhibited keyholes, each of which had a pore.

The measured geometric features of Figure 7.22 are presented in Table 7.7.

Table 7.7 Measured dimensions of the cross-sectional features of the single tracks shown in Figure 7.24 (50 µm layer thickness).

Track width (cross section) (µm)	Track height (µm)	Track depth (µm)	Aspect ratio	Scanning speed (mm/s)	Linear energy density (J/m)
108.24	22.17	139.41	1,29	700	200.00
120.20	16.97	123.30	1,02	800	175.00

© Central University of Technology, Free State

120.19	28.23	98.87	0,82	900	155,55
112.07	22.69	83.99	0,75	1000	140.00
110.49	47.11	150.67	1,36	1100	127.27

It was garnered from the data on depth-to-width ratios in Table 7.8 that all the tracks were expected to have keyholes, with the most prominent ones expected at scanning speeds of 700 mm/s, 800 mm/s and 1100 mm/s. Therefore, the combination of the laser scanning speeds, and scanning powers used to build this set of single tracks was not suitable for building multiple tracks of layers, as the presence of keyholes in them and the surface irregularities of powder would lead to the formation of parts with poor mechanical properties and poor surface finish.

The values presented in Table 7.7 are plotted in Figures 7.23–7.25.

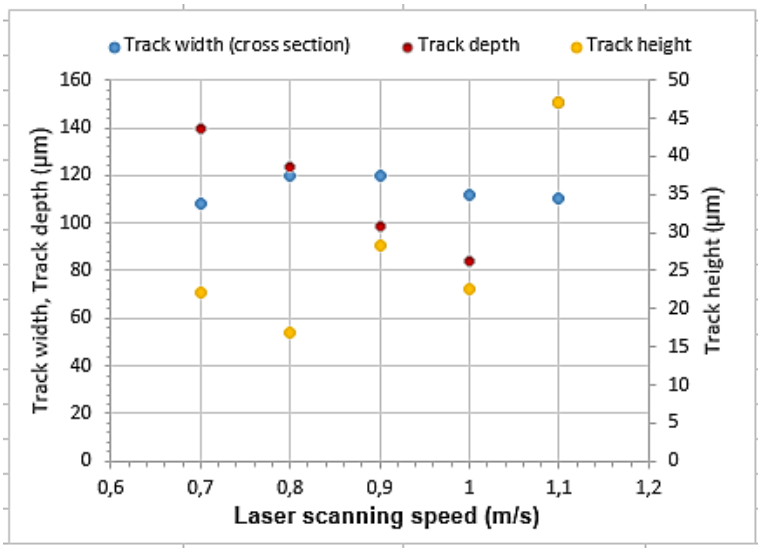

Figure 7.23 Plotted geometrical characteristics of depth, height, and width of tracks at a laser power of 140 W and scanning speeds of 500–900 mm/s

In Figure 7.23, the depths of penetration of the tracks decreased continuously with increasing scanning speed for the lowest four scanning speeds and increased for the highest scanning speed. The smallest width of the tracks occurred at the lowest scanning speed of 700 mm/s. This was rather peculiar since the LED at this scanning speed was the highest and was thus expected to form a large melt pool with the widest width. This trend is similar to the one observed at laser powers of 60 W, 80 W, 100 W, and 120 W. The widest and second widest tracks in the same figure occurred at scanning speeds of 800 mm/s and 900 mm/s, where the linear energy densities were 175 J./m and 155.55 J/m, respectively. The height of the tracks fell from one scanning

© Central University of Technology, Free State

speed to the other as the scanning speed increased and was at its highest at 1100 mm/s.

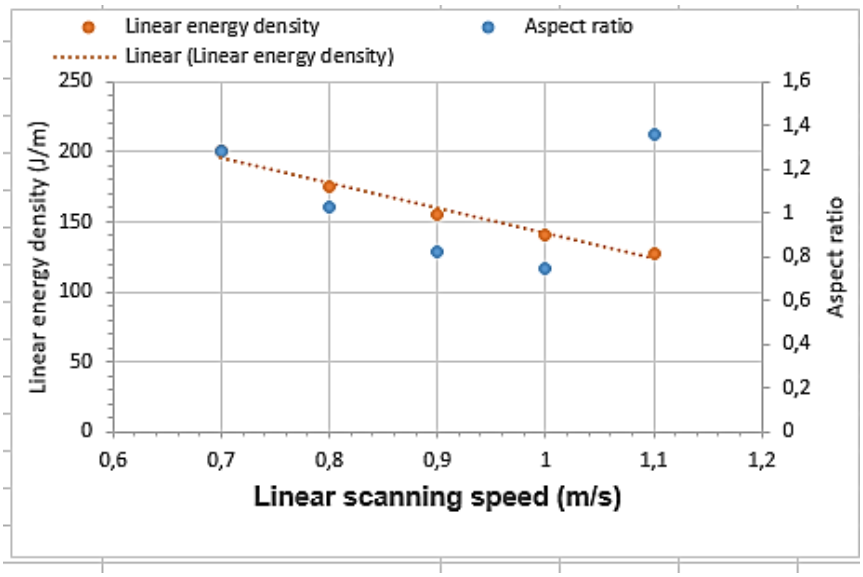

Figure 7.24 Plotted geometrical characteristics of aspect ratio and LED at scanning speeds of 700–1100 mm/s

The aspect ratios in Figure 7.24 point to the formation of keyholes as they all fall above the threshold of 0.5. It is curious to note that the deepest keyhole was formed at the lowest scanning speed of 1100 mm/s, where the linear energy density was lowest, contrary to expectations.

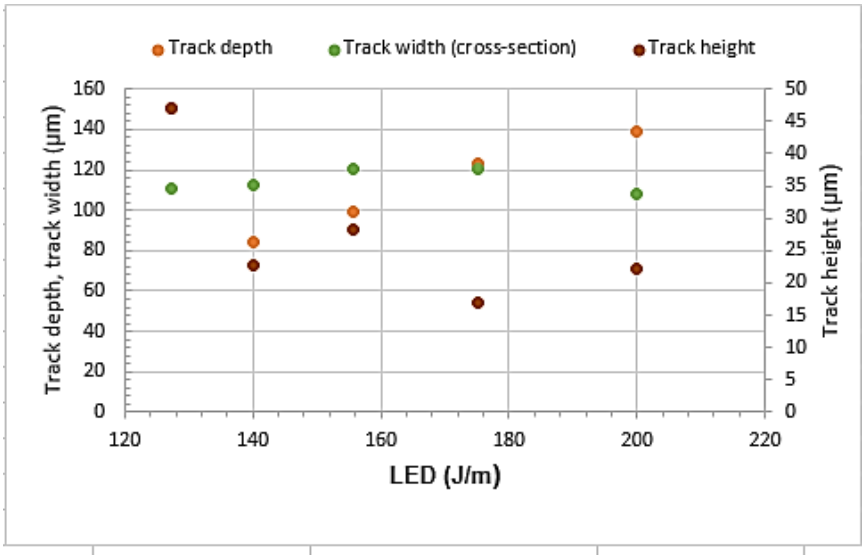

Figure 7.25 Influence of LED on geometrical features at alaser power of 140 W and scanning speeds between 700–1100 mm/s

© Central University of Technology, Free State

The data gathered from Figure 7.25 follows the same trend as that in Figure 7.24, where at the lowest linear energy density and highest scanning speed a deep keyhole impression is formed.

The values of the aspect ratio in Table 7.8 and Figure 7.25 are above the threshold of 0.5 for all scanning speeds adopted here. Therefore, no process parameter set in this case is optimal, and they cannot be used to print good layers or 3D parts.

7.2.6 Single Tracks of 3 % CNTs in Ti6Al4V(ELI) Built With a Laser Power of 160 W and Scanning Speeds between 800–1200 mm/s

Figure 7.26 shows the top surfaces of single tracks, built at a laser power of 160 W and scanning speeds between 800–1200 mm/s.

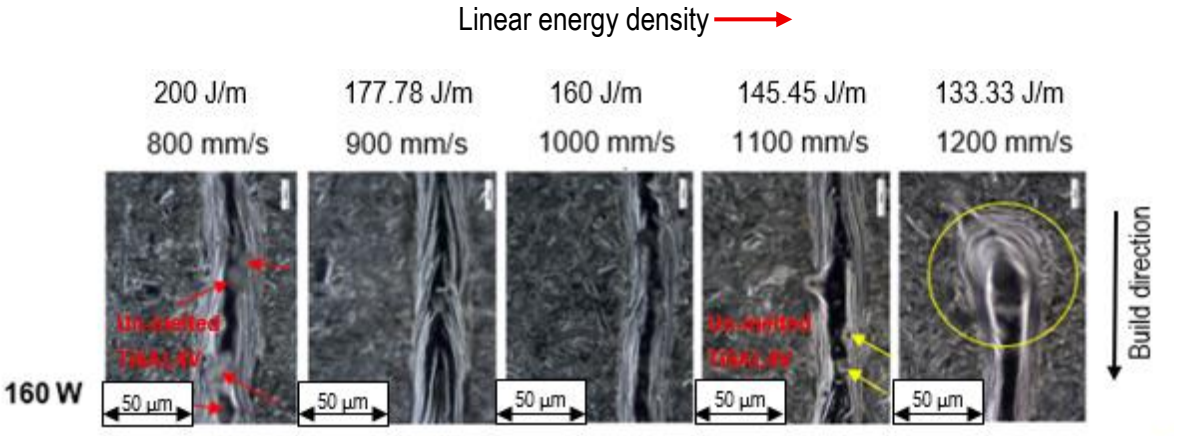

Figure 7.26 Optical micrographs of track builds at a laser power of 160 W and scanning speeds between 800–1200 mm/s

An inspection of Figure 7.26 shows all the tracks to be ridges and with reasonably even widths. Unmelted particles of Ti6Al4V(ELI) were found at scanning speeds of 800 mm/s and 1200 mm/s. This was surprising at the lower scanning speed, with its LED of 200.00 J/m, but not so at the higher scanning speed, with its lower LED of 133.33 J/m. The tracks built at scanning speeds of 900 mm/s and 1000 mm/s showed no unmelted particles or spatter particles. The track built at 900 mm/s exhibited sharp elongated ripples, while those built at scanning speeds of 800 mm/s, 1000 mm/s and 1100 mm/s were all open in the middle. Open ripples at a scanning speed of 800 mm/s and closed ones at a higher scanning speed of 900 mm/s are surprising as the opening up of ripples is expected to be a result of high scanning speeds.

© Central University of Technology, Free State

Further analysis of the built tracks, shown in Figure 7.26, was carried out on the basis of their cross-sections, whose OM images are shown in Figure 7.27

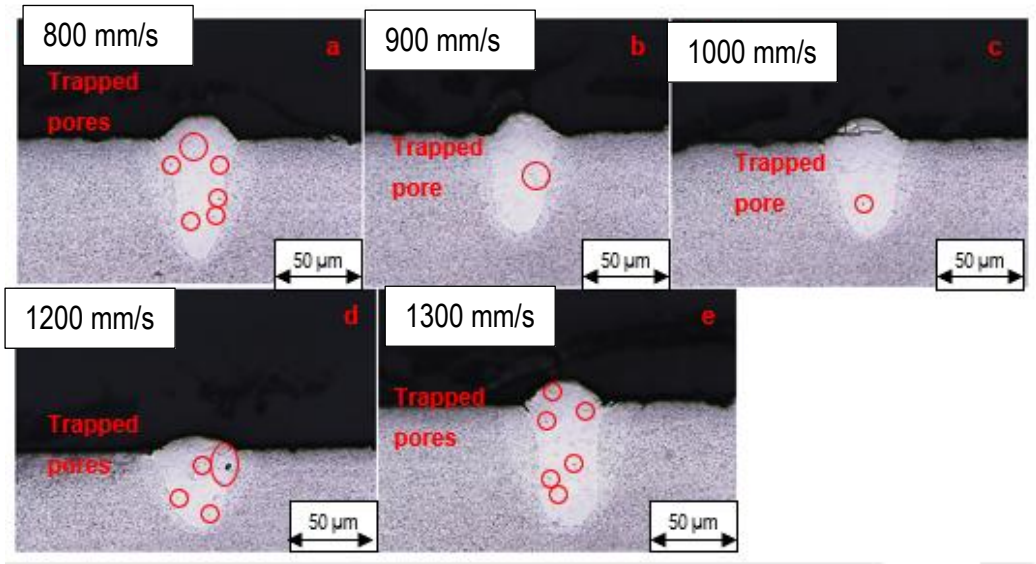

Figure 7.27 Optical micrographs of the cross-sections of single-track builds at a laser power of 160 W and scanning speeds between 800–1200 mm/s

All the tracks built at this laser power manifested keyholes. The tracks also exhibited a high number of pores, the highest seen in this work. The depth of the keyhole at a scanning speed of 1100 mm/s was smaller than those for the other scanning speeds, which are all seen in Table 7.9 to have higher depth-to-width ratios.

The measured geometric features of Figure 7.27 are presented in Table 7.9.

Table 7.8 Measured dimensions of the cross-sectional features of the single tracks shown in Figure 7.27 (50 µm layer thickness).

Track width (cross section) (µm)	Track height (µm)	Track depth (µm)	Aspect ratio	Scanning speed (mm/s)	Linear energy density (J/m)
118.98	30.83	149.63	1.26	800	200.00
109.80	28.75	123.30	1.12	900	177.78
112.92	30.48	117.94	1.04	1000	160.00
111.38	21.65	96.65	0.87	1100	145.45
115.86	32.39	155.35	1.34	1200	133.33

The values presented in Table 7.8 are plotted in Figures 7.28–7.30.

© Central University of Technology, Free State

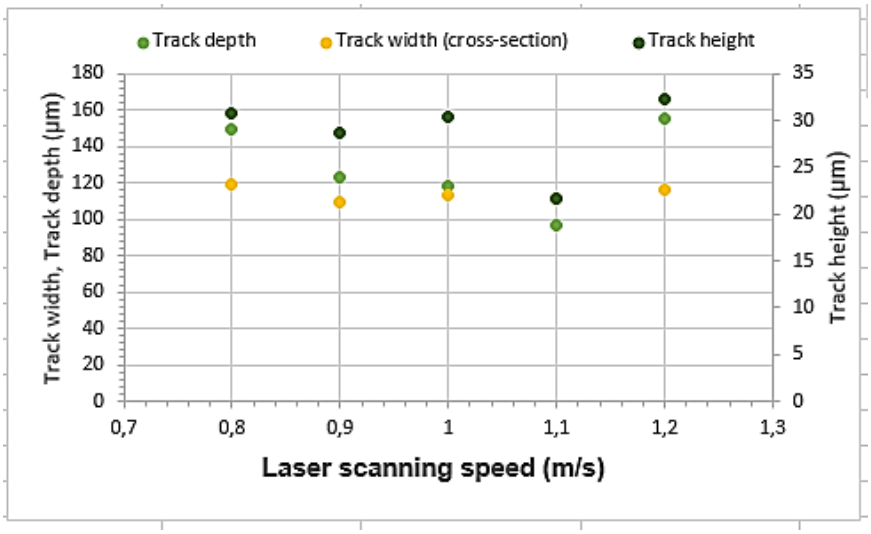

Figure 7.28 Plotted geometrical characteristics of depth, height, and width of tracks at a laser power of 160 W and scanning speeds of 800–1200 mm/s

The depth of penetration of the tracks in Figure 7.28 decreased with increasing scanning speeds. However, as with previous observations, it experienced a sharp increase at the highest scanning speed of 1200 mm/s. This trend was common from previous observations in the lowest scanning speeds. The widths and heights of the tracks decreased and increased irregularly with increasing scanning speed. While the behaviour of the heights of tracks is consistent with previous observations in this chapter, this is not so for the widths of the tracks, and it is not clear what causes this deviation in behaviour.

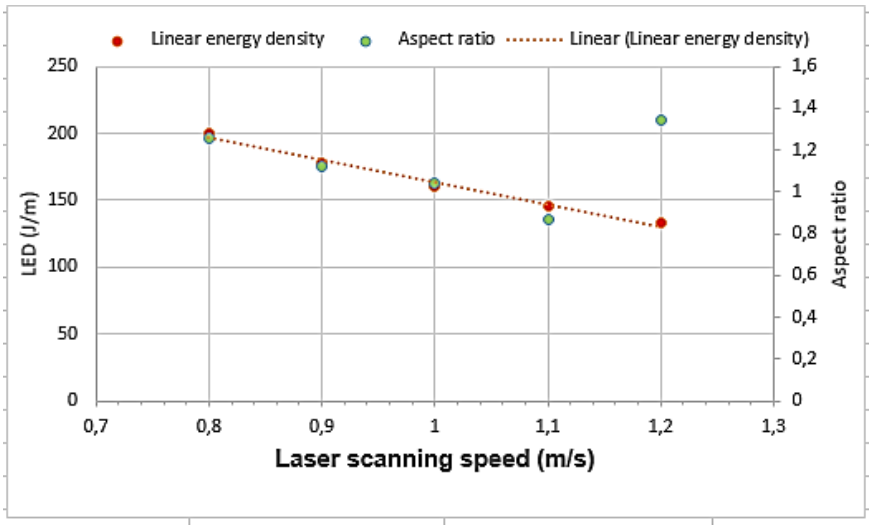

Figure 7.29 Plotted geometrical characteristics of aspect ratio and LED at scanning speeds between 800–1200 mm/s

© Central University of Technology, Free State

In Figure 7.29, the aspect ratio decreased with increasing scanning speed up until the last speed, at which point it increased in a manner similar to what was observed for the other values of laser power.

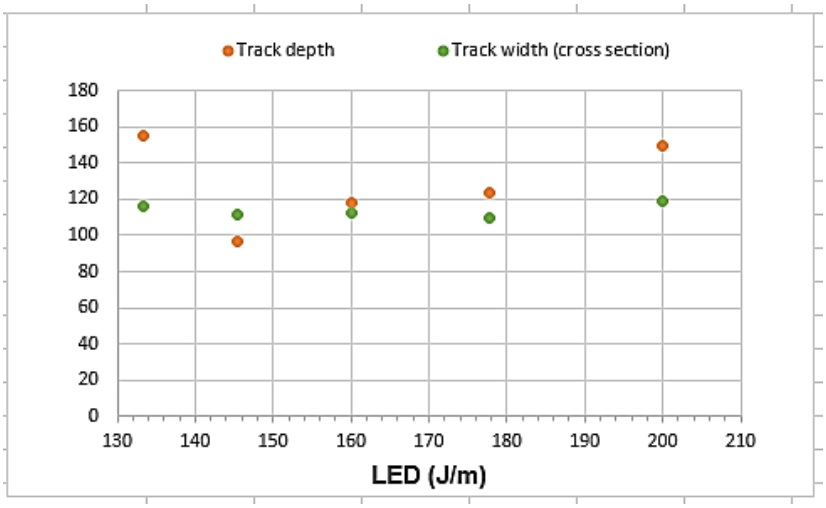

Figure 7.30 Influence of LED on geometrical features at a laser power of 160 W and scanning speeds between 800–1200 mm/s

A similar trend to the one for the depths of tracks built at other values of laser power is seen to prevail in this figure as well. Not so, though, for the width of tracks whose values vary up and down randomly with increasing values of LED. The LED is linear, in this case, as opposed to previous scanning powers. Future studies will investigate this trend in detail.

The large aspect ratios in Figure 7.30 and Table 7.9 imply the absence of a set of best process parameters of scanning speed and laser power that are not suitable for printing layers or 3D parts. The presence of a large number of pores noted in the cross-sections in Figure 7.27 also mitigates against the use of these sets of process parameters for the printing of layers and 3D specimens.

7.2.7 Single Tracks of 3 % CNTs in Ti6Al4V(ELI) Built With a Laser Power of 180 W and Scanning Speeds Between 900–1300 mm/s

Figure 7.31 contains images of the top surfaces of single tracks built at a laser power of 180 W and scanning speeds between 900–1300 mm/s.

© Central University of Technology, Free State

Central University of Technology, Free State

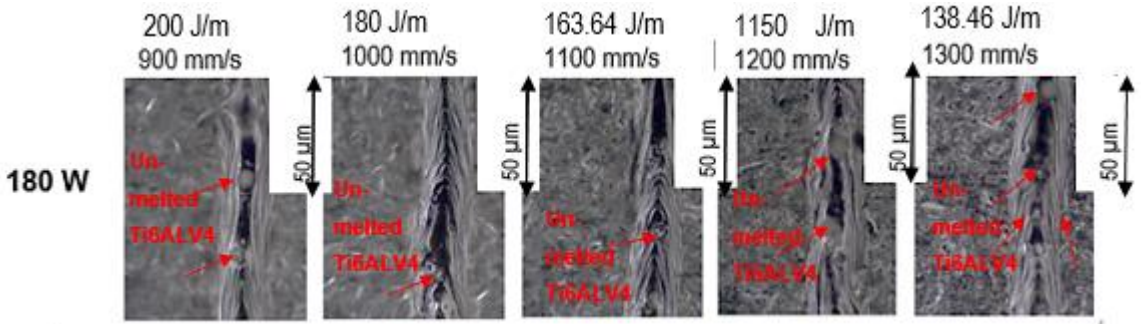

Figure 7.31 Optical micrographs of track builds at a laser power of 180 W and scanning speeds between 900–1300 mm/s

Figure 7.31 revealed a higher prevalence of unmelted Ti6Al4V(ELI), with all but the track build at a scanning speed of 1000 mm/s exhibiting them. It was also evident that no dark circular or elongated spots with ripples around them were present in any of the five tracks shown in this figure. All five tracks were continuous with reasonably even widths, had ripples that were open and aligned to the longitudinal direction of the tracks, and a good number of spatter particles.

Further analysis of the built tracks in Figure 7.31 was carried out on the basis of their cross-sections, whose OM images are shown in Figure 7.32.

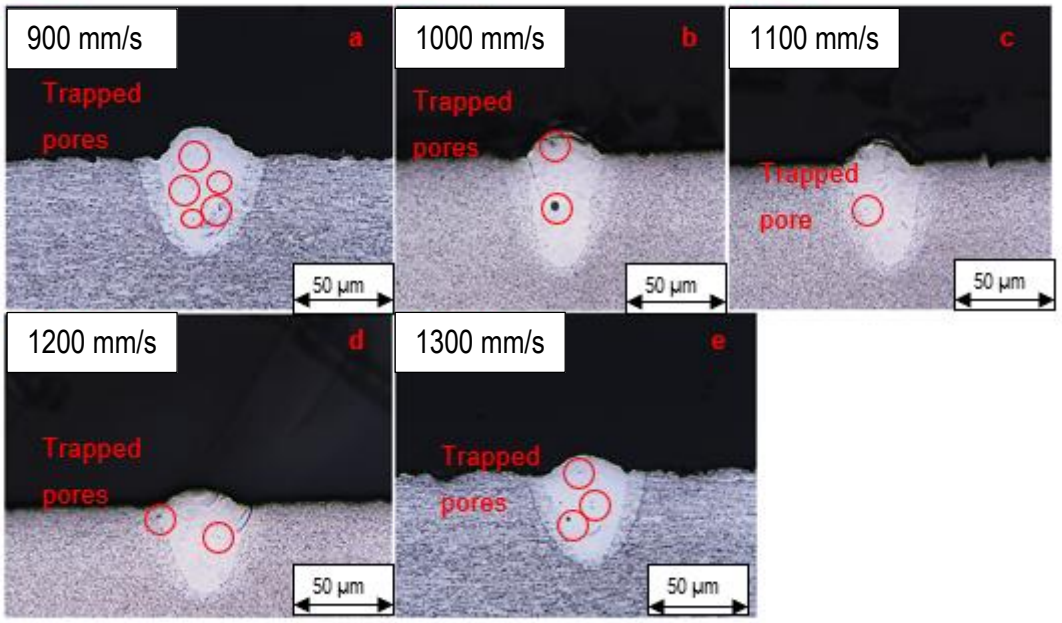

Figure 7.32 Optical micrographs of the cross-sections of single-track builds at a laser power of 180 W and scanning speeds between 900–1300 mm/s

© Central University of Technology, Free State

The presence of pores was observed at all scanning speeds used in this case, as was the case at a laser power of 160 W. Visual observation of the images in the figure also reviews the presence of keyholes for all the scanning speeds.

The measured geometric features of Figure 7.32 are presented in Table 7.10.

Table 7.9 Measured dimensions of the cross-sectional features of the single tracks shown in Figure 7.32 (50 µm layer thickness).

Track width (cross-section) (µm)	Track height (µm)	Track depth (µm)	Aspect ratio	Scanning speed (mm/s)	Linear energy density (J/m)
119.9	27.04	141.15	1.18	900	200.00
109.79	30.83	121.75	1.11	1000	180.00
118.63	29.10	109.28	0.92	1100	163.64
111.28	21.01	94.70	0.85	1200	150.00
102.18	19.40	118.29	1.16	1300	138.46

The values presented in Table 7.9 are plotted in Figures 7.33–7.35.

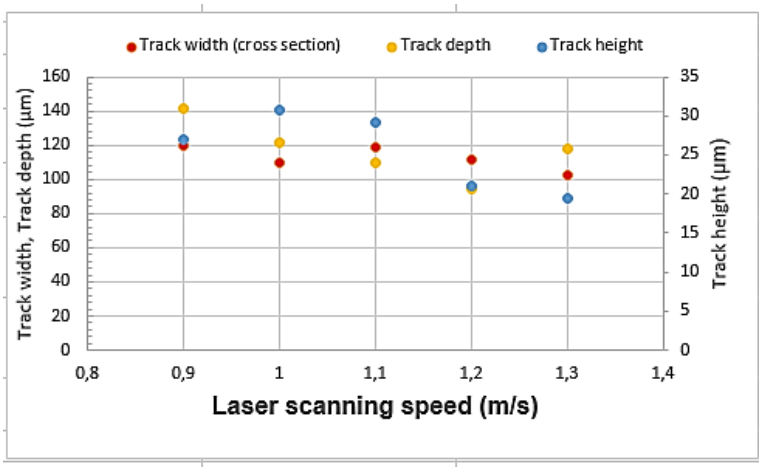

Figure 7.33 Plotted geometrical characteristics of depth, height, and width of tracks at a laser power of 180 W and scanning speeds of 900–1300 mm/s

In Figure 7.33, the depths of penetration and widths of the tracks decreased initially with increasing scanning speed and then increased at a scanning speed of 1300 mm/s. The track widths increased and decreased between the laser scanning speeds, an unusual trend observed in this case. The height of tracks experienced an

© Central University of Technology, Free State

initial increase followed by a decrease, with increasing scanning speed. The trend for the heights of the tracks for the two highest scanning speeds follows a different trend from that observed in section 7.3.3.1 in Figure 7.13, for which a detailed explanation is given. The track heights were expected to be higher due to the decrease in the volumetric energy density. This leads to a decrease in temperature and, therefore, surface tension and an increase in viscosity of the melt pool, which limits the lateral flow of the melt pool, thus, the formation of greater heights. In this case, further analysis would be required to describe this anomaly.

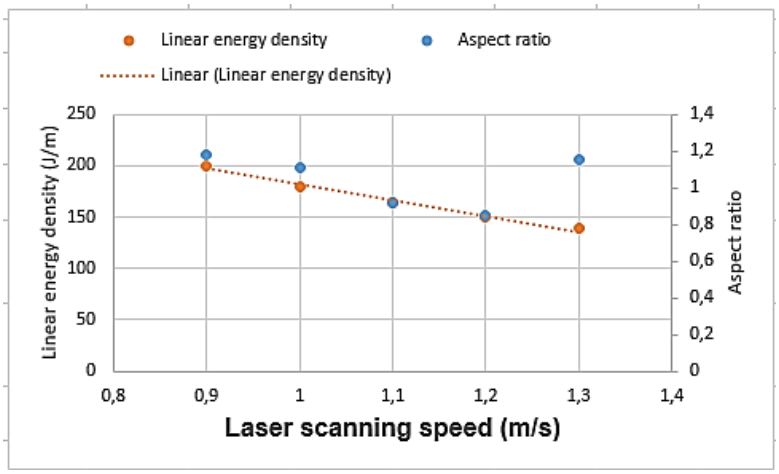

Figure 7.34 Plotted geometrical characteristics of aspect ratio and LED at scanning speeds of 900–1300 mm/s

While the LED showed an inverse linear relationship with the scanning speed, the aspect ratio showed an initial decrease followed by an increase for the highest scanning speed. This is a behaviour similar to the trend observed at values of laser power of 60 W somewhat, as well as 100 W, 140 W and 160 W. The curves at values of laser power of 80 W and 120 W were inverted. This difference in behaviour warrants further investigation.

All the images shown in this figure exhibited keyholes, most of them with numerous pores. The presence of keyholes and pores for all process parameter sets used in this case implies that none were suitable for use in producing 3D parts with good mechanical and physical properties.

7.3 Conclusions

Preliminary track builds were carried out using process parameter sets in a matrix that was developed for a 3% vol. CNTs in Ti6Al4V(ELI) mixture. Stable tracks were

© Central University of Technology, Free State

obtained at values of laser power of 60 W and 80 W. However, the geometrical features produced track builds with aspect ratios above 0.5. The predicted optimum values obtained from Table 7.2 could not be verified through experimental results. The results obtained fell outside the predicted optimum values. The formation of keyholes became dominant for tracks built at values of laser power of 100 W to 180 W, and the formation of pores increased for values of laser power of 160 W to 180 W.

Linear energy density showed an inverse linear relationship with the scanning speed, and the aspect ratio showed an initial decrease followed by an increase in the highest scanning speed. This is a behaviour similar to the trend observed at values of laser power of 60 W, 100 W, 140 W, and 160 W. The curves at values of laser power of 80 W and 120 W were inverted. This difference in behaviour warrants further investigation. There was nonlinearity of LED between values of laser power of 60–140 W; however, linearity occurred at values of laser power of 160–180 W, which warrants further research. Ripples occurred across the built tracks for all laser powers and scanning speeds, which tended to become elongated at the centre of the tracks with increasing scanning speeds and opened up at the centre of tracks at very high scanning speeds.

Extrapolation of the curves of aspect ratio for tracks built at values of laser power of 80 W and 120 W is possible at higher and lower values of scanning speed to obtain ranges of scanning speed beyond which the threshold value of aspect ratio prevails. However, the difference between their curvature and those of the tracks built at the other values of laser power raises questions as to whether this curvature was not in error. Therefore, repeat testing is necessary before such extrapolation is attempted.

For all the other values of laser power used in this work apart from 60 W, the concave upwards curves of aspect ratio and the fact that the minimum values of aspect ratio are higher than the threshold value of 0.5 imply that optimum process parameter sets of laser power and scanning speed do not exist.

References

1. Alya, S., Vundru, C., Ankamreddy, B. and Singh, R., 2019. Characterization and modeling of deposition geometry in directed energy deposition over inclined surfaces. *Procedia Manufacturing*, *34*, pp. 695–70.

© Central University of Technology, Free State

2. Ayalew, A. A., Han, X. and Sakairi, M., 2023. A critical review of additive material manufacturing through electrochemical deposition techniques. *Additive Manufacturing*, pp. 103796.
3. Balhara, H., Botcha, B., Wolff, S. and Bukkapatnam, S., 2021. Ripple formation and its effect on the multi-scale microstructure of Directed Energy Deposition (DED)-printed 316L components. *arXiv preprint arXiv:2111.11601*.
4. Edwards, P. and Ramulu, M., 2014. Fatigue performance evaluation of selective laser melted Ti–6Al–4V. *Materials Science and Engineering: A, 598*, pp. 327–337.
5. Gong, H., Rafi, K., Gu, H., Ram, G. J., Starr, T. and Stucker, B., 2015. Influence of defects on mechanical properties of Ti–6Al–4 V components produced by selective laser melting and electron beam melting. *Materials & Design, 86*, pp. 545–554.
6. Leuders, S., Thöne, M., Riemer, A., Niendorf, T., Tröster, T., Richard, H. A. and Maier, H. J., 2013. On the mechanical behaviour of titanium alloy TiAl6V4 manufactured by selective laser melting: Fatigue resistance and crack growth performance. *International Journal of Fatigue, 48*, pp. 300–307.
7. Li, Z., Kucukkoc, I., Zhang, D. Z. and Liu, F., 2018. Optimising the process parameters of selective laser melting for the fabrication of Ti6Al4V alloy. *Rapid Prototyping Journal, 24*(1), pp. 150–159.
8. Liu, Q. C., Elambasseril, J., Sun, S. J., Leary, M., Brandt, M. and Sharp, P. K., 2014. The effect of manufacturing defects on the fatigue behaviour of Ti-6Al-4V specimens fabricated using selective laser melting. *Advanced Materials Research, 891*, pp. 1519–1524.
9. Miao, S. Q., Li, H. P. and Chen, G., 2014. Temperature dependence of thermal diffusivity, specific heat capacity, and thermal conductivity for several types of rocks. *Journal of Thermal Analysis and Calorimetry*, *115*, pp. 1057–1063.
10. Qiu, C., Adkins, N. J. and Attallah, M. M., 2013. Microstructure and tensile properties of selectively laser-melted and of HIPed laser-melted Ti–6Al–4V. *Materials Science and Engineering: A, 578*, pp. 230–239.
11. Ran, Q., Yang, W., Hu, Y., Shen, X., Yu, Y., Xiang, Y. and Cai, K., 2018. Osteogenesis of 3D printed porous Ti6Al4V implants with different pore sizes. *Journal of the Mechanical Behavior of Biomedical Materials, 84*, pp. 1–11.

© Central University of Technology, Free State

12. Sillani, F., de Gasparo, F., Schmid, M. and Wegener, K., 2021. Influence of packing density and fillers on thermal conductivity of polymer powders for additive manufacturing. *The International Journal of Advanced Manufacturing Technology*, *117*(7), pp. 2049-2058.
13. Simonelli, M., Tse, Y. and Tuck, C. J., 2014. On the texture formation of selective laser melted Ti-6Al-4V. *Metallurgical and Materials Transactions A 45,* pp. 2863–2872.
14. Sinha, S. and Mukherjee, T., 2024. Mitigation of gas porosity in additive manufacturing using experimental data analysis and mechanistic modeling. *Materials*, *17*(7), pp. 1569.
15. Song, B., Dong, S., Zhang, B., Liao, H. and Coddet, C., 2012. Effects of processing parameters on microstructure and mechanical property of selective laser melted Ti6Al4V. *Materials & Design, 35*, pp. 120–125.
16. Tchuindjang, J. T., Paydas, H., Tran, H. S., Carrus, R., Duchêne, L., Mertens, A. and Habraken, A. M., 2021. A new concept for modeling phase transformations in Ti6Al4V alloy manufactured by directed energy deposition. *Materials*, *14*(11), pp. 2985.
17. Wang, Z., Walayat, K. and Liu, M., Ripple Formation and Whole-Process Modelling of Selective Laser Melting. *Cell*, *2*(2), pp. 2.
18. Xu, W., Brandt, M., Sun, S., Elambasseril, J., Liu, Q., Latham, K., Xia, K. and Qian, M., 2015. Additive manufacturing of strong and ductile Ti–6Al–4V by selective laser melting via in situ martensite decomposition. *Acta Materialia, 85*, pp. 74–84.
19. Yadroitsava, I., Els, J., Booysen, G. and Yadroitsev, I., 2015. Peculiarities of single track formation from Ti6AL4V alloy at different laser power densities by selective laser melting. *South African Journal of Industrial Engineering*, *26*(3), pp. 86–95.
20. Zhang, B., Li, Y. and Bai, Q., 2017. Defect formation mechanisms in selective laser melting: a review. *Chinese Journal of Mechanical Engineering*, *30*, pp. 515–527.
21. Zheng, Q., Hao, M., Miao, R., Schaadt, J. and Dames, C., 2021. Advances in thermal conductivity for energy applications: a review. *Progress in Energy*, *3*(1), pp. 012002.

© Central University of Technology, Free State

CHAPTER 8 - CONCLUSIONS AND RECOMMENDATIONS

- Preliminary powder mixing of powders showed that:

1) Manual mixing of dry powders produced large-sized CNT agglomerates and proved to be a poor mixing technique.
2) Ethanol provided better dispersion due to the tendency of CNTs to occur in various places in the matrix.
3) Acetone produced smaller agglomerates, thus achieving deagglomeration of CNTs; however, because of the limited occurrence of these CNTs in Ti6AL4V(ELI), it was poor in dispersing CNTs.
4) Comparison of the three methods using Image analysis provided a basis for quantifying the effectiveness of the mixing method by measuring the sizes and counting the number of CNTs obtained in each mixing method. Plotting the results on one graph gave a depiction of the effectiveness of the three methods with respect to size of the agglomerates.
5) The outcome of the results necessitated the need for better mixing methods in achieving better dispersion and homogeneity of CNT/Ti6AL4V(ELI) powder mixtures.

- Secondary preliminary testing using ethanol as a processing agent and three mixing methods showed that:

1) Preliminary testing showed manual mixing to be a poor mixing technique. However, the use of ethanol with manual mixing improved this mixing method. Dispersion of CNTs was improved, and the appearance of large-sized CNT agglomerates was significantly reduced. However, as is the case with the combined mixing technique, particle defects were also obtained from this mixing technique.
2) Turbula mixing of powders produced the poorest dispersion of CNTs of the three mixing techniques. Instead, agglomeration of CNTs increased in the samples. Separation of CNTs from Ti6AL4V(ELI) powders

© Central University of Technology, Free State

increased at higher rotational speeds of 350 rpm. Low separation was observed at low rotational speeds of 140 rpm.

3) Combined mixing provided better dispersion of CNTs. However, due to the increase in manual mixing applied in the effort to overcome the separation of powders in turbula mixing, particle defects of Ti6AL4V(ELI) particles arose from this mixing technique. The particle defects were of various forms, including surface damage, particle fusion, and particle morphology changes.
4) The effectiveness of mixing is better achieved at low vol.% of CNTs in Ti6AL4V(ELI) at 3 % and 8 %.
5) Increasing the vol.% of CNTs in Ti6Al4V(ELI) leads to re-agglomeration of CNTs in the matrix. This was especially observed at vol.% of 15%-30% of CNTs
6) The volume fractions of 25 % and 30 % had a prominent presence of CNTs, which overshadowed Ti6AL4V(ELI) particles.
7) Reinforcement of Ti6Al4V(ELI) will decrease at the increasing volume fraction of CNTs in Ti6Al4V(ELI) due to the increase in CNT agglomeration at increasing volume fractions.
8) The longer sonication times improved the dispersion of CNTs from the short sonication times of five minutes that were used in preliminary testing samples.
9) The particle defects found in the secondary mixing, which were not found in preliminary testing, are largely due to the type of mixing tool used in the two mixing processes; a sturdier and more robust tool was used in the secondary mixing method.
10) Particles defects were largely prominent in 3%, 8%, 15%, 20%, an 25% vol. of CNTs in Ti6Al4V.
11) There were no discernible particle defects in the combined mixing method at 30 % vol. of CNTs. This is due to the presence of large amounts of CNTs within the mixture, which limited particle-to-particle interactions of Ti6Al4V(ELI) during manual mixing that led to defects at lower volume fractions of CNTs.

© Central University of Technology, Free State

12) The presence of particle defects will affect the printability of the powder mixtures, as it has been demonstrated amply in literature that spherical powders are required for better absorption of the laser energy density.
13) The presence of single CNT fibres is better observed at low volume fractions of 3 % and 8 %.
14) The presence of single fibres the proves that by combined mixing was more effective in de-agglomerating CNTs, since it points to the extent to which de-agglomeration of CNTs was achieved, which is required for better dispersion.
15) The combined mixing and manual methods had, in some instances, surface attachments of CNTs in the form of fibres (this is in reference to the 8% vol. of CNTs). However, this was at a low scale (Figure 5.2 b, 5.2d, Figure 5.14, Figure 5.15), compared to what is desired, which is increased surface attachments of most, if not all, Ti6Al4V(ELI) particles. The tendency for nanofibres to agglomerate with their increasing volume fraction due to their increasing closer proximity and the Van der Waal forces existing in between them as observed in literature.

- Powder mixing using SDS as a surfactant showed that:
  1) SDS adsorbs to the CNT agglomerates and unzips the end of the tube to achieve a single tube.
  2) In manual mixing, SDS achieved dispersion of CNTs in the Ti6l4V(ELI) matrix; however, re-agglomeration of CNTs occurred at 8 % and 30 % vol. of CNTs. In this case, the 8 % vol. of CNTs in Ti6Al4V(ELI) is an unexpected result that deviates on what is expected based on literature as re-agglomeration is expected only at higher content of CNTs.
  3) Having used manual mixing as a technique of homogenising the two powders, 8 % vol. of CNTs in the Ti6Al4V(ELI) powder sample achieved homogeneity. However, increased satellite particles compared to Figure 4.2a of the Ti6Al4V(ELI) un-mixed powder) were also observed in this sample. This mixing technique produced particle defects at 8 %, 25 %, and 30 % vol. of CNTs in the Ti6Al4V(ELI) matrix. There were surface defects at 8 % and 25 % vol. of CNTs in theTi6Al4V(ELI), while the defect at 30 % vol. of CNTs in the Ti6l4V(ELI) is likened to plastic deformation.

© Central University of Technology, Free State

4) When turbula mixing was used as a mixing technique, the CNT agglomerates increased from 15 % to 30 % vol. of CNTs in Ti6Al4V(ELI) matrix. Clusters of CNTs and Ti6Al4V(ELI) particles increased at 25 % and 30 % vol. of CNTs in the Ti6Al4V(ELI), likely due to the due to the de-agglomeration effect of SDS. Higher rotation speed is not thought to have had a contribution here as its effect is more centrifugal dispersion of particles towards the periphery of mixers The powder samples associated with this mixing technique also showed increased particle-to-CNT interaction through the surface attachment of CNTs on particles and particle-particle with CNTs in between them at 20 %, 25 %, and 30 % vol. of CNTs in theTi6Al4V(ELI) matrix.
5) The SEM images showed visible ribbons of crushed CNTs at 3 % and 8 % vol. of CNTs in the Ti6Al4V(ELI) matrix owing to the low content and effectiveness of SDS at these low-volume fractions. As the vol. of CNTs in Ti6Al4V(ELI) increased, the strands diminished; instead, entangled fibres were observed at 15 % vol. of CNTs, which reduced to sheets at 20 % and lastly, re-agglomeration at 25 % vol. of CNTs in theTi6Al4V(ELI) matrix. This shows the increased likelihood of reinforcement decreasing as the volume of CNTs in the Ti6Al4V(ELI) matrix is increased. Two particle defects were detected at 3 % vol. of CNTs in Ti6Al4V(ELI): a particle smearing onto a spherical Ti6Al4V(ELI) particle, and at 30 % vol. of CNTs in Ti6Al4V(ELI), a surface defect was seen.
6) Turbula mixing followed by manual mixing produced clusters of tightly packed Ti6Al4V(ELI) particles and CNTs, which were most prominent at 8 % and 15 % vol. of CNTs in the Ti6Al4V(ELI) matrix. At 20 %, 25 %, and 30 % vol. of CNTs in the Ti6Al4V(ELI) matrix, re-agglomeration of CNTs occurred. This mixing technique produced more particle defects out of the three, in their different forms at 3 %, 8 %, 20 %, 25 %, and 30 % vol. of CNTs in the Ti6Al4V(ELI) matrix, while the others were surface defects. The most severe cases were found at 3 % and 30% vol. of CNTs in the Ti6Al4V(ELI) matrix. During the observation of different forms of CNTs at various content levels, visible strands were seen at 3 %, while a thin sheet was found at 8 %. More sheets were discovered at 15 %,

© Central University of Technology, Free State

while there were agglomerated sheets at 25 % and 30 % vol. of CNTs in the Ti6Al4V(ELI) matrix.

- Preliminary optimisation of process parameters showed that
    1) Continuous tracks were obtained at a laser power of 60 W and 200–300 mm/s. These also had conduction modes at cross-sectional builds.
    2) Continuous tracks were also obtained at a laser power of 80 W and scanning speed between 300–400 mm/s. However, these were not in conduction mode and could not be used to build single layers.
    3) Laser powers between 100–180 W produced unstable tracks and melt pools in keyhole modes.
- Secondary optimisation of process parameters.

    1) In the first part of the analysis, at constant scanning power, the formation of stable tracks was found at increasing laser power and decreasing scanning speed. At 70 W scanning power, stable tracks were produced throughout the scanning speed range of 0.9–0.4 m/s.
    2) The same trend was observed at a laser power 90 W with stable tracks produced from the lowest to the highest scanning speed.
    3) At a laser power of 110 W, stable tracks were produced between 0.2–0.4 m/s scanning speed and became unstable as the laser density decreased due to a decreasing scanning speed.
    4) The second part of the analysis considered a case where closely packed clusters of CNT fibres-Ti6Al4V(ELI) particles were formed due to reducing the surface tension of Ti6Al4V(ELI) particles to allow better attachment of CNTs. The tracks showed that due to the reduced surface area of these clusters, absorption of laser energy intensity would be reduced, thus reducing the melt pool temperature and producing unstable tracks and, in some instances, discontinuity in tracks.
    5) The mixing method and volume fraction of CNTs in Ti6AL4V(ELI) influence the linear energy density characteristics.
    6) The same process parameters at the same volume fraction will not work for the three mixing methods.

© Central University of Technology, Free State

7) The best process parameters were identified through results obtained from microscope images by evaluating continuity in tracks, and geometrical features.
8) The effective mixing method requires a new set of process parameters to accommodate the fibres and de-agglomerated tubes.

Recommendations

- It is recommended that the process parameters should be optimised for each volume fraction and type of mixing method used.
- The use of SDS as a surfactant should be studied further, and the correct amounts of SDS in the mixtures should be determined through experimental procedures.
- The use of other processing agents should be explored further to best determine their effectiveness.
- It is also recommended that chemically treated CNTs should be acquired.
- Reinforcement of CNTs should be carried out at low-volume fractions of 3 % and 8 % due to the tendency of increased agglomeration and possible re-agglomeration even after mixing at higher-volume fractions
- To avoid and minimise particle defects, less manual mixing should be applied.
- It was also recommended that sonication of the slurry mixtures formed before oven-drying be carried out repeatedly over a period of two days to allow increased agitation to increase the de-entangling of CNT agglomerates.

© Central University of Technology, Free State

APPENDIX A

Section A.1 Powder mixture sample for 3 % vol. of CNTs in Ti6Al4V(ELI) in preliminary mixing

A powder sample of 3% vol. CNTs in TI6AL4V(ELI) is presented in Figure A.1(a–c).

Figure A.1 Powder mixture samples or 3 % vol. CNTs in Ti6Al4V(ELI)

Figure A1 presents CNT and Ti6Al4V(ELI) powder mixtures at various stages of mixing. In Figure A.1(a), the powder samples consist of visible CNTs (black) and Ti6AlV(ELI) powders (grey), which form a wetted mixture as ethanol is still present. Figure A.1(b) presents the powder mixture with visible lumps of powder mixture after partial oven-drying. Once the ethanol in the powder mixture is vaporised fully, the powder mixture remains in the form of loose particles, as seen in Figure A1(c). Visible carbon material inside the container, as shown in Figure A.1(c), posed a health and safety issue. The red arrows in Figure A.1(b & c) show the presence of CNTs on the surface of the mixture, which is thought to have been due to the density of CNTs being lower than that of Ti6Al4V(ELI).

Section A.2 Powder samples from secondary mixing

Section A.2.1 Samples of powder mixtures for the three mixing methods and varying CNTs vol.%.

The powder samples for the CNT/Ti6Al4V(ELI) powder mixtures are presented in Figure A.2, Figure A.3, and Figure A.4 for mechanical, turbula, and combined mixing, respectively.

© Central University of Technology, Free State

Section A.2.1.1 Mechanical mixed powder samples

The resulting samples are presented in Figure A.2 for the various nanotube reinforcement percentages of (a) 3 %, (b) 8 %, (c) 15 %, (d) 20 %, (e) 25 %, and (f) 30 %.

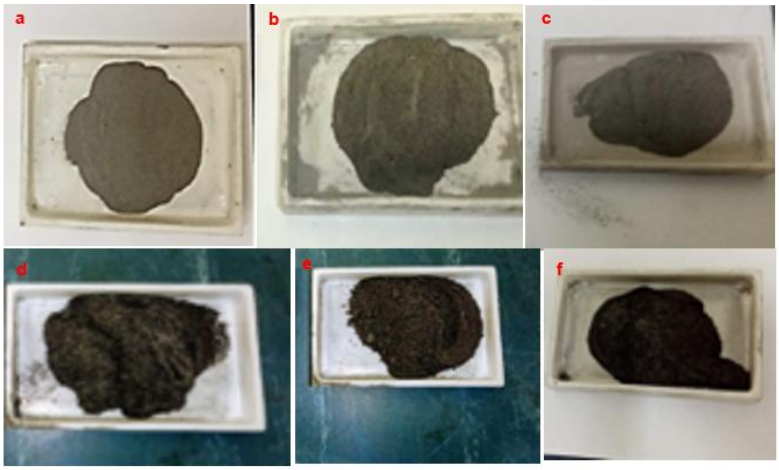

Figure A.2 Mechanically mixed powder samples after oven-drying and further manual mixing in the order of increasing vol. of CNTs in Ti6Al4V(ELI) from 3–30 % (a–f)

The powder mixtures in Figure A.3 were well blended with no separation of CNTs from Ti6Al4V(ELI). The samples darkened at higher volumes of CNTs in Ti6Al4V(ELI), more especially at 20–30 %. Powder samples that were mixed mechanically after initial treatment with ethanol exhibited homogeneity with no segregation of the two powders observed. Clearly, the use of a tool to assist in the manual mixing process was effective in blending the two powder materials.

Section A.2.1.2 Turbula mixed powder samples

Mixing of CNT and Ti6Al4V(ELI) powders, with the former first dispersed in ethanol, was carried out at various speeds to try and establish the right speed of operation to minimise separation of the two powders. The samples were mixed at 140 rpm and 180 rpm for 30 minutes at each volume fraction for volume fractions of CNTs of 3 %, 8 %, 15 %, and 20 %. At 25 % and 30 % vol. CNTs, the samples were mixed at a higher speed of 350 rpm for 30 minutes because of the increased amount of CNTs present in the mixture.

The images of two samples for 3% vol. of CNTs that were mixed at 140 rpm for the first sample and the second sample at 180 rpm are shown in Figure 3.7(a–b). It was

© Central University of Technology, Free State

observed from Figure A.3(a) that in the case where a speed of 140 rpm speed was used, there was less segregation of CNTs away from the Ti6Al4V particles compared to the sample where a speed at 180 rpm (Figure A.3(b)) was used. This is attributed to the centrifugal forces created by the 3D mixer, which increased as the speed of rotation increased.

Figure A.3 Turbula mixed samples of 3 % vol. of CNTs in Ti6Al4V(ELI)

The images of two samples for 8% vol. CNTs that were mixed, one at a speed of 140 rpm and the other at 180 rpm, are shown in Figure A.4(a–b). The samples showed segregation in both instances. However, at 180 rpm (Figure 3.8(b)), the segregation was higher. The sample that was mixed at the lower rotational speed of 140 rpm (Figure A.5(a)) also shows some degree of blending, in addition to the segregation of CNTs.

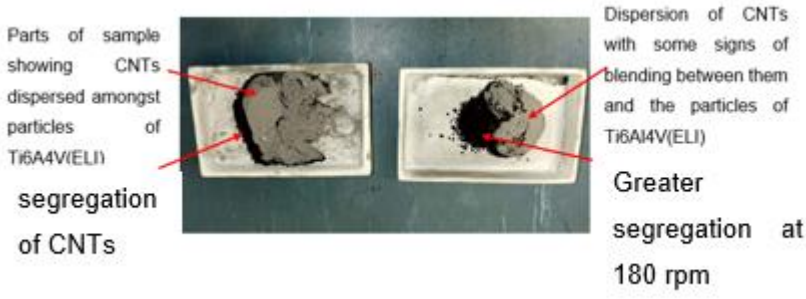

Figure A.4 Turbula mixed samples of 8 % vol. of CNTs in Ti6Al4V(ELI)

The images of the samples at a 15 % vol. CNTs are shown in Figure 3.9(a–b). In the case where a rotational speed of 140 rpm (Figure 3.9(a)) was used for the first sample, the blending of CNTs and Ti6Al4V particles was clearly evident. This was not so when a rotational speed of 180 rpm (Figure 3.9(b)) was used. The mixture showed small amounts of dispersion and large amounts of segregated CNTs that aggregated together.

© Central University of Technology, Free State

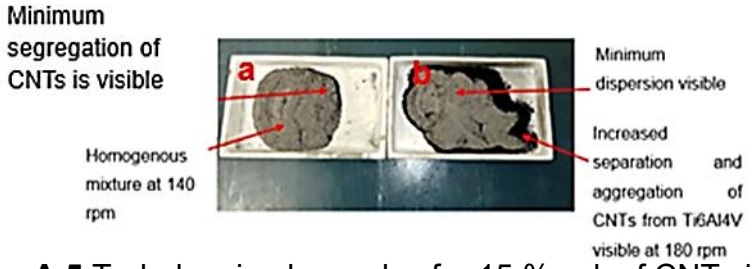

Figure A.5 Turbula mixed samples for 15 % vol. of CNTs in Ti6Al4V(ELI)

The images of the samples for 20 % vol. CNTs are presented in Figure 3.10. At this volume fraction, segregation of the CNTs was visible at the lower rotational speed of the sample of 140 rpm (Figure A.6), and thus a homogenous mixture was not achieved. The second sample that was mixed at a rotational speed of 180 rpm (Figure A.6) showed even greater separation compared to the first sample at 140 rpm. The CNTs surrounded the Ti6Al4V matrix and did not mix into the matrix.

Figure A.6 Turbula mixed samples for 20 % vol. of CNTs dispersed in Ti6Al4V(ELI)

The images of samples for 25 % vol. and 30 % vol. CNTs shown in Figure A.7(a & B) exhibited no homogeneity of the two powders but rather a large segregation of CNTs. The two samples were mixed at a rotational speed of 350 rpm due to the increased amount of CNTs in the Ti6Al4V matrix.

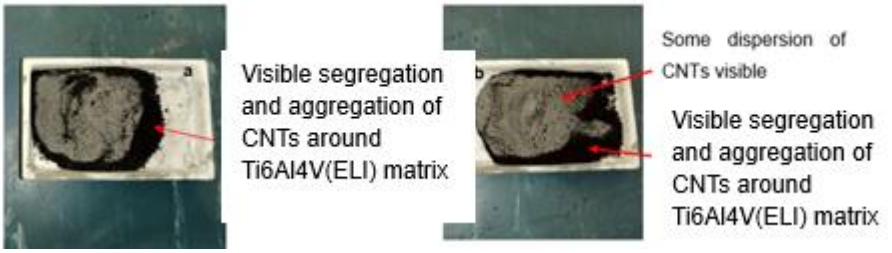

Figure A.7 Turbula mixed samples for (a) 25 % vol. of CNTs, and (b) 30 % vol. of CNTs dispersed in a Ti6Al4V (ELI) with turbula mixing

© Central University of Technology, Free State

Section A.2.1.3 Combined mixing powder samples

To correct the shortcoming of the segregation of CNTs observed for turbula mixing, an approach was adopted first to apply manual mixing, followed by turbula mixing, and then further manual mixing (combined mixing). Sonication of the CNTs dispersed in ethanol was first carried out for 90 minutes per sample. Ti6Al4V powder was then weighed and added to this slurry of CNTs. The same tool was used in manual mixing to mix the two powders mechanically. This was followed by turbula mixing at 350 rpm for a short period of 10 minutes, followed by further manual mixing. The samples obtained from this process did not show any segregation of CNTs from the Ti6Al4V particles. The initial manual mixing is thought to have helped break up the van der Waal forces holding the CNTs together, which normally causes them to agglomerate. Though subsequent turbula mixing did result in the segregation of the two powders, the shortened time of rotation minimised this process. Applying further manual mixing reduced the segregation caused by turbula mixing.

It had been observed earlier during turbula mixing that mixing the samples in their completely dry form promoted the segregation of CNTs from the Ti6Al4V. Therefore, the samples in the present case were not dried completely in the oven drier before going through the turbula mixer. Rather, they were dried just enough to allow them to mix properly in the turbula mixer and thereafter dried completely to the powder form.

Figure A.8 shows the images of powder samples for (a) 3 % vol. of CNTs, (b) 8 % vol. of CNTs, (c) 15 % vol. of CNTs, (d) 20 % vol. of CNTs, (e) 25 % vol. of CNTs, and (f) 30 % vol. of CNTs in Ti6Al4V(ELI). Figure A.8(a) showed the powder mixture with dispersion of CNTs in ethanol, for which there was no evidence of dispersion or agglomeration of CNTs. The other images in this figure, while showing no segregation of CNTs, did show evidence of dispersion of the CNTs. This is a good indication that employing sonification, manual mixing, followed by turbula mixing and then further manual mixing achieved good, blended mixtures.

© Central University of Technology, Free State

Figure 8.A Combined mixing powder samples at (a) 3 % vol. of CNTs, (b) 8 % vol. CNTs, (c) 15 % vol. CNTs, (d) 20 % CNTs, (e) 25 % CNTs, and (b) 30 % vol. of CNTs dispersed in a Ti6Al4V (ELI) matrix

Section A.2 Powder samples from tertiary mixing

Figure 4(a) shows dry powder mixtures of SDS and CNTs, Figure A.9(b) typical slurry mixtures of SDS, CNTs, ethanol, and Ti6Al4V(ELI), while Figure A.9(c) shows a final mixture of all three powders in zirconium plates, destined for oven-drying, all following the process of mixing described in section 3.1.4 in Chapter 3.

Figure A.9 Powder mixtures at various stages of mixing (a) mixture of CNTs and SDS, (b) slurry comprising CNTs, SDS, Ti6Al4V(ELI) and ethanol, (c) slurry placed on zircon plates for oven-drying

Oven-drying produced a mixture with a hard surface. Figure A.10 shows oven-dried mixtures of SDC, CNTs and Ti6Al4V(ELI) with hard surfaces that sometimes broke down into flakes, as shown in Figure A.10(b). Both of these then required more mechanical work to ensure there were no lumps in them.

© Central University of Technology, Free State

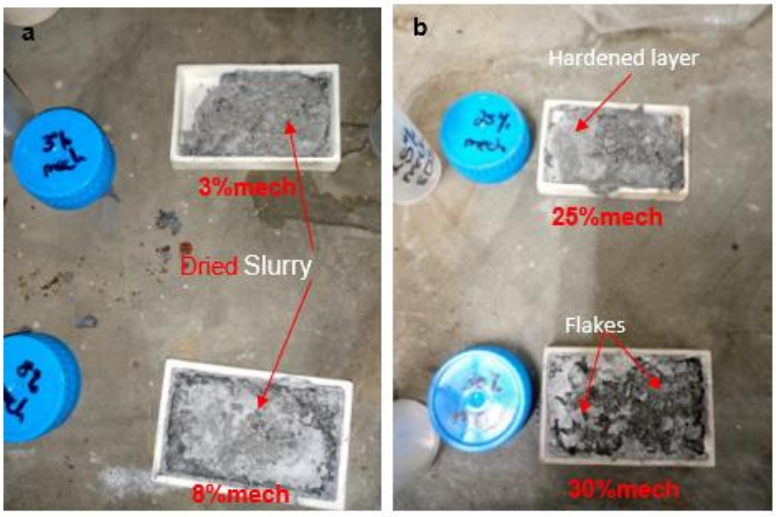

Figure A.10 Powder samples after oven-drying (a) 3 % and 8 % CNTs powder samples, and (b) 25 % and 30 % CNTs with hardened top layer and flakes

The mixed and dried powder samples at each volume fraction of CNTs are shown in Figure A.11.

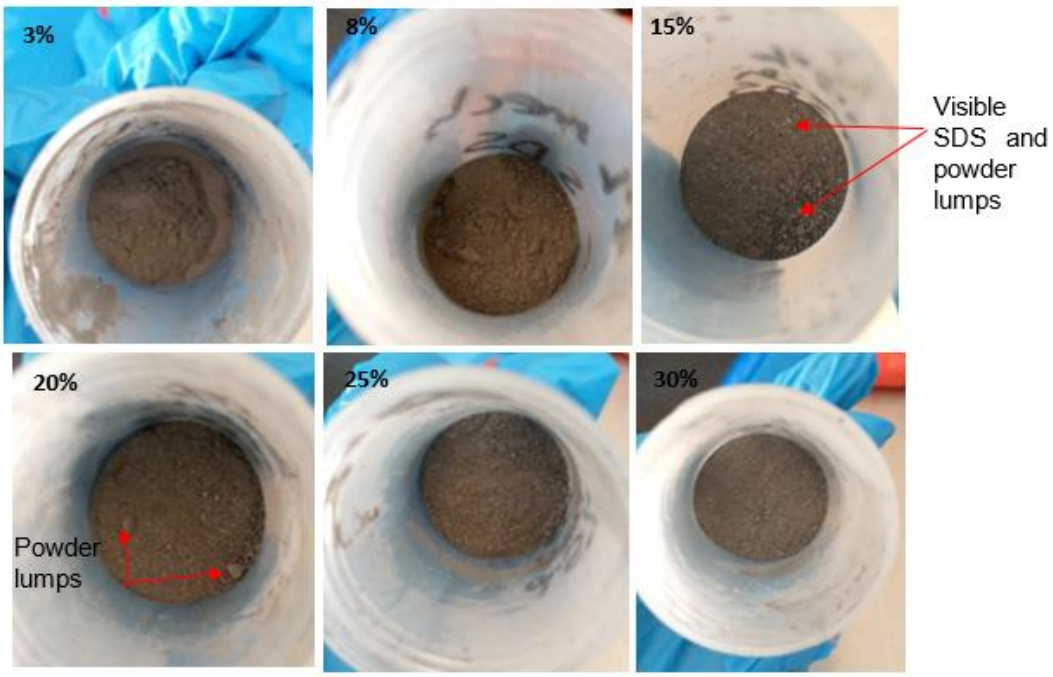

Figure A.11 Powder samples for various volume fraction of CNTs

The 3 % vol. sample of CNTs mixed with SDS powder did not have any flakes and exhibited few visible SDS particles. The 8 % vol. sample of CNTs mixed with SDS powder showed few visible SDS particles, with no lumps of powder mixture. In the

© Central University of Technology, Free State

15 % vol. sample of CNTs mixed with SDS powder, more SDS particles were visible compared to the case for the 3 % and 8 % CNTs/SDS powder samples. Lumps of mixed powder were also visible in this sample. The 25 % sample of mixed CNTs/SDS powders also has visible SDS particles and lumps of mixed powder. The 30 % sample of mixed CNTs/SDS powders exhibited SDS particles but had fewer lumps of mixed powder. It was observed that as the percentage of CNTs increased, a hard layer formed on the surface of slurries during oven-drying. This required mechanical work to break it down, and thus, more lumps of powder were present at the higher volume fractions of CNTs. For all the powder samples, a second round of oven-drying was applied to ensure that the lumps of powder formed were dry enough to be broken down easily by mechanical working. The powder samples for the 15 %, 20 %, 25 %, and 30 % volume fractions of CNTs had a grainy texture in contrast to the case for 3 % and 8 % CNTs/SDS samples of mixed powder that exhibited none.

The spheres had rough surfaces, which affected the mixing process due to powder sticking to their surfaces during the turbula mixing process. It is likely that this affected the volume fractions of the powders; however, this will need to be quantified by determining the volume fractions before and after to calculate how much of it was lost.

Figure A.12(a–c) shows mixed and oven-dried powder samples at various volume fractions of CNTs.

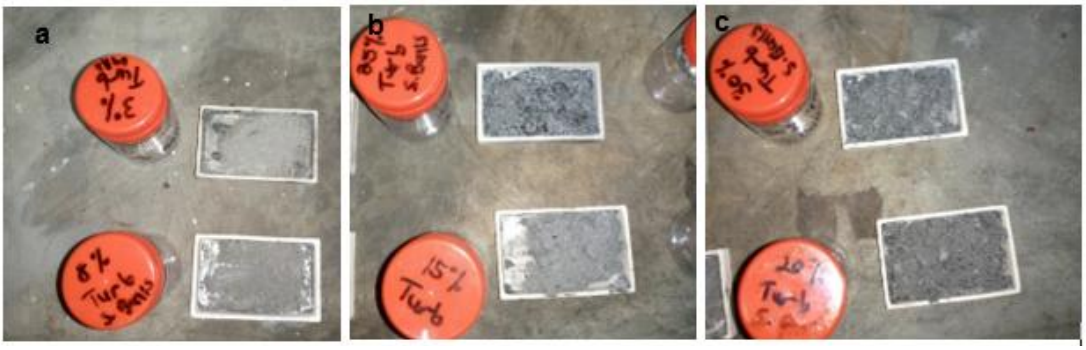

Figure A.12 Powder samples after oven-drying (a) 3 % and 8 % vol. CNTs/SDS powder samples, (b) 15% and 25% vol. CNTs/SDS powder samples, (c) 20 % and 30 % vol. CNTs/SDS powder samples

Figure A.13 shows combined mixed powders after oven-drying.

© Central University of Technology, Free State

Figure A.13 Powder mixtures after oven-drying (a) 3 % vol. CNTs, (b) 8 % vol. CNTs, (c) 15 % vol. CNTs, (d) 20 % vol. CNTs, (e) 25 % vol. CNTs, and (f) 30 % vol. CNTs

The powder samples after turbula and manual mixing are shown in Figure A.14. The powder sample for 3 % vol. CNTs exhibited small grains of mixed powder, with the SDS visible as white particles amongst them. No lumps of powder were visible in this sample. At 8 % and 15 % vol. CNTs, lumps of powder were visible, as indicated by the yellow arrows in the figure. The samples of mixed powder at 20 %, 25 % and 30 % vol. of CNTs exhibited large grains in the powder comprising of SDS and CNT powders, which was thought to be due to the increased volume content of CNTs.

© Central University of Technology, Free State

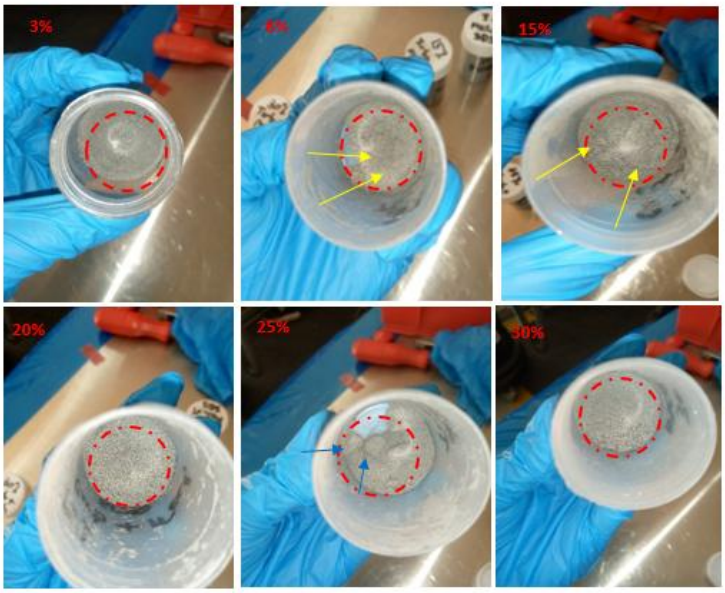

Figure A.14 Mixed samples of powder for combined mixed CNTs/Ti6Al4V(ELI) powder samples ranging between 3 %–30 % vol. of CNTs

© Central University of Technology, Free State

APPENDIX B

SABINANO
Innovation In Carbon Nanotechnology, Research & Development And Industrial Applications

SABINANO (PTY) LTD
200 Malibongwe Drive, Strijdom Park, Randburg, 2194, Johannesburg

SabinanoTubes™

Multiwalled Carbon Nanotubes 8-15 nm: Technical Specifications

Property	Specification
Synthesis Process	Catalytic chemical vapour deposition
Purification process	Acid treatment chemistry
Outer diameter	8 – 15 nm (average 10 nm)
Inside diameter	2 – 5 nm
Purity (carbon basis)	> 98 wt%
Length	~ 50 – 150 µm
Specific surface area	~ 270 m^2/g

Note: Analysis of CNT samples were independently done by the DSI-CSIR National Nanotechnology Innovation (TEM, SEM, EDS, BET) and the University of the Witwatersrand (TEM, TGA) and the University of South Africa (XRD).

Tel: (+2711) 709 4798 Email: info@sabinano.co.za web address: www.sabinano.co.za
Registration number: 2017/254908/07 Tax number: 90239830228

© Central University of Technology, Free State

Central University of Technology, Free State

SABINANO
Innovation In Carbon Nanotechnology, Research & Development And Industrial Applications

SABINANO (PTY) LTD
200 Malibongwe Drive, Strijdom Park, Randburg, 2194, Johannesburg

Transmission electron microscopy (TEM) analysis

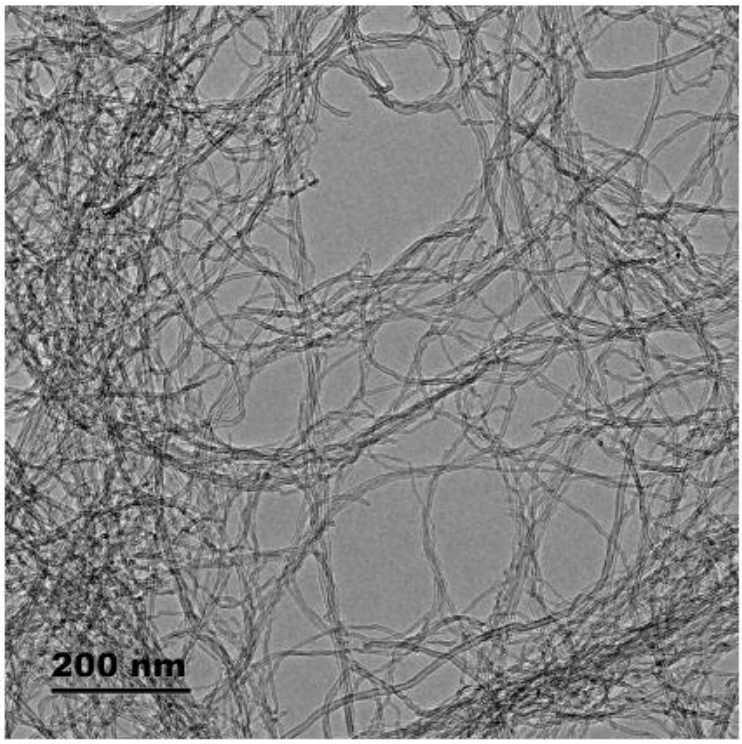

Tel: (+2711) 709 4798 Email: info@sabinano.co.za web address: www.sabinano.co.za
Registration number: 2017/254908/07 Tax number: 90239830228

© Central University of Technology, Free State

Central University of Technology, Free State

SABINANO
Innovation In Carbon Nanotechnology, Research & Development And Industrial Applications

SABINANO (PTY) LTD
200 Malibongwe Drive, Strijdom Park, Randburg, 2194, Johannesburg

Scanning electron microscopy (SEM) analysis

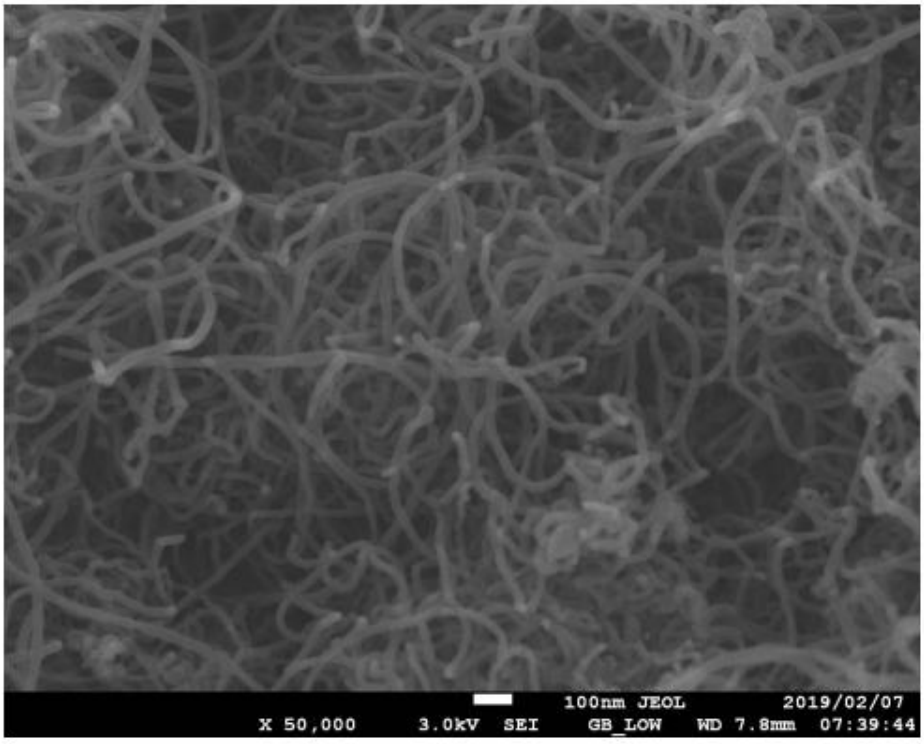

© Central University of Technology, Free State

Energy Dispersive X-ray Spectroscopy (EDS) analysis

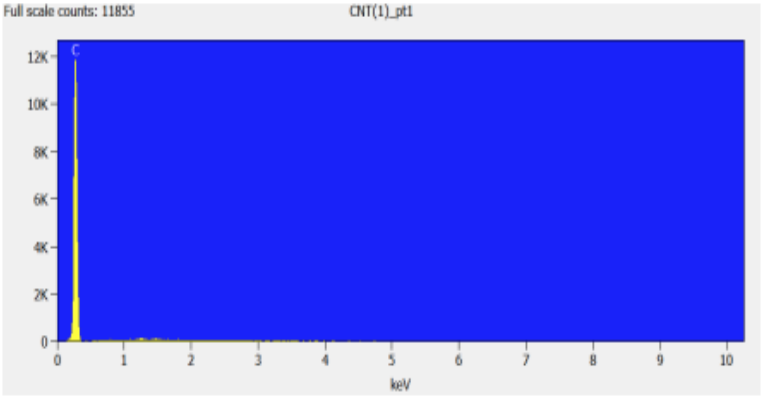

WDS Setup | WDS Acquisition Status | P&S Select | Analysis Automation
Element Setup | Analysis Setup | Compare Information | Quant Results | Processing

```
Thu Sep 26 11:00:14 2019
Filter Fit  Chi² value: 961.557
Correction Method: Proza (Phi-Rho-Z)
Acc.Voltage: 15.0 kV    Take Off Angle: 29.9°

Element     Element     Norm.     Atom %     Compnd     Compnd     Norm.
 Line         Wt.%       Wt.%                Formula      Wt.%     Compnd
C  K          100.0      100.0      100.0    C            100.0      100.0
           ----------  ----------  ----------             ----------  ----------
Total        100.0      100.0      100.0                  100.0      100.0
```

© Central University of Technology, Free State

APPENDIX C

The details of the risk assessment carried out presently is contained in the table appended below that is based on a template used at CRPM.

REFERENCE: OCCUPATIONAL USE OF CARBON NANOTUBES	LEVELS OF RISK RANGE FROM 1 – 5 IN ORDER OF SEVERITY. Level 1 - low, level 2 – moderate, level 3 – high, level 4 – very high, I level 5 – catastrophic.	**REV**	**0**
`DATE: 09/02/2021			

SCOPE OF RISK ASSSESSMENT: MINIMIZE HUMAN EXPOSURE TO UNBOUND ENGINEERED NANOSCALE PARTICLES

No.	**POTENTIAL HAZARD**	**EXPOSURE ROUTES**	**POSSIBLE HEALTH RISKS**	**LEVEL OF RISK**	**OCCURENCE**	**RISK INDEX**	**ACTIONS TO MINIMIZE RISK (MITIGATION)**	**LEVEL OF RISK**	**OCCURENCE**	**RISK INDEX**	**REFERENCE**
1	Physiochemical factors such as particle size[1], and size², surface modifications can possibly affect the toxicity of the material	May enter the eyes during occupational exposure. Inhalation during occupational exposure. Dermal exposure (particles may enter through skin) during occupational	May cause eye irritation. May cause respiratory irritation or formation of lung granulomas (small areas of swelling). Potential hazards unknown.	3 5	1 2	3 10	Avoid release to environment by always keeping the nano tubes in enclosed containers when not in use. Knowledge of the chemical properties can help the user take safety precautions	2 3 2	1 2 1	2 6 2	SabiNano safety data sheet Su, P., Haghpanah, B., Doerr, W. W., Karimi, Z., Hassan, S., Gritzo, L., Busnaina, A. A., & Vaziri, A. (2014). Decontamination of surfaces exposed to carbon-based nanotubes and nanomaterials. *Journal of Nanomaterials*, *2014*. https://doi.org/10.1155/2014/249603 ASTM E2535-07(2018)

© Central University of Technology, Free State

		exposure.					during handling Wearing of PPE (masks gloves, sleeves, coats, gowns, smocks, safety glasses, dust goggles and encapsulating units, air purifying respirators) to avoid inhaling and direct contact with the nano tubes				
2	Physical properties such size distribution, [3]*shape, surface area, agglomeration state, massy, [4]*density, [5]*length, and[6]* size identified as a hazard	May enter the eyes during occupational exposure. Inhalation during occupational exposure. Dermal exposure (particles may enter through skin) during occupational exposure.	May cause eye irritation. May cause respiratory irritation or formation of lung granulomas (small areas of swelling). Potential hazards unknown.	5 5 5	3 2 2	15 10 10	Avoid release to environment by always keeping the nano tubes in enclosed containers when not in use. Knowledge of the physical properties can help the user take safe precautions during handling Wearing of PPE (masks gloves,	3 2	2 1	6 2	ASTM E2535-07(2018)

© Central University of Technology, Free State

							sleeves, coats, gowns, smocks, safety glasses, dust goggles and encapsulating units, air purifying respirators) to avoid inhaling and direct contact with the nano tubes				
	Direct manual handling of large quantities	Dermal exposure (particles may enter through skin) during occupational exposure	Potential hazards unknown	3	1	3	Wearing of PPE (masks gloves, sleeves, coats, gowns, smocks, safety glasses, dust goggles and encapsulating units, air purifying respirators)	3	2	6	ASTM E2535-07(2018) *OSHA Technical Manual (OTM) | Section VIII: Chapter 1 - Chemical Protective Clothing* |. https://www.osha.gov/dts/osta/otm/otm_viii/otm_viii_1.html
		Ingestion during occupational exposure	May cause liver damage,	5	2	10	Wearing of a full face mask to avoid ingesting the carbon nano tubes.	2	2	4	
		Eye exposure					Wearing of a full face mask to avoid ingesting the carbon nano tubes.	?	?	?	

© Central University of Technology, Free State

1	Accidental release/ spill	Use of vessels or containers that are open to the atmosphere. During the addition or removal of nano tubes from their vessels or containers.	The spilled particles may enter the body through the eyes, skin, inhalation and through ingestion.	3	1	3	Recover released /spilled particles using HEPA-filter vacuum cleaners . wetting powders down, using a damp cloth and applying absorbent material (kitty litter, or vermiculite). The preferred method is damp cleaning with soaps or cleaning oils.	3	1	3	ASTM E2535-07(2018) Amoabediny, G., Naderi, A., Malakootikhah, J., Koohi, M. K., Mortazavi, S. A., Naderi, M., & Rashedi, H. (2008). Guidelines for Safe Handling, Use and Disposal of Nanoparticles. *Journal of Physics: Conference Series OPEN ACCESS Nanosafe*, *170*, 12037. https://doi.org/10.1088/1742-6596/170/1/012037 *Spill Kits, Spills, and Waste Disposal of Nanomaterials at UAB Spill Kits*.
							Remove individuals from the area and restrict access only to designated cleaning personnel Decontaminate (using the process mentioned under prolonged exposure of nano materials) the exposed area and dispose	2	1	2	

© Central University of Technology, Free State

							of the equipment and material used during cleaning				
	Ventilation control systems	The carbon nano tubes can get trapped in the local ventilation systems (filters, traps, baffles, clean-outs, and containment technologies)	Trapped particles may be released to the environment during cleaning and maintenance of the equip ment.	5	5	15	Avoid creating turbulence in the vicinity of the powders.	4	2	8	ASTM E2535-07(2018)
							To handle dry powder low-velocity chemical hoods, cabinets, vented safety balance enclosures, and glove boxes should be used	3	2	6	
	Thermal decomposition (the walls will begin to deteriorate and form bundles) or combustion may produce smoke	Ventilation and filtration systems	Decomposition of nano particles leads to agglomeration (greater than 500 nm) and deposition into the respiratory tract	5	2	10	Conduct regular and timely inspection of equipment (including ventilation and filtration systems	2	1	2	ASTM E2535-07(2018)
							Use minimum heating temperature	2	2	4	
	Prolonged exposure of nano materials	Skin, eyes and inhalation and ingestion exposure.	Prolonged exposure can lead to dermal defects, inflammation, interstiti	5	4	20	Decontaminating equipment (instruments, piping, process units, and	3	2	6	ASTM E2535-07(2018) Su, P., Haghpanah, B., Doerr, W. W., Karimi, Z., Hassan, S., Gritzo, L., Busnaina, A. A., & Vaziri, A. (2014). Decontamination of surfaces exposed to carbon-based nanotubes and nanomaterials. *Journal of Nanomaterials*,

© Central University of Technology, Free State

			al fibrosis, mutagenesis, lung tumours, and vascular defects				others) using HEPA filters to trap particles suspended in the air, using a physical force (wiping, brushing) on surfaces to remove the particles or using a fluid (such as ultrasonic, megasonic cleaning (a type of acoustic cleaning), or a fluid jet). Once visible particles are removed, use wet or microfiber cleaning cloths to remove residual particles from surfaces.				*2014*. https://doi.org/10.1155/2014/249603 Oberdörster, G., Castranova, V., Asgharian, B. and Sayre, P., 2015. Inhalation exposure to carbon nanotubes (CNT) and carbon nanofibers (CNF): Methodology and dosimetry. *Journal of Toxicology and Environmental Health, Part B*, *18*(3-4), pp.121-212.

© Central University of Technology, Free State

							Exposure should be limited to 0.1 fibers per cubic centimetre during an 8-hour period.	4	2	8	

[1]*Studies conducted on air pollution and mineral dust particles showed that inhaled particles with a size <100nm caused lung injury through reactive oxygen species (ROS), inflammation, and cell damage.

[2]*Acid purified MWCNTs reduce cell viability and increase inflammatory mediators

[3]*The fibre-like character of carbon nanotubes is of a concern in particular when the aspect ratio is greater than 3:1 with a length greater than 5 micron as fibers are not easily cleared from the body

[4]*Concentration levels of multiwalled carbon nanotubes (MWCNTs) from 3 to 30µg/ml significantly induce death of the murine bone marrow-derived dendritic cells (BMDCs), but for RAW264.7 cells a concentration of 300µg/ml MWCNTs presented no cytotoxicity

[5]*Long MWCNTs are cytotoxic to macrophages, whilst short MWCNTs do not induce cytotoxicity with the exception short length of 0.6µm which increased ROS generation in human alveolar macrophages. long MWCNTs (20µm) significantly decrease cell viability.

[6]*Nano toxicological research shows that the toxicology of nanomaterials is inversely related to particle size. The study shows MWCNTs <8nm diameter are more toxic than larger diameter MWCNTs. In contrast MWCNTs>50nm diameter was more toxic than smaller diameter size in RAW264.7 cells. In a different study thin MWCNTs ~50nm induced cytotoxicity and carcinogenicity mesothelial cells, however thick MWCNTS ~150nm were less toxic, carcinogenic, and inflammogenic.

© Central University of Technology, Free State

APPENDIX D

Powder Properties

EOS Titanium Ti64 Grade 5 powder is classified ex Grade 5 titanium alloy according to ASTM B348. The chemical composition is in compliance with standards ISO5832-3, ASTM F1472, ASTM F2924, and ASTM F3302.

Powder chemical composition (wt-%)

Element	Min.	Max.
Ti	Balance	
Al	5.50	6.75
V	3.50	4.50
O	-	0.20
N	-	0.05
C	-	0.08
H	-	0.015
Fe	-	0.30
Y	-	0.005
Other elements, each	-	0.10
Other elements, total	-	0.40

Powder particle size

Generic particle size distribution	20 – 60 µm

SEM picture of EOS Titanium Ti64 Grade 5 powder.

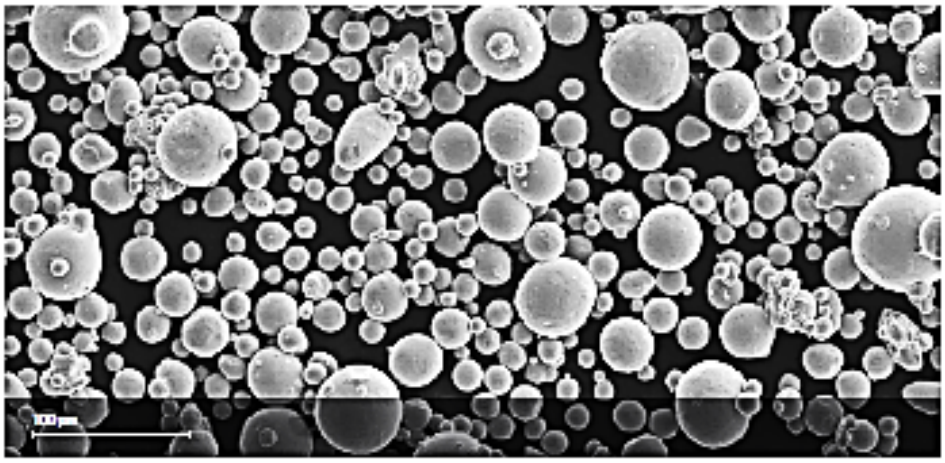

© Central University of Technology, Free State

APPENDIX E

Section E.1 Detailed Images of Manual Mixed Powder Samples

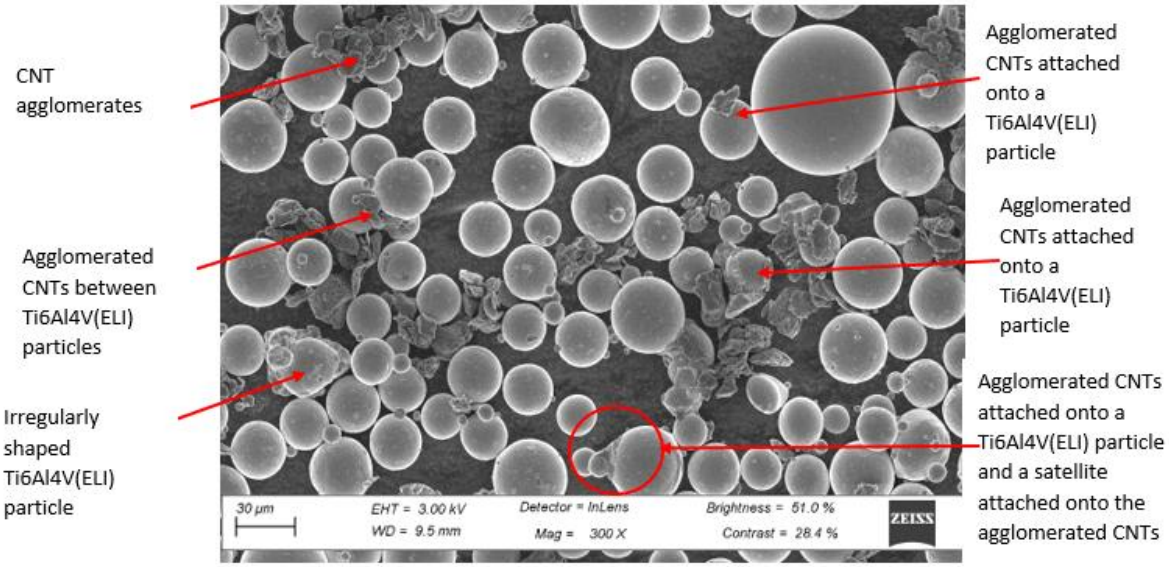

SCANNING ELECTRON MICROSCOPE image of 3% vol. CNTs in a Ti6Al4V(ELI) matrix at 300x

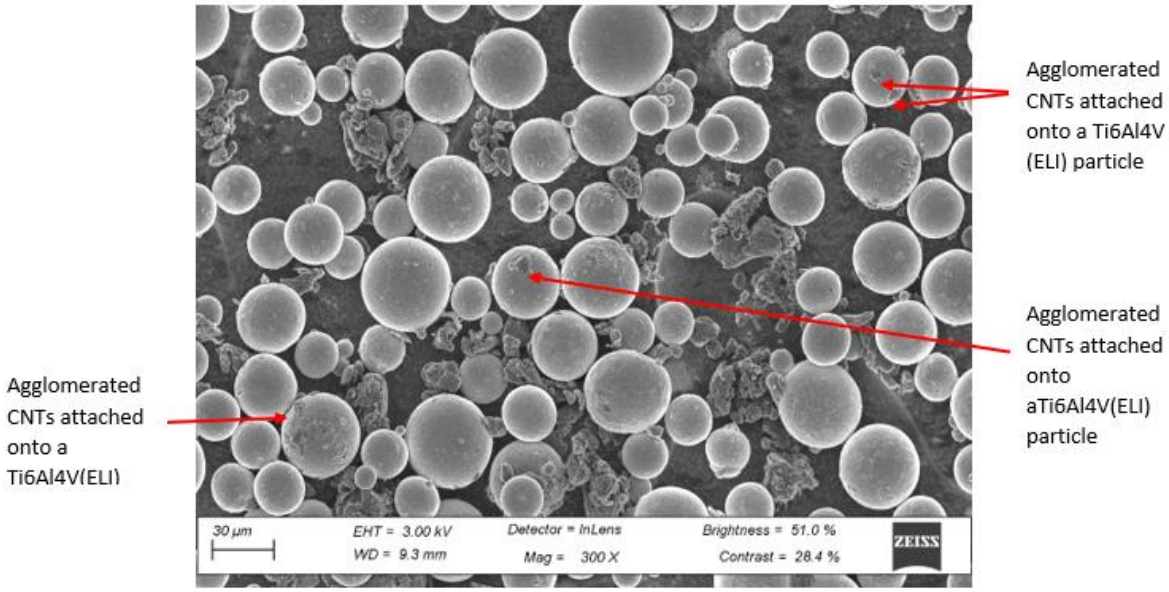

SCANNING ELECTRON MICROSCOPE image of 8% vol. CNTs in a Ti6Al4V(ELI) matrix at 300x

© Central University of Technology, Free State

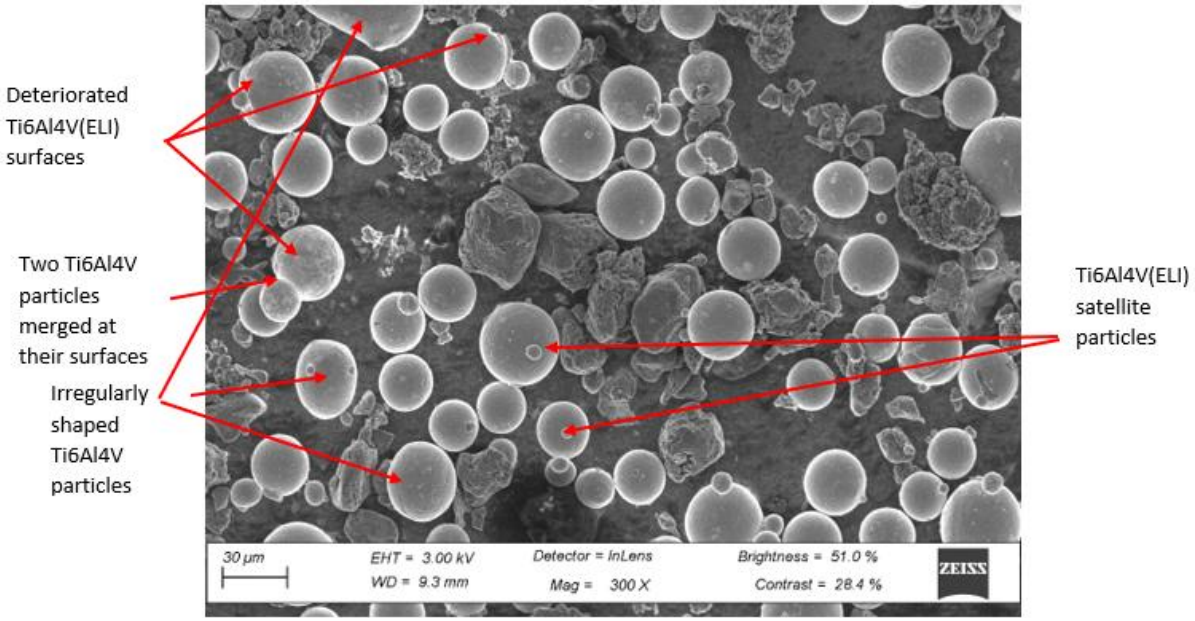

SCANNING ELECTRON MICROSCOPE image of 15% vol. CNTs in a Ti6Al4V(ELI) matrix at 300x

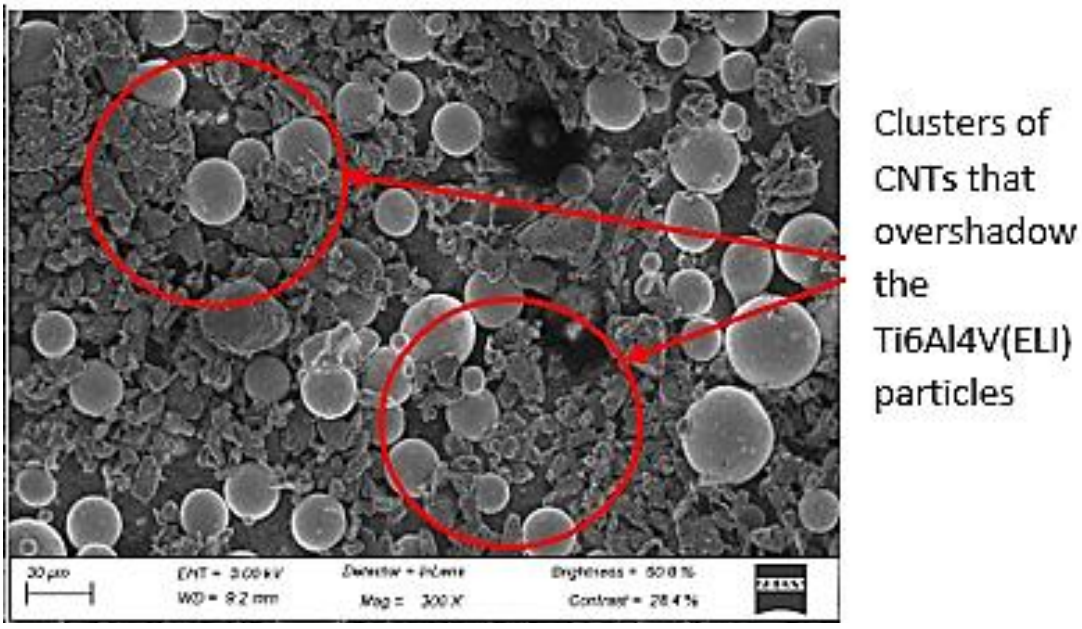

SCANNING ELECTRON MICROSCOPE image of 20% vol. CNTs in a Ti6Al4V(ELI) matrix at 300x

© Central University of Technology, Free State

Section E.1 Detailed Images of Combined Mixed Powder Samples

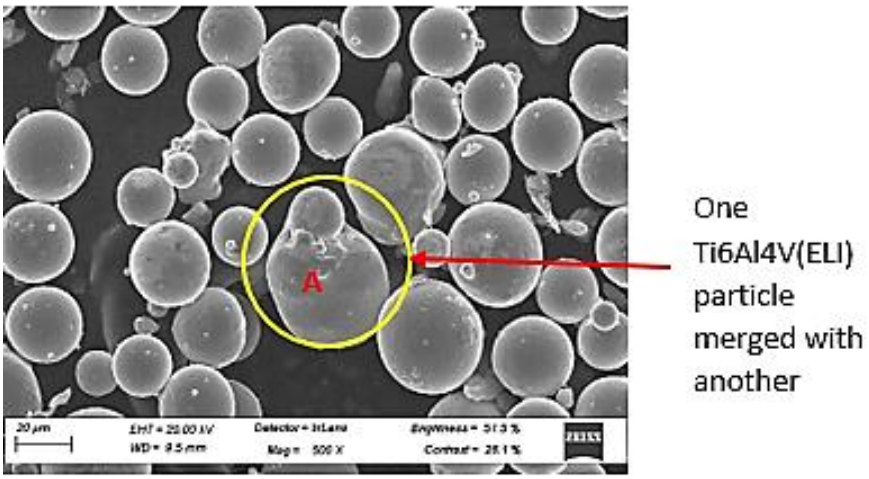

SCANNING ELECTRON MICROSCOPE image of 8% vol. CNTs in a Ti6Al4V(ELI) matrix at 300x

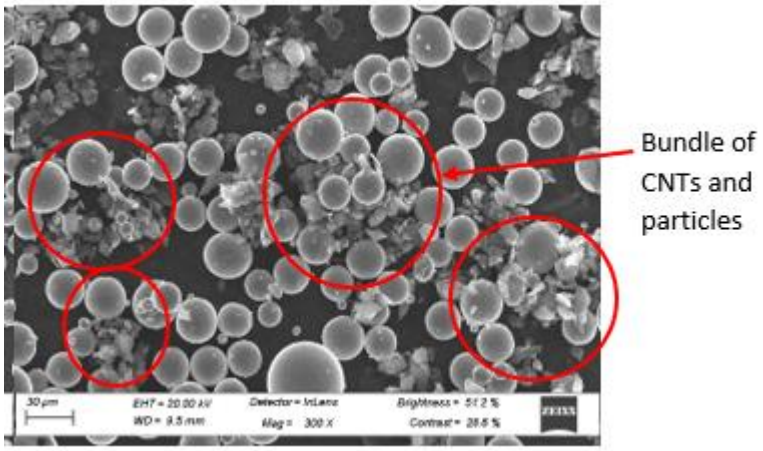

SCANNING ELECTRON MICROSCOPE image of 8% vol. CNTs in a Ti6Al4V(ELI) matrix at 300x

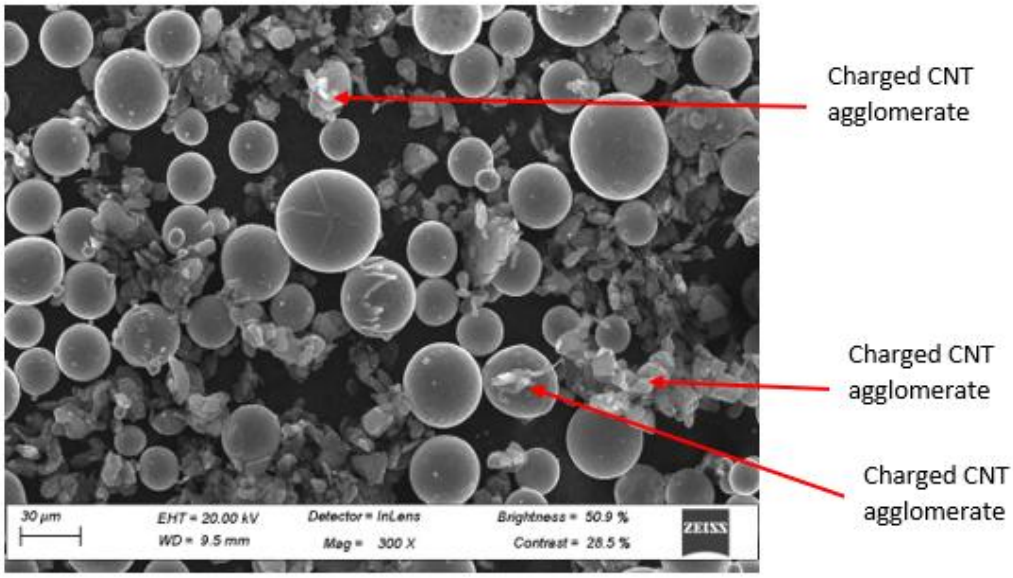

SCANNING ELECTRON MICROSCOPE image of 15% vol. CNTs in a Ti6Al4V(ELI) matrix at 300x

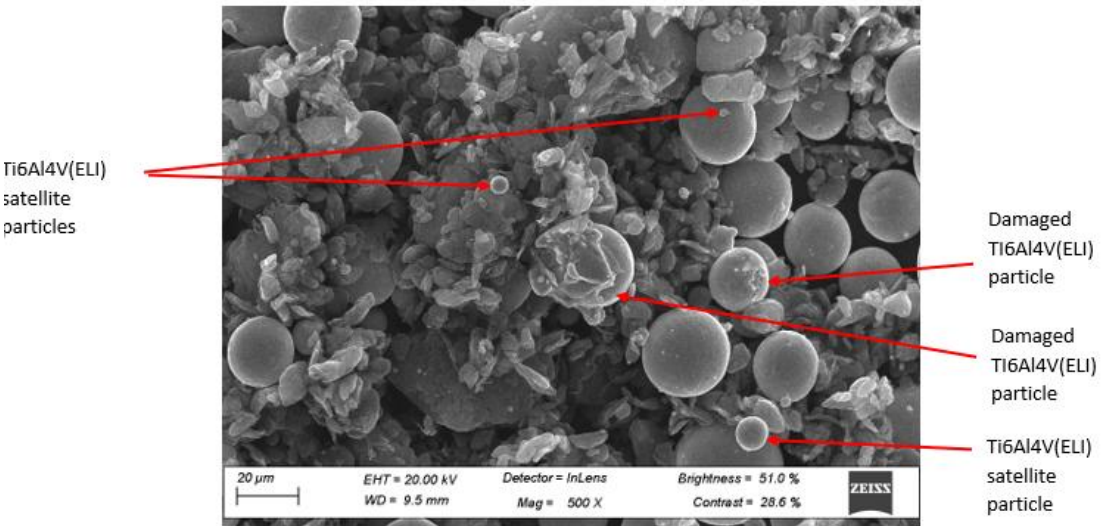

SCANNING ELECTRON MICROSCOPE image of 20% vol. CNTs in a Ti6Al4V(ELI) matrix at 300x

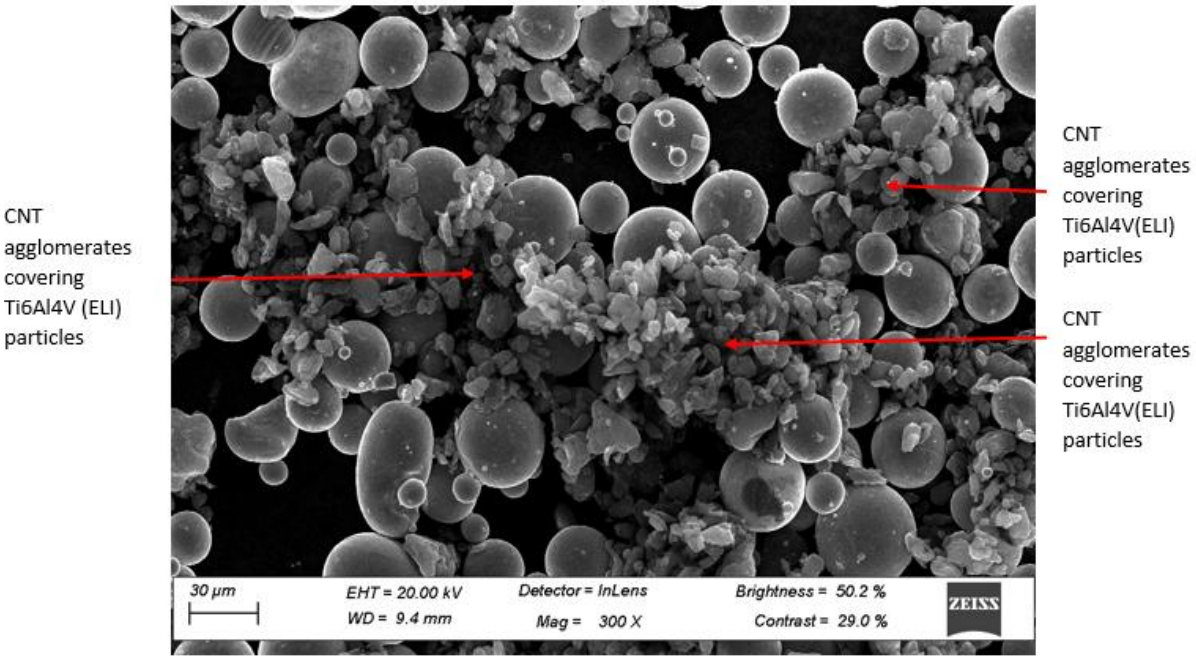

SCANNING ELECTRON MICROSCOPE image of 30% vol. CNTs in a Ti6Al4V(ELI) matrix at 300x

© Central University of Technology, Free State